To the Graduate Council:

I am submitting herewith a dissertation written by Xin-Tao Liu entitled "One and Two-Neutron Transfer Reactions with Very Heavy Ions". I have examined the final copy of this dissertation for form and content and recommend that it be accepted in partial fulfillment of the requirements for the Doctor of Philosophy Degree, with a major in Physics.

M. W. Guidry, Major Professor

We have read this dissertation
and recommend its acceptance:

S. L. Sobenser

Carrol R. Bingham

Hugo L. Scholzer

Joseph R. Peterson

Accepted for the Council:

Vice Provost
and Dean of the Graduate School

ONE AND TWO-NEUTRON TRANSFER REACTIONS WITH VERY HEAVY IONS

A Dissertation

Presented for the

Doctor of Philosophy

Degree

The University of Tennessee, Knoxville

Xin-Tao Liu

December 1988

This dissertation

is

dedicated

to my wife

Rui-Fang Zhang

ACKNOWLEDGEMENTS

I would like to thank the Nuclear Physics Group at the University of Tennessee of which I have been a member of for the past five years for offering me the position of a research assistant. Thanks go to Dr. S. P. Sorensen, Dr. C. R. Bingham, and Dr. L. L. Riedinger for their support and encouragement. Special thanks go to M. W. Guidry, my thesis advisor, for his guidance and encouragement; I also especially would like to thank him for checking the language and contents of this thesis.

I would also like to thank the two postdoctoral fellows, Dr. C. Y. Wu and Dr. S. Juutinen; I have had the pleasure to work directly with them during my stay here. A special thanks goes to Dr. C. Y. Wu for his help, advice and encouragement. I am also thankful to have been associated with my fellow students, Wayne Kincaid, Michael Carpenter, and Lane Courtney. I would like to extend one more personal thanks to Dr. X. L. Han for her contribution on the data analysis of ^{112}Sn experiment.

I would like to thank our experimental collaborators at Nuclear Structure Research Laboratory of Rochester University under the direction of Dr. D. Cline, for having good cooperation for many years and for without them the data for this thesis would not have been collected.

I also would like to thank other experimental collaborators, Dr. L. Y. Lee, Dr. M. L. Halbert, Dr. C. Baktash at Oak Ridge National Laboratory; Dr. J. O. Rasmussen and Mr. Mark Stoyer at Lawrence Berkeley Laboratory; Dr. D. G. Sarentites, Dr. T. M. Semkow at Washington University.

Finally, I greatly appreciate the opportunity I have had in discussing my research with the theoreticians, Dr. S. Landowne and Dr. C. Price at Argonne National Laboratory

I would like to end this section with some personal acknowledgements. I would like especially to thank my wife Rui-Fang Zhang and my sons Ming-Bo and

Ming-Xu for their support, encouragement, and sacrifice during many years of hard work.

ABSTRACT

The one and two-neutron transfer reactions with 637 MeV ^{116}Sn and 270 Mev and 345 MeV ^{58}Ni beams on the rare earth ^{161}Dy and ^{162}Dy targets, 325 MeV ^{58}Ni beam on the actinide ^{235}U target, and 570 MeV ^{112}Sn on the spherical nuclei ^{117}Sn and ^{118}Sn targets were measured. These measurements were performed at Oak Ridge National Laborotary using the Tandem, Cyclotron and the Spin Spectrometer.

The particle-particle-γ coincidence methold was employed to identify the reaction exit channels; the Spin Spectrometer provided the γ-ray total energy and muitiplicity to identify reaction entry channels.

In the present work, the cross sections and probabilities for one and two-neutron transfer reactions were measured; the transfer mechanism and nuclear structure effects are discussed.

Contents

1 INTRODUCTION 1

2 THEORY OF TRANSFER REACTIONS WITH HEAVY-IONS 6
2.1 General Aspects of Transfer Reactions with Heavy-ions 6
2.2 The Semi-classical Approach 9
2.3 The Distorted Wave Born Approximation (DWBA) 13
2.4 Theory for Very Heavy Ion Induced Transfer Reactions 18

3 EXPERIMENTAL TECHNIQUES 24
3.1 Experimental Methods 24
3.2 Beam and Target 27
3.3 Particle Detector 32
3.4 The Spin Spectrometer 33
3.5 Electronic Setup 36
3.6 Experimental Data 39
3.6.1 Experiments with the ^{58}Ni Beam in 1983 40
3.6.2 Experiments with the ^{116}Sn Beam in 1985 41
3.6.3 Experiments with the ^{58}Ni Beam in 1985 41
3.6.4 Additional Experiments with the ^{58}Ni Beam in 1986 41
3.6.5 Experiments with the ^{112}Sn Beam in 1987 42
3.6.6 Experiments with the ^{206}Pb Beam in 1987 42

4 DATA ANALYSIS 43
4.1 Introduction 43
4.2 Energy and Efficiency Calibration for the Ge Detectors 43
4.3 Calibration of the Spin Spectrometer 46
4.4 Unfolding of Two-Dimensional (H,K) Map 49
4.5 The Identification of Particles 50
4.6 The Reaction Q-Value 55
4.7 Identification of γ-rays and Neutrons 58
4.8 Doppler Shift Correction of γ-rays 60
4.9 Corrections for Target Contamination 60

5 EXPERIMENTAL RESULTS AND ANALYSIS 63
5.1 General Features of Data 63
5.1.1 Reaction Q-Values and Neutron Multiplicity 63
5.1.2 γ-ray Spectra 66
5.1.3 Entry-state Distributions for Total Energy and Multiplicity . 70
5.1.4 Schematic Model for One and Two-neutron Transfer 72
5.2 The Entry State Distribution and γ-ray Spectra 80
5.2.1 Experiments with 270 and 285 MeV ^{58}Ni Beams 82
5.2.2 Experiments with 345 MeV ^{58}Ni Beam 89
5.2.3 Experiments with 637 MeV ^{116}Sn Beam 89
5.2.4 Experiment with 325 Mev ^{58}Ni on the Actinide Target ^{235}U . . 99
5.3 Cross Sections for One and Two-Neutron Transfer Reactions 101
5.3.1 Introduction 101
5.3.2 Cross Section for Direct Population of the Dy Yrast States . . 103
5.3.3 Rotational Signatures for Transfer to High-Spin States 112
5.4 Probability for One and Two-Neutron Transfer Reactions 117
5.4.1 Introduction 117
5.4.2 The Probability of One and Two-Neutron Transfer Reactions with Heavy-Ions on Spherical Target Nuclei 122
5.4.3 The Probabilities of One and Two-Neutron Transfer Reactions with Heavy-Ions on Deformed Nuclei Targets 124
5.5 Pairing Effects in Transfer Reactions with Very Heavy Ions 136
5.5.1 Introduction 136
5.5.2 Two-Neutron Pairing Enhancement Factors 138

6 SUMMARY AND CONCLUSION 146

BIBLIOGRAPHY 150

VITA 159

List of Figures

1.1 Total energy vs. spin predicted for entry distributions in some (heavy-ion, xn) reactions, and the general region populated in transfer reactions with very heavy ions. Reproduced from Guidry (1985c). 4

2.1 Mechanism for transfer reactions with heavy-ions. 7
2.2 The maximum angular momentum near the turning point for some heavy ion systems in grazing collisions. Reproduced from Guidry and Kincaid (1985b) 8
2.3 Coulomb trajectories in the center-of-mass system. 11
2.4 Vector diagram for a transfer reaction A + C_2 → C_1 + B (C_1, C_2 cores; x transferred particle; A = C_1 + x, B = C_2 + x). 15
2.5 Pair transfer matrix elements for the nucleus ^{160}Dy (full line) and the gap parameter $\Delta(I) = G < A|(a^+a^+)_0(aa)_0|A >^{1/2}$ (dashed line) as a function of the angular momentum I. Reproduced from Canto *et al.* (1987). 20
2.6 Differential cross section for the ground band rotational states excited in the reaction ^{162}Dy(^{116}Sn,^{118}Sn)^{160}Dy at an energy E_{lab} = 637 MeV. Reproduced from Price *et al.* (1987). 23

3.1 A typical experimental set-up. The particle detectors are placed inside the Spin Spectrometer. 25
3.2 Schematic of a BGO Compton-suppression shield used in the Spin Spectrometer. Reproduced from Johnson *et al.* (1985). 28
3.3 ^{60}Co spectra taken with the Compton-suppression unit shown in Fig. 3.2. The heights of the full-energy peaks at 1173 and 1333 keV are off scale, but have been normalized in this data. Reproduced from Johnson *et al.* (1985). 28
3.4 A schematic view of the 25-MV HHIRF tandem accelerator system at the Oak Ridge National Laboratory. 29
3.5 Ion energy performance of the HHIRF. The curve for coupled mode is for a beam intensity of 10^{11} particles/sec. 30

3.6 (a)Geometry of the Spin Spectrometer based on the truncated pentagonal hexecontahedron. The black areas represent the twelve regular pentagons. (b) The archimedean pentagonal hexecontahedron. The polyhedron of (a) orginates from truncation of the sharp corners of the twelve groups of five pentagons of (b). Reproduced from Jääskeläinen *et al.* (1983). 35
3.7 Schematic diagram of the electronics for the Spin Spectrometer. Reproduced from Jääskeläinen, *et al.* (1983). 37
3.8 A typical schematic diagram of the electronic setup for a transfer experiment in the Spin Spectrometer. 38

4.1 Total γ-ray spectra of ^{60}Co source. The numbers indicate the total counts in the corresponding peaks. 45
4.2 The absolute efficiency curve for the ^{160}Dy + (285 MeV) ^{58}Ni experiment. 47
4.3 An (H,K)-map and the corresponding unfolded (E,M)-map. The reaction is ^{162}Dy(^{116}Sn,^{118}Sn)^{160}Dy at 637 MeV. 51
4.4 The coordinate system for the Spin Spectrometer. 52
4.5 Mass spectrum for the ^{162}Dy+ ^{116}Sn reaction. 56
4.6 The Q-spectrum for the ^{162}Dy + ^{116}Sn reaction. 57
4.7 Timing spectra of NaI detectors in the Spin Spectrometer for different angles gated on 2 - 2.8 MeV pulse heights for the ^{162}Dy+ ^{58}Ni reaction. 59
4.8 The effect of the Doppler shift correction on a typical Ge spectrum. 61

5.1 Total Q-value spectra for the reaction ^{162}Dy+ ^{58}Ni at bombarding energies above (A) and near (B) the Coulomb barrier. 64
5.2 (a) Total neutron multiplicity (K_N) spectra for the reaction ^{162}Dy+ ^{58}Ni. (b, c) The neutron multiplicity spectra of one and two-neutron transfer, and inelastic scattering, at bombarding energies above and near the Coulomb barrier. 65
5.3 Q-value spectrum gated on K_N for the ^{162}Dy+ ^{116}Sn reaction (E_{lab} = 637 MeV). 67
5.4 A particle-particle-γ coincidence spectrum for the reaction ^{58}Ni (E_{Lab}=270 MeV) + ^{161}Dy reaction. Ground band transitions in the transfer product ^{160}Dy are marked. 68
5.5 A particle-particle-γ coincidence spectrum for the ^{58}Ni (E_{Lab}=285 MeV) + ^{162}Dy reaction. Ground band transitions in the ^{160}Dy transfer product are marked. 69
5.6 Total energy vs. multiplicity for (A) ^{161}Dy(^{58}Ni,^{59}Ni)^{160}Dy and (B) ^{162}Dy(^{58}Ni,^{60}Ni)^{160}Dy. The dashed lines are the approximate ^{160}Dy yrast line, assuming no Ni excitation. 71
5.7 Low-lying bands in ^{160}Dy calculated using the cranked shell model with parameters $\beta_2 = 0.25$, $\beta_4 = 0$, $\Delta = 0.128\ \hbar\omega_0$. 74

5.8 Evolution of one-neutron transfer in the E vs. I plane. Contours of the energy window are shown as dashed lines. Discret states in the ground bands of ^{160}Dy and ^{161}Dy are indicated by horizontal lines, assuming no Ni excitation. 76
5.9 A schematic picture of a one-neutron transfer reaction populating even-even nuclei. 77
5.10 The transfer amplitudes f(r', θ') for some configurations involving only a single rare-earth neutron orbital. Reproduced from Guidry *et al.* (1981). 79
5.11 A schematic picture of a two-neutron transfer reaction populating even-even nuclei. 81
5.12 Q-value spectra gated on K_N for the reaction ^{162}Dy + ^{58}Ni. 83
5.13 (H,K) maps gated on individual ground band transitions of ^{160}Dy for the reaction ^{161}Dy(^{58}Ni,^{59}Ni)^{160}Dy. 84
5.14 (H,K) maps gated on individual ground band transitions of ^{160}Dy for the reaction ^{162}Dy(^{58}Ni,^{60}Ni)^{160}Dy. 85
5.15 Unfolded (E,M) maps gated on individual ground band transitions of ^{160}Dy for the reaction ^{162}Dy(^{58}Ni,^{60}Ni)^{160}Dy. That is, these (E,M) distributions folded with the Spin Spectrometer response correspond to the (H,K) distributions in Fig. 15.14. 86
5.16 γ-γ coincidence spectrum gated on all ground band transitions of ^{160}Dy for the reaction ^{161}Dy(^{58}Ni,^{59}Ni)^{160}Dy. 87
5.17 γ-γ coincidence spectrum gated on some ground band transitions of ^{160}Dy for the reaction ^{162}Dy(^{58}Ni,^{60}Ni)^{160}Dy at E_{lab} = 285 MeV. The Doppler shift correction is (a) for the target-like ion, (b) for the projectile-like ions. 88
5.18 Q-value spectra gated on K_N for the reaction ^{162}Dy + ^{58}Ni (345 MeV). 90
5.19 (E, M) maps gated on strong ground band transitions of ^{160}Dy for the reactions ^{161}Dy(^{58}Ni,^{59}Ni)^{160}Dy and ^{162}Dy(^{58}Ni,^{60}Ni)^{160}Dy at E_{lab} = 345 MeV. 91
5.20 Particle-γ coincidence spectra for the reaction ^{161}Dy(^{58}Ni,^{59}Ni)^{160}Dy at E_{lab} = 345 MeV. Ground-band transitions in ^{160}Dy are marked. . . . 92
5.21 Particle-γ coincidence spectra for the reaction ^{162}Dy(^{58}Ni,^{60}Ni)^{160}Dy at E_{lab} = 345 MeV. Ground-band transitions in ^{160}Dy are marked. . . . 93
5.22 (H,K) maps gated on ground band transitions of ^{160}Dy for the reaction ^{161}Dy(^{116}Sn,^{117}Sn)^{160}Dy, E_{lab} = 637 MeV. 94
5.23 (H,K) maps gated on ground band transitions of ^{160}Dy for the reaction ^{162}Dy(^{116}Sn,^{118}Sn)^{160}Dy, E_{lab} = 637 MeV. 95
5.24 Unfolded (E,M) map gated on ground band transition of ^{160}Dy for the reaction ^{161}Dy(^{116}Sn,^{117}Sn)^{160}Dy, E_{lab} = 637 MeV. 96
5.25 Particle-γ coincidence spectrum taken at the grazing angle for the one-neutron pickup reaction ^{161}Dy(^{116}Sn,^{117}Sn)^{160}Dy at E_{lab} = 637 MeV. 97

5.26 Particle-γ coincidence spectrum taken at the grazing angle for the two-neutron pickup reaction ^{162}Dy(^{116}Sn,^{118}Sn)^{160}Dy at E_{lab} = 637 MeV. Ground-band transitions in ^{160}Dy are marked. 98
5.27 Total γ-ray energy and multiplicity plot for the one-neutron pickup reaction ^{235}U(^{58}Ni,^{59}Ni)^{234}U. The dashed line is the approximate yrast line for ^{234}U, assuming no ^{58}Ni excitation. 100
5.28 γ-ray spectra integrated over lab angle between 104° and 152° around the grazing angle $\sim$ 130° for the reaction ^{235}U + 325 MeV ^{58}Ni. . . 102
5.29 Summed NaI γ-ray energies in the inelastic and transfer channels for reactions with 637 MeV ^{116}Sn beam. 104
5.30 Summed NaI γ-ray energies in the inelastic and transfer channels for reactions with 345 MeV ^{58}Ni beam. 105
5.31 Summed NaI γ-ray energies in the inelastic and two-neutron transfer channels for reaction with 285 MeV ^{58}Ni beam. 106
5.32 Cross sections for the reaction ^{161}Dy(^{116}Sn,^{117}Sn)^{160}Dy. 107
5.33 Cross sections for the reaction ^{162}Dy(^{116}Sn,^{118}Sn)^{160}Dy. 108
5.34 Cross sections for direct population of individual ground band states in the reaction ^{161}Dy(^{116}Sn,^{117}Sn)^{160}Dy. 110
5.35 Cross sections for direct population of individual ground band states in the reaction ^{162}Dy(^{116}Sn,^{118}Sn)^{160}Dy. 111
5.36 Rotational population signatures for one (1N) and two-neutron (2N) pickup reactions ^{161}Dy(^{58}Ni,^{59}Ni)^{160}Dy, ^{162}Dy(^{58}Ni,^{60}Ni)^{160}Dy, and the inelastic scattering reaction ^{162}Dy(^{58}Ni,^{58}Ni)^{162}Dy. 113
5.37 Rotational population signatures for one (1N) and two-neutron (2N) pickup reactions ^{161}Dy(^{116}Sn,^{117}Sn)^{160}Dy, ^{162}Dy(^{116}Sn,^{118}Sn)^{160}Dy, and the inelastic scattering reaction ^{162}Dy(^{116}Sn,^{116}Sn)^{162}Dy. 115
5.38 The quantity $d\sigma/d\sigma_{Ruth}$ is the ratio of singles relative to the calculated Rutherford cross section. 118
5.39 A schematic view of the projectile and target potential wells. In a pickup reaction the neutron bound by an energy E_B in the target tunnels from R_2 to R_1. 119
5.40 The measured transfer probabilities as a function of the separation parameter (equation 2.9) for one-neutron transfer in the reaction ^{117}Sn(^{112}Sn, ^{113}Sn)^{116}Sn, and for two-neutron transfer in the reaction ^{118}Sn(^{112}Sn, ^{114}Sn)^{116}Sn. 123
5.41 Transfer probability versus distance of closest approach assuming Rutherford trajectories. Probabilities are for the $4^+ \rightarrow 2^+$ ground-band transitions of the deformed product nucleus, and are gated on neutron multiplicity zero. Solid lines are exponential fits. dashed and dotted lines are calculated from Eq. 5.8 with experimental binding energies. 125

5.42 Transfer probability versus distance of closest approach assuming Rutherford trajectories. Probabilities are for the $4^+ \rightarrow 2^+$ ground-band transitions of the deformed product nucleus, and are gated on neutron multiplicity zero. Solid lines are exponential fits. dashed and dotted lines are calculated from Eq. 5.8 with experimental binding energies. 126
5.43 Total γ-ray energy versus γ-ray multiplicity for the reaction shown in Fig 5.41. The data are gated on neutron multiplicity zero. The dashed line is an approximate system yrast line assuming no projectile excitation. 128
5.44 Transfer probability versus distance of closest approach assuming Rutherford trajectories with total energy and multiplicity (E,M) gates set. The three sets of data points correspond in descending order to gates 1, 2, 3 of Table 5.3. The dashed line defines the slope expected from Eq. 5.7-5.10. 130
5.45 One-neutron transfer probability for ground-band and two-quasiparticle band population versus distance of closest approach in reaction, assuming Rutherford trajectories. Probabilities are for the $4^+ \rightarrow 2^+$ ground-band transitions of the deformed product nucleus ^{160}Dy, and are gated on neutron multiplicity zero. 131
5.46 Two-neutron transfer probability for ground-band and two-quasiparticle band population versus distance of closest approach in the reaction, assuming Rutherford trajectories. Probabilities are for the $4^+ \rightarrow 2^+$ ground-band transitions of the deformed product nucleus ^{160}Dy, and are gated on neutron multiplicity zero. 132
5.47 One-neutron transfer probability for ground-band and two-quasiparticle band population versus distance of closest approach in the reaction, assuming Rutherford trajectories. Probabilities are for the $4^+ \rightarrow 2^+$ ground-band transitions of the deformed product nucleus ^{160}Dy, and are gated on neutron multiplicity zero. 133
5.48 Two-neutron transfer probability for ground-band and two-quasiparticle band population versus distance of closest approach in the reaction, assuming Rutherford trajectories. Probabilities are for the $4^+ \rightarrow 2^+$ ground-band transitions of the deformed product nucleus ^{160}Dy, and are gated on neutron multiplicity zero. 134
5.49 Total enhancement factors as a function of separation distance for the reactions ^{161}Dy(^{116}Sn,^{117}Sn)^{160}Dy and ^{162}Dy(^{116}Sn,^{118}Sn)^{160}Dy. . 139
5.50 Total enhancement factors as a function of separation distance for the reactions ^{161}Dy(^{58}Ni,^{59}Ni)^{160}Dy and ^{162}Dy(^{58}Ni,^{60}Ni)^{160}Dy. . . . 140
5.51 Enhancement factors for the ground band population and two-quasiparticle band population as a function of separation distance for the reactions ^{161}Dy(^{116}Sn,^{117}Sn)^{160}Dy and ^{162}Dy(^{116}Sn,^{118}Sn)^{160}Dy. 142

5.52 Enhancement factors for the ground band population and two-quasiparticle band population as a function of separation distance for the reactions ^{161}Dy(^{58}Ni,^{59}Ni)^{160}Dy and ^{162}Dy(^{58}Ni,^{60}Ni)^{160}Dy. 143
5.53 Enhancement factors as a function of surface-surface distance (Eq.5.12) between target and projectile nuclei for Sn (A) and Ni (B) experiments. 144

List of Tables

3.1 Isotopic Abundance in Dy Targets. 32
3.2 Angular position of Ge detectors in the four Spin Spectrometer experiments with Dy targets. 36
3.3 Some properties of the Spin Spectrometer experiments studied; ΔN represents one or two-neutron transfer. 40

4.1 The sources used for the response calibration of the Spin Spectrometer. 48

5.1 Two-neutron transfer amplitudes for ^{160}Dy normalized to unity for I = 0. Reproduced from Canto *et al.* (1987) 116
5.2 Decay constants and binding energies for the transferred particles in one and two-neutron transfer reactions. 122
5.3 Values for the slope parameter 2α (the typical uncertainty in α is 10-20%). Gate 1 is E = 0 - 0.9 Mev, M = 0 - 3; Gate 2 is E = 0.7 - 4.7 Mev; M = 3 - 7. Gate 3 is E > 3.3 MeV, M = 7 - 15. 127

CHAPTER 1

INTRODUCTION

A direct nuclear transfer reaction is a reaction in which one or more nucleons are transferred between a projectile and a target without the formation of a complex intermediate state. For the past 40 years the study of direct nuclear reactions has been one of the most fruitful in nuclear physics. Direct transfer reactions with light-ion projectiles have played an important role in the development of nuclear physics. A well-known example is the deuteron stripping reaction. The (d, p) reaction transfers a neutron from the incident deutron to the target nucleus, and the scattered proton carries information on the angular momentum $l\hbar$ with which the neutron has entered the nucleus. Because this process can be treated as the transfer of a neutron into a definite single particle orbital in the final nucleus without excitation of other degrees of freedom, the (d, p) reaction is a useful spectroscopic tool.

The first experimental investigations of the heavier deformed nuclei by the (d, p) reaction were those of G. B. Holm *et al.*, (1961) and A. Isoya (1963). Later M. N. Vergnes and R. K. Sheline (1963) performed high resolution experiments, and they found remarkable agreement between the experimental cross sections for a number of rotational bands in ^{177}Yb and ^{170}Hf and those predicted by the stripping theory of Satchler (1964), who used the nuclear wave function of Nilsson and the distorted-wave Born Approximation (DWBA).

Experimental activity in the field of nucleon transfer reactions expanded rapidly during the period 1965-1975, parallel to the continued development of technical facilities and theoretical methods of analysis. Much of the pioneering work on heavy-ion-induced transfer was done in the mid-sixties at Yale (Sachs, *et al.*, 1965) and Heidelberg (Bock, *et al.*, 1966). Both laboratories concentrated on light nucleus-

nucleus systems (mainly 1p-shell nuclei), where nuclear structure calculations and light-ion induced transfer data were available for comparison.

Near the end of the 1970's transfer reactions with very heavy-ion beams become possible. W. von Oertzen *et al.* (1983 and 1987) at GSI used a magnetic spectrograph to study neutron transfer between low-lying states of Tin isotopes. Himmele *et al.* (1983) at GSI studied the system ^{184}W on ^{238}U with a novel method of conversion electron detection. F. W. N. de Boer *et al.* (1984) at GSI used particle-γ coincidence techniques to study ^{152}Sm, ^{160}Gd, and ^{232}Th with ^{206,208}Pb beams. Macchiavelli *et al.* (1985) at LBL used the $\gamma-\gamma$ coincidence method to study ^{132}Xe on ^{154}Sm, ^{176}Yb, and ^{171}Yb. None of these experiments could separate the ground band population from other bands in exit transfer channels due to poor energy resolution (for example, in W. von Oertzen's experiments the energy resolution was 5-10 MeV) or no information of γ-ray total energy and multiplicity.

We report here on one and two-neutron transfer reactions with ^{116}Sn and ^{58}Ni beams on the deformed nuclei ^{161}Dy and ^{162}Dy targets, and with ^{112}Sn beam on the spherical nuclei ^{118}Sn and ^{117}Sn targets. The ^{116}Sn, ^{58}Ni, and ^{112}Sn beams were supplied by the Holifield Tandem Accelerator at the Oak Ridge National Laboratory. The particle-particle-γ coincidence technique was employed to identify the exit channels and scattering angles; the Spin Spectrometer provided exit channel total energy and γ-ray multiplicity information. The main advantage of our transfer experiments is that we use the Spin Spectrometer, which gives γ-ray total energy and multiplicity information; we have sufficient energy resolution to separate the ground band population from other populations.

There are many reasons why we are interested in transfer reactions with very heavy-ions:

1. Transfer reactions with heavier ions can provide information similar to that obtained with light-ion reactions, but collective excitation in both the entrance

and exit channels is much stronger in heavy-ion transfer reactions. For example, there may be appreciable angular momentum transfer associated with inelastic excitation, which should lead to qualititively new features not found in transfer reactions with light ions.

2. In these reactions the strong entrance and exit channel excitation implies a localization in coordinate space which is not present with light ions.

3. Transfer reactions can populate states that can't be produced with other reactions. For example, in Fig. 1.1 the expected entry distributions for some (heavy-ion, xn) reactions are compared to those for the transfer reactions.

4. The strong entrance and exit channel excitation implies that transfer can be induced between states which are collectively excited. For example, single particle and pairing modes can be studied under influence of high collective angular momentum.

In the present work we have developed particle-particle-γ coincidence methods for very heavy-ion transfer reactions; we have set up new data analysis methods to identify the exit particles; from the reaction total energy and γ-ray multiplicity provided by the Spin Spectrometer we have studied the transfer mechanism; by gating on total energy and γ-ray multiplicity the ground band has been separated from other bands, allowing us to resolve the heavy-ion two-neutron transfer slope anomaly; we have gotten the absolute cross section and probability for one and two-neutron transfer reactions, and we have measured the large pairing enhancement in 2-neutron transfer reactions.

Results from this work have been previously reported in Guidry *et al.* (1985a, 1985b, and 1985c), Liu *et al.* (1985a, 1985b, 1986, 1988a, and 1988b) Juutinen *et*

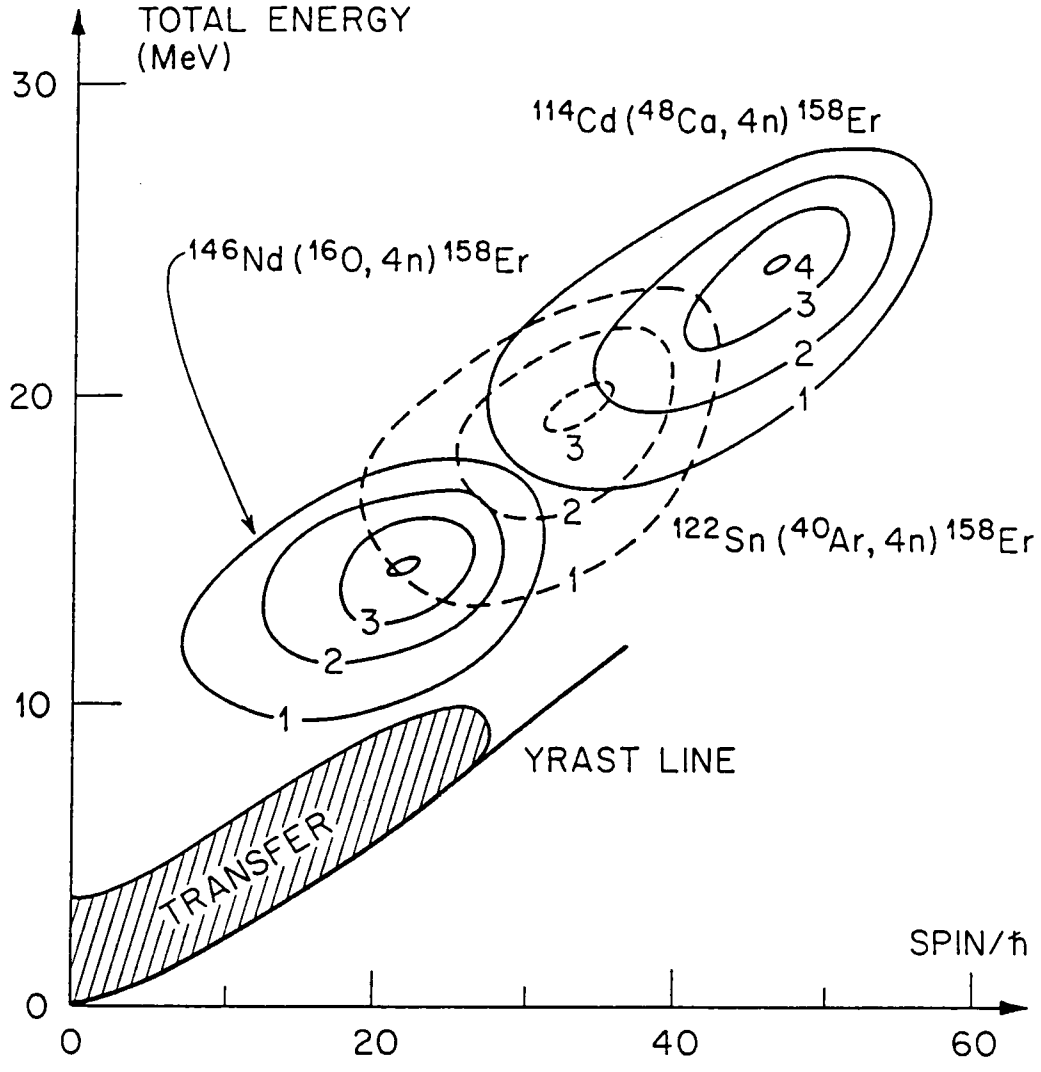


Figure 1.1: Total energy vs. spin predicted for entry distributions in some (heavy-ion, xn) reactions, and the general region populated in transfer reactions with very heavy ions. Reproduced from Guidry (1985c).

al. (1987), and Wu *et al.* (1987 and 1988).

CHAPTER 2

THEORY OF TRANSFER REACTIONS WITH HEAVY-IONS

2.1 General Aspects of Transfer Reactions with Heavy-ions

Transfer reactions with heavy-ions introduce specific features into the reaction process. The charge product $Z_1 Z_2$ of the two heavy colliding nuclei is large, which implies that effects of the Coulomb interaction play an important role. For example, the strong Coulomb field leads to the observation of Fresnel diffraction patterns (instead of Fraunhofer diffraction) in elastic scattering (Frahn, 1971). In transfer reactions with heavy-ions the collective excitation in both the entrance and exit channels is strong. This type of reaction is illustrated schematically in Fig. 2.1: strong inelastic excitation in the entrance channel, transfer of nucleons near the radial turning point, and strong exit channel inelastic excitation.

Transfer reactions with deformed target nuclei are a particularly good illustration of the general statement made above. In Fig. 2.2 we show an estimate of the maximum collective angular momentum in some heavy-ion systems near the classical turning point. These calculations indicate that transfer from states in the range 10-20 $\hbar$ for rare earths and 20-30 $\hbar$ in actinides should be feasible.

Another important consequence of the large charge product was already recognized early in the study of heavy-ion interactions (Breit, 1959), and can be expressed in terms of the Sommerfeld parameter η

$$\eta = \frac{Z_1 Z_2 e^2}{\hbar v} = \frac{0.157 Z_1 Z_2 \sqrt{A_2}}{\sqrt{E_{lab}}} = \frac{R_{min}}{2\lambda} \tag{2.1}$$

Here v is the relative velocity in the center-of-mass (CM) system, e the unit of charge, E_{lab} the energy of the projectile in the laboratory system, λ the deBroglie wavelength, and R_{min} the minimum separation in a scattering process which occurs

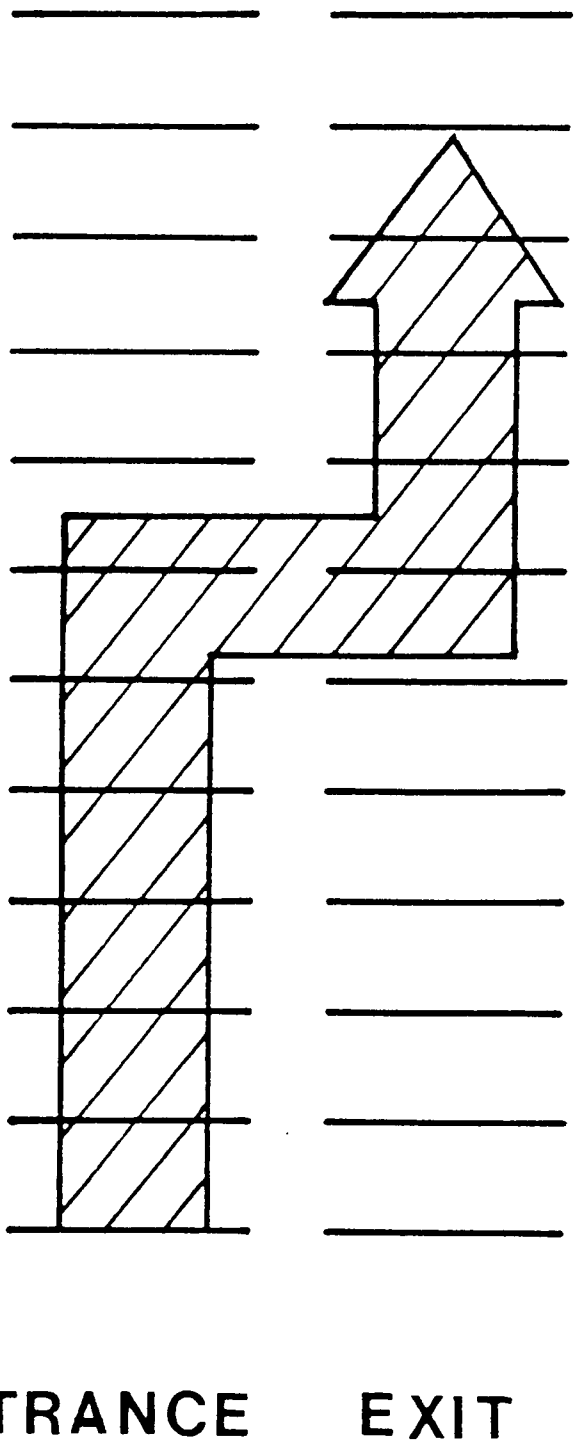


Figure 2.1: Mechanism for transfer reactions with heavy-ions.

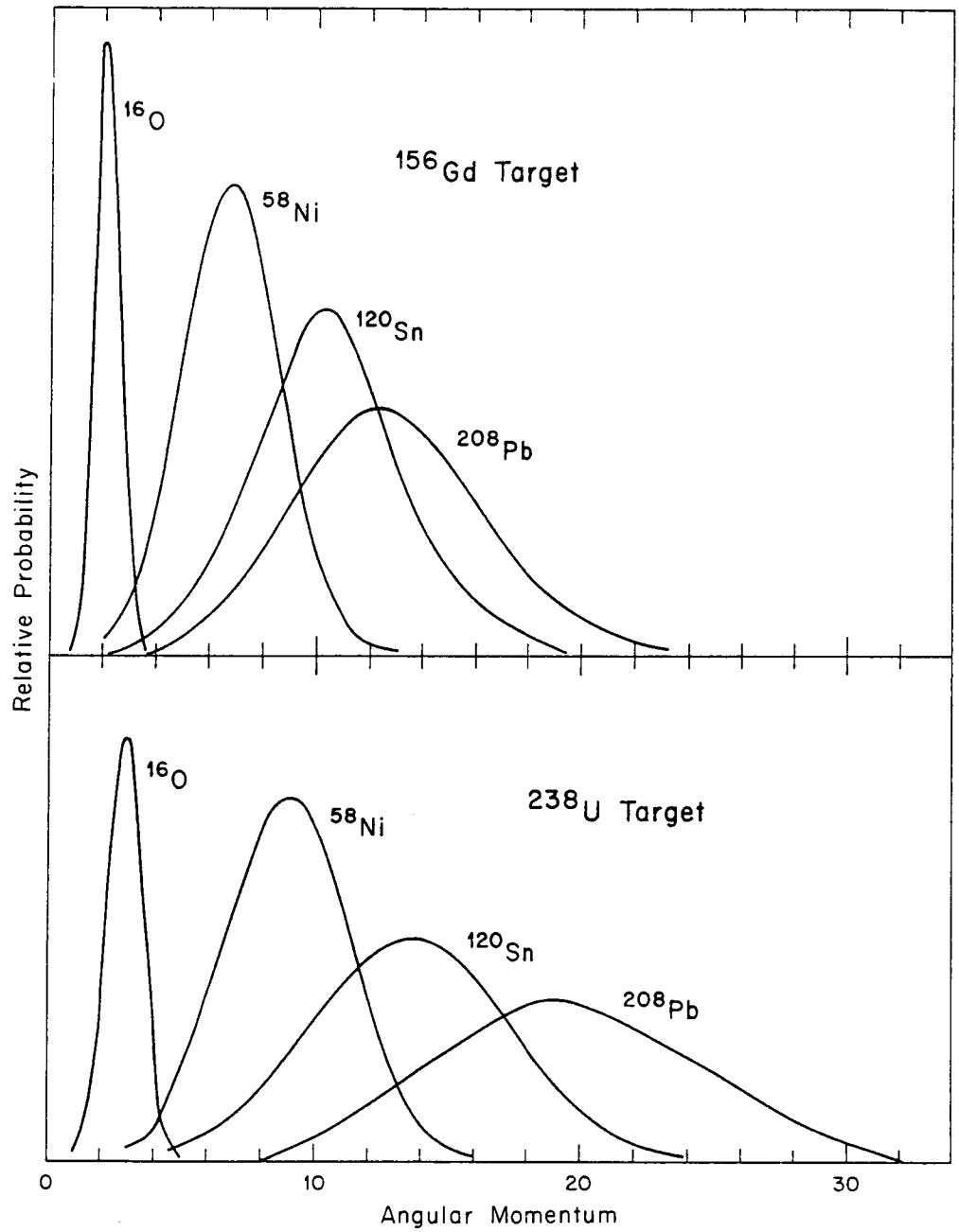


Figure 2.2: The maximum angular momentum near the turning point for some heavy ion systems in grazing collisions. Reproduced from Guidry and Kincaid (1985b)

at a deflection angle of 180°. If $\eta \gg 1$, the minimum distance R_{min} is large relative to the deBroglie wavelength (from equation 2.1), and the process exhibits semiclassical properties because the wave packets are sufficiently localized in space. A large Sommerfeld parameter $\eta \gg 1$, together with a small amount of mass, angular momentum, energy, and charge transfer,($\Delta M/M$, $\Delta L/L$, $\Delta E/E$ and $\Delta Z/Z \ll 1$), give the possibility of defining a localized classical trajectory for the reaction.

Another important property of heavy-ion transfer reactions is the strong absorption at small internuclear distance. If the minimum distance becomes smaller than a certain value R_0, the cross section in simple transfer reaction channels becomes small and the incoming flux is absorbed into more complicated reactions like the formation of a compound nucleus or deep inelastic scattering. Therefore the cross sections for inelastic scattering and transfer processes decrease sharply beyond a certain scattering angle θ^{gr}. This angle is called the *grazing angle.*

The classical nature of the relative motion, together with strong absorption at short distances, leads to striking kinematic selectivities in transfer reaction with heavy-ions. Final states with high angular momentum and high excitation energy may be populated in contrast to transfer reactions with light-ions.

2.2 The Semi-classical Approach

The semi-classical approach has been very successful in quantitative and qualitative descriptions of transfer reactions. The semi-classical description utilizes the fact that the wavelength associated with the relative motion of the centers of mass of the colliding nuclei is very small. Thus for reactions below the Coulomb barrier the wavelength should be compared to the distance of closest approach, while for reactions above the Coulomb barrier it may be compared to the sum of the nuclear radii. As discussed in section 1, the Sommerfeld parameter $\eta = \mathrm{R}_{min}/2\lambda$

represents such a comparison. The condition

$$\eta \gg 1 \tag{2.2}$$

suffices to ensure the applicability of classical physics for the elastic scattering. In the transfer reaction there is a transfer of energy ΔE, mass ΔM, angular momentum ΔL, and charge ΔZ, and condition (2.2) must be supplemented by the following conditions.

$$\frac{\Delta E}{E} \ll 1, \quad \frac{\Delta M}{M} \ll 1, \quad \frac{\Delta L}{L} \ll 1, \quad \frac{\Delta Z}{Z} \ll 1 \tag{2.3}$$

As mentioned in section 1, transfer reactions with heavy-ions satisfy very well conditions (2.2) and (2.3), and the motion of the center of the colliding nuclei can be described by classical orbits. We consider scattering in the Coulomb field. Fig. 2.3 shows the classical trajectories of two colliding ions in the center-of-mass system. The kinetic energy and relative momentum are

$$E_{CM} = \frac{m}{2}(A_1 v_1^2 + A_2 v_2^2) = \frac{\mu}{2} v_\infty^2 \tag{2.4}$$

$$P_{CM} = m(A_1 v_1 + A_2 v_2) = \mu v_\infty \tag{2.5}$$

where the subscripts 1 and 2 identify the target and projectile and m is the nucleon mass. The symbol μ denotes the reduced mass, which is given by

$$\mu = m\frac{A_1 A_2}{A_1 + A_2} \tag{2.6}$$

The distance of closest approach between the two centers of gravity D is related to the scattering angle θ by

$$D = \frac{Z_1 Z_2 e^2}{2E_{CM}}(1 + \csc\frac{\theta_{CM}}{2}) \tag{2.7}$$

The relation between θ_{LAB} and θ_{CM} is given by

$$\theta_{CM} = \theta_{LAB} + \arcsin(\frac{A_2}{A_1}\sin\theta_{LAB}) \tag{2.8}$$

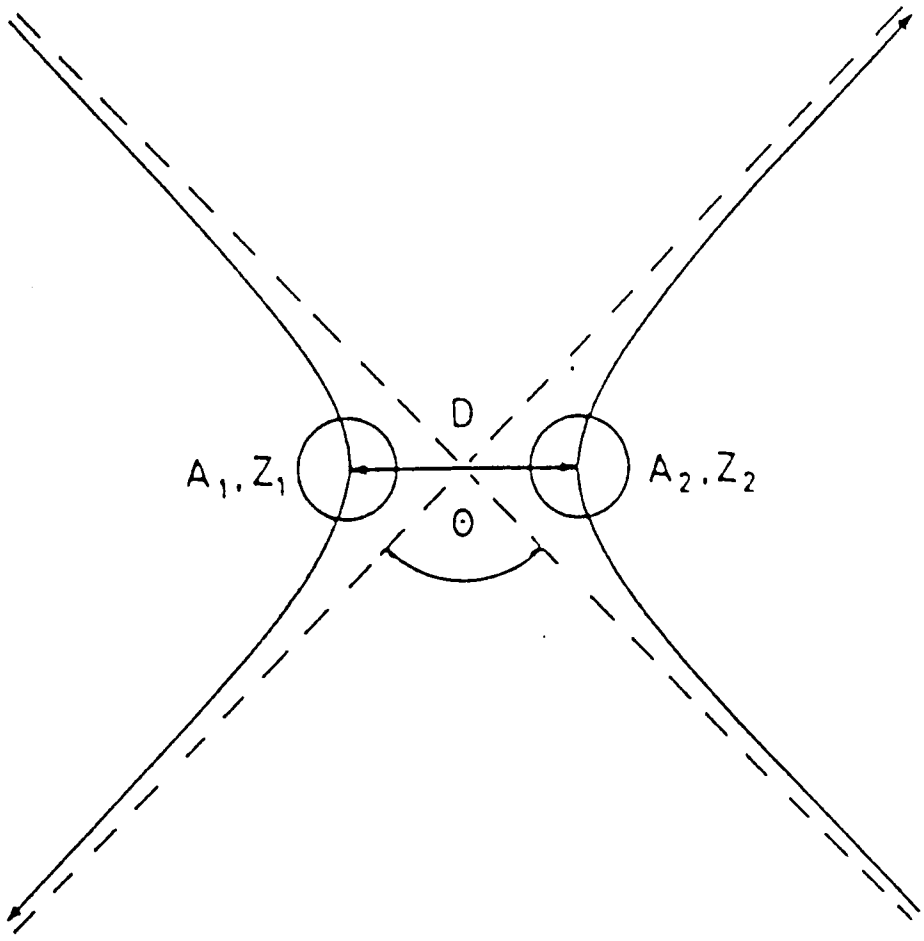


Figure 2.3: Coulomb trajectories in the center-of-mass system.

The distance of closest approach D is a very important quantity, because the form factor is scanned by the scattering orbit as a function of D. Instead of plotting $P(\theta)$ we will always transform θ to D. We also use a reduced quantity d_0, where the size of the nuclei is divided out:

$$d_0 = \frac{D}{(\sqrt[3]{A_1} + \sqrt[3]{A_2})} \tag{2.9}$$

At some internuclear distance $D \sim D_C$, the nuclear interaction will become effective. We define the Coulomb barrier E_C as the asymptotic kinetic energy in the center-of-mass system at the (classical) threshold for nuclear reactions,

$$E_C = \frac{Z_1 Z_2 e^2}{D_C} \tag{2.10}$$

Due to the diffuse nature of the nuclear surface and the finite range of the nuclear interaction, D_C will be larger than the sum of the effective matter radii of the colliding nuclei. From grazing collisions in our transfer reactions we find empirically that for one-neutron transfer reaction

$$D_C \simeq 1.47(\sqrt[3]{A_1} + \sqrt[3]{A_2}) \tag{2.11}$$

for two-neutron trnasfer reaction

$$D_C \simeq 1.4(\sqrt[3]{A_1} + \sqrt[3]{A_2}) \tag{2.12}$$

At bombarding energies above the Coulomb barrier we have to distinguish two different kinematic situations, depending on whether the distance of closest approach is larger or smaller than D_C. For large impact parameters, corresponding to small scattering angles, the Coulomb trajectories as shown in Fig. 2.3 are valid. For small impact parameters the collision is dominated by nuclear interactions which lead to inelastic and transfer processes. The limiting case of a "grazing collision" ($D = D_C$) is of particular interest; the corresponding Coulomb scattering angle θ^{gr}

is defined through

$$\sin\frac{\theta_{lab}^{gr}}{2} = \frac{\eta}{kD_C - \eta} \tag{2.13}$$

The corresponding grazing angle in center-of-mass system is

$$\theta_{CM}^{gr} = \theta_{Lab}^{gr} + \arcsin(\frac{A_2 \sin\theta_{Lab}^{gr}}{A_1}) \tag{2.14}$$

Because of the restrictions of Eq. 2.3, the classical orbit must not be disturbed appreciably by the transfer of charge and mass in the reaction. The orbit in the entrance and exit channels must be well matched so that the change in turning point which occurs when the transfer takes place is of the order of λ and no greater. If these conditions are satisfied, and $\lambda \ll$D, the differential cross section $d\sigma(\theta)/d\Omega$ for transfer can be factored in the form (Phillips, 1977)

$$\frac{d\sigma(\theta)}{d\Omega} = \left[\frac{d\sigma(\theta)}{d\Omega}\right]_{elastic} P \tag{2.15}$$

where P is the integrated probability of transfer along the orbit appropriate to the scattering angle θ. The probability for transfer is given by an integral of the formfactor $f_t(r)$ along the scattering orbit

$$P_t(\theta) = \left[\frac{1}{\hbar}\int_{-\infty}^{+\infty} dt f_t(r(t))\right]^2 \tag{2.16}$$

The formfactor is obtained in DWBA as the overlap of the nuclear wave function of the initial and final states. The next section will discuss the calculation of the formfactor.

2.3 The Distorted Wave Born Approximation (DWBA)

The distorted-wave Born approximation has proved to be one of the most powerful tools for the analysis of nuclear direct reactions. As its name implies, the relative motion before and after the non-elastic event are described, not by plane waves, but in term of waves distorted by elastic scattering and its accompanying

absorption. Hence this approximation is likely to be valid when the most important single event to take place when two nuclei collide is elastic scattering; then other reactions can be treated as perturbations – as weak transitions between elastic scattering states. The DWBA is valid for transfer reactions provided three principal assumptions are satisfied:

1. The transfer is assumed to take place directly from the initial to final state.

2. The wave function for the relative motion between partners in the reaction is assumed to be correctly described by the optical potential model.

3. The transfer reaction is assumed to be sufficiently weak that it can be treated in lowest order.

A transfer reaction can be defined as a nuclear collision during which a nucleon or a group of nucleons, denoted by x, are transferred from a core C_1 to a core C_2. We can write (Bass, 1980)

$$A + C_2 \rightarrow C_1 + B \tag{2.17}$$

where A = C_1 + x and B = C_2 + x. Neglecting the internal structure of x, C_1, and C_2, we can represent the relative position of the various fragments during the reaction by the diagram shown in Fig. 2.4. Each of the five relative vectors $\mathbf{r}_{1x}$, $\mathbf{r}_{2x}$, $\mathbf{r}_{12}$, $\mathbf{r}_i$, $\mathbf{r}_f$ can be expressed in terms of two independent basis vectors. Using for the latter either $\mathbf{r}_{12}$ and $\mathbf{r}_{1x}$ or $\mathbf{r}_{12}$ and $\mathbf{r}_{2x}$ we have (Bass, 1980)

$$\mathbf{r}_i = \mathbf{r}_{12} + \frac{m_x}{M_1 + m_x}\mathbf{r}_{1x} = \frac{M_1}{M_1 + m_x}\mathbf{r}_{12} + \frac{m_x}{M_1 + m_x}\mathbf{r}_{2x} \tag{2.18}$$

$$\mathbf{r}_f = \frac{M_2}{M_2 + m_x}\mathbf{r}_{12} - \frac{m_x}{M_2 + m_x}\mathbf{r}_{1x} = \mathbf{r}_{12} - \frac{m_x}{M_2 + m_x}\mathbf{r}_{2x} \tag{2.19}$$

The cross section can be written (Bass, 1980)

$$\frac{d\sigma}{d\Omega} = \frac{\mu_i \mu_f}{(2\pi\hbar^2)^2}\frac{k_f}{k_i}\frac{1}{(2I_A + 1)(2I_{C_2} + 1)}\sum_{m_i m_f}\left|T_{m_i m_f}\right|^2 \tag{2.20}$$

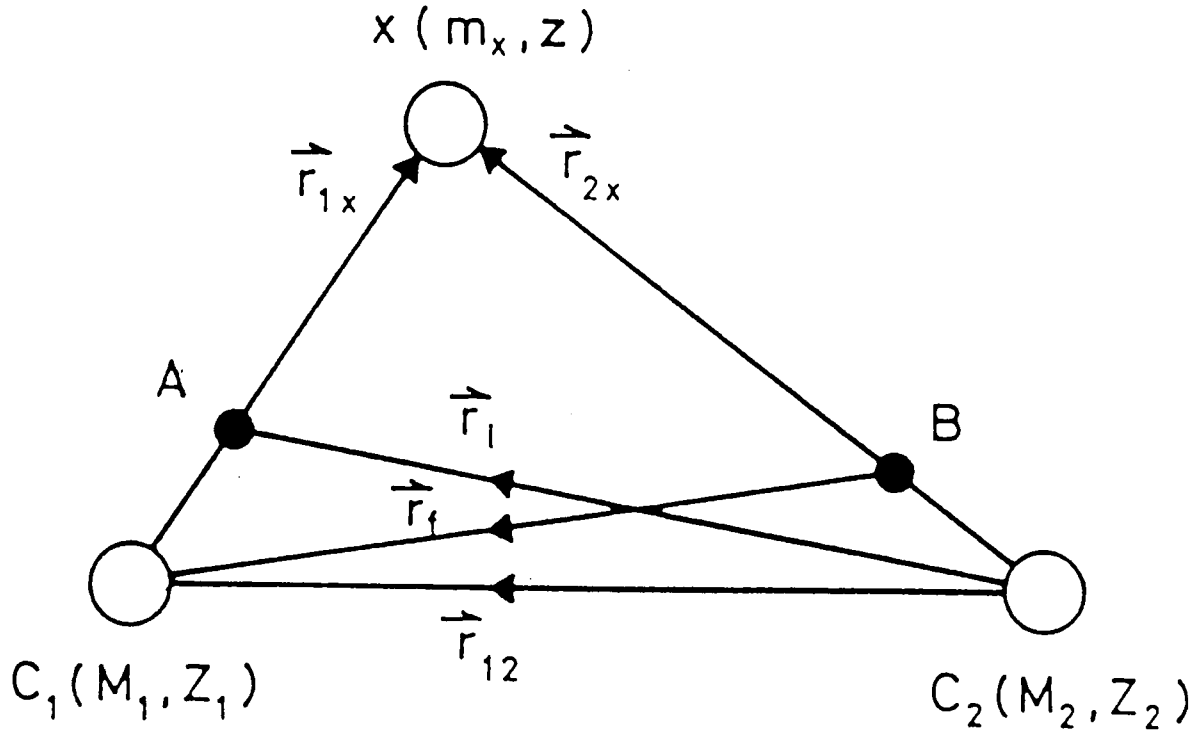


Figure 2.4: Vector diagram for a transfer reaction A + C_2 → C_1 + B (C_1, C_2 cores; x transferred particle; A = C_1 + x, B = C_2 + x).

where the sum on the right side runs over the intrinsic spin projections of the initial and final fragments ($m_i = m_A, m_{C_2}$; $m_f = m_B, m_{C_1}$). Dropping for simplicity the subscripts m_i and m_f, the transfer amplitudes can be written by the six-dimensional integral (Bass, 1980)

$$T = \int \chi_f^{(-)*}(\mathbf{k}_f, \mathbf{r}_f) G(\mathbf{r}_i, \mathbf{r}_f) \chi_i^{(+)}(\mathbf{k}_i, \mathbf{r}_i) d\mathbf{r}_i d\mathbf{r}_f \tag{2.21}$$

Here $\chi_i^{(+)}$ and $\chi_f^{(-)}$ are the ingoing and outgoing "distorted waves"; they describe elastic scattering in the initial and final channel, and are determined from appropriate optical model potentials. The "transfer function" $G(\mathbf{r}_i,\mathbf{r}_f)$ is defined as (Bass , 1980)

$$G(\mathbf{r}_i, \mathbf{r}_f) = \psi_B^*(\mathbf{r}_{2x}) V_{if} \psi_A(\mathbf{r}_{1x}) \tag{2.22}$$

here ψ_A and ψ_B are the bound state wave functions for particle x bound to the cores C_1 and C_2 respectively, and V_{if} is the interaction responsible for the transition, which may be approximated as

$$V_{if} \approx V_{C_2x}^N(\mathbf{r}_{2x}) + V_{C_2x}^C + V_{C_1C_2}^C - V_{C_2A}^C \tag{2.23}$$

where the superscripts (N) and (C) denote nuclear and Coulomb potentials (for neutron transfer the Coulomb terms are often disregarded). The integral for the transfer amplitude is six-dimensional (Eq. 2.21). In order to make this calculation, it is useful to reduce the six-dimensional integral to a three-dimensional integral by suitable approximations. Although computer codes for an exact evaluation of the six-dimension integral are now available, some approximate methods give better insight into the physics involved.

The "zero-range approximation" substitutes a delta function of the appropriate vector for $V_{if}\psi_B(\mathbf{r}_{2x})$, and $\mathbf{r}_i$, $\mathbf{r}_f$, and $\mathbf{r}_{1x}$ have following relations

$$\mathbf{r}_{1x} = -\mathbf{r}_{12}, \quad \mathbf{r}_{2x} = 0, \quad \mathbf{r}_i = \frac{M_1}{M_1 + m_x}\mathbf{r}_{12}, \quad \mathbf{r}_f = \mathbf{r}_{12} \tag{2.24}$$

which allows the transfer amplitude to be calculated as a three-dimensional integral over $\mathbf{r}_{12}$.

The "zero-range approximation" is not suitable for transfer between heavier cores. The "no-recoil approximation", introduced by Buttle and Goldfarb (1966), allows the transfer amplitude to be reduced to three dimensional integrals in such cases. The method consists of two essential steps. First Eq. 2.24 is used for the arguments $\mathbf{r}_i$ and $\mathbf{r}_f$ of the distorted waves (thus neglecting the "recoil effect"), but not for $\mathbf{r}_{1x}$ and $\mathbf{r}_{2x}$ of the transfer function (thus retaining the finite range of the interaction V_{12}). Introducing a *"form factor"* $F(\mathbf{r}_{12})$, which can be defined as (Bass, 1980)

$$F(\mathbf{r}_{12}) = \int \psi_B^*(\mathbf{r}_{2x}) V_{C_{2x}}^{(N)}(\mathbf{r}_{2x}) \psi_A(\mathbf{r}_{2x} - \mathbf{r}_{12}) d(\mathbf{r}_{2x}) \tag{2.25}$$

the transfer amplitude T is

$$T \approx \int \chi_f^{(-)*}(\mathbf{k}_f, \mathbf{r}_f) F(\mathbf{r}_{12}) \chi_i^{(+)}(\mathbf{k}_i, \mathbf{r}_i) d(\mathbf{r}_{12}) \tag{2.26}$$

The second approximation uses the fact that for transfer reactions at energies around the Coulomb barrier only the tails of the wave function of the transferred particle enter into the reaction. For neutron transfer we can substitute for the bound-state wave functions ψ_A and ψ_B spherical Hankel functions to describe the asymptotic behaviour of a neutral particle x with appropriate binding energy E_A or E_B:

$$\psi_A(\mathbf{r}_{2x} - \mathbf{r}_{12}) \approx S_A^{1/2}(l_1, j_1) N_A h_{l_1}^{(1)}(ik_1 |\mathbf{r}_{2x} - \mathbf{r}_{12}|) Y_{l_1 m_1}(\mathbf{r}_{2x} - \mathbf{r}_{12}) \tag{2.27}$$

$$\psi_B(\mathbf{r}_{2x}) \approx S_B^{1/2}(l_2, j_2) N_B h_{l_2}^{(1)}(ik_2 r_{2x}) Y_{l_2 m_2}(\mathbf{r}_{2x}) \tag{2.28}$$

$$k_{1,2} = \left(\frac{2\mu_{A,B} E_{A,B}}{\hbar^2} \right)^{1/2} \tag{2.29}$$

here S_A and S_B are spectroscopic factors, which are difined as overlapes of the physical state A and B with single particle state $c_1 + x_{l_1 j_1}$ and $c_2 + x_{l_2 j_2}$, h is a

spherical Hankel function, and N is a normalized constant. After some manipulation the cross section for $j_x = 1/2$ (one neutron transfer) can be written (Bass,1980)

$$\frac{d\sigma}{d\Omega} = \frac{\mu_i \mu_f}{(2\pi\hbar^2)^2} \frac{k_f}{k_i} \frac{2I_B + 1}{2I_{c_2} + 1} \times \sum_{j_1 j_2 l} N_A^2 S_A(l_1, j_1) N_B^2 S_B(l_2, j_2) C(j_1, j_2, l) |I|^2 \sum_m |T_{lm}(\Theta)|^2 \tag{2.30}$$

where $C(j_1,j_2,l)$ is a geometrical coefficient, I is a one-dimensional radial integral involving the bound-state wave functions, and the amplitudes $T_{lm}(\Theta)$ are three-dimensional integrals involving the initial and final distorted waves.

2.4 Theory for Very Heavy Ion Induced Transfer Reactions

Although the DWBA is an extremly successful technique for analyses of transfer reactions, it is not well suited to the study of transfer reactions involving very heavy ions on nuclei far removed from closed shells. The strong coupling of the ground state to collective states invalidates the perturbation theory on which DWBA is based. A quantitative description of such transfer reactions involves a set of coupled equations, which describe explicitly those channels coupled strongly to the incident or outgoing channel. Such coupled-channels treatments have been developed both in the framework of semiclassical theory (Broglia *et al.*, 1972 and 1973) (Weiss, 1979) (Guidry *et al.*, 1981), and as an extension of the (quantum mechanical) DWBA in the coupled-channel Born approximation (CCBA).

The calculation of Guidry (1981) employed the no-recoil limit for transfer and the sudden limit for inelastic excitation (Massmann *et al.*, 1975), and included a deformed Wood-Saxon potential to describe both the real and imaginary nuclear potentials for the spherical projectile on even-even deformed target nuclei. Several calculations for Xe projectiles on rare-earth targets indicated that the rotational population signatures for 2-neutron transfer are quite different from those expected for the analogous inelastic scattering case, and suggested that these reactions can

provide a unique probe of nuclear structure in high angular momentum states.

Nikam and Ring (1986 and 1987) have used Hartree-Fock-Bogoliubov theory in the rotating frame to calculate the two-neutron transfer amplitude $< A+2, I|(a^+a^+)_{L=0}|A, I >$ between rotating superfluid deformed nuclei. A new and unexpected behavior was found. In simple BCS approximation the pair transfer matrix element is directly proportional to the gap parameter Δ, but their calculation indicated that this matrix element is proportional to the gap only for very small angular momentum. At higher angular momentum it falls dramatically, goes through zero and changes sign. These regions where the matrix element vanishes were called regions of diabolic pair transfer. After the first zero the transfer matrix element has negative values. In some cases there exists more than one such diabolic region and the matrix element oscillates around zero for high angular velocities. This oscillating behavior of the pair transfer matrix element as a function of the angular velocity is similar to the oscillation of the amplitude of an electric DC-current in a Superconducting Quantum Interference Devices (SQUID) as a function of the magnetic field (Barine *et al.*, 1982). In Fig. 2.5 the pair transfer amplitudes are presented as a function of angular momentum. A diabolic point is observed between spins I = 10 and 12 $\hbar$, where the amplitude vanishes and changes sign. The gap parameter Δ(I) is also given in Fig. 2.5; it shows only a small reduction in this region.

C. Price, H. Esbensen, and S. Landowne (1987) showed recently that quantum mechanical calculations for pair transfer to high spin states can be carried out rather straightforwardly by combining the macroscopic pair transfer model (Dasso and Vitturi, 1986) with a sudden limit approximation for the rotational excitation. A key feature of the macroscopic approach is that the transfer reaction depends on the orientation θ of the deformed surface with respect to the beam axis. In the sudden limit this dynamical variable is "frozen". One makes scattering calculations as a function of θ and then projects out the physical amplitudes. The coupled equations

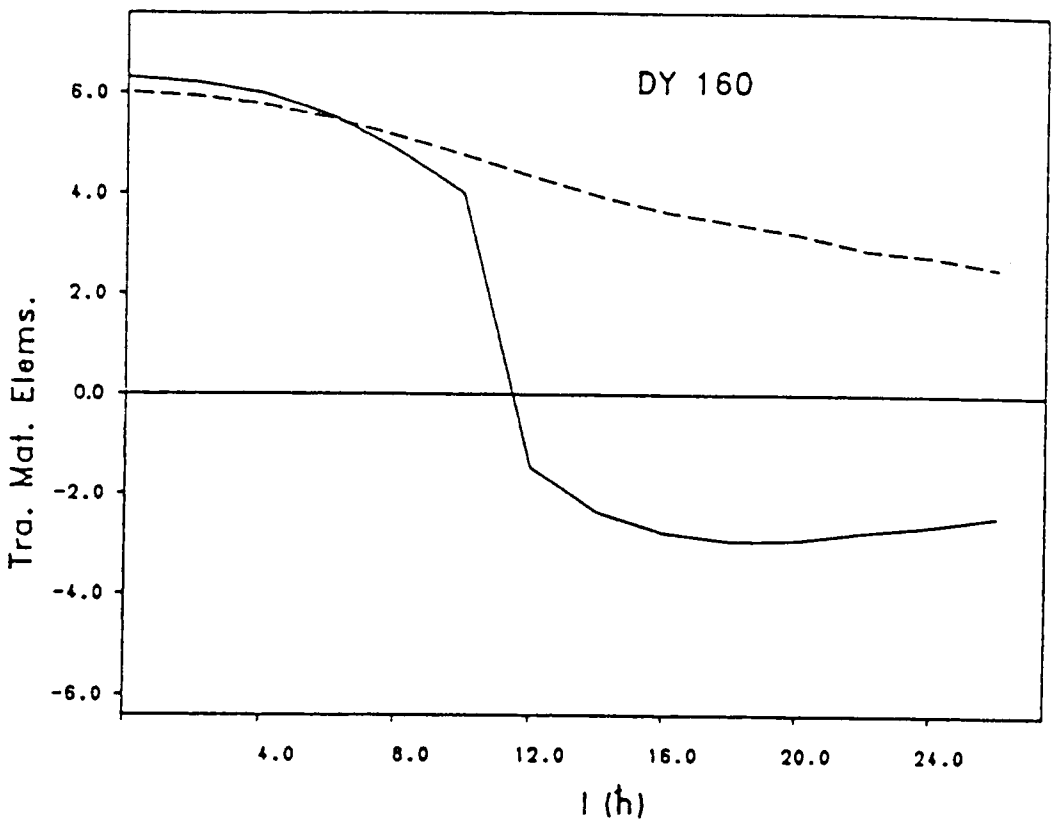


Figure 2.5: Pair transfer matrix elements for the nucleus ^{160}Dy (full line) and the gap parameter $\Delta(I) = G < A|(a^+a^+)_0(aa)_0|A >^{1/2}$ (dashed line) as function of the angular momentum I. Reproduced from Canto *et al.* (1987).

for transfer are given as

$$\frac{\hbar^2}{2\mu_1}\left[-\frac{d^2}{dr^2}+\frac{J(J+1)}{r^2}+\frac{\eta k_1}{r}-k_1^2+V(r,\theta)\right]u_J^1(r,\theta)=-V_{cp1}(r,\theta)u_J^2(r,\theta) \quad (2.31)$$

$$\frac{\hbar^2}{2\mu_2}\left[-\frac{d^2}{dr^2}+\frac{J(J+1)}{r^2}+\frac{\eta k_2}{r}-k_2^2+V(r,\theta)\right]u_J^2(r,\theta)=-V_{cp1}(r,\theta)u_J^1(r,\theta) \quad (2.32)$$

where θ is the orientation angle, and V_{cp1} is given by

$$V_{cp1}=-\sigma_T\frac{d}{dr}V_N(r,\theta)[1+\beta Y_{20}(r,\theta)] \quad (2.33)$$

where σ_T is the transfer coupling strength. The total deformed potential V is given by

$$V=V_C(r,\theta)+V_N(r,\theta) \quad (2.34)$$

here subscripts (N) and (C) denote nuclear and Coulomb potentials. For the ^{162}Dy(^{58}Ni, ^{60}Ni)^{160}Dy reaction the deformed nuclear potential was

$$U_N=-\frac{(100+i40)\ MeV}{1+exp\{[r-R_1-R_2-R_2\beta_2^nY_{20}(\theta)]/0.6\ fm\}} \quad (2.35)$$

here $R_1 = 4.65$ fm (the radius of the ^{58}Ni nucleus), $R_2 = 6.54$ fm (the radius of the ^{162}Dy nucleus) and $\beta_2^n = 0.34$. The quadrupole deformed Coulomb potential was given by

$$U_C(r,\theta)=\frac{Z_1Z_2e^2}{r}\left[1+\frac{3}{5}(\frac{R_2}{r})^2\beta_2^cY_{20}(\theta)\right] \quad (2.36)$$

with $\beta_2^c = 0.31$, and a transfer coupling strength of $\sigma_T = 0.15$ fm was used.

By solving the coupled equations 2.29 and 2.30 with appropriate scattering boundary conditions, we can specify that the radial waves behave asymptotically as

$$u_{il}(r,\theta)\rightarrow\delta_{i,1}e^{-i\phi_{il}(r)}-\sqrt{\frac{v_1}{v_i}}S_{il}(\theta)e+i\phi_{il}(r) \quad (2.37)$$

where v_i is the relative velocity and

$$\phi_{il}(r)=k_ir-\eta_iln(2k_ir)-\frac{l\pi}{2}+\sigma_{il} \quad (2.38)$$

here η_i is the Sommerfeld parameter, $K_i = \mu_i v_i/\hbar$ is the relative wave number, and $\sigma_{il} = \arg(\Gamma(l+1+i\eta_i))$ is the Coulomb partial wave phase shift. We obtain an angle dependent S-matrix, $S_{il}(\theta)$ for each channel. The S-matrix for the individual spin states I is obtained by projection:

$$S_{iIJ} = \int d\Omega Y^*_{I0}(\theta,0) S_{il}(\theta) Y_{00}(\theta,0) \tag{2.39}$$

Finally, the unpolarized differential cross sections are given by (Esbensen *et al.*, 1987a, 1987b)

$$\frac{d\sigma^i_I}{d\Omega}(\theta) = \frac{v_i}{v_1}\left|\frac{i\sqrt{\pi}}{k_1}\sum_l \sqrt{2l+1}\; Y_{l0}(\theta)\left[\delta_{i,1}\delta_{I,0} - \sqrt{\frac{v_1}{v_i}} S_{ilI} e^{i(\sigma_{1l}+\sigma_{2l})}\right]\right|^2 \tag{2.40}$$

In Fig. 2.6 we show differential cross section calculations for the reaction ^{162}Dy(^{116}Sn,^{118}Sn)^{160}Dy at a bombarding energy of E_{lab} = 637 MeV, and note the existence of a pronounced structure in the angular distribution for lower spin states. In chapter 5 we will show our experimental cross sections for the same reaction, which support the existence of this structure.

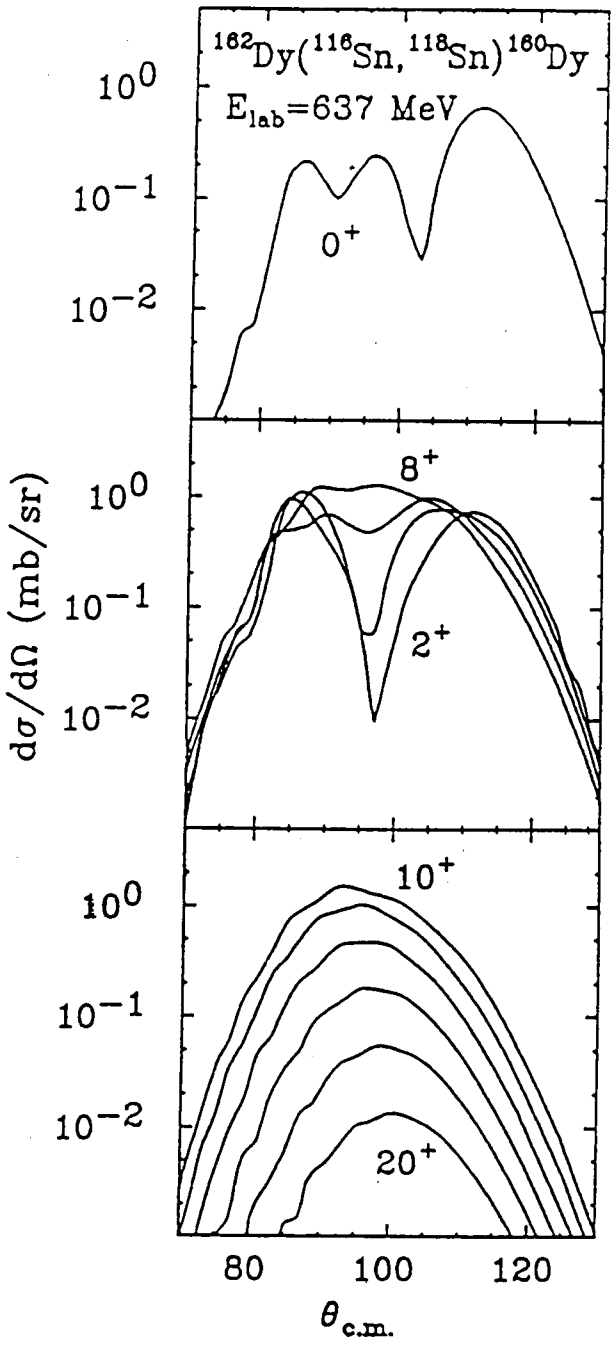


Figure 2.6: Differential cross section for the ground band rotational states excited in the reaction ^{162}Dy(^{116}Sn,^{118}Sn)^{160}Dy at an energy E_{lab} = 637 MeV. Reproduced from Price *et al.* (1987).

CHAPTER 3

EXPERIMENTAL TECHNIQUES

3.1 Experimental Methods

In this section, we discuss how measurements on transfer reactions are made and the particular experimental difficulties that they present. The study of heavy-ion transfer reaction poses severe problems for the traditional methods of investigating light-ion transfer reactions. In light-ion transfer reactions using charged-particle spectroscopy the resolution in energy is good enough to separate different states populated in the reaction. In heavy-ion transfer reactions the energy resolution becomes worse due to increasing energy loss and scattering of recoiling fragments in the target. For a given thickness target multiple scattering of the heavy-ion in the target material imposes a severe limit on the energy and angle resolution. To avoid these problems, we employ the particle-particle-γ coincidence method.

A typical experimental arrangement is shown in Fig. 3.1. The position-sensitive parallel-plate avalanche counters (PPAC) have no energy resolution but are used to define the scattering angle and time of flight difference for target-like and beam-like ions. Gamma rays are detected in coincidence with the scattered ions. Both the recoiling target-like and the projectile-like nuclei are detected in kinematic coincidence and can be distinguished on the basis of kinematical correlations between the two scattering angles and their time-of-flight difference. The information about the scattering angle of the excited nucleus allows a correction for the large Doppler shifts of the emitted γ-ray due to the high recoil velocities (up to $\sim$ 10% of the velocity of light). The measurement of the scattering angle provides information on the impact parameter dependence of the γ-ray yields. It is estimated that the

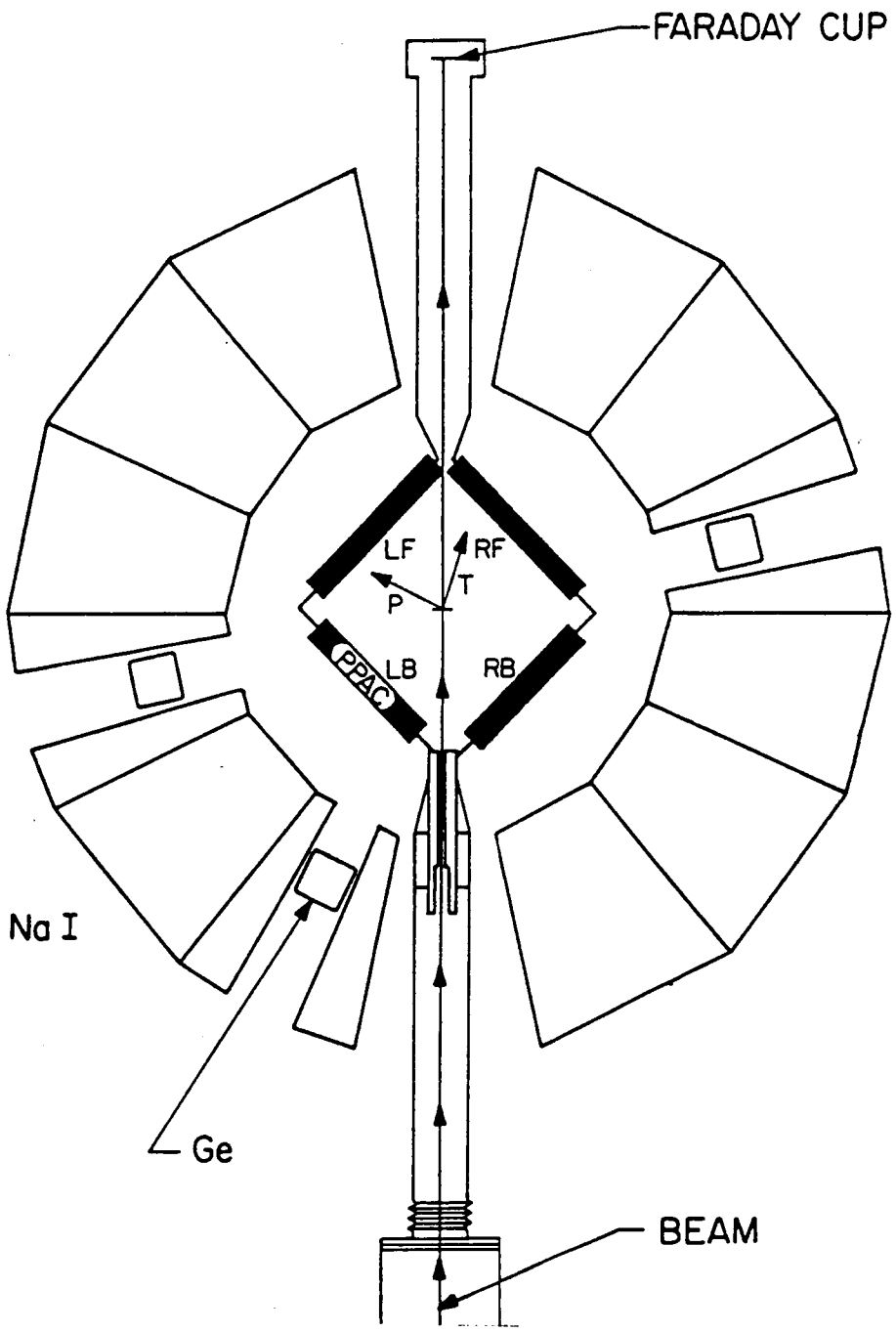


Figure 3.1: A typical experimental set-up. The particle detectors are placed inside the Spin Spectrometer.

position resolution of the particle counter corresponds to a resolution of the transferred mass $\Delta m \sim 16$ (amu), or a Q-value resolution $\Delta Q \sim 30$ MeV. This apparatus is placed in the Spin Spectrometer at the Oak Ridge National Laboratory, which is used to record the total energy and multiplicity of the γ-ray cascade associated with a particle-particle-γ coincidence.

The energy spectra of the deformed nuclei are complex, and to study them requires high energy resolution. In a typical odd-mass deformed nucleus in the rare earth region approximately five Nilsson particle states and five hole states can be expected below 1 MeV of excitation. For each band, suppose three rotational states are populated with appreciable intensity; then about 30 groups can be expected below 1 MeV in the spectrum, and the average level spacing is ~ 30 keV (Elbek and Tjϕm, 1969).

Two types of γ-ray detectors were employed: high-purity Ge, and Ge(Li). Ge(Li) detectors have to continually be stored at liquid nitrogen temperatures to reduce the mobility of the Li atoms; high-purity Ge detectors need only be placed at liquid nitrogen temperatures when high voltage bias is on, to prevent thermal excitation of electron-hole pairs. The performance of Ge detectors is better than that of Ge(Li) detectors: they have better timing, greater energy range, and more resilience to damage by neutrons. Most of the data presented here has been taken with Ge detectors.

Another typical experimental problem in heavy-ion transfer reactions is the large ratio between the inelastic scattering cross section and transfer reaction cross section, especially in the two-neutron transfer reaction. Due to the low detection efficiency of the Ge crystal and strong inelastic excitation, a γ-ray spectrum has a large background component related to the Compton scattering of photons. To improve the transfer peak-to-background ratio we used Compton-suppression shields which entirely surround the Ge detectors. The main purpose of the Comp-

ton shield is to detect the Compton scattered photons from the Ge crystal, and to make an anticoincidence with γ-rays detected by the Ge detectors in order to veto Compton events. We used two kind of shields, NaI and BGO. Bismuth-germanate (BGO) crystals ($Bi_4(GeO_4)_3$) have higher density (7.13 g/cm^3) compared to NaI (3.67 g/cm^3). Thus a given volume of BGO is about three times more efficient at Compton suppression than the corresponding volume of NaI. The BGO shield can be built smaller, leading to a more compact spectrometer.

Fig. 3.2 shows a schematic diagram of a full BGO Compton-suppressed Ge detector unit used in the Spin Spectrometer. Fig. 3.3 shows ^{60}Co spectra taken with the Compton-suppression unit in Fig. 3.2. The top spectrum is the unsuppressed spectrum detected by the Ge detector; the middle spectrum is the portion of events rejected by the suppression shield; the bottom spectrum is the result of the Compton suppression. The rejection of Compton events and enhancement of peak-to-background ratios allow the observation of weak transfer peaks which are buried in the background of unsuppressed Ge spectra.

3.2 Beam and Target

Most of the deformed nuclei are heavy nuclei, for which high bombarding energies are required to initiate the transfer reactions, because of the higher Coulomb barriers. Considerable progress in this field is connected with the advent of large tandem electrostatic accelerators. Fig. 3.4 is schematic view of the 25-MV Tandem van de Graaff accelerator of the Holified Heavy Ion Research Facility (HHIRF) at the Oak Ridge National Laboratory. The tandem accelerator can be operated alone or in coupled operation with the Oak Ridge Isochronous Cyclotron (ORIC). The maximum energy available in this coupled operation as a function of projectile mass is given in Fig. 3.5.

The beams which we have used, 325 MeV and 345 ^{58}Ni, 637 MeV ^{116}Sn,

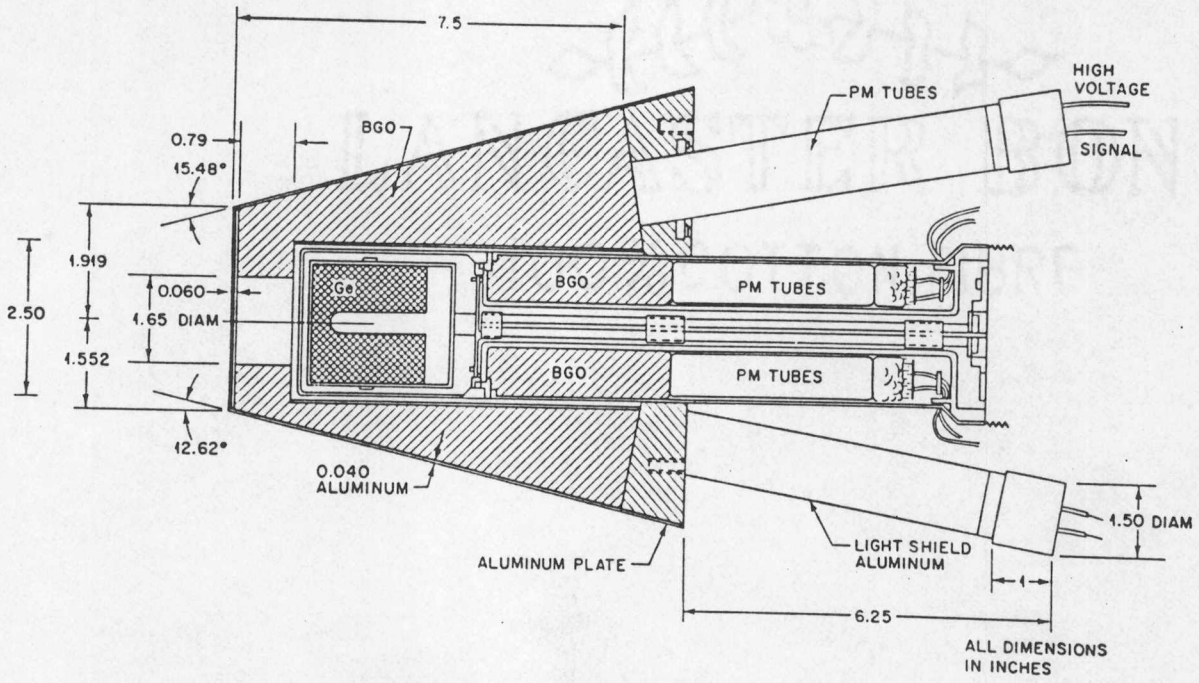


Figure 3.2: Schematic of a BGO Compton-suppression shield used in the Spin Spectrometer. Reproduced from Johnson *et al.* (1985).

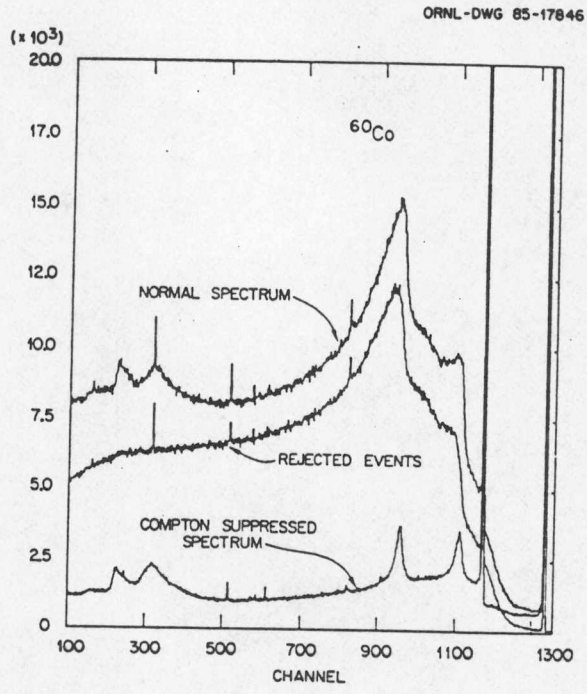


Figure 3.3: ^{60}Co spectra taken with the Compton-suppression unit shown in Fig. 3.2. The heights of the full-energy peaks at 1173 and 1333 keV are off scale, but have been normalized in this data. Reproduced from Johnson *et al.* (1985).

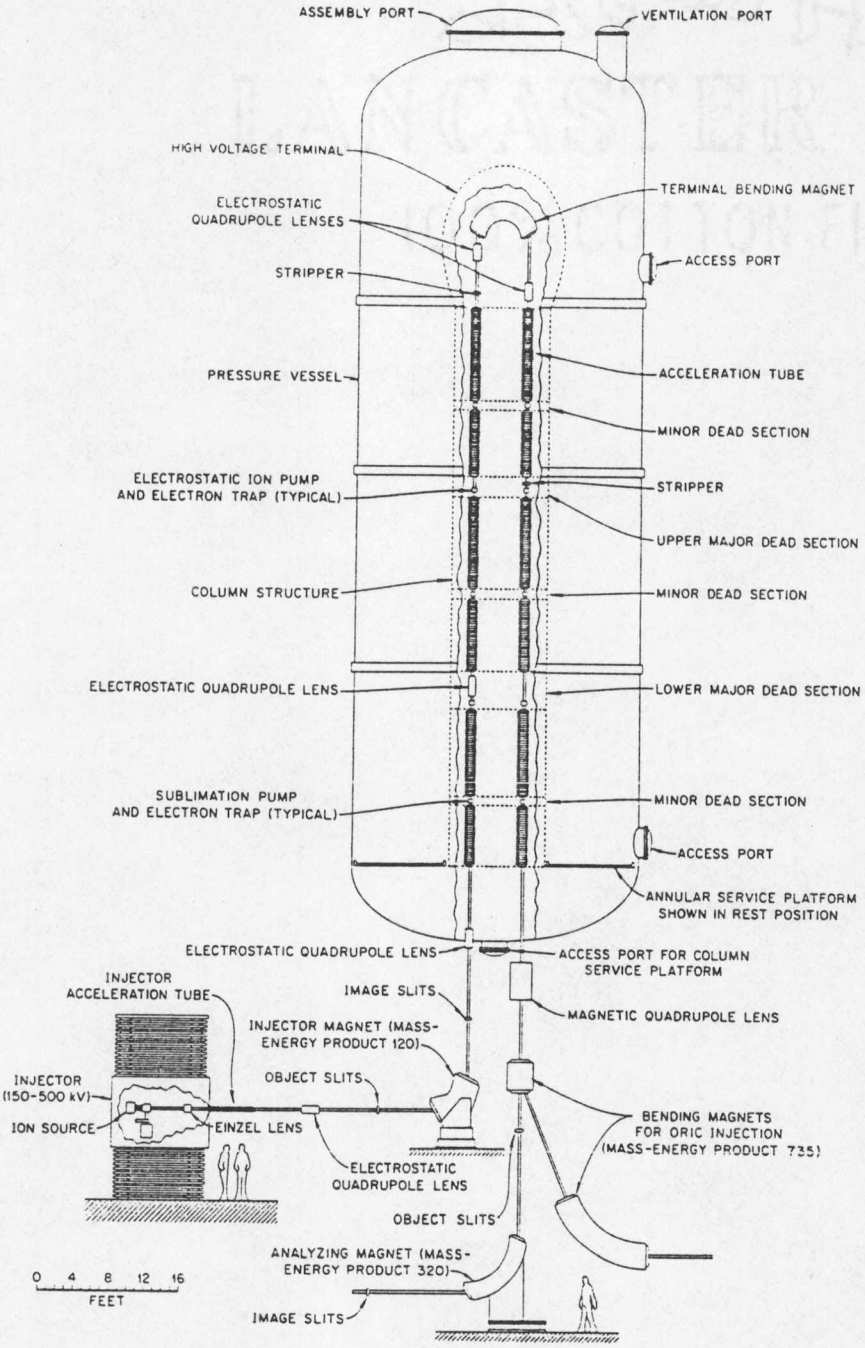


Figure 3.4: A schematic view of the 25-MV HHIRF tandem accelerator system at the Oak Ridge National Laboratory.

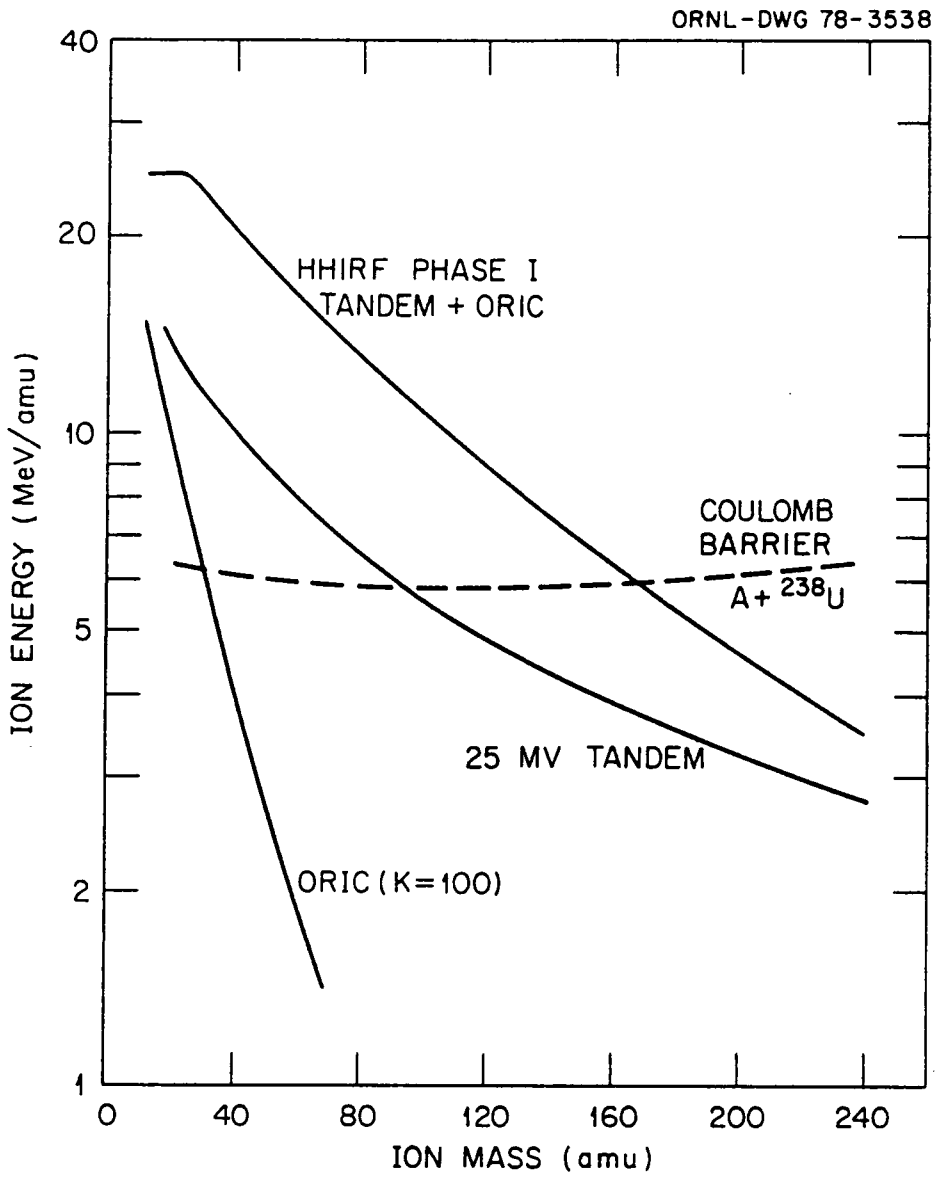


Figure 3.5: Ion energy performance of the HHIRF. The curve for coupled mode is for a beam intensity of 10^{11} particles/sec.

and 570 MeV ^{112}Sn beams were supplied in coupled operation, in which case the tandem accelerator serves as the injector to the cyclotron; 270 and 285 MeV ^{58}Ni beams were supplied by the tandem operating alone.

The selection of beam energy is based on the following consideration: the projectile energy should be near or above the Coulomb barrier to optimize the transfer cross section, and the grazing angle should be in a suitable position. For transferring more angular momentum to the final nuclei, we would like the grazing angle to be around 90°, but the particle detectors used in these experiments can only cover the angle ranges 20°-80° and 106°-160°. Due to this limit, we set the grazing angle on $\sim$ 60° (a 637 MeV ^{116}Sn beam) or $\sim$ 120° (a 285 MeV ^{58}Ni beam).

We take the ^{162}Dy(^{58}Ni, ^{60}Ni)^{160}Dy reaction as an example. According to Eq. 2.12, the sum of the grazing radii for the two nuclei is

$$D = 1.4(\sqrt[3]{A_1} + \sqrt[3]{A_2}) = 13.1\ fm \tag{3.1}$$

If the grazing angle in the laboratory system is 120°, according to Eq. 2.8 the corresponding grazing angle in the center-of-mass system is

$$\theta^{gr}_{cm} = \theta^{gr}_{lab} + \arcsin(\frac{A_2 \sin\theta_{lab}}{A_1}) = 138° \tag{3.2}$$

Assuming the projectile to follow a Rutherford trajectory, the energy of the projectile corresponding to this grazing angle is

$$E_{cm} = \frac{0.72 Z_1 Z_2}{13.7}(1 + csc(\frac{\theta cm}{2})) = 210\ MeV \tag{3.3}$$

$$E_{lab} = \frac{A_1 + A_2}{A_1} E_{cm} = 285\ MeV \tag{3.4}$$

The enriched Dy targets used were 540 μg/cm^2 - 600 μg/cm^2 thick self-supporting foils. Table 3.1 gives the isotopic composition of the targets.

Table 3.1: Isotopic Abundance in Dy Targets.

	Atomic Percent			
Isotope	^{161}Dy	^{162}Dy	^{163}Dy	^{164}Dy
156	<0.05	<0.02	<0.02	<0.01
158	<0.05	<0.02	<0.02	<0.01
160	0.22	0.08	0.07	0.02
161	95.94	1.22	0.71	0.15
162	2.46	96.26	2.63	0.35
163	0.86	1.75	93.07	1.05
164	0.52	0.69	3.35	98.43

3.3 Particle Detector

The particle detectors, position-sensitive parallel-plate avalanche detectors (PPAC),were designed and built by the research group of Dr. D. Cline (University of Rochester). The particle detectors are position sensitive in the θ and ϕ direction, θ being the polar angle with respect to the beam axis, ϕ being the azimuthal angle. They consist of an anode, cathode, and pressure window. The anode was made of polypropylene which was stretched to $\sim 40\mu g/cm^2$ first, then coated with a layer of aluminum by evaporation. The anode was divided into three parts for identifying ϕ. The cathode was a printed circuit board consisting of stripes of constant θ with a θ-angle spacing of 2°. The $\sim$ 260 $\mu g/cm^2$ mylar pressure window was used to hold the gas. The gap between the anode and cathode was 3 mm. The stripes on the cathode plate were connected to a tapped delay-line (1 ns per stripe) for the position signal read out.

During the experiment the counters were operated at $\sim$ 400 V and 4 Torr of isobutane. A continuous flow of gas was fed through the counters, and the pressure was held constant to $\pm$ 0.2 Torr by a feedback system incorporating a Baratron pressure transducer. The counters can be operated at very high counting rates (up to several MHz) and had $<$ 1.0 ns timing resolution. The angular resolution

was better than 2°. The times between the anode and both ends of the cathode were recorded, and the position was defined by the difference between this time. Every 1000th singles event was recorded along with the coincident events in order to calibrate the detection efficiency of the counters, and to measure the particle flux for calculation of absolute cross section.

3.4 The Spin Spectrometer

Nuclear γ-ray spectroscopy has been an important research tool. It is not only one of the main sources of information about the structure of nuclei, it also plays an important role in heavy-ion reaction studies. The main use of γ-ray spectroscopy in heavy-ion reaction studies is to investigate special properties of the reaction mechanism by particle-γ correlation measurements, and to determine the amount of angular momentum and excitation energy tied up in the residual reaction products. The total intrinsic excitation energy can be deduced from the sum of the energies of all γ rays. The γ-multiplicity is a measure of the total intrinsic spin because the γ-decay proceeds, at least in deformed nuclei, predominantly via E2-cascades, with each γ-ray removing two units of angular momentum. Therefore, experiments were improved by combining Ge detectors with two types of NaI-detector arrangements. The first was multiplicity filters (Hillis *et al.*, 1979)–arrays of individual NaI detectors which provided information about the γ-multiplicity. The other was sum-energy spectrometers (Tjϕm *et al.*, 1978)–large NaI detectors with the target positioned in its center so that most of the energy of the γ-rays is absorbed in the crystal.

It was soon realized that further progress in high-spin and heavy-ion reaction studies would require a new γ-ray spectrometer. It should have a γ-detection efficiency approaching 100% of 4π, a good energy, time, and angle resolution, the ability to measure simultaneously the γ-ray multiplicity and the total energy, and

the capability to handle events involving a large number of coincident γ rays.

At the end of the 1970's the Washington University research group led by D. G. Sarantites first designed and built this kind of γ-ray spectrometer, the Spin Spectrometer (Sarantites *et al.*, 1978 and 1980). It was installed at the Holifield Heavy Ion Research Facility (HHIRF) at the Oak Ridge National Laboratory. For a detailed description of the device see Jääskeläinen *et al.* (1983).

The Spin Spectrometer consists of an array of up to 72 closely-packed NaI detectors approximating a hollow sphere with an inner radius of 178 mm and shell thickness of 178 mm. The cross section of twelve of the detectors is a regular pentagon; each of the pentagonal detectors is surrounded by five identical detectors of irregular hexagonal cross section. The geometry of the shell surface of the spectrometer is illustrated in Fig. 3.6. Each detector is a tapped prism that can be removed easily, and can be replaced by Ge or Ge(Li) detectors with BGO or NaI Compton-suppression shields. One pentagon is removed for the beam line entrance, while its partner can be removed for beam exit, or to be replaced by an external detector. The apparatus stands on two independently movable platforms, and the halves may be rolled back on tracks perpendicular to the beam line to give access to the reaction chamber.

In Table 3.2 a summary of the angular position of the Ge detectors for some experiments can be found. The effective solid angle of each NaI crystal is 1.344% of 4π for a total solid angle of 96.8%. The 3.2% loss is due to the wall thickness (1 mm) of the aluminum cans housing the NaI crystal, and the internal light-reflecting material inside cans. The average energy resolution of the detectors is 82.5 keV FWHM for the 1.3 MeV γ-ray in ^{60}Co. The average time resolution is 2 ns FWHM for the same transition. Due to strong x-rays from the target, absorbers of 7 mil Cu and 7 mil Sn typically were placed on the front of the Ge detectors.

A schematic diagram of the electronics for the Spin Spectrometer is shown

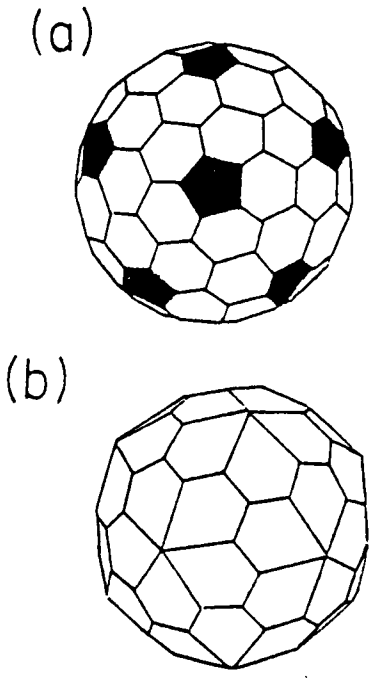


Figure 3.6: (a)Geometry of the Spin Spectrometer based on the truncated pentagonal hexecontahedron. The black areas represent the twelve regular pentagons. (b) The archimedean pentagonal hexecontahedron. The polyhedron of (a) orginates from truncation of the sharp corners of the twelve groups of five pentagons of (b). Reproduced from Jääskeläinen *et al.* (1983).

Table 3.2: Angular position of Ge detectors in the four Spin Spectrometer experiments with Dy targets.

Ge	^{58}Ni(1,2)		^{58}Ni(1)		^{58}Ni(2)		^{116}Sn	
ID	$\theta°$	$\phi°$	$\theta°$	$\phi°$	$\theta°$	$\phi°$	$\theta°$	$\phi°$
1	24.4	13.1	63.4	−36.8	155.6	94.9		
2	24.4	157.1	63.4	108.0	116.6	72.0	116.6	144.0
3	155.6	22.9	116.6	−72.0	63.4	108.0	63.4	−108.0
4	155.6	166.9	116.6	72.0	63.4	−36.0	116.6	−72.0
5			63.4	36.0	116.6	144.0	63.4	−36.0
6			24.4	−130.9	24.4	85.1	63.4	108.0
7			115.6	−49.1	116.6	−144.0	116.6	72.0
8			63.4	−108.0	116.6	−72.0	24.4	85.1
9			116.6	144.0	138.4	−86.0	155.6	94.9
10			24.4	85.1	63.4	−108		
11					41.6	−94.0		
12					130.5	96.3		
13					63.4	36.0		
14					24.4	−58.9		

in Fig. 3.7. The entire system must be triggered by an external signal satisfying the criteria for an acceptable event. We used the coincident particle signal as a master trigger for the system, and recorded the particle-particle-γ coincidence events.

3.5 Electronic Setup

A particle-particle-γ coincidence event occurs when two particle detectors (left and right) detect the beam-like ion and projectile-like ion within a 70 ns time window, and at least one Ge detector sees a γ-ray within a 250 ns time window. The electronic setup determines what time scale constitutes a particle-particle-γ coincident event, and whether or not the time and energy information associated with the event should be recorded.

Fig. 3.8 is a typical schematic diagram of the electronic setup for a transfer experiment in the Spin Spectrometer. The setup is divided into three parts: the

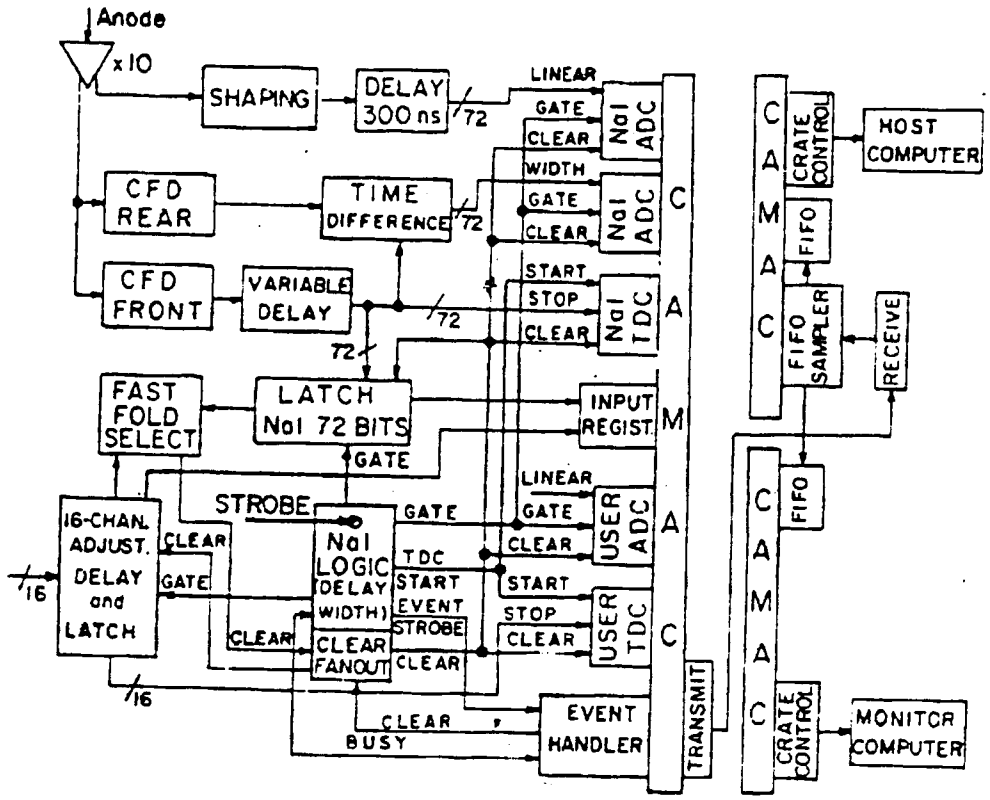


Figure 3.7: Schematic diagram of the electronics for the Spin Spectrometer. Reproduced from Jääskeläinen *et al.* (1983).

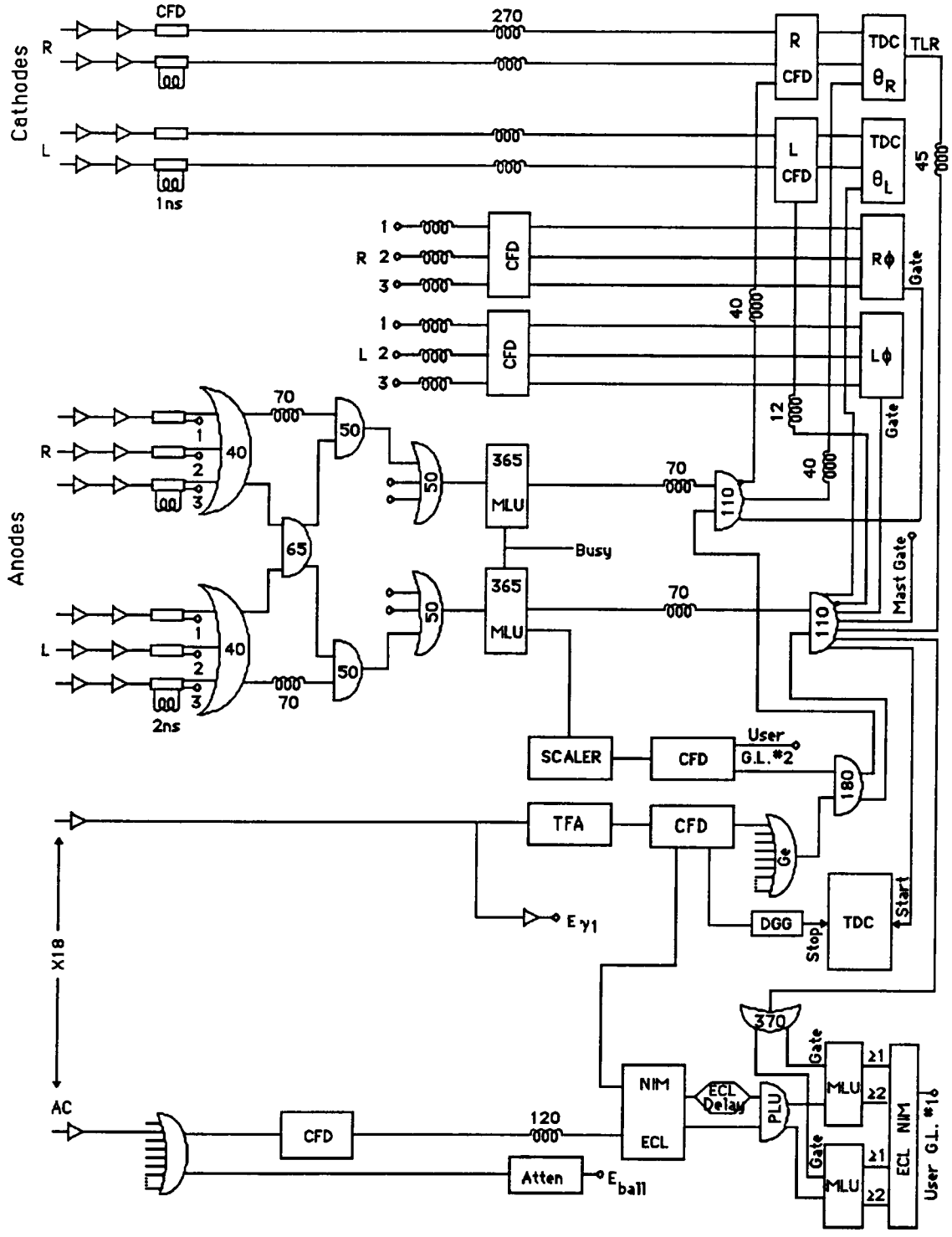


Figure 3.8: A typical schematic diagram of the electronic setup for a transfer experiment in the Spin Spectrometer.

electronics connected with the particle counters, the electronics associated with the Ge detectors, and the interface with the Spin Spectrometer.

To insure two-body kinematics, an event is stored only when both left and right particle counters fire (we assume that the detection efficiency of the particle counters is 100%); i.e. the detection of the scattered ion by the left (or right) counter must be accompanied by detection of the corresponding recoil ion by right (or left) particle counter. This kinematic coincidence was done by the prompt anode signals of the two counters within a 70 ns time window. The particle-particle coincidence signal makes a coincidence with the γ-ray to produce a particle-particle-γ coincidence signal. This signal with appropriate delay and 250 ns time width adjustments is used as a master trigger to gate the ADC and to start the TDC of all Ge detectors, the particle counters, and each NaI detector in the Spin Spectrometer. Thus the particle-particle-γ coincidence signal defines an acceptable event. All spectrometer ADCs and TDCs, as well as ADCs and TDCs for the Ge and particle counters, are interfaced with computer through a CAMAC system.

The data acquisition system is managed by the Event Handler, a programmable CAMAC-based controller. The Event Handler places data in a suitable format, transmits them to the on-line computer (a Perkin-Elmer 32/20), and writes them to magnetic tape for permanent storage.

3.6 Experimental Data

We have done a series of transfer experiments in the Spin Spectrometer. In table 3.3 we list all reactions, with some interesting parameters. here the sum of nuclear radii R_{sum}, and the Coulomb barrier V_C^{lab} are defined as:

$$R_{sum} = 1.16(\sqrt[3]{A_1} + \sqrt[3]{A_2} + 2) \tag{3.5}$$

$$V_c^{lab} = \frac{1.44 Z_1 Z_2}{R_{sum}} \left(\frac{A_1 + A_2}{A_1} \right) \tag{3.6}$$

Table 3.3: Some properties of the Spin Spectrometer experiments studied; ΔN represents one or two-neutron transfer.

ID	Reaction	ΔN	E_{lab}(MeV)	V_c^{lab}(MeV)	Q_{gg}(MeV)	R_{sum}(fm)
1	^{58}Ni+^{161}Dy	1N	270.0	275.9	2.5	13.1
2	^{58}Ni+^{162}Dy	2N	285.0	275.2	5.7	13.1
3	^{58}Ni+^{161}Dy	1N	345.0	275.9	2.5	13.1
4	^{58}Ni+^{162}Dy	2N	345.0	275.2	5.7	13.1
7	^{116}Sn+^{161}Dy	1N	637.0	572.2	0.5	14.3
8	^{116}Sn+^{162}Dy	2N	637.0	570.2	1.6	14.3
9	^{116}Sn+^{163}Dy	1N	637.0	568.5	0.7	14.3
10	^{116}Sn+^{164}Dy	2N	637.0	566.3	2.3	14.3
11	^{112}Sn+^{117}Sn	1N	570.5	518.7	0.8	13.6
12	^{112}Sn+^{118}Sn	2N	570.5	515.9	1.8	13.6
13	^{58}Ni+^{235}U	1N	325.0	331.3	3.7	14.0

3.6.1 Experiments with the ^{58}Ni Beam in 1983

In these experiments we studied one and two-neutron transfer reactions at two different beam energy: near and 20% above the Coulomb barrier. The 345 MeV ^{58}Ni beam was incident on ^{161}Dy and ^{162}Dy targets; the 270 MeV ^{58}Ni beam was incident on a ^{161}Dy target, and the 285 MeV ^{58}Ni beam was incident on a ^{162}Dy target. The target thickness was 600μg/cm^2 for ^{162}Dy and 547μg/cm^2 for ^{161}Dy. We used four particle counters and four Ge(Li) detectors in the Spin Spectrometer. A kinematic coincidence between left and right particle counters with at least one γ-ray in the Ge(Li) detectors defined an event. Both forward and backward angle scattering data were collected. For each event the TDC and ADC of the NaI and Ge(Li) detectors which fired, the total energy and multiplicity from the Spin Spectrometer, and 9 parameters from the particle counters were written to the tape. A total of 30 high-density (6250 bpi) tapes of data was collected.

3.6.2 Experiments with the ^{116}Sn Beam in 1985

A series of nuclei, ^{161}Dy, ^{162}Dy, ^{163}Dy, and ^{164}Dy, was used to study one and two-neutron transfer reactions. A superfluid nucleus, ^{116}Sn, was chosen as the beam. The beam energy was 10% above the Coulomb barrier. The target thickness was 547μg/cm^2 for ^{161}Dy, 600μg/cm^2 for ^{162}Dy and ^{163}Dy, and 836μg/cm^2 for ^{164}Dy. Eight Ge detectors with six Compton-suppressed shields were installed in the Spin Spectrometer. Four particle counters were used. A particle-particle-γ coincidence defined an event. A total of 130 high density data tapes was collected.

3.6.3 Experiments with the ^{58}Ni Beam in 1985

In this experiment we concentrated on the one-neutron transfer reaction with a 270 MeV ^{58}Ni beam on a ^{161}Dy target to study the population of the ground band and sidebands in ^{160}Dy. The Spin Spectrometer comprised an array of ten Ge detectors and sixty NaI detectors; five of the Ge detectors were Compton suppressed. Two backward-angle particle detectors were used. Events were collected when a backscattered Ni-like ion was detected in the particle detectors (which had an angular range 104°-162°), and when any one Ge detector and any one of the sixty NaI elements fired. Approximately 18×10^6 such events were recorded, of which 1.5×10^6 events corresponded to two Ge detectors firing simultaneously. One-half of all recorded events corresponded to the one-neutron pick up channel.

3.6.4 Additional Experiments with the ^{58}Ni Beam in 1986

At this time we did two different kinds of experiments. First we concentrated on two-neutron transfer reactions with the 285 MeV ^{58}Ni beam on a rare-earth ^{162}Dy target to study the role of pairing in the even-even deformed nucleus; second we used a 325 MeV ^{58}Ni beam on ^{235}U to extend high-spin one-neutron transfer

reactions to the actinide region. The target thickness was 542μg/cm^2 for ^{162}Dy, and 300μg/cm^2 for ^{235}U with a nickel backing (110 μg/cm^2). 14 Ge detectors with 8 NaI Compton-suppressed and 4 BGO Compton-suppressed shields were installed in the Spin Spectrometer, and 4 particle detectors were used. A total of 37 high density data tapes for the ^{162}Dy experiment and 16 high density data tapes for the ^{235}U experiment was collected.

3.6.5 Experiments with the ^{112}Sn Beam in 1987

A 570 MeV ^{112}Sn beam was used to bombard ^{117}Sn and ^{118}Sn in order to study one and two-neutron transfer between superfluid nuclei. The target thicknesses were 400 μg/cm^2 for ^{117}Sn and 420 μg/cm^2 for ^{118}Sn. The Spin Spectrometer consisted of 17 Compton-suppressed Ge detectors and 53 NaI detectors, which were operated in coincidence with two particle counters.

3.6.6 Experiments with the ^{206}Pb Beam in 1987

The experiment was performed by bombarding ^{233}U and ^{235}U with 1566 MeV and 1394 MeV ^{206}Pb ions respectively from SuperHILAC at the Lawrence Berkeley Laboratory in order to study the population of high-spin states in the actinide region. The ^{233}U target, of thickness 430 μg/cm^2 on a 2 mg/cm^2 Be backing, was enriched to 99% with a 0.0038 % ^{232}U contamination. The ^{235}U target, with thickness 280 μg/cm^2 on a 110 μg/cm^2 Ni backing, was enriched to 99.89% with a 0.034% ^{234}U contamination. Two particle counters were placed in the LBL Ge ball (HERA), which consisted of 14 Compton-suppressed Ge detectors.

CHAPTER 4

DATA ANALYSIS

4.1 Introduction

The data analysis methods contain three procedures: calibration, prescan, and scan. The calibration includes particle counter position calibration, energy and efficiency calibration of the Ge detectors, and response calibration of the Spin Spectrometer. The prescan includes a shift of energy and timing according to the calibrations, identification of events which come from projectile-like or target-like ions, Doppler correction for the γ-spectrum, neutron and γ separation, and the creation of derived quantities: for example, the mass spectrum, Q-value spectrum, neutron multiplicity, etc. Next we scan the prescan tapes to construct a two-dimensional matrix gated on different parameters. From this matrix we study the correlation of different quantities.

4.2 Energy and Efficiency Calibration for the Ge Detectors

We used ^{152}Eu and ^{182}Ta sources for energy calibration of the Ge detectors. For the efficiency calibration we used a mixed-radionuclide point-source standard. This standard provided γ-rays from 27 to 1274 keV.

Usually we used the following formula to calculate the absolute efficiency of the Ge detectors:

$$\epsilon(E_\gamma) = \frac{A(E_\gamma)}{BT(1-D)S} \tag{4.1}$$

where A is the number of γ-rays detected by the Ge detectors, B is the branching ratio, T the elapsed time, D the system dead time, and S is the intensity of the calibration source.

In the Spin Spectrometer experiments there is an array of Ge detectors at a variety of angles, so we can ignore the angular correlation of γ-rays. When we were interested in the total efficiency of all Ge detectors, we used another method to calculate the absolute efficiency. First we calculated the relative efficiency, then we determined the absolute efficiency at a particular energy by the measurement of γ-γ coincidences. Finally, we converted the relative efficiency to the absolute efficiency by normalizing at this particular energy.

We used a ^{60}Co source which emits two γ-rays in cascade with a branching ratio 1. The energies of γ_1 and γ_2 are 1173 keV and 1332 keV. If one γ-ray is detected by a Ge detector, the other γ-ray must be emitted inside the Spin Spectrometer. Assuming the photopeak efficiency for detection of γ_1 and γ_2 to be ϵ_1 and ϵ_2, the total number of events for detection of the single γ_1 are:

$$N(\gamma_1) = NN_{Ge}\epsilon_1 \tag{4.2}$$

were N is the total number of cascade events and N_{Ge} is the number of Ge detectors in the Spin Spectrometer. For the detection of γ_1 and γ_2 coincident events the total number of events is:

$$N(\gamma_1, \gamma_2) = NN_{Ge}(N_{Ge} - 1)\epsilon_1\epsilon_2 \tag{4.3}$$

Dividing Eq.(4.3) by Eq.(4.2) gives

$$\epsilon_2 = \frac{N(\gamma_1, \gamma_2)}{(N_{Ge} - 1)N\gamma_1} \tag{4.4}$$

Therefore the total efficiency for detection of γ_1 is

$$\epsilon_{total} = \frac{N_{Ge}N(\gamma_1, \gamma_2)}{(N_{Ge} - 1)N(\gamma_1)} \tag{4.5}$$

Fig. 4.1 shows the total γ-ray spectrum of a ^{60}Co source in the ^{58}Ni expriment; (A) is the one-fold spectrum; (B) is the ungated 2-fold spectrum; (C) is the 2-fold spectra gated on 1173 keV; (D) is the 2-fold spectra gated on 1332 keV. Fig.

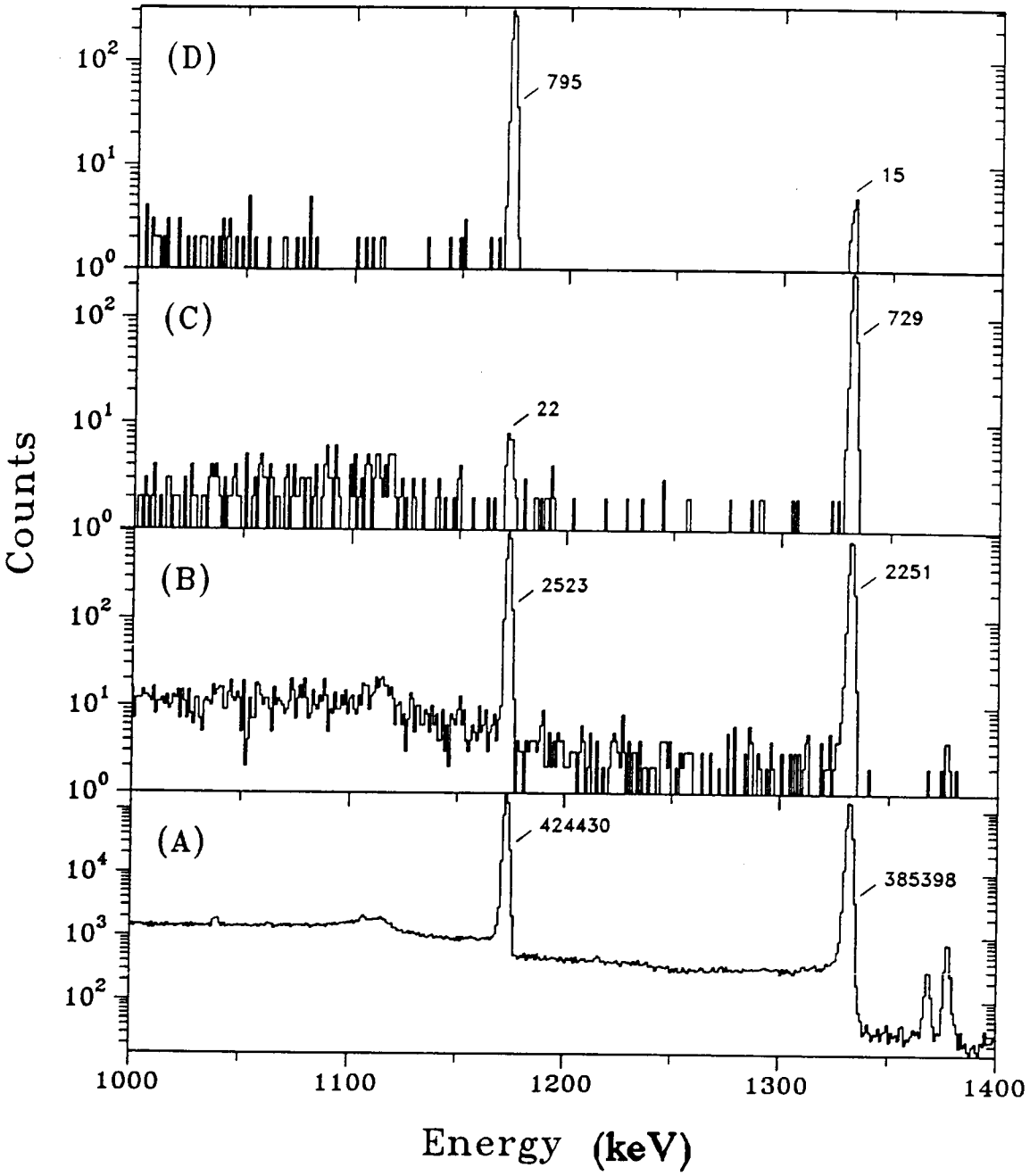


Figure 4.1: Total γ-ray spectra of ^{60}Co source. The numbers indicate the total counts in the corresponding peaks.

4.2 illustrates the absolute efficiency curve for the same experiment, determined by the method just described.

4.3 Calibration of the Spin Spectrometer

It is of fundamental importance to predict the outcome of an event consisting of $[E_i]_{i=1,...m}$ γ-rays. A calibration of the Spin Spectrometer is required to determine this response. The response is determined by several physical effects that depend on the properties of the γ-cascades, and other emitted penetrating radiation. The most significant effects are:

1. Incomplete detection of γ-rays.

2. Detector-to-detector scattering.

3. Coincidence summing in each detector element.

4. Pulses originating from other sources (neutrons and high-energy protons).

The first three of these are connected to the detection of one or more γ-rays by one or more detectors in the spectrometer, and must be taken into account quantitatively in the calibrations. In order to achieve better resolution in multiplicity and total energy for the spectrometer, it is important to discriminate against pulses which are not due to γ-rays. Most of the neutrons can be identified by their time of flight; in section 4.7 we will discuss neutron-γ separation.

An analytic expression of the response function P_N(EM,HK) has been derived (Sarantites *et al.*, 1980) for a system of N detectors to record a total pulse height H and fold K for an input event of total energy E and multiplicity M, where $H = \sum_{i=1}^{N} h_i$ is the sum of pulse heights above some threshold h_{tr}, and $E = \sum_{i=1}^{N} E_i$ is the sum over the γ-ray energies in the cascade.

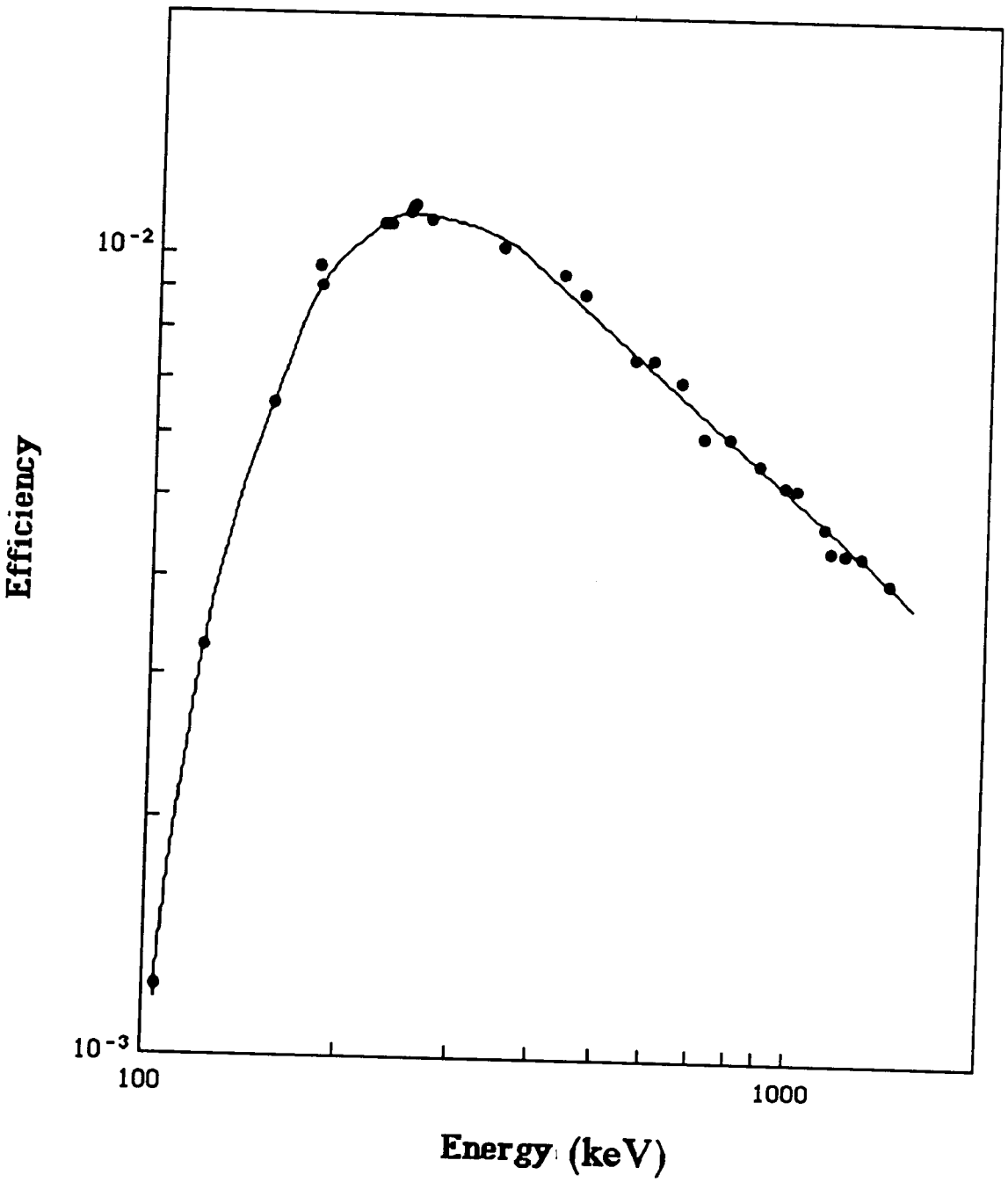


Figure 4.2: The absolute efficiency curve for the ^{160}Dy + (285 MeV) ^{58}Ni experiment.

An experimental method to obtain a complete characterization of P(EM, HK) was presented by Jääskeläinen *et al.* (1983). This is based on the use of sources that have only two γ rays in cascade with essentially 100% branching ratio. If one of these γ-rays is detected in a Ge detector, this ensures that the second γ-ray was emitted at the target position inside the Spin Spectrometer. The sources used for the response calibration are listed in table 4.1:

Table 4.1: The sources used for the response calibration of the Spin Spectrometer.

Source	Half life	Energy (keV)	Intensity
^{75}Se	118.5 d	136.0	93.1
	118.5 d	264.65	100.0
^{207}Bi	38.0 y	569.65	100.0
	38.0 y	1063.63	75.5
^{88}Y	106.6 d	898.02	91.9
	106.6 d	1836.13	100.0
^{60}Co	5.3 y	1173.21	100.0
	5.3 y	1332.47	100.0
^{24}Na	15.0 h	1368.53	100.0
	15.0 h	2753.91	100.0

We place the source in the spectrometer, a Ge detector is used to trigger the data acquisition system, and the response of the entire spectrometer is recorded on magnetic tape by writing all the pulse heights and related times of the detectors that fire in an event-by-event mode. On the playback of event data, in order to construct the P(EM,HK) responses we do the following: project the Ge singles from all sources; determine the limits of the Ge energy peak; project the TDC of the NaI detectors gated by Ge peaks; set gates on the time spectra; create a TDC file; scan the source calibration data for clean events; scan clean events for ω_K, ω_T, ω_E efficiencies, and single responses; and from singles responses construct the multiple-photon responses P(EM,HK).

4.4 Unfolding of Two-Dimensional (H,K) Map

For a given input γ-ray spectrum $E_{i=1,...,M}$ with $E=\sum_{i=1}^{M} E_i$ the mapping (E,M) $\rightarrow$ (H,K) is defined by

$$\mathbf{M}(H,K) = \mathbf{S}\mathbf{M}(E,M) \tag{4.6}$$

where **M**(H,K) is the experimentally measured (H,K)-map, **S** is the response matrix of the Spin Spectrometer as discussed in section 4.3, and **M**(E,M) is the (E,M)-map which we are seeking. In contrast, the reverse mapping (H,K) $\rightarrow$ (E,M) is defined as

$$\mathbf{M}(E,M) = \mathbf{S}^{-1}\mathbf{M}(H,K) \tag{4.7}$$

where $\mathbf{S}^{-1}$ is the inverse matrix of **S**. Since the matrix is too large to invert, S. Sorensen developed an iterative method based on the decomposition of the Euclidian norm to solve Eq. 4.6. The algorithm is iterative; in the n^{th} step the residuals $\mathbf{R}_n$ corresponding to the n^{th} estimated solution $\mathbf{M}(E,M)_n$ are

$$\mathbf{R}_n = \mathbf{S}\mathbf{M}(E,M) - \mathbf{M}(H,K) \tag{4.8}$$

If the Euclidian norm for a vector v is denoted E(v), then the $(n+1)^{th}$ estimated solution is

$$\mathbf{M}(E,M)_{n+1} = \mathbf{M}(E,M)_n - \lambda \left[\frac{E(\mathbf{R}_n)}{E(\mathbf{S}^t\mathbf{R}_n)}\right]^2 \mathbf{S}^t\mathbf{R}_n \tag{4.9}$$

where $\mathbf{S}^t$ is the transpose of **S**, the vector $\mathbf{S}^t\mathbf{R}_n$ gives the direction for the next step and the scalar in the brackets is the steplength, and λ is the iteration parameter, which is chosen to optimize the convergence of the iteration. Typical values for λ are 0.5 in the first step, decreasing to values of 0.1 - 0.2 if more then 5 iterations are needed. The new iterated spectrum M(E,M) is the geometric mean between $\mathbf{M}(E,M)_n$ and $\mathbf{M}(E,M)_{n+1}$. The basis for this algorithm is described in N. Gastinel's *Linear Numerical Analysis* (1970).

We guess a M(E,M)-map according to the original M(H,K)-map and the efficiency of the Spin Spectrometer, multiply it by the response matrix, then subtract this from the original (H,K)-map to find the difference, correct the original guess, and try again. When the **SM**(E,M) is close to the original (H,K)-map, the final corrected guess is accepted as a good estimate of the M(E,M)-map. Typically 10 iterations are needed to get a good convegence: after 10 iterations the residuals generally do not change and nothing is gained by further iteration.

In Fig. 4.3 is shown the (H,K)-map and the corresponding M(E,M)-map for the reaction ^{162}Dy(^{116}Sn,^{118}Sn)^{160}Dy. In general the distribution of the (E,M)-map is similar in shape to the original distribution of the (H,K)-map, but it is shifted approximately a half unit along the M-axis, and approximately 20% up on the E-axis, and the resolution is improved.

4.5 The Identification of Particles

We use the information provided by the particle counters to calculate the mass spectrum of outgoing particles according to two-body kinematics, and then identify whether the particles are beam-like or target-like ions.

The coordinate system normally used for the Spin Spectrometer is shown in Fig. 4.4. A line orthogonal to the left counter plane through the origin has the direction $(\theta_{lc}, \phi_{lc}) = (45°, 270°)$. For the right counter the corresponding angles are $(\theta_{rc}, \phi_{rc}) = (45°, 90°)$. Throughout the calculation the following definitions have been used: particle 1 is the projectile nucleus, 2 the target nucleus, 3 the scattered projectile-like ion, 4 the scattered target-like ion, L the ion hitting the left counter, R the ion hitting the right counter, LR either L or R, C either the left or right counter. The following units have been chosen: [P] = MeV/ns, [M] = amu, [E] = MeV, [v] = cm/ns, [length] = cm, [t] = ns.

Suppose the beam energy is E_{beam}; the projectile energy in the middle of

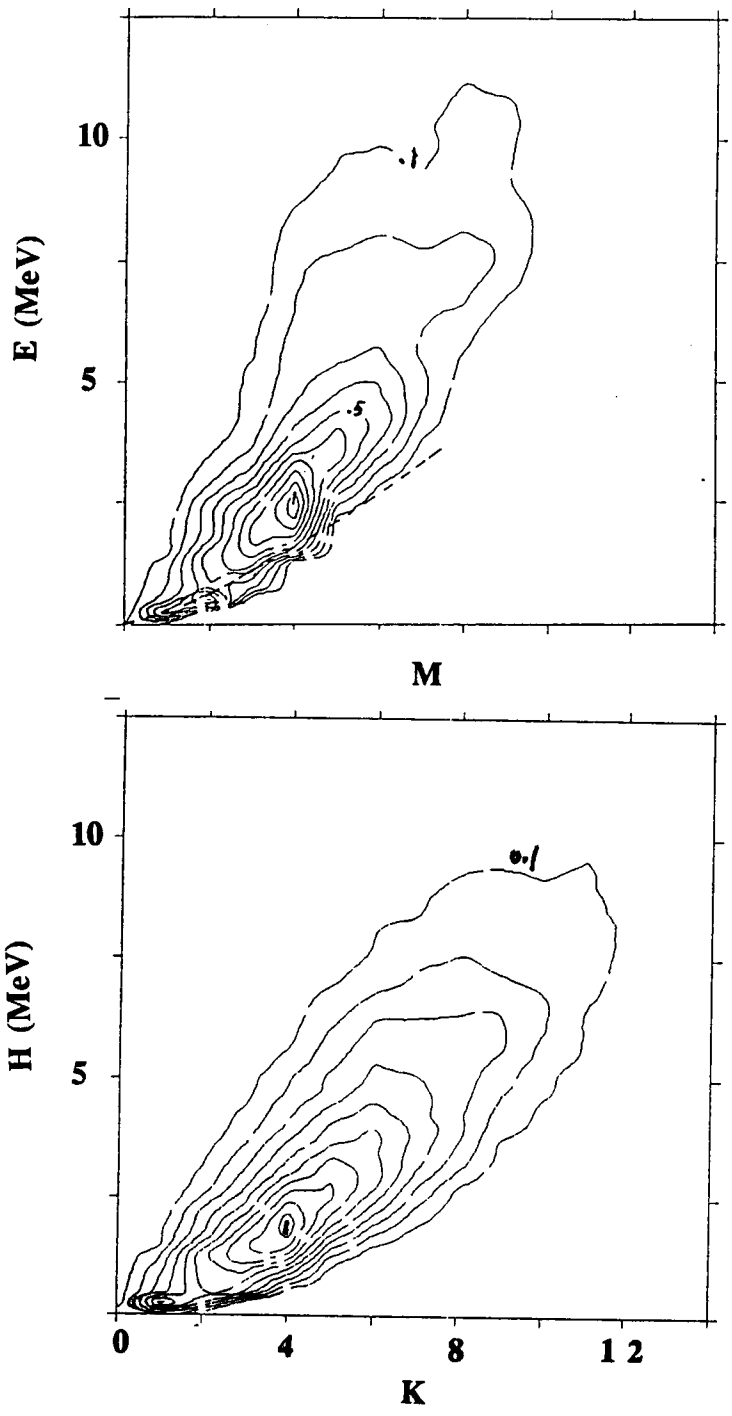


Figure 4.3: An (H,K)-map and the corresponding unfolded (E,M)-map. The reaction is ^{162}Dy(^{116}Sn,^{118}Sn)^{160}Dy at 637 MeV.

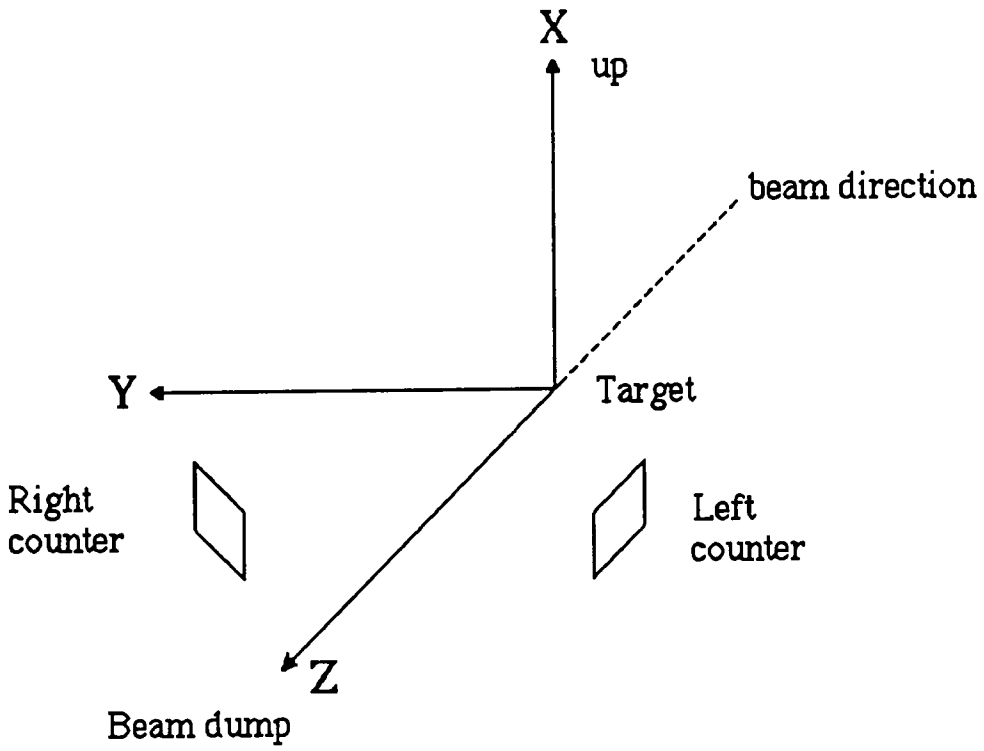


Figure 4.4: The coordinate system for the Spin Spectrometer.

the target is

$$E_1 = E_{beam} - \Delta E_{loss} \tag{4.10}$$

and the momentum of the projectile is

$$P_1 = (2m_1E_1)^{1/2} = 43.162(m_1E_1)^{1/2} \tag{4.11}$$

Under the assumption of two-body kinematics, momentum conservation implies

$$P_L \cos\theta_L + P_R \cos\theta_R = P_1 \tag{4.12}$$

$$P_L \sin\theta_L - P_R \sin\theta_R = 0 \tag{4.13}$$

These two linear equations in P_L and P_R have the solutions

$$P_L = P_1 \frac{\sin\theta_R}{\sin(\theta_L + \theta_R)} \tag{4.14}$$

$$P_R = P_1 \frac{\sin\theta_L}{\sin(\theta_L + \theta_L)} \tag{4.15}$$

The above-mentioned orthogonal vector characterizing the position of each counter is

$$\vec{\alpha}_C = d_C \begin{pmatrix} \sin\theta_C \cos\phi_C \\ \sin\theta_C \sin\phi_C \\ \cos\theta_c \end{pmatrix} \tag{4.16}$$

where d_C (d_L or d_r) is the smallest distance between the target and the counter, and $d_L = d_R = 10.0$ cm. From the angles $\theta_L = \theta_R = 45°$, $\phi_L = 270°$, and $\phi_R = 90°$ we obtain

$$\vec{\alpha}_{LC} = \frac{d_L}{\sqrt{2}} \begin{pmatrix} 0 \\ -1 \\ 1 \end{pmatrix} \tag{4.17}$$

A unit vector pointing in the direction of the motion of the ion hitting the counter C is

$$\vec{e}_{LR} = \begin{pmatrix} \sin\theta_{LR}\cos\phi_{LR} \\ \sin\theta_{LR}\sin\phi_{LR} \\ \cos\theta_{LR} \end{pmatrix} \tag{4.18}$$

The flight path of the particle from the target to the counter is of length

$$\frac{d_C}{\cos(\vec{\alpha}_{LR}, \vec{e}_{LR})} \tag{4.19}$$

The function $\cos(\vec{\alpha}_{LR}, \vec{e}_{LR})$ can be found from a scalar product of the two vectors

$$\cos(\vec{\alpha}_{LR}, \vec{e}_{LR}) = \frac{\vec{\alpha}_{LR} \cdot \vec{e}_{LR}}{|\vec{\alpha}_{LR}|\,|\vec{e}_{LR}|} = \frac{1}{\sqrt{2}}(\cos\theta_{LR} - \sin\theta_{LR}\sin\phi_{LR}) \tag{4.20}$$

The flight path is

$$S_{LR} = \frac{\sqrt{2}d_c}{\cos\theta_{LR} - \sin\theta_{LR}\sin\phi_{LR}} \tag{4.21}$$

The difference in time-of-flight, ΔT, between the left and right ions can be used now to calculate the mass of the outgoing ion, and thereby to decide whether the projectile-like ion is going left or right. The velocity can be expressed as

$$v_{LR} = \frac{P_{LR}}{M_u c M_{LR}} \tag{4.22}$$

where M_u is the atomic mass unit, and M_{LR} the atomic mass number of the fragment. The time-of-flight is

$$T_{LR} = \frac{S_{LR}}{v_{LR}} = \frac{S_{LR} M_u M_{LR}}{P_{LR}} \tag{4.23}$$

and the time difference is

$$\Delta T = T_R - T_L = M_u c\left(\frac{S_R}{P_R} M_R - \frac{S_L}{P_L} M_L\right) \tag{4.24}$$

Remembering that the total number of nucleons is conserved,

$$M_R + M_L = M_{total} \tag{4.25}$$

from Eq. 4.24 and 4.25 we obtain the mass formulas

$$M_L = \frac{-\frac{\Delta T}{M_u} + \frac{S_R}{P_R} M_{total}}{\frac{S_L}{P_L} + \frac{S_R}{P_R}} \tag{4.26}$$

$$M_R = \frac{\frac{\Delta T}{M_u} + \frac{S_L}{P_L} M_{total}}{\frac{S_L}{P_L} + \frac{S_R}{P_R}} \tag{4.27}$$

From these formulas we calculate the masses in every event to determine whether the beam-like fragment is going to the left or right.

The TDC calibration for the ΔT signal

$$\Delta T\ [ns] = C_1 \Delta T + C_0 \tag{4.28}$$

was determined by delaying the signal from the right PPAD. In the ^{116}Sn experiment this delay was 13 ns, and C_1 = 0.0655 ns/channel, C_0 = -61.9 ns/ channel. The mass spectrum determined by these methods for the ^{162}Dy+ ^{116}Sn reaction is shown in Fig. 4.5

4.6 The Reaction Q-Value

Once it has been determined whether particle 3 is going left or right, the label 3 and 4 can be used instead of L and R. The reaction Q-value (in MeV) can be calculated from the formula

$$Q = E_3 + E_4 - E_1 = (2 \times 931.48)^{-1}\left(\frac{P_3^2}{m_3} + \frac{P_4^2}{m_4}\right) - E_1 \tag{4.29}$$

The total Q-value for the ^{162}Dy + ^{116}Sn reaction is shown in Fig. 4.6, The right large peak with Q $\sim$ 0 MeV corresponds to the quasielastic events, *e.g.*, inelastic and transfer reactions; the left small bump with Q $\sim$ 50 MeV corresponds to deep inelastic events. The resolution in Q-value is about 30 MeV. The poor resolution in Q-value comes from the angular resolution of the particle counters and from energy loss in the target.

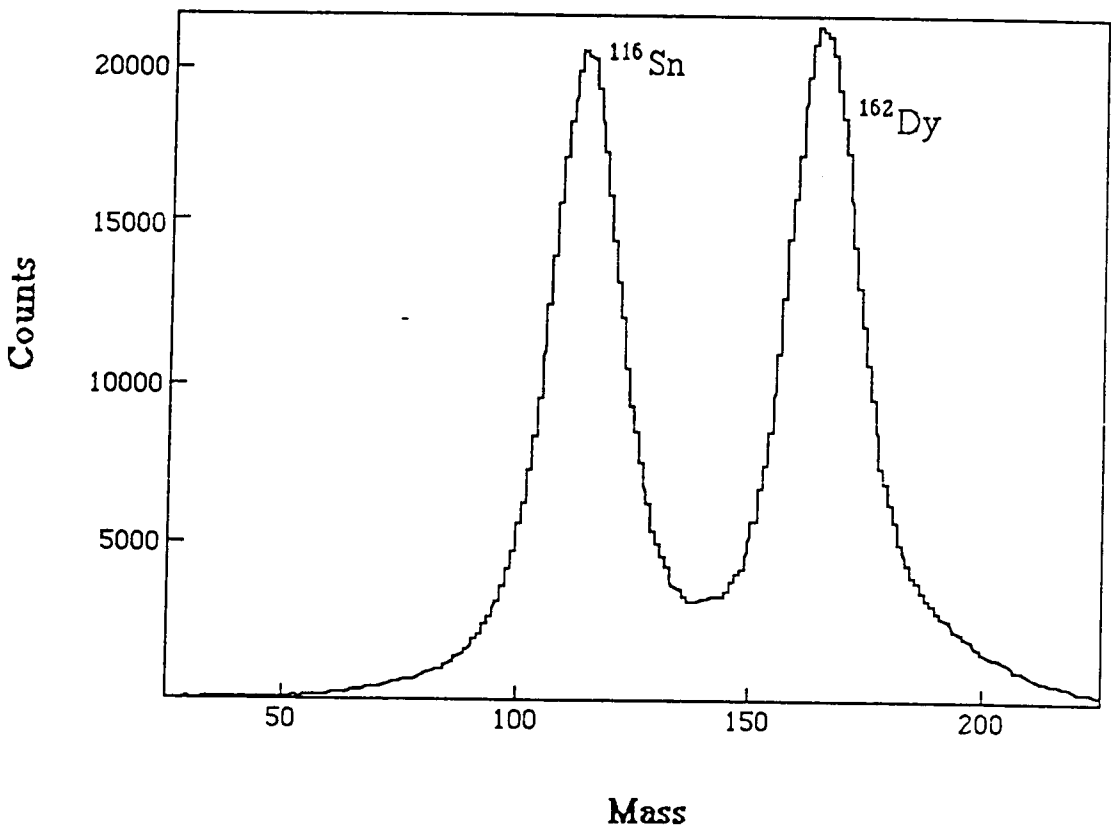


Figure 4.5: Mass spectrum for the ^{162}Dy+ ^{116}Sn reaction.

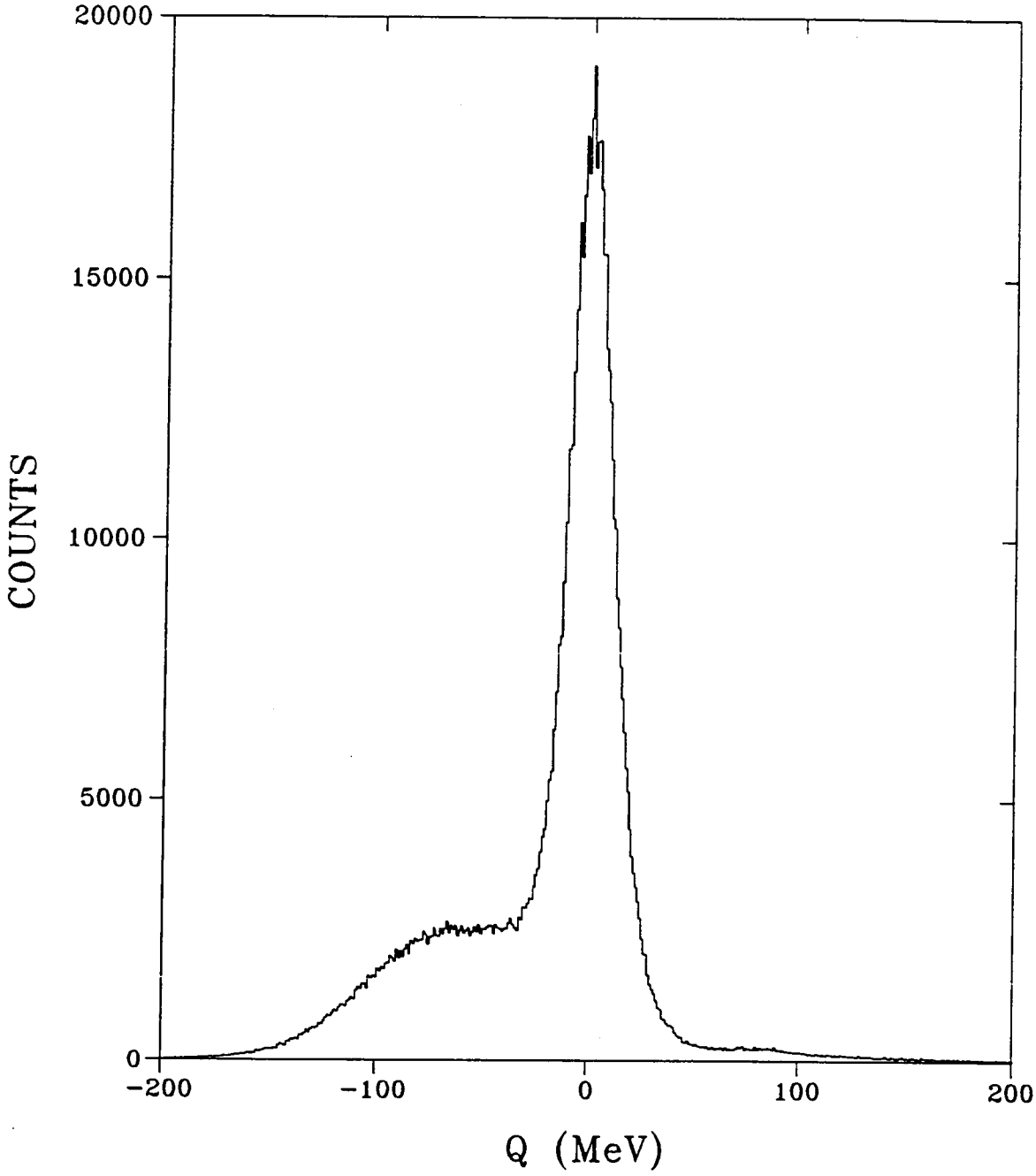


Figure 4.6: The Q-spectrum for the ^{162}Dy + ^{116}Sn reaction.

4.7 Identification of γ-rays and Neutrons

A major problem in the analysis of γ-ray data is the contamination of neutron events. This contamination is especially strong in the deep inelastic reaction, where many neutrons might be emitted in each event. In our case, we are working close to the Coulomb barrier, where neutrons are not so dominant, but they still represent a significant fraction of the pulses in the NaI. The large cross section for inelastic scattering of neutrons on iodine combined with the large thickness of NaI may cause significant interference due to the response to neutrons. Perhaps 10% of our events have sufficient excitation energy to involve emission of neutrons. The pulses due to neutrons must be identified

The limited timing resolution does not permit a clear separation of the neutron events from the γ-rays. To improve this separation the time from each of the NaI detectors is shifted by some amount so as to match the detectors to 0.2 ns, then we correct by the true start time t_0 event-by-event. The true time of the reaction related to the trigger time can be determined as the time-of-flight of the left particle

$$t_0 = t_L = 31.071 \frac{S_L}{P_L} m_L \tag{4.30}$$

To determine the masks for the γ-neutron separation, two-parameter (t,h) [time vs. pulse height] maps for each NaI detector must be created. This must be done with timing corrections using reaction data. Then we create time projections for several pulse height groups of increasing widths for large pulse height to determine the position of the γ-neutron separation in these 1-dimensional slices; the events above these positions are related to neutrons. In Fig 4.7 are shown the timing maps for different angles (forward, 90°, and backward angles) gated on different pulse heights. The separation of γ-rays and neutrons we have taken is indicated by vertical lines. In the prescanning we set a new parameter, neutron multiplicity K_N,

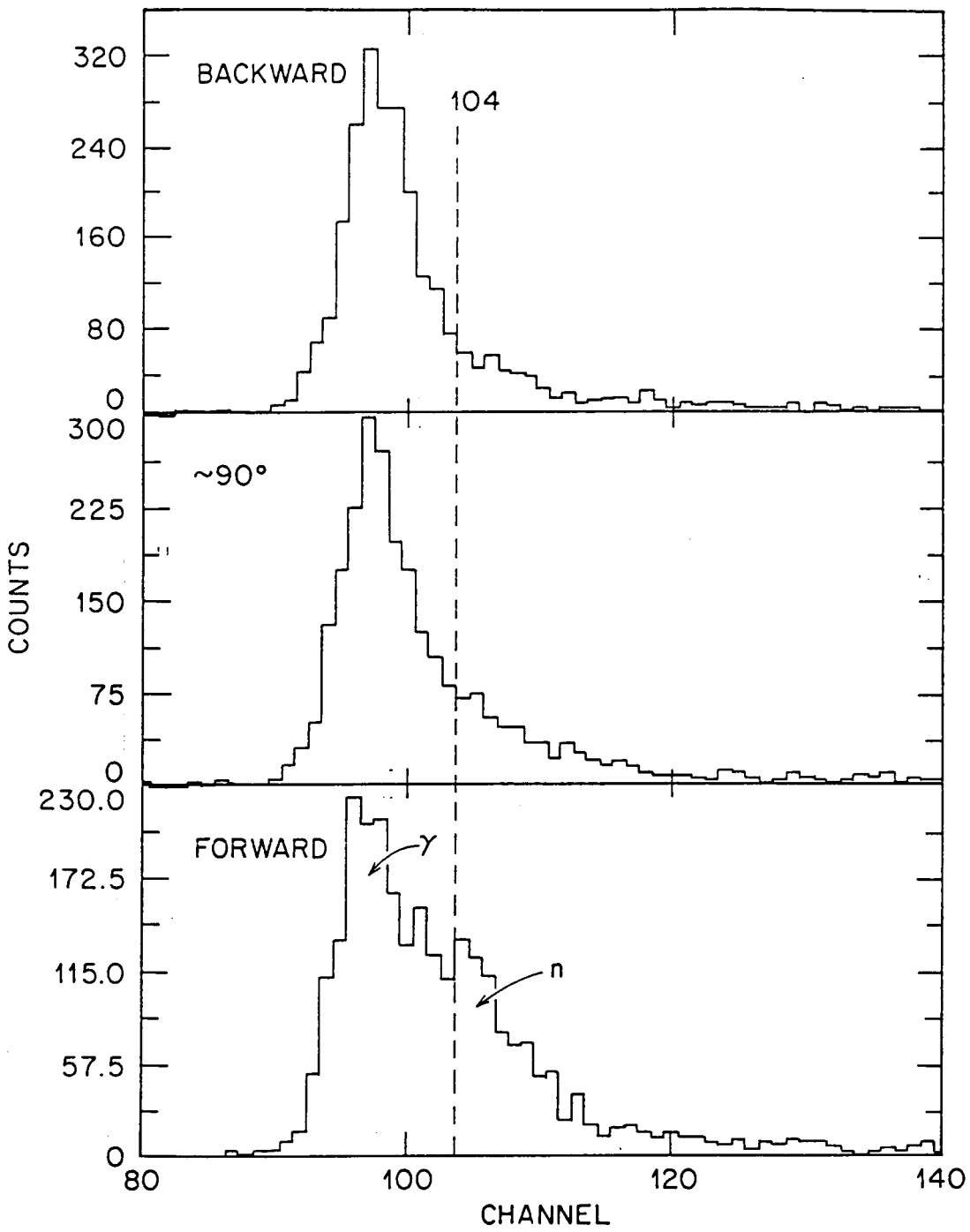


Figure 4.7: Timing spectra of NaI detectors in the Spin Spectrometer for different angles gated on 2 - 2.8 MeV pulse heights for the ^{162}Dy+ ^{58}Ni reaction.

to store the neutron events. K_N is a very important parameter in our data analysis, and the K_N spectra will be shown in next chapter.

4.8 Doppler Shift Correction of γ-rays

Suppose the i^{th} Ge detector is situated in the direction (θ_i, ϕ_i). A unit vector in this direction will be

$$\vec{e}_i = \begin{pmatrix} \sin\theta_i \cos\phi_i \\ \sin\theta_i \sin\phi_i \\ \cos\theta_i \end{pmatrix} \tag{4.31}$$

If the observed γ-ray energy is E'_γ, then the Doppler shift corrected value will be

$$E_\gamma = \frac{E'_\gamma}{1 - \frac{v_f}{c}\vec{e}_i \cdot \vec{e}_f} \tag{4.32}$$

where $\vec{e}_f$ is a unit vector in the direction of motion of either 3 or 4. The Doppler shift correction was done twice for each γ-ray, once for each outgoing ion kinematic solution, since the origin (target-like or projectile-like ion) of the γ-ray can not be determined on an event-by-event basis. An example of the effect of the Doppler correction on the γ-rays is shown in Fig 4.8. Note how much sharper all γ-ray lines became after the Doppler correction.

4.9 Corrections for Target Contamination

Due to the strong inelastic excitation in these reactions, the corrections for Coulomb excitation of target contamination are very important. In the even-even mass nucleus ^{162}Dy target we see from Table 3.1 that there is 0.08% ^{160}Dy, and the inelastic excitation of ^{160}Dy will contaminate the two-neutron transfer peaks. We used the ^{162}Dy inelastic yield times 0.08% as the correction for the corresponding two-neutron transfer yield, because the ^{160}Dy and ^{162}Dy have similar inelastic excitation cross sections. In the ^{161}Dy target there is 0.22% ^{160}Dy, and 2.46% ^{162}Dy

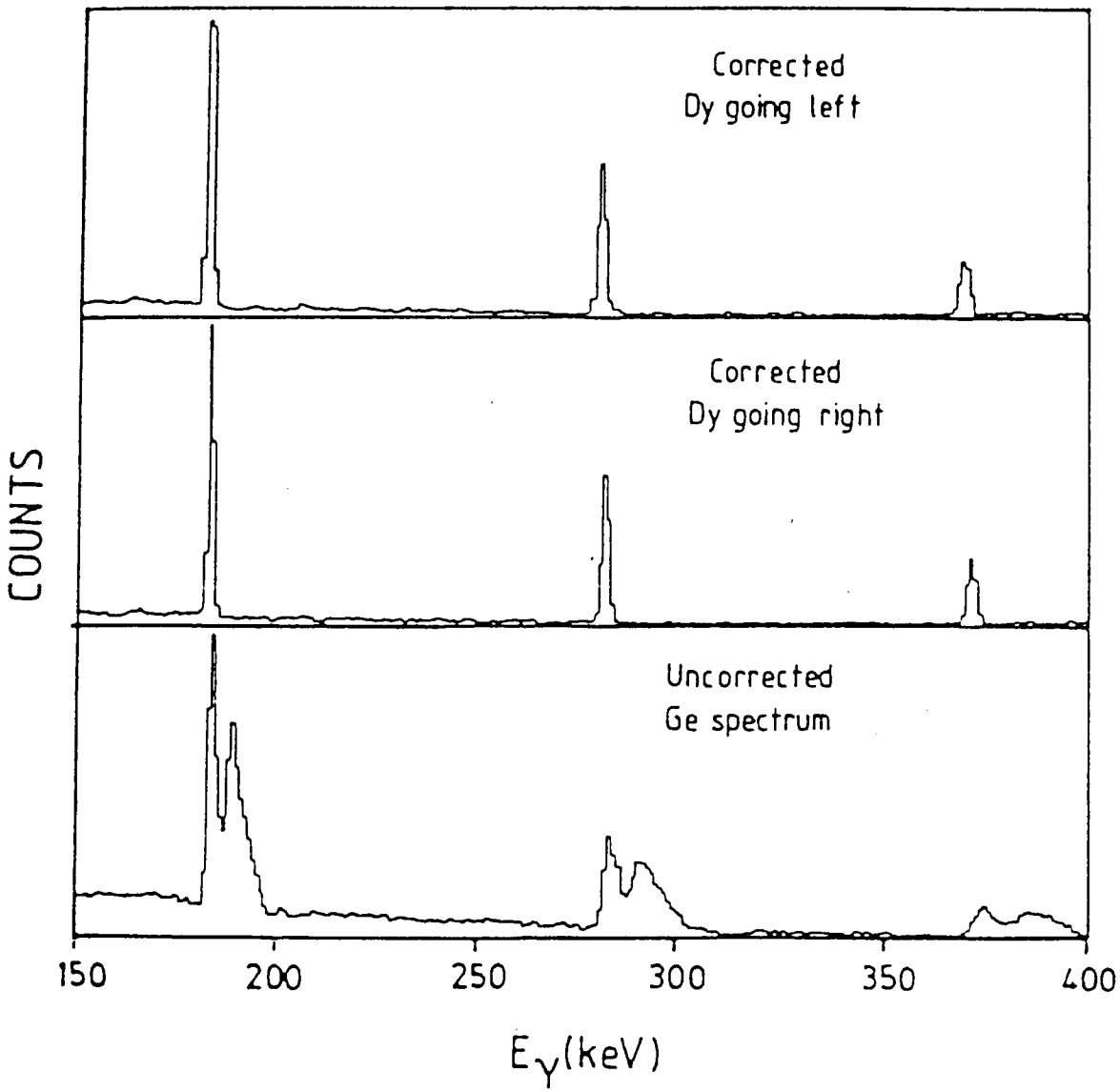


Figure 4.8: The effect of the Doppler shift correction on a typical Ge spectrum.

(Table 3.1). We used the ^{162}Dy inelastic yield times 0.089 (0.22/2.46) as the correction for the corresponding one-neutron transfer yield. The same methods were used to correct the (H, K) maps.

CHAPTER 5

EXPERIMENTAL RESULTS AND ANALYSIS

5.1 General Features of Data

5.1.1 Reaction Q-Values and Neutron Multiplicity

In order to establish whether the neutron transfer process is a direct reaction or an indirect reaction associated with neutron evaporation, Q-value and neutron multiplicity (K_N) spectra must be investigated. Fig. 5.1 shows the total Q-spectrum for the reaction ^{160}Dy+ ^{58}Ni at bombarding energies above and near the Coulomb barrier. One component with Q$\sim$ 0 dominates the Q-spectrum; this corresponds to quasielastic reaction events (inelastic and transfer). When the beam energy is near the Coulomb barrier most events are quasielastic as curve B shows. When the beam energy is increased, another component with large negative Q-value becomes important; this component presumably corresponds to deep inelastic events.

Fig. 5.2(a) shows the total K_N spectra of the same experiments. K_N=0, corresponding to quasielastic events, dominates the K_N spectra. At the Coulomb barrier (solid curve) only a few neutrons are detected, but when the bombarding energy is above the Coulomb barrier (dashed curve) events related to neutron emission become important. The tail of the K_N distribution reaches up to 15; these values result from the large neutron scattering probability in the NaI crystal and do not correspond to the actual emission of that many neutrons. Figs. 5.2 (b) and (c) show K_N spectra for inelastic, one, and two neutron transfer reactions. The tails of these spectra are primarily associated with incomplete neutron-γ separation. At 345 MeV the tail extends to $K_N \sim 6$ for the two-neutron transfer reaction. Incomplete neutron-γ separation can not explain so large a tail, so the deep inelastic reaction

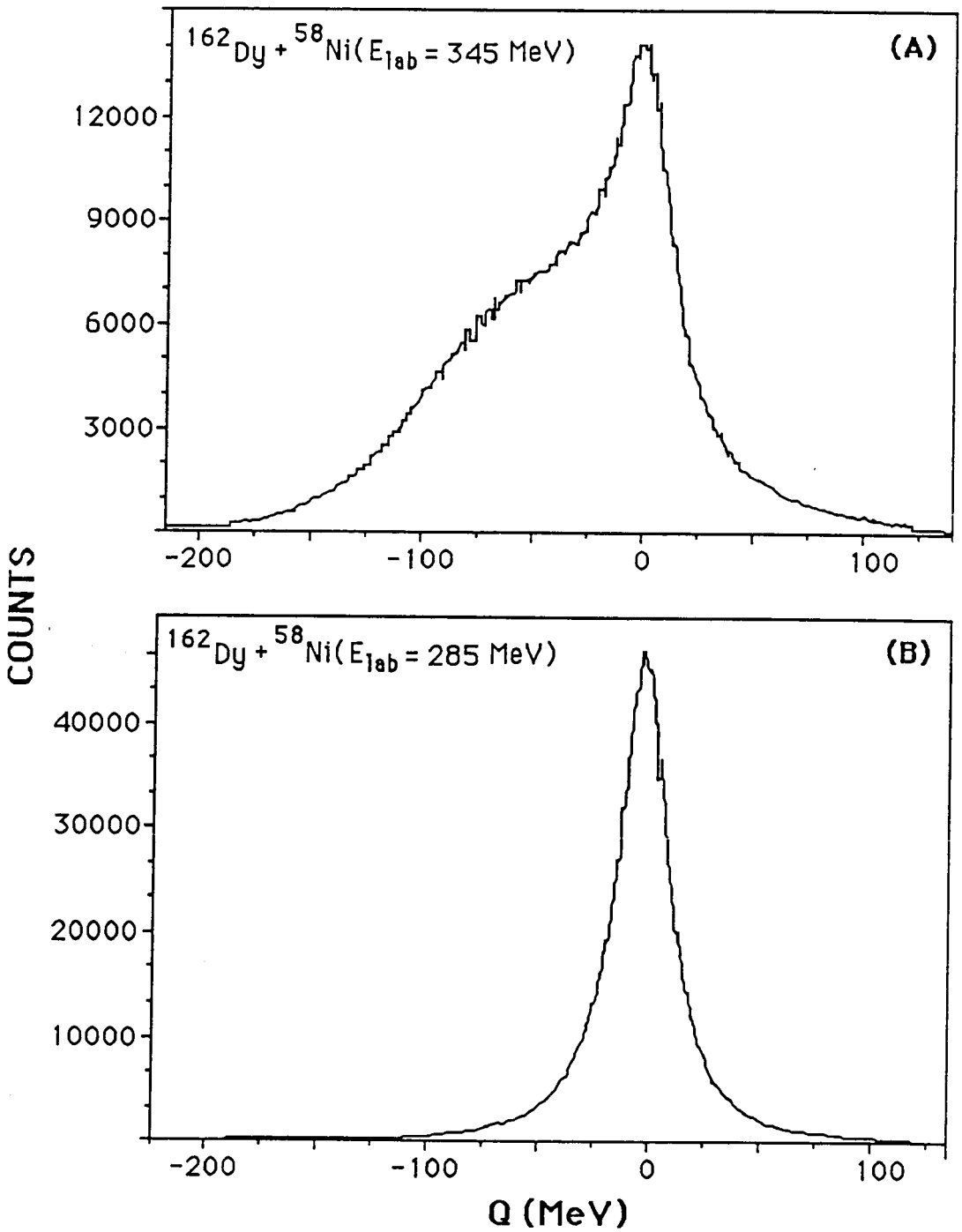


Figure 5.1: Total Q-value spectra for the reaction ^{162}Dy+ ^{58}Ni at bombarding energies above (A) and near (B) the Coulomb barrier.

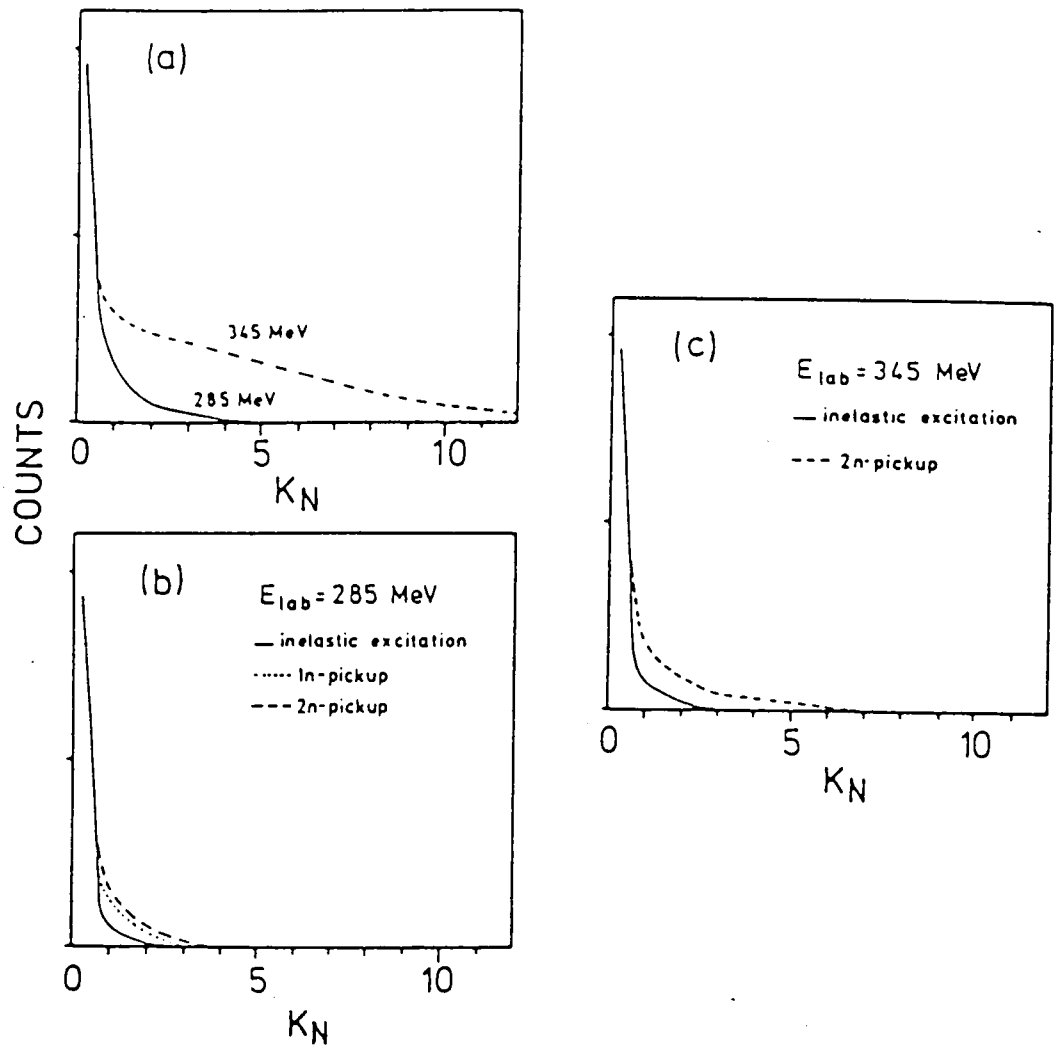


Figure 5.2: (a) Total neutron multiplicity (K_N) spectra for the reaction ^{162}Dy+ ^{58}Ni. (b, c) The neutron multiplicity spectra of one and two-neutron transfer, and inelastic scattering, at bombarding energies above and near the Coulomb barrier.

may contribute to this tail.

The events that are associated with the deep inelastic reactions should be removed. Fig. 5.3 shows the Q-value spectra gated on K_N for the reaction ^{162}Dy+ ^{116}Sn; when $K_N = 0$ most of these events are suppressed. In following discussion we will concentrate on transfer reactions. In order to make sure that the spectra for one and two neutron pick up reactions contain as little neutron evaporation as possible, events which have $K_N \geq 1$ are rejected in the data which will be discussed.

5.1.2 γ-ray Spectra

The experimental method outlined in Chapter 3 involves detection of γ-rays by Ge detectors in coincidence with scattered target-like and projectile-like ions, which are observed using four particle detectors. Figs. 5.4 - 5.5 show γ-ray spectra integrated over the grazing distribution for the reactions ^{58}Ni + ^{161}Dy (E_{lab} = 270 MeV) and ^{58}Ni + ^{162}Dy (E_{lab} = 285 MeV). These spectra were obtained after a Doppler shift correction assuming that the γ-rays were emitted by the Dy-like ion. A number of common features are apparent in the spectra:

1. The Ge spectra have low background; the peak-to-background ratio is comparable to that for sub-barrier reactions.

2. The channels observed are highly restricted. In most of the experiments inelastic scattering and one or two neutron transfer dominate the discrete-line γ-ray spectra.

3. Transfer cross sections are large and concentrated at grazing angles. One-neutron transfer peaks are typically comparable in size to inelastic peaks at the grazing angle, while two-neutron transfer peaks may be 10% as large as

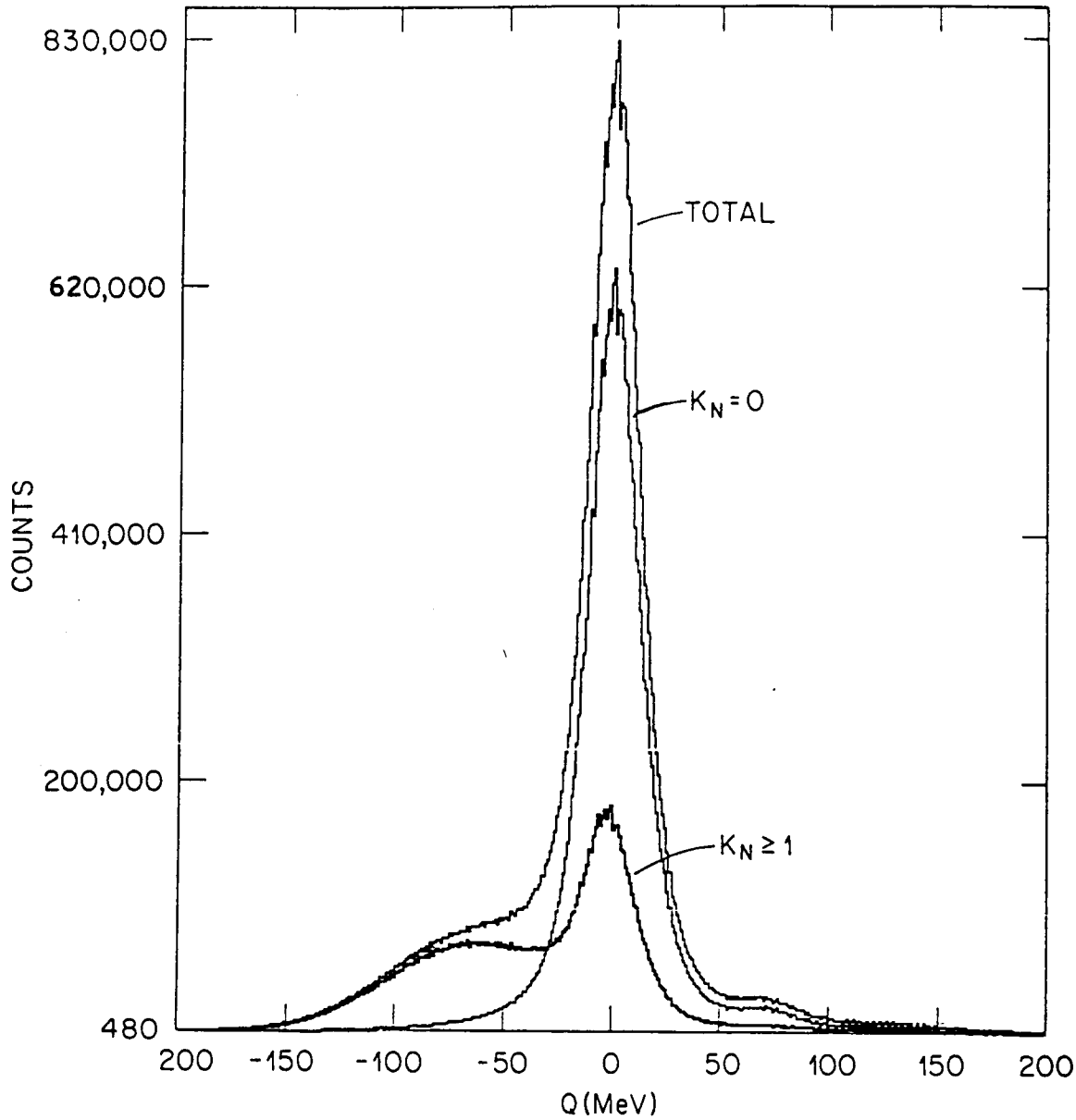


Figure 5.3: Q-value spectrum gated on K_N for the ^{162}Dy+ ^{116}Sn reaction (E_{lab} = 637 MeV).

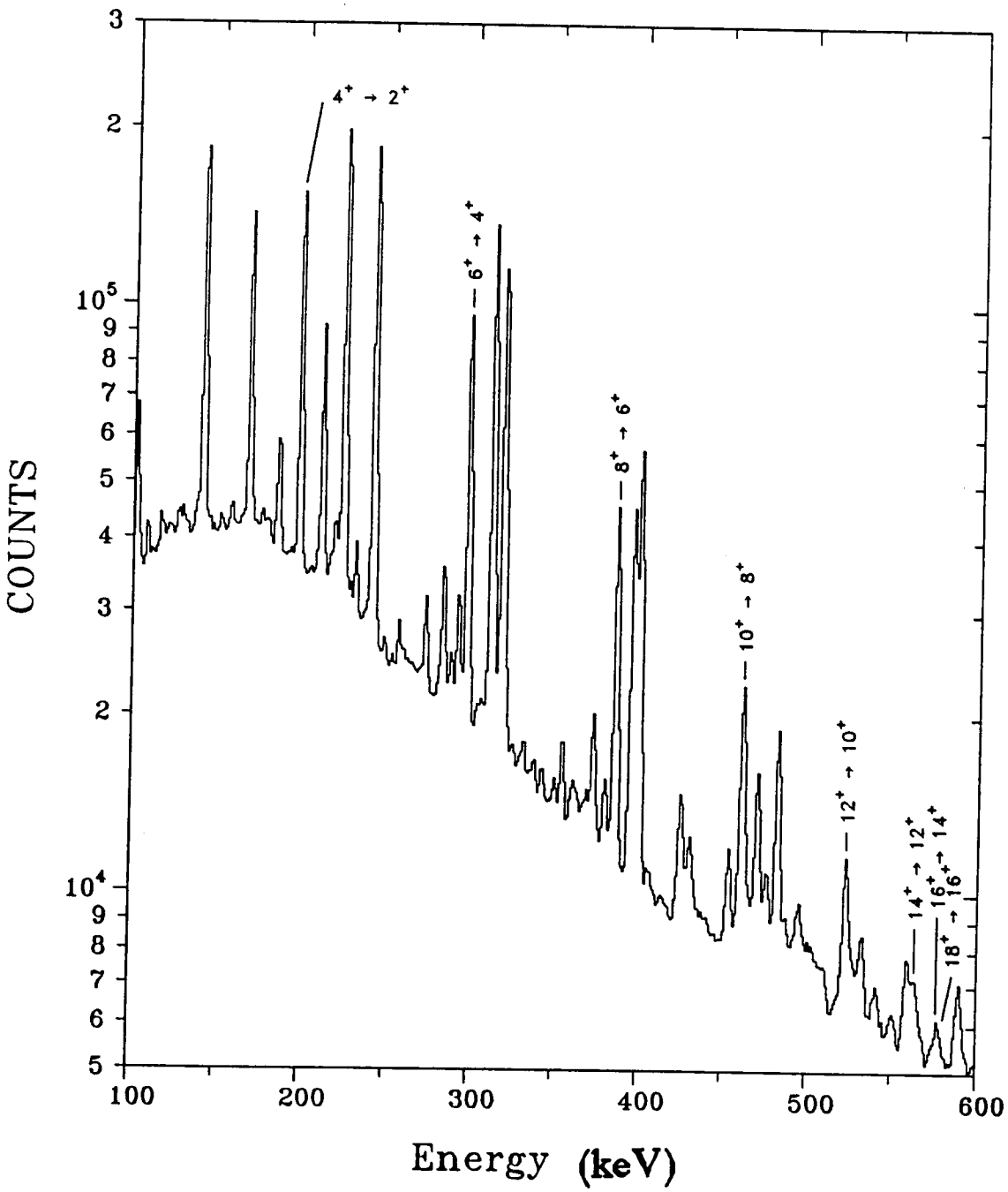


Figure 5.4: A particle-particle-γ coincidence spectrum for the reaction ^{58}Ni (E_{Lab}=270 MeV) + ^{161}Dy reaction. Ground band transitions in the transfer product ^{160}Dy are marked.

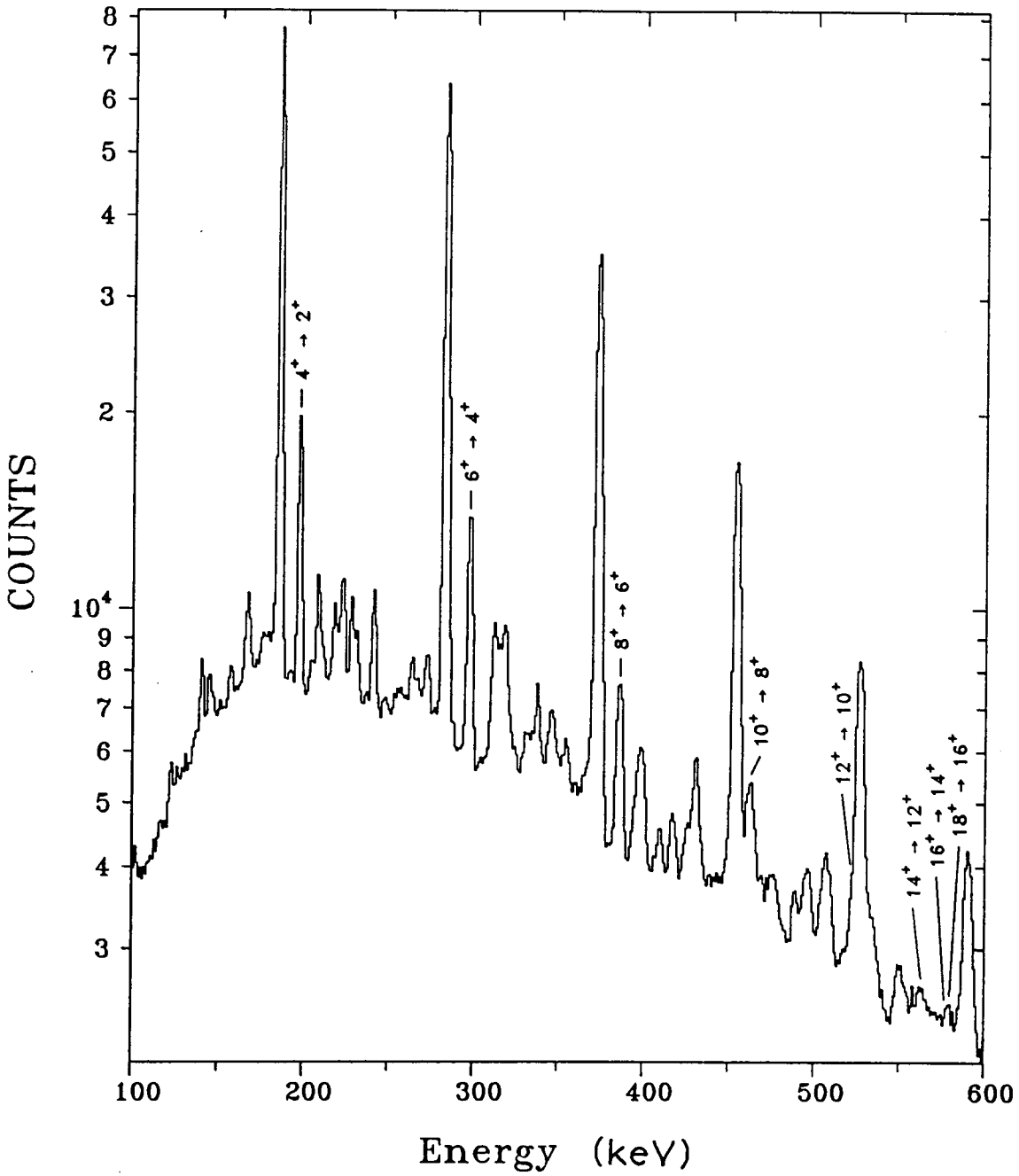


Figure 5.5: A particle-particle-γ coincidence spectrum for the ^{58}Ni (E_{Lab}=285 MeV) + ^{162}Dy reaction. Ground band transitions in the ^{160}Dy transfer product are marked.

inelastic ones.

4. High spin states are excited.

In most cases the highest spin populated in the transfer is comparable to or larger than that expected from inelastic excitation of the final transfer product nuclei. In 1-neutron transfer the spins are considerably larger than for inelastic. This is consistent with an assumed reaction mechanism of strong inelastic excitation before transfer, transfer of one or two particles between collectively excited states near the point of closest approach, and strong inelastic excitation following the transfer.

In both one-neutron and two-neutron transfer reactions discrete lines up to about the $18^+ \rightarrow 16^+$ yrast transition are seen for the reaction product ^{160}Dy(the lowest is $2^+ \rightarrow 0^+$, which we don not see very well because of γ-ray efficiency and internal conversion). The present data suggest that transfer reactions populating states with I $\sim$ 20 $\hbar$ in the rare-earth region and I $\sim$ 30 $\hbar$ in the actinide region are feasible; indeed in more recent experiments which will be discussed below we have observed transfer to I = 26 $\hbar$ in the actinide region (Wu *et al.*, 1987).

5.1.3 Entry-state Distributions for Total Energy and Multiplicity

As discussed in Chapter 3, the Spin Spectrometer was used to provide crucial information on entry-state energy and angular momentum. In Fig. 5.6 some representative total energy vs. multiplicity (E,M) plots are shown for the reaction ^{161}Dy(^{58}Ni,^{59}Ni)^{160}Dy and ^{162}Dy(^{58}Ni,^{60}Ni)^{160}Dy. The distributions are gated on the stronger ground band transitions in ^{160}Dy, as observed by Ge detectors, with a backgound subtracted and with a target impurity correction. These distributions did not include the contribution of the gating transition in the Ge detectors. The dashed line represents the ^{160}Dy yrast line, assuming that Ni is not excited in the reaction.

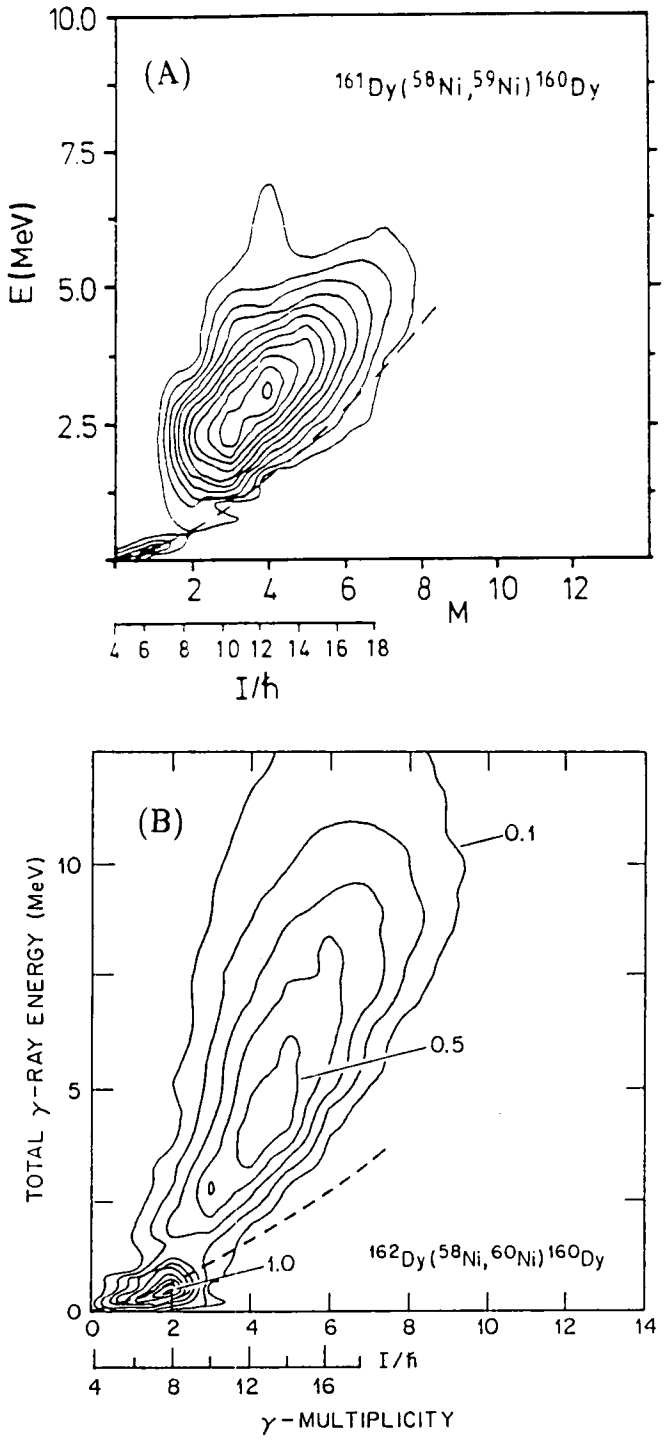


Figure 5.6: Total energy vs. multiplicity for (A) ^{161}Dy(^{58}Ni,^{59}Ni)^{160}Dy and (B) ^{162}Dy(^{58}Ni,^{60}Ni)^{160}Dy. The dashed lines are the approximate ^{160}Dy yrast line, assuming no Ni excitation.

Events below the yrast line reflect the finite resolution of the Spin Spectrometer. The approximate angular momentum scale ($I/\hbar$) is valid only for the ^{160}Dy yrast line with no Ni excitation. Its construction is described in Guidry *et al.*, 1985a. Several interesting features are evident in Fig. 5.6:

1. The (E,M) distributions for one and two neutron transfer reactions have two maxima.

2. The lower multiplicity transfer maximum approximately coincides with the single maximum for inelastic scattering.

3. Transfer population of ^{160}Dy is remarkable cold, lying mostly within 1-2 MeV of the yrast line.

4. High angular momenta ($I \sim 20\hbar$) appear to be populated.

5.1.4 Schematic Model for One and Two-neutron Transfer

The general structure observed in Fig. 5.6 can be understood in terms of a simple model for transfer reactions and the cranked shell model (Guidry *et al.*, 1985a).

We concentrate on the one-neutron transfer reaction first. In Fig. 5.6 (A) the (E,M) distribution appears to be a superposition of two distributions: one narrow in energy peaked at $M \simeq 1$ and a stronger distribution broader in energy and peaked at $M \simeq 4$. The lower multiplicity distribution represents direct population of the ^{160}Dy ground band by pickup of the unpaired $\Omega = 5/2$, $i_{13/2}$ neutron of the ^{161}Dy target while the ^{58}Ni is populated in the ground or first two excited states.

The upper peak in Fig. 5.6(A) receives a contribution which involves breaking a pair in ^{161}Dy, leaving the residual ^{160}Dy nucleus in an excited two-quasiparticle

configuration and the ^{59}Ni in one of the states at less than 500 keV. The angular momentum of the Dy state finally populated is the vector sum of the collective angular momentum of the core and the two quasiparticles.

A second possible contribution to the high multiplicity peak corresponds to excitation of the ground band or quasiparticle states of ^{160}Dy coincident with excitation of the $g_{9/2}$ (3.06 MeV) state of ^{59}Ni, with the Ni expected to contribute $\sim$ 3 MeV and $\sim$ 2.5 multiplicity units to Fig. 5.6 (A). However, the absence of transitions in the γ-ray spectrum deexciting the Ni $g_{9/2}$ state indicates that it is weakly excited, and we assume the bulk of the higher multiplicity peak in Fig. 5.6 (A) to represent two-quasiparticle Dy excitation.

Fig. 5.7 shows a cranked shell model calculation (Bengtsson and Frauendorf, 1979) for bands near the yrast line in ^{160}Dy. Based on transfer cross sections, we assume the transfer itself is perturbative, but inelastic excitation occurring before and after the transfer is not; it must be treated by coupled channels methods. Neglecting Coriolis mixing, the two-quasiparticle states populated have at least one particle in the Ω=5/2, $i_{13/2}$ orbital. Even with Coriolis mixing, this particle would be in an orbital that is predominantly $i_{13/2}$ in character. The mean aligned angular momentum for these bands within $\sim$ 2 MeV of the ground-state band is about 6 $\hbar$ according to the cranking calculation.

An energy window which limits the states that can be populated is also shown in Fig. 5.7. (see Guidry *et al.*, 1985a) The energy window is the product of a Gaussian Q-window and a factor decreasing exponentially in $(B + \delta)^{1/2}$, where B is the binding energy for a nucleon and δ is the excitation energy with respect to the yrast line of the states populated in ^{160}Dy. In order to get a large transfer cross section the entrance and exit channel relative motion wavefunctions must be matched. This can be achieved by transferring an energy corresponding approximately to the reaction Q_{gg}-value from the relative motion of reaction partners to excitation energy

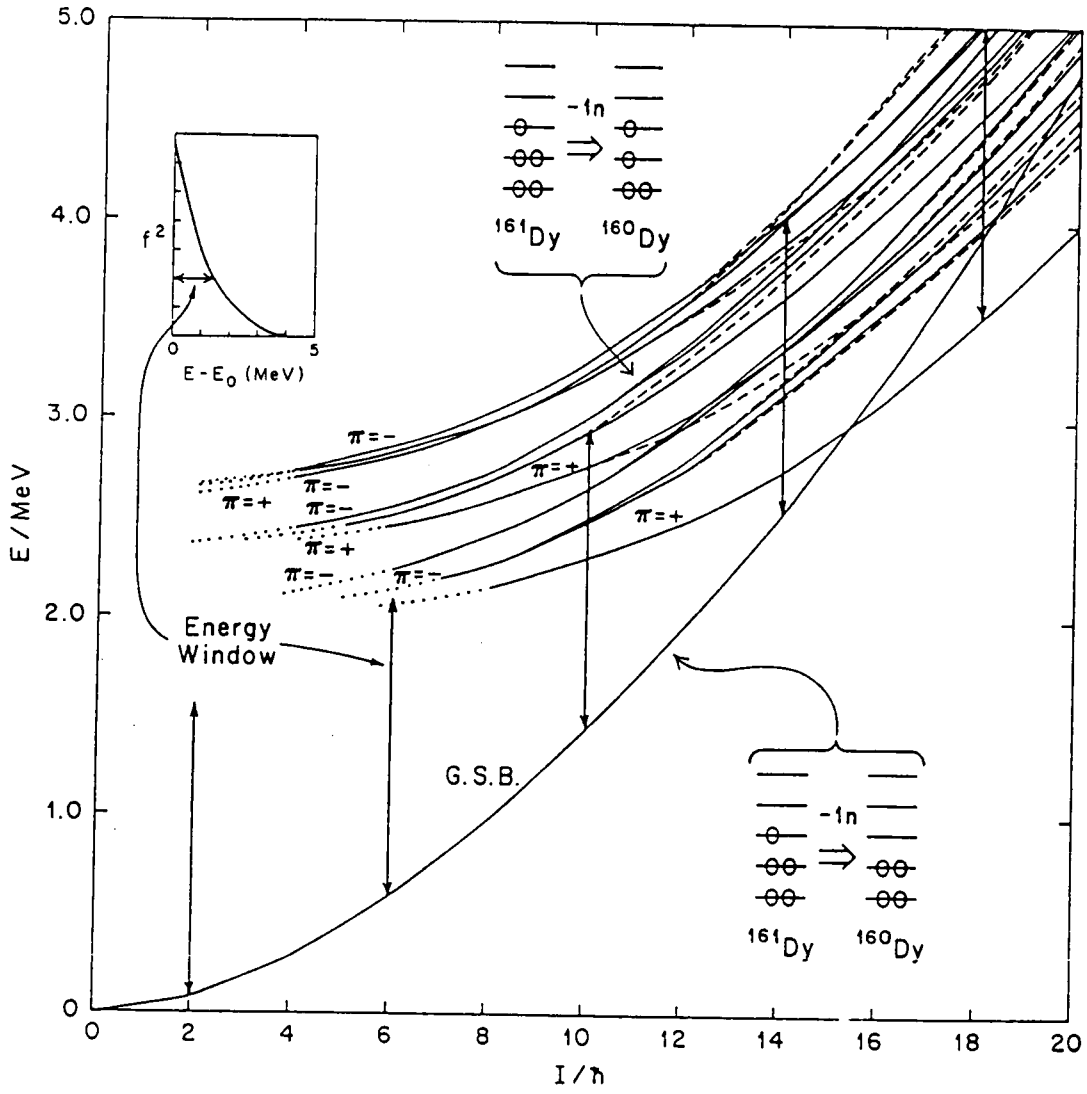


Figure 5.7: Low-lying bands in ^{160}Dy calculated using the cranked shell model with parameters $\beta_2 = 0.25$, $\beta_4 = 0$, $\Delta = 0.128$ hω_0.

of the exit channel.

Contours of the product of these two factors are shown as dashed lines in Fig. 5.8. The yrast lines of ^{161}Dy and ^{160}Dy are plotted in the (E, I) plane by starting the yrast line of ^{160}Dy at the origin and the yrast line ^{161}Dy at 2.5 MeV (Q_{gg}-value), assuming that both ^{58}Ni and ^{59}Ni are in their ground states. The transfer is most likely to occur near the point of closest approach; a reasonable estimate of the average angular momentum at the turning point for the ^{160}Dy is $(17/2)^+$. A cranked shell model calculation indicates that the Ω=$5/2^+$ unpaired neutron is carrying $\sim$ 4 units of aligned angular momentum for this state. Thus a typical average value of the core angular momentum is $\sim$ 4 $\hbar$ at transfer, so the transfer must proceed to states in ^{160}Dy which also have $\sim$ 4 units of core angular momentum (the first-order single particle transfer can not change the collective core angular momentum).

Thus, we can find two general regions within the energy window that are accessible to the one-neutron transfer. The transfer can occur either backwards in spin to the members of the ground-band or other collective bands around spin I = 4 - 6 units, or to the two-quasiparticle states with I $\simeq$ 10 units (which have an average alignment of 6 $\hbar$). Once the transfer is made the final nucleus ^{160}Dy may receive further collective excitation, provided the state populated is in a collective band.

A schematic model for one-neutron pickup is shown in Fig. 5.9. There are two ways of picking up one neutron. If the unpaired neutron is picked up, the reaction leads to population of the ground-band; when one of the paired neutrons is picked up, the reaction leads to population of two-quasiparticle bands. The population of the ground band is at an angular momentum comparable to that for inelastic excitation, and the population of two-quasiparticle bands is at higher angular momentum, with the difference in angular momentum between two the regions approximately given by the average aligned angular momentum in the two-quasiparticle

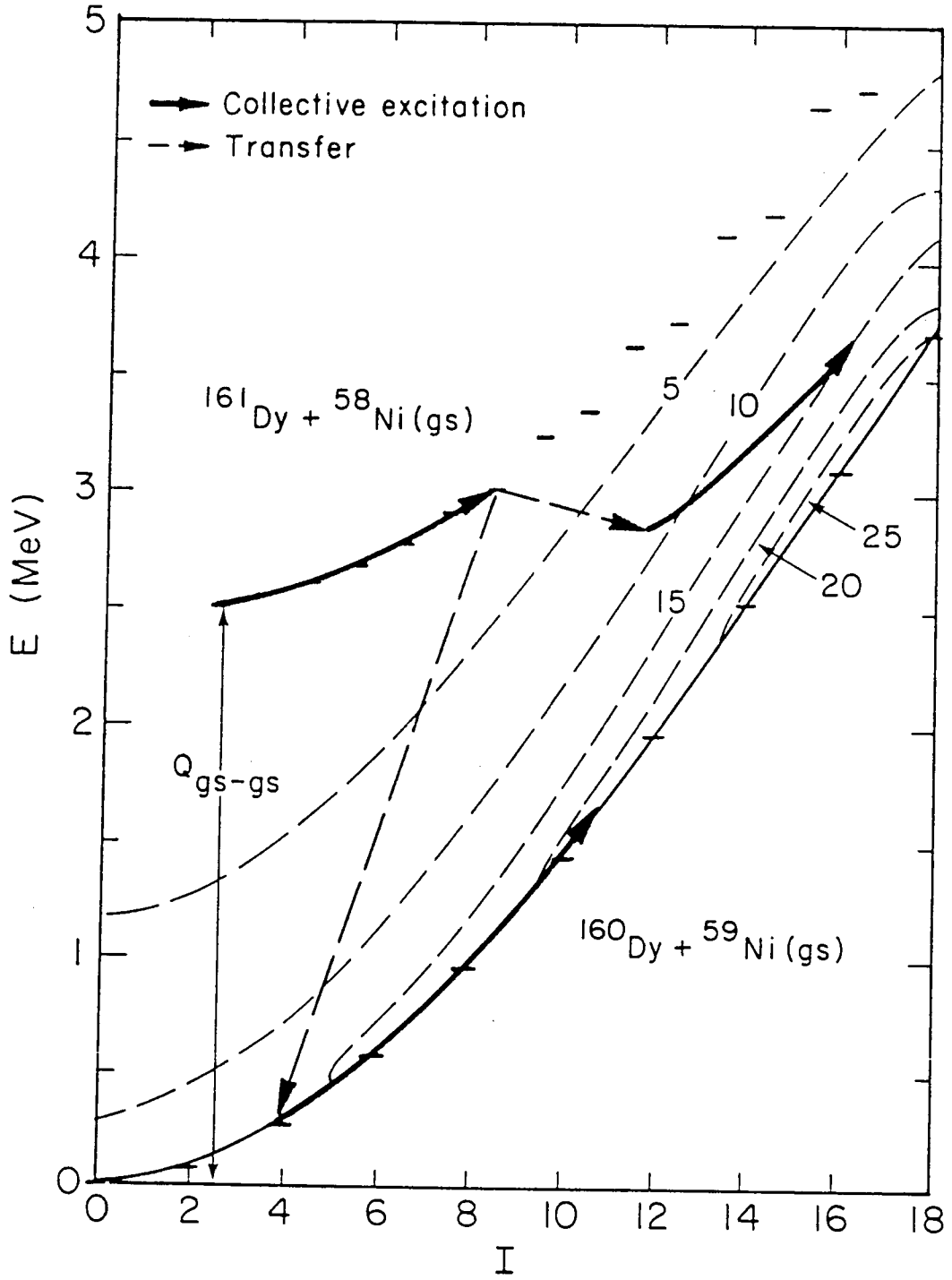


Figure 5.8: Evolution of one-neutron transfer in the E vs. I plane. Contours of the energy window are shown as dashed lines. Discret states in the ground bands of ^{160}Dy and ^{161}Dy are indicated by horizontal lines, assuming no Ni excitation.

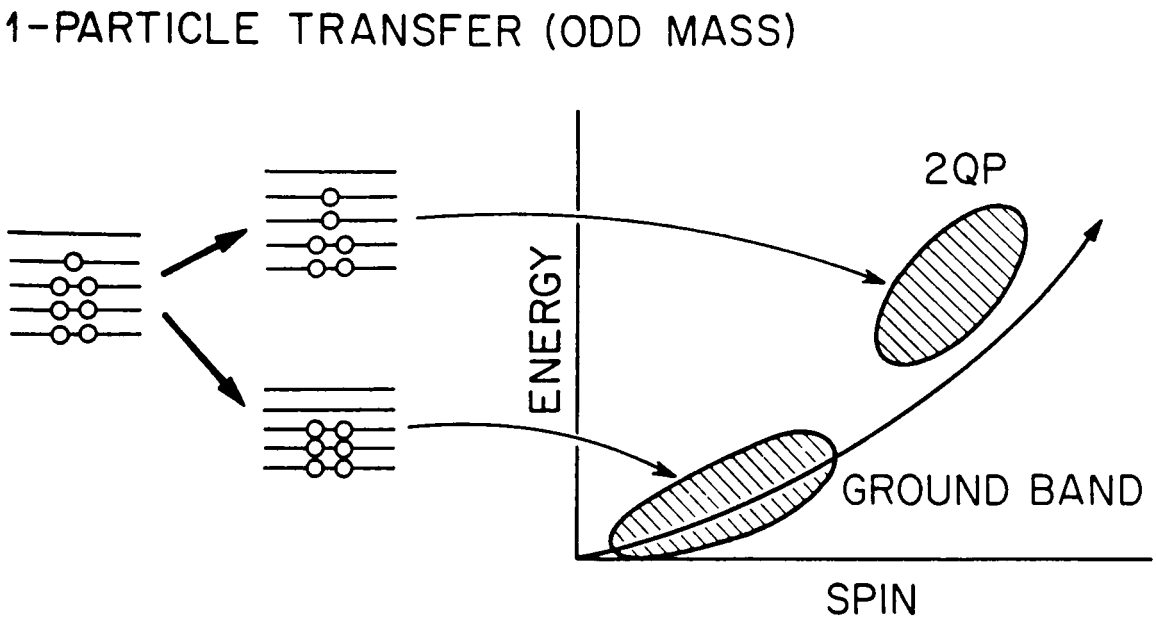


Figure 5.9: A schematic picture of one-neutron transfer reaction populating even - even nuclei.

bands (Guidry *et al.*, 1985a). The (E,M) map in Fig. 5.6(A) is qualitatively and quantitatively in agreement with this picture. For example, the gap between the two maxima is about 6 units of angular momentum, as expected from the above analysis.

In Fig. 5.6(B) the (E,M) distribution for a two-neutron transfer reaction gated on the ground-band transitions in ^{160}Dy shows similar features as the corresponding one for the one-neutron transfer reaction. There is a rather localized population maximum near the yrast line peaked at M $\sim$ 2, but the main fraction of the cross section is distributed at M $\sim$ 3 - 8. The position of the lower maximum corresponds to spin 6-8 in the ground-band of ^{160}Dy. The population in the upper maximum is peaked at M $\sim$ 5 and about 2.5 MeV above the yrast line. However, there are also some obvious differences between one and two-neutron transfer reactions. Most noticeably, the two-neutron transfer distribution peaks at, and extends to, higher multiplicity and total energy.

We may interpret the two-neutron transfer distribution in a similar manner as we interpreted the one-neutron case. However, there are some differences:

1. The ground state Q-value is 5.7 MeV in this case, compared with 2.5 MeV in the one-neutron transfer.

2. If we assume the transfer to proceed by the lowest possible order, it is no longer necessary that a two-quasiparticle state populated in ^{160}Dy involve the cranked shell model orbit arising from the $\Omega = 5/2$ orbit. The other lightly bound neutrons also have major lobes at intermediate latitude ($45° \pm 20°$) on the deformed nuclear surface, so large Coulomb excitation is favored. For example, Fig. 5.10 shows the transfer amplitudes f(r', θ'), which are defined in Guidry *et al.* (1981), for some configurations involving only a single rare-earth orbital. The plots are contour plots in the intrinsic coordinate system

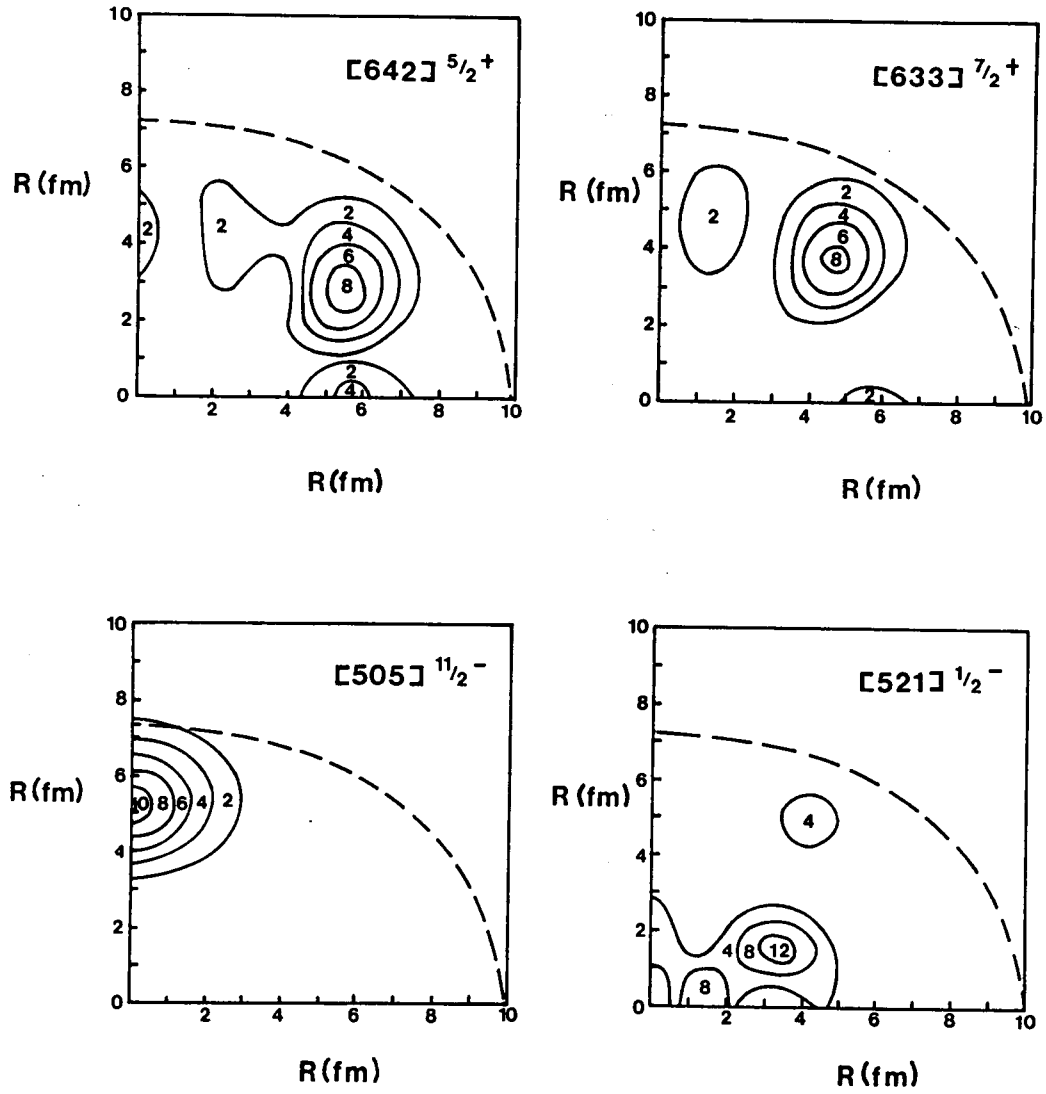


Figure 5.10: The transfer amplitudes f(r', θ') for some configurations involving only a single rare-earth neutron orbital. Reproduced from Guidry *et al.* (1981).

r', θ' plane, and the orbitals are labeled by the standard asymptotic Nilsson quantum numbers.

3. The yrast line of ^{162}Dy is more parallel to the ^{160}Dy yrast line than is the ^{161}Dy yrast line. These differences will tend to force the two-quasiparticle population to higher energy and to higher angular momentum in the two-neutron case relative to the one-neutron case.

A schematic model for two-neutron pickup is shown in Fig. 5.11. There are three different ways of picking up two neutrons. If the least-bound pair of neutrons is transferred, the reaction leads to population of the ground-band (pairing rotational transition). When some other pair of neutrons is transferred, bands based on excited pairs will be populated (pairing vibrational transition). Finally, breaking of two neutron pairs leads to population of two-quasiparticle bands, which can have large angular momentum alignment. In the first two cases the range of angular momentum in the states populated should be similar to that for the inelastic scattering of ^{58}Ni + ^{162}Dy, because the pairs are not expected to carry much angular momentum. In the final case, angular momenta comparable to the sum of that caring from inelastic excitation and the alignment of the 2 quasiparticle state can occur. Thus, the lower peak of the distribution for the reaction ^{162}Dy(^{58}Ni,^{60}Ni)^{160}Dy represents direct population of the ground band, and the upper peak primarily represents population of two-quasiparticle states.

5.2 The Entry State Distribution and γ-ray Spectra

In this section we will present (E,M) distributions and γ-ray spectra for one and two-neutron transfer reactions. The (E,M) distribution provided by the Spin Spectrometer provides detailed information about the region in the energy and angular momentum plane populated by transfer reactions. The ground band

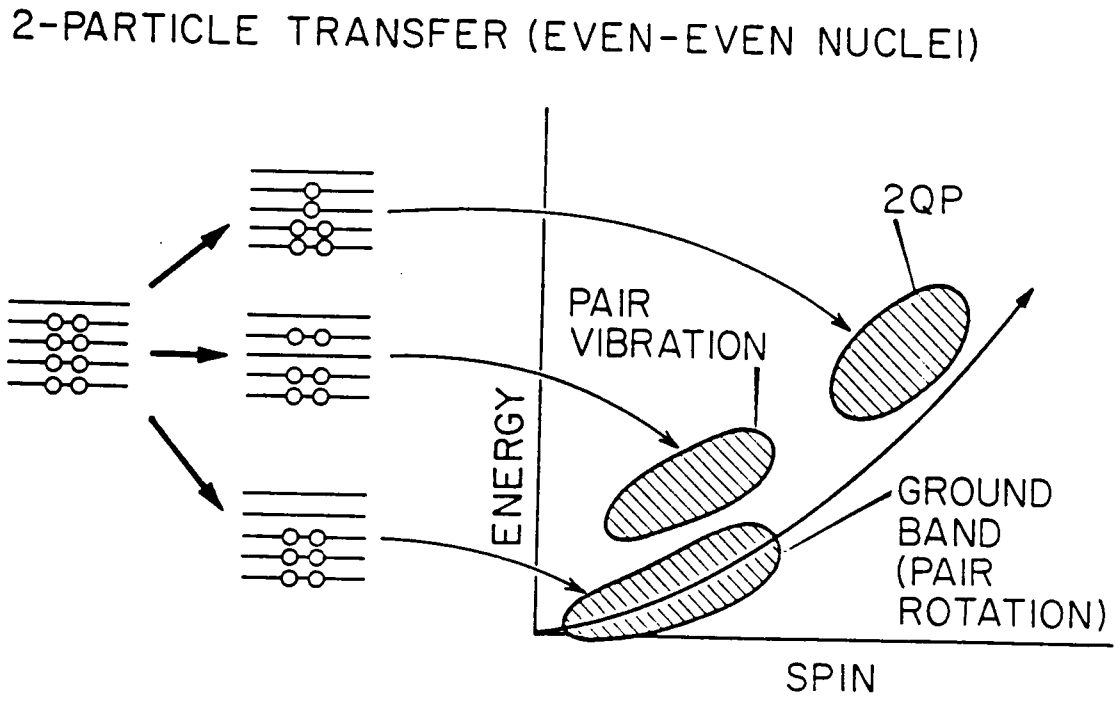


Figure 5.11: A schematic picture of a two-neutron transfer reaction populating even-even nuclei.

can be distinguished from the other bands by gating on the (H,K) plane, and Ge γ-ray spectra provide identification of exit channels.

5.2.1 Experiments with 270 and 285 MeV ^{58}Ni Beams

Fig. 5.12 shows the Q-value spectrum gated on K_N for the reaction ^{162}Dy + ^{58}Ni. The beam energy is near the Coulomb barrier (the Coulomb barrier is 275 MeV), and quasielastic events with Q $\sim$ 0 dominate the Q-value spectrum. There are very few deep inelastic events. In the following all data are gated on K_N=0.

Figs. 5.13 and 5.14 show (H,K) maps gated on ^{160}Dy ground band transitions for one and two-neutron transfer reactions (these maps do not include the contribution of the gating transitions in the Ge detector) . We see the same features as discussed in section 5.1.3. Fig. 5.15 shows the unfolded (E,M) maps for the two-neutron transfer reaction. The dashed line in the map is the average yrast line for ^{160}Dy assuming no excitation of Ni; its construction is described in Guidry *et al.* (1985a).

Fig. 5.16 shows the $\gamma - \gamma$ coincidence spectrum for the reaction ^{161}Dy(^{58}Ni,^{59}Ni)^{160}Dy gated on the $4^+ \rightarrow 2^+$, $6^+ \rightarrow 4^+$, and $8^+ \rightarrow 6^+$ transitions of ^{160}Dy. The ground band of ^{160}Dy is observed up to spin 18, and the population of some negative parity bands up to $I_i = 15^-$, and the γ-band up to $I_i = 11^+_\gamma$ are observed. Fig. 5.17 shows the $\gamma - \gamma$ coincidence spectrum for the reaction ^{162}Dy(^{58}Ni,^{60}Ni)^{160}Dy gated on the $6^+ \rightarrow 4^+$, $8^+ \rightarrow 6^+$, and $10^+ \rightarrow 8^+$ transitions of ^{160}Dy. The Doppler shift corrections for both reaction partners are presented in Fig. 5.17. In spectrum (b), where the Doppler shift correction is done for Ni-like ions, the $2^+ \rightarrow 0^+$ and $4^+ \rightarrow 2^+$ are the only Ni transitions seen.

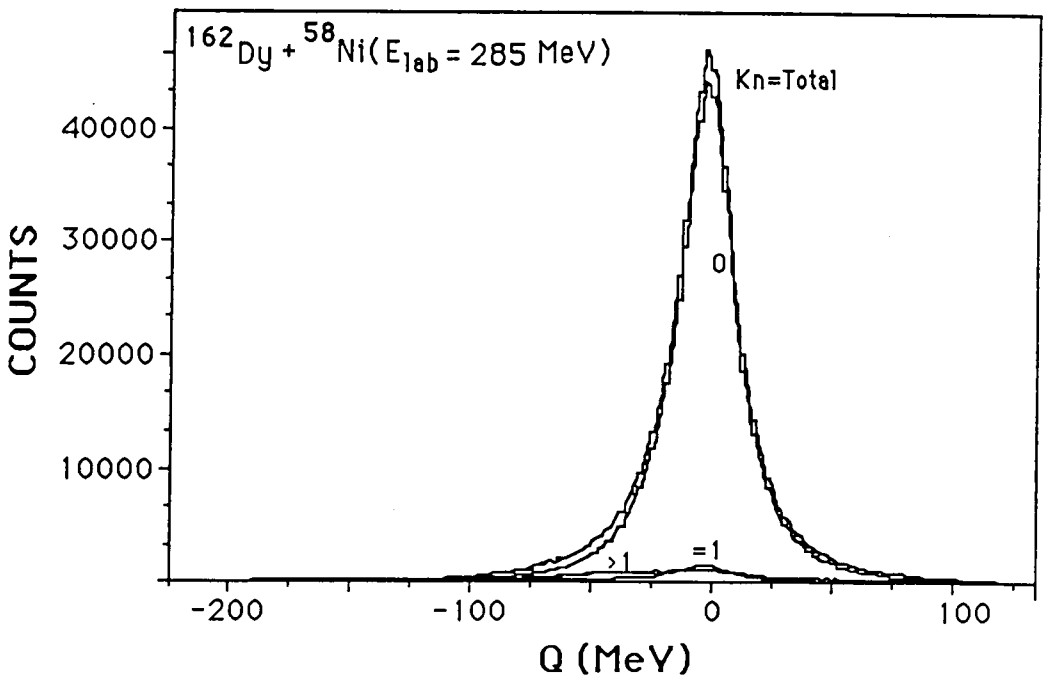


Figure 5.12: Q-value spectra gated on K_N for the reaction ^{162}Dy + ^{58}Ni.

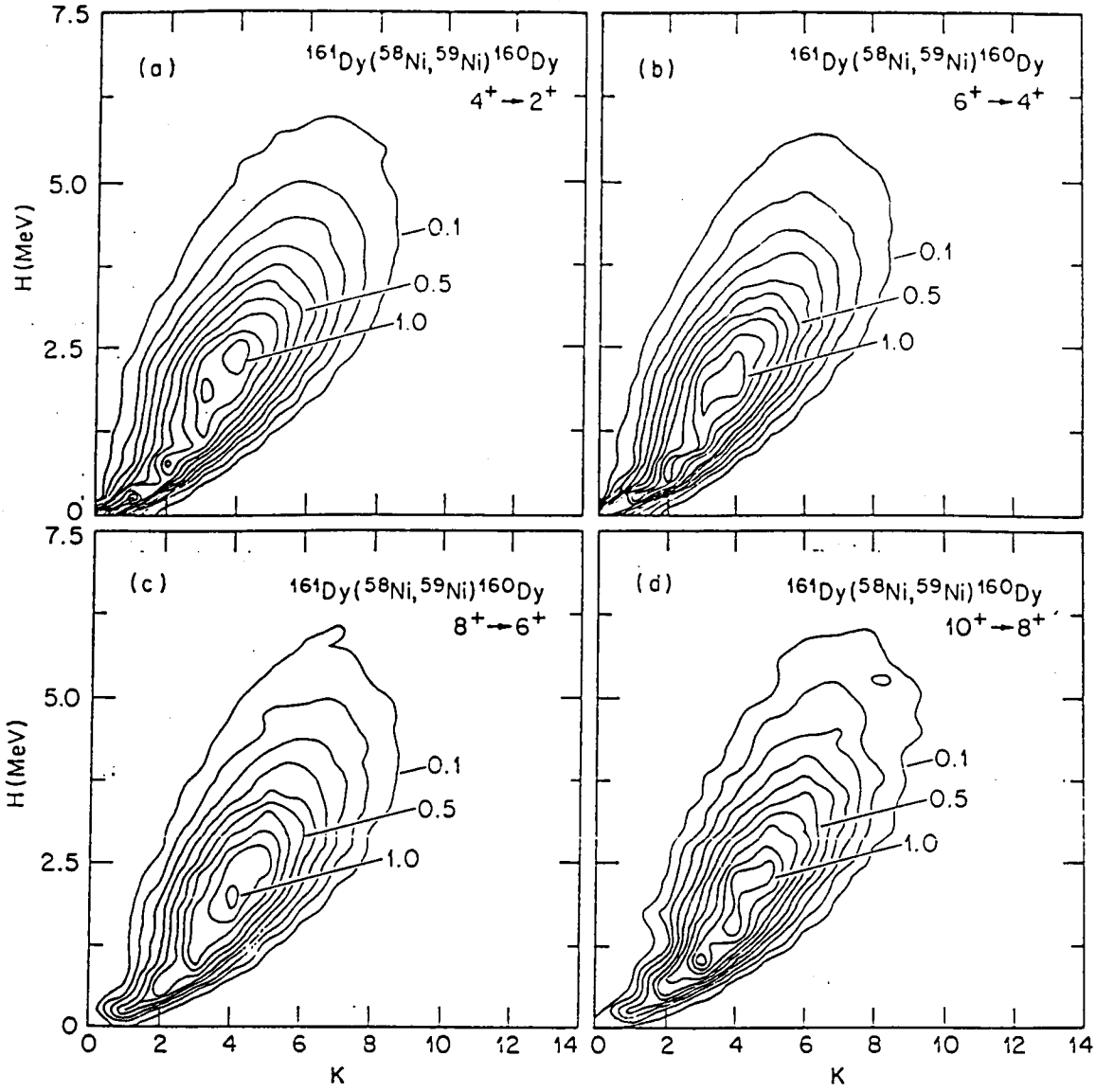


Figure 5.13: (H,K) maps gated on individual ground band transitions of ^{160}Dy for the reaction ^{161}Dy(^{58}Ni,^{59}Ni)^{160}Dy.

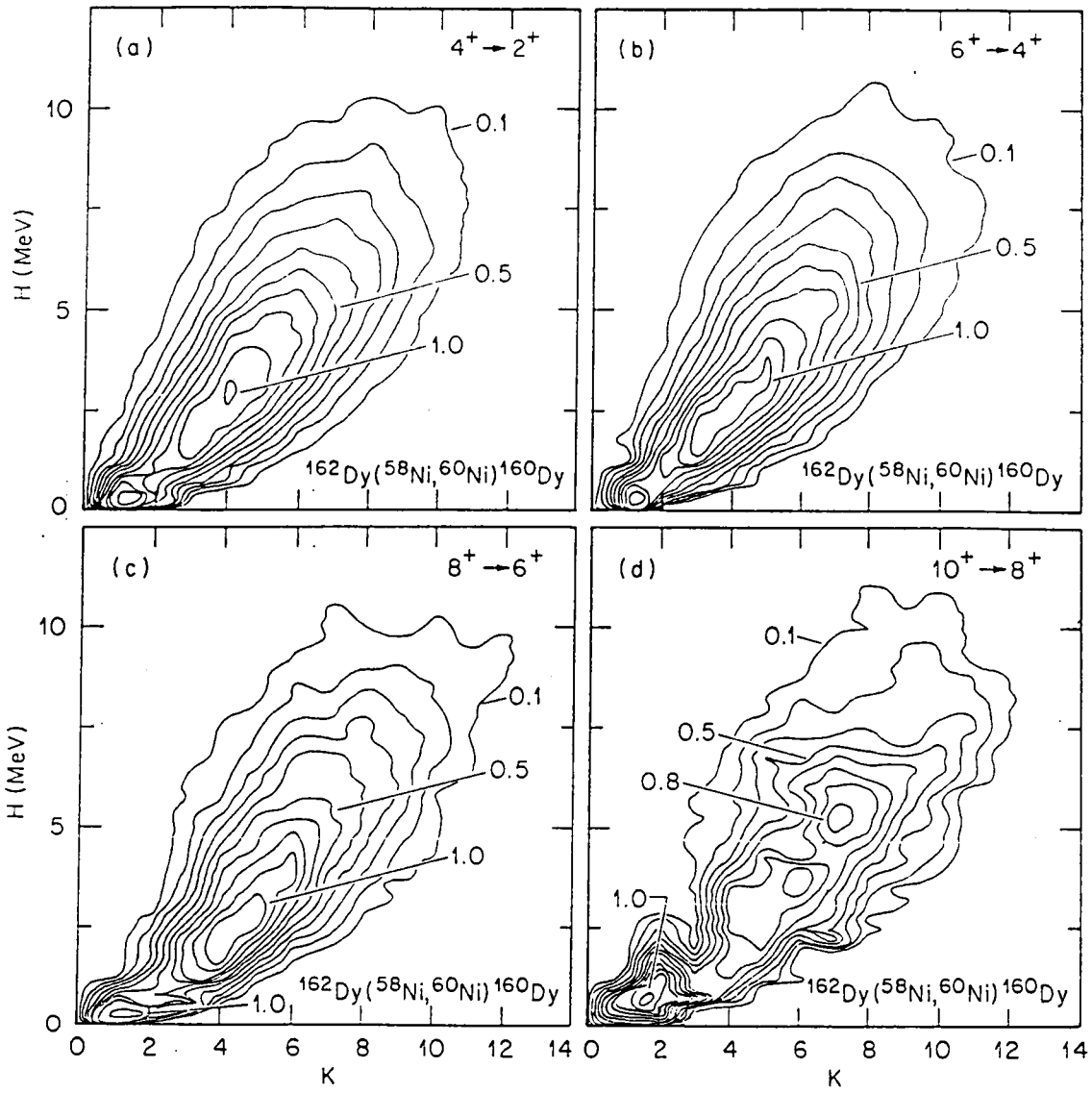


Figure 5.14: (H,K) maps gated on individual ground band transitions of ^{160}Dy for the reaction ^{162}Dy(^{58}Ni,^{60}Ni)^{160}Dy.

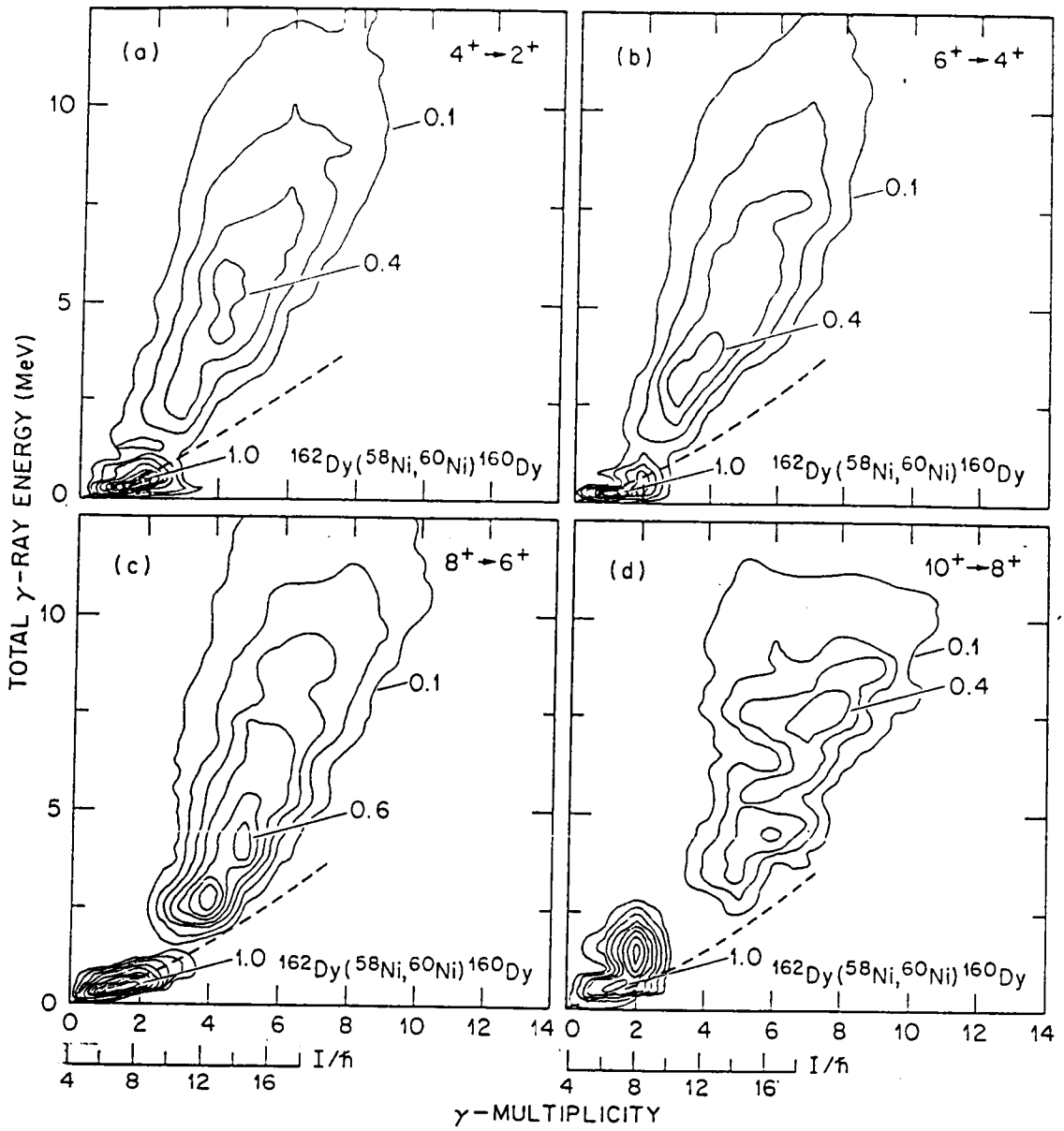


Figure 5.15: Unfolded (E,M) maps gated on individual ground band transitions of ^{160}Dy for the reaction ^{162}Dy(^{58}Ni,^{60}Ni)^{160}Dy. That is, these (E,M) distributions folded with the Spin Spectrometer response correspond to the (H,K) distributions in Fig. 5.14.

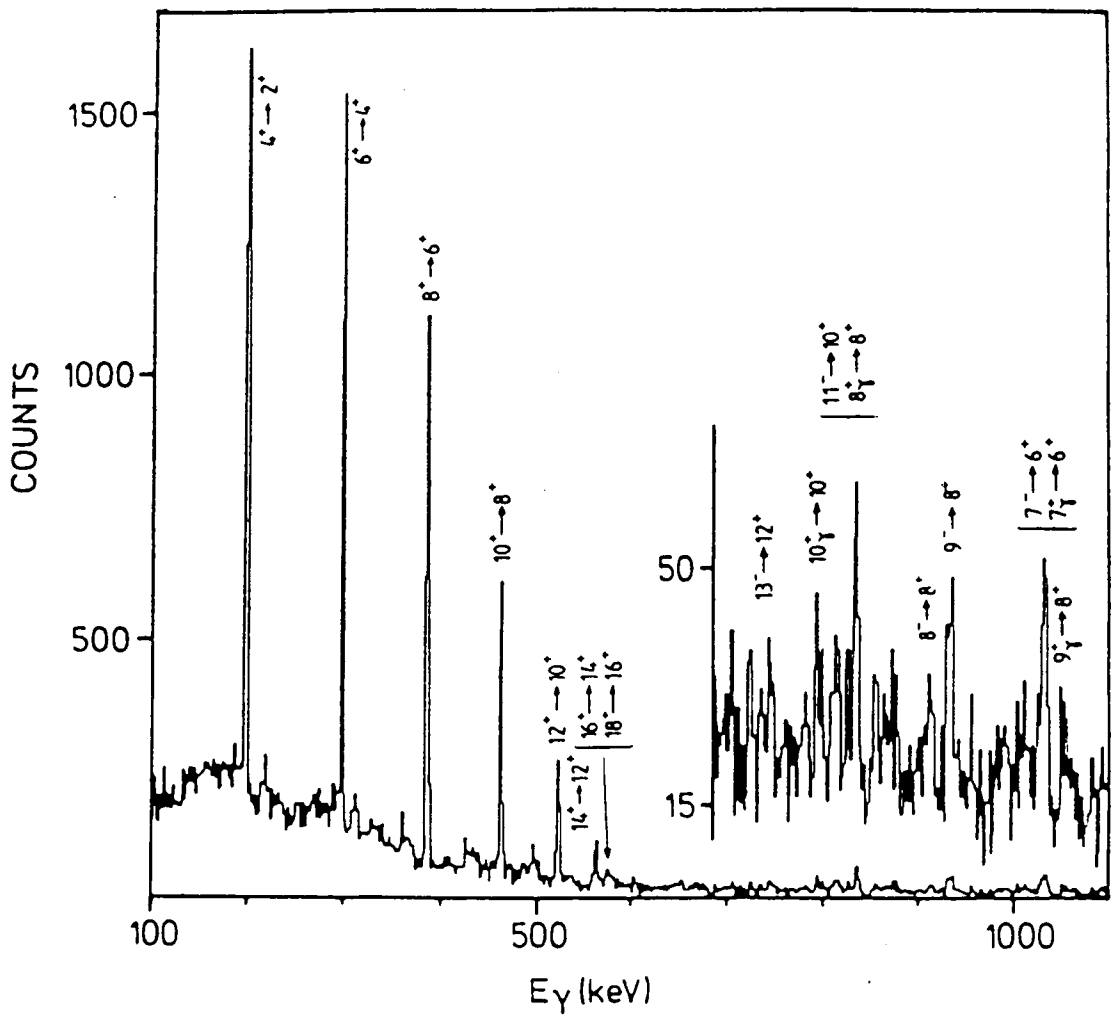


Figure 5.16: γ-γ coincidence spectrum gated on all ground band transitions of ^{160}Dy for the reaction ^{161}Dy(^{58}Ni,^{59}Ni)^{160}Dy.

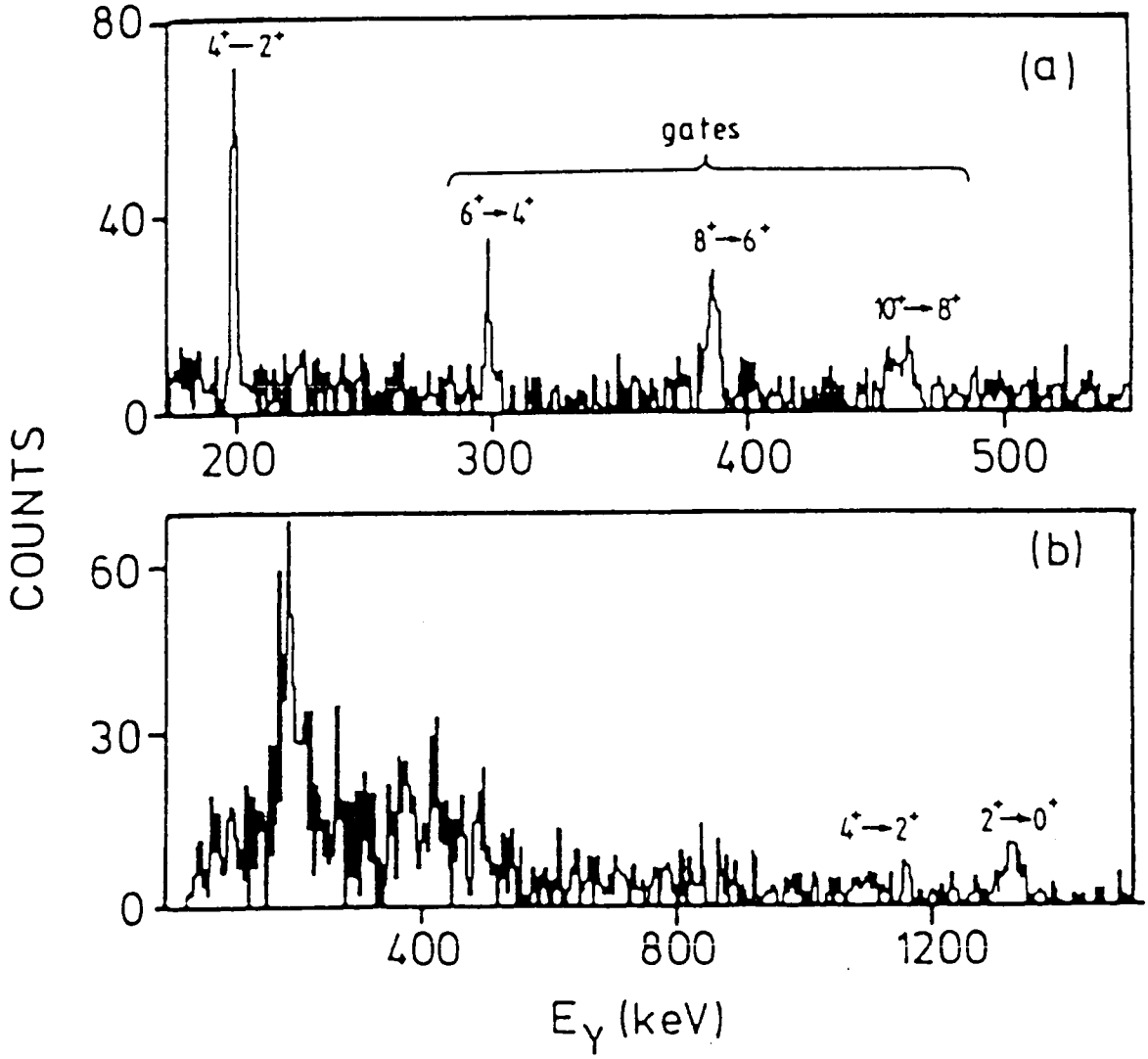


Figure 5.17: γ-γ coincidence spectrum gated on some ground band transitions of ^{160}Dy for the reaction ^{162}Dy(^{58}Ni,^{60}Ni)^{160}Dyat E_{lab} = 285 MeV. The Doppler shift correction is (a) for the target-like ion, (b) for the projectile-like ion.

5.2.2 Experiments with 345 MeV ^{58}Ni Beam

Fig. 5.18 shows the Q-value spectra for the reactions ^{160}Dy+ ^{58}Ni (345 MeV). The beam energy is now 20% above the Coulomb barrier, and the deep inelastic events are comparable in strength with the quasielastic events. Gating on $K_N = 0$ makes most deep inelastic events disappear. Fig. 5.19 shows the (E, M) maps for the reaction ^{161}Dy(^{58}Ni,^{59}Ni)^{160}Dy and ^{162}Dy(^{58}Ni,^{60}Ni)^{160}Dy. Fig. 5.20 and 5.21 show the particle-γ coincidence spectra integrated over the grazing angle.

5.2.3 Experiments with 637 MeV ^{116}Sn Beam

The beam energies are $\sim$ 10% above the Coulomb barrier (the Coulomb barrier is 572 MeV). The Q spectrum was already shown in Fig. 5.3. Quasielastic events dominate the Q-value spectrum, with deep inelastic events comprising $\leq$ 10% of the total events in Fig. 5.3. When the condition $K_N = 0$ is imposed, most of these deep inelastic events are removed.

Figs. 5.22 and 5.23 show (H,K) maps gated on ^{160}Dy ground band transitions; these maps do not include the contribution of the gating transitions in the Ge detector. The same features as discussed in section 5.1.3 are observed. Fig. 5.24 shows the unfolded (E,M) map. The dashed line is the average yrast line for ^{160}Dy assuming no excitation of Sn.

The γ-ray spectra integrated over the grazing angle distribution are shown in Figs. 5.25 - 5.26. Discrete lines up to the $18^+ \rightarrow 16^+$ yrast transition for the reactions ^{161}Dy(^{116}Sn,^{117}Sn)^{160}Dy and ^{162}Dy(^{116}Sn,^{118}Sn)^{160}Dy are seen. The inelastic population is stronger than in the corresponding reactions with the ^{58}Ni beam due to the higher Z (more Coulomb excitation) for the heavier ion.

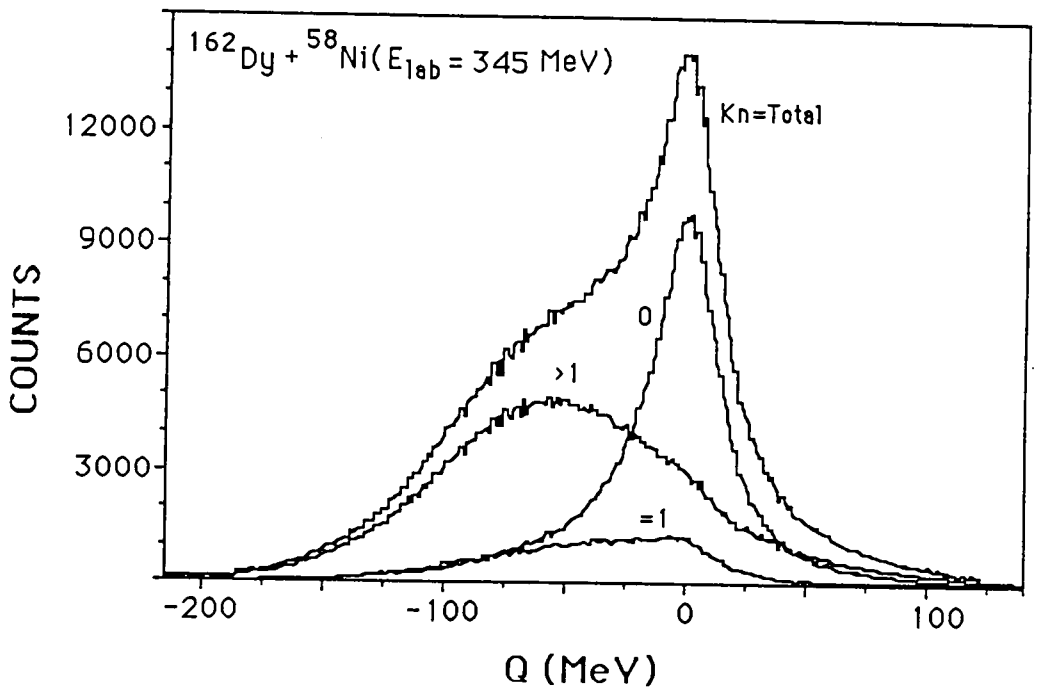


Figure 5.18: Q-value spectra gated on K_N for the reaction ^{162}Dy + ^{58}Ni (345 MeV).

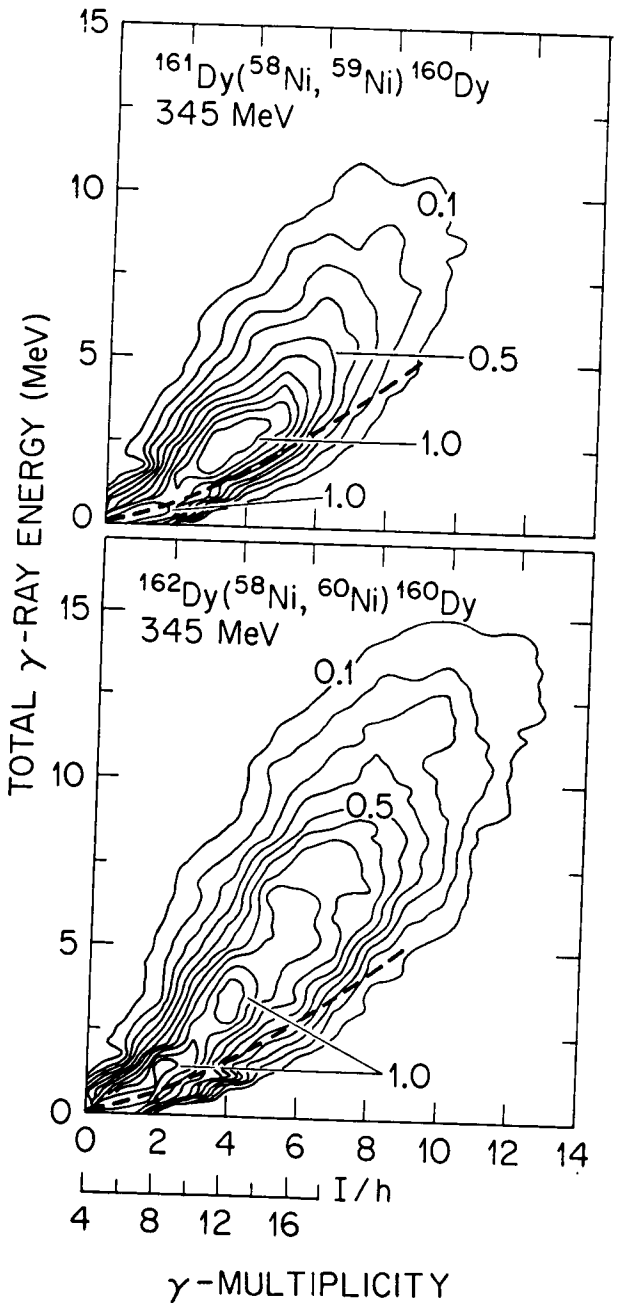


Figure 5.19: (E, M) maps gated on strong ground band transitions of ^{160}Dy for the reactions ^{161}Dy(^{58}Ni,^{59}Ni)^{160}Dy and ^{162}Dy(^{58}Ni,^{60}Ni)^{160}Dy at E_{lab} = 345 MeV.

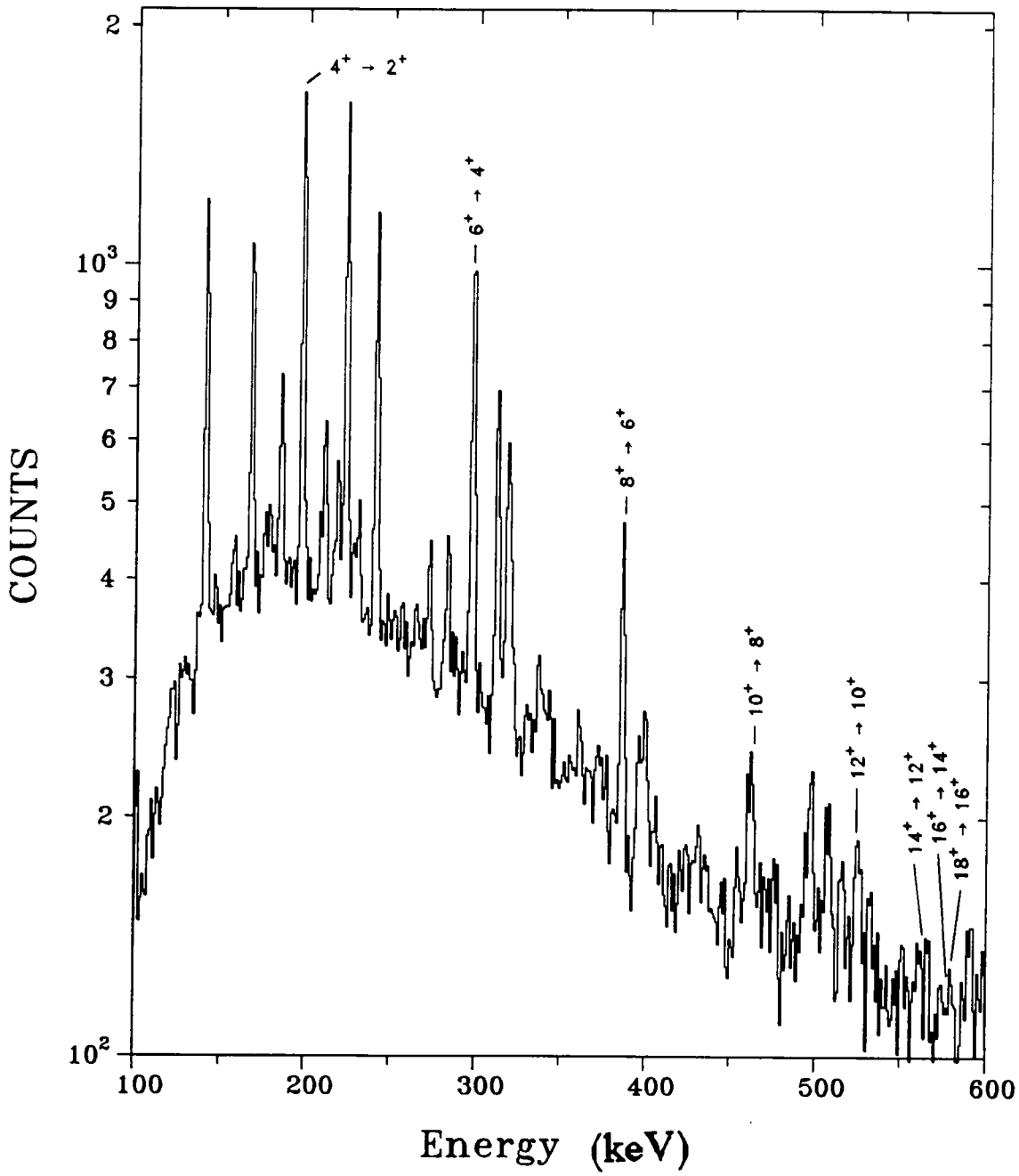


Figure 5.20: Particle-γ coincidence spectra for the reaction ^{161}Dy(^{58}Ni,^{59}Ni)^{160}Dy at E_{lab} = 345 MeV. Ground-band transitions in ^{160}Dy are marked.

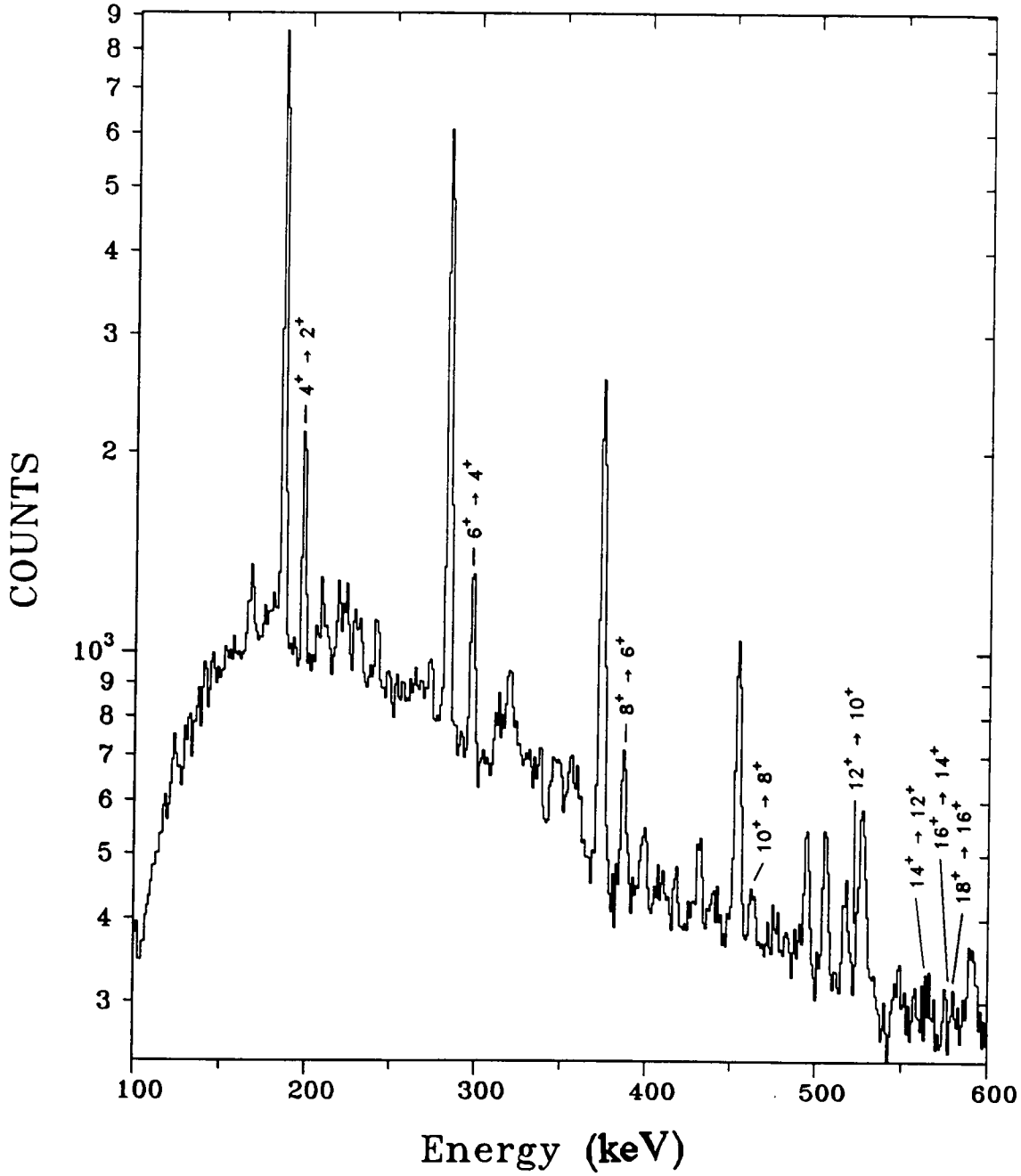


Figure 5.21: Particle-γ coincidence spectra for the reaction ^{162}Dy(^{58}Ni,^{60}Ni)^{160}Dy at E_{lab} = 345 MeV. Ground-band transitions in ^{160}Dy are marked.

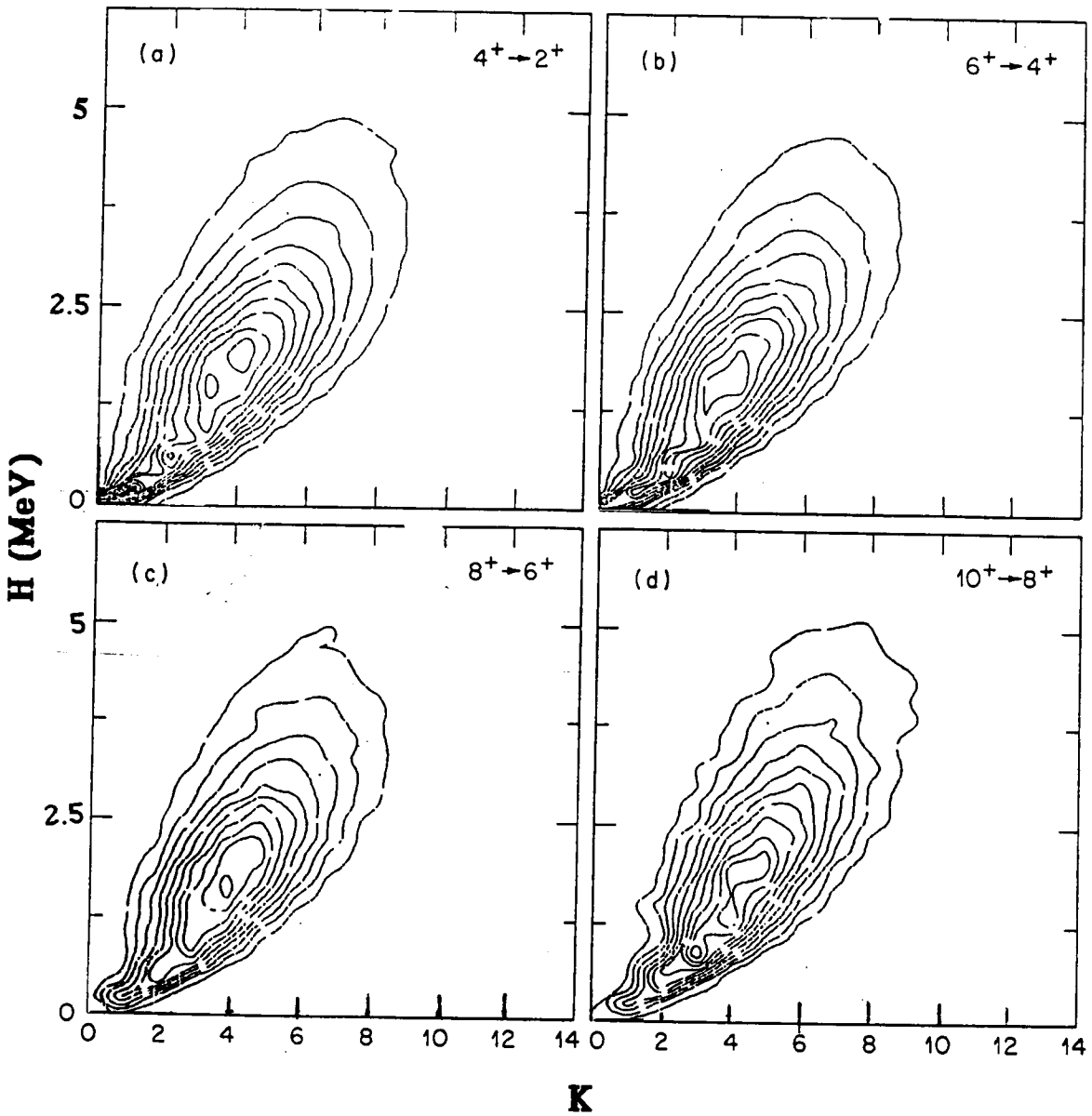


Figure 5.22: (H,K) maps gated on ground band transitions of ^{160}Dy for the reaction ^{161}Dy(^{116}Sn,^{117}Sn)^{160}Dy, E_{lab} = 637 MeV.

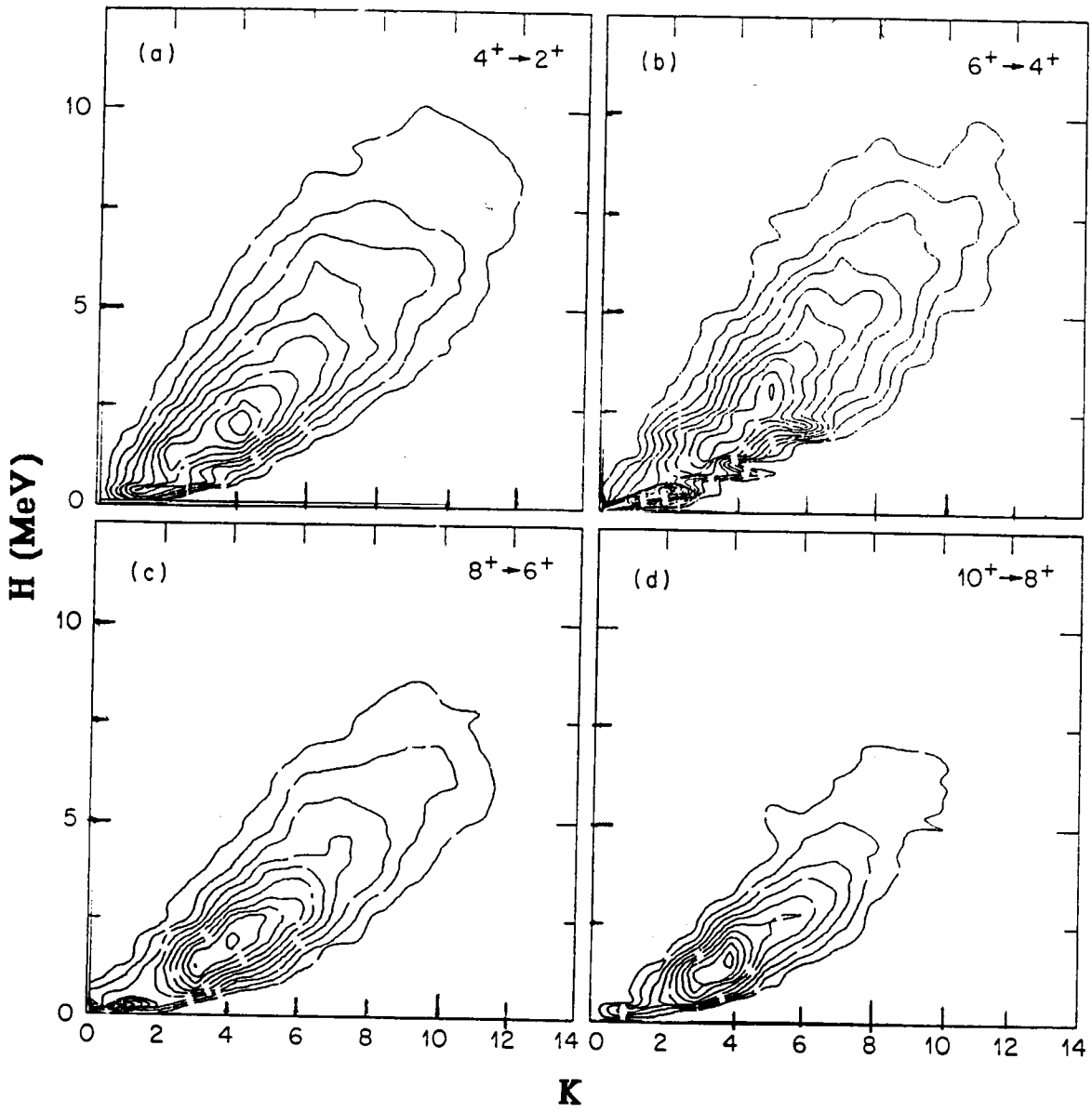


Figure 5.23: (H,K) maps gated on ground band transitions of ^{160}Dy for the reaction ^{162}Dy(^{116}Sn,^{118}Sn)^{160}Dy, E_{lab} = 637 MeV.

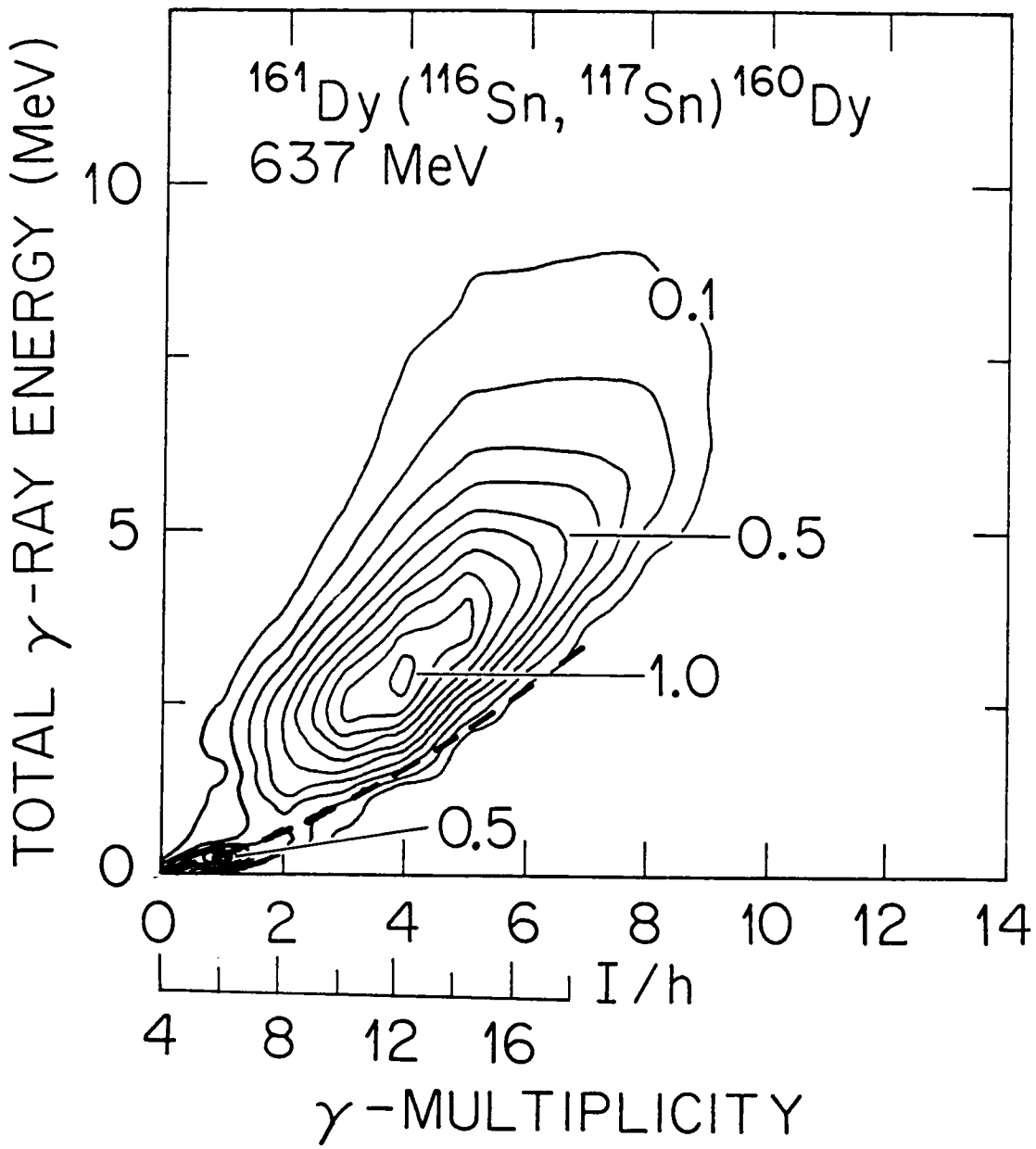


Figure 5.24: Unfolded (E,M) map gated on ground band transition of ^{160}Dy for the reaction ^{161}Dy(^{116}Sn,^{117}Sn)^{160}Dy, E_{lab} = 637 MeV.

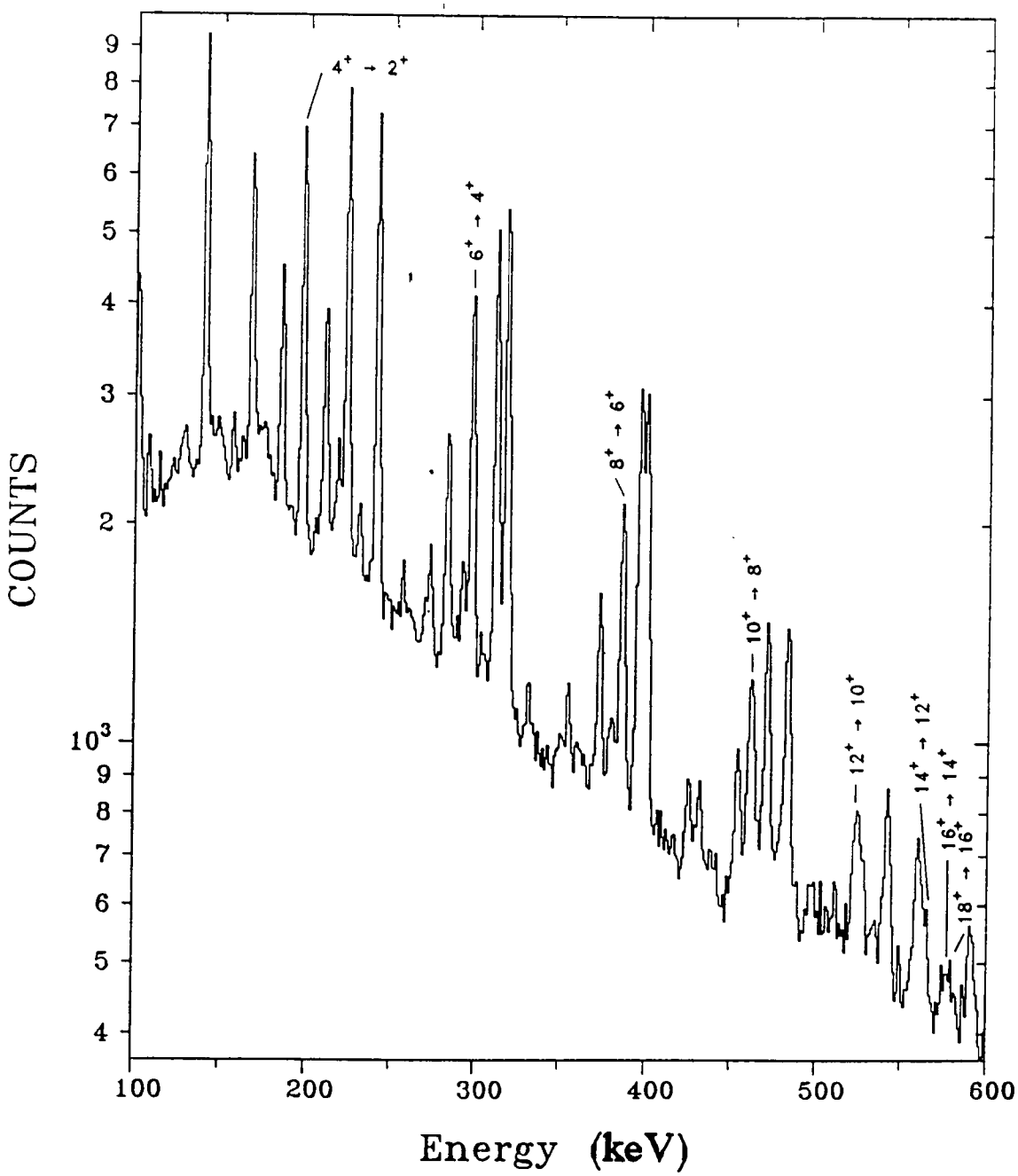


Figure 5.25: Particle-γ coincidence spectrum taken at the grazing angle for the one-neutron pickup reaction ^{161}Dy(^{116}Sn,^{117}Sn)^{160}Dy at E_{lab} = 637 MeV.

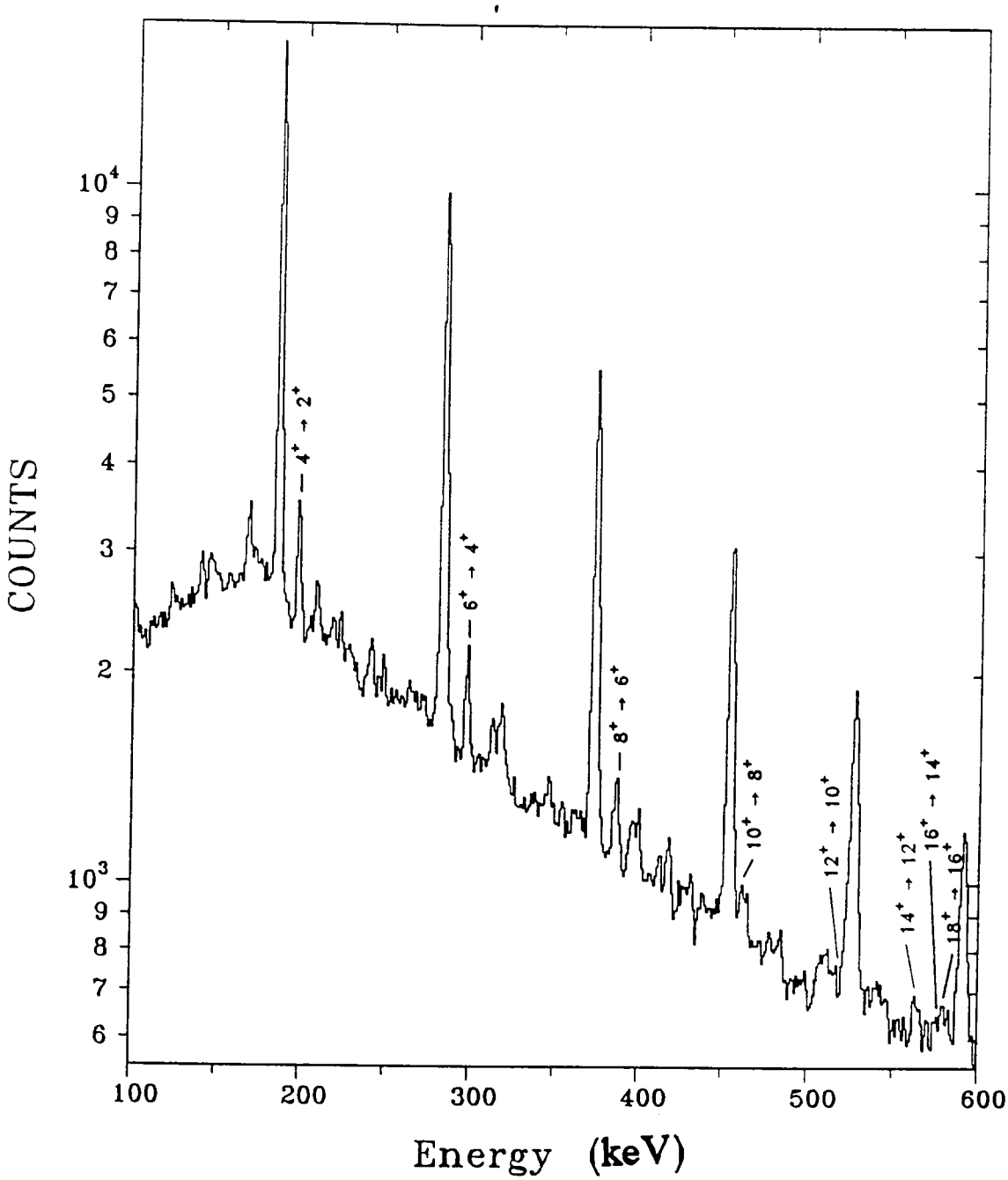


Figure 5.26: Particle-γ coincidence spectrum taken at the grazing angle for the two-neutron pickup reaction ^{162}Dy(^{116}Sn,^{118}Sn)^{160}Dy at E_{lab} = 637 MeV. Ground-band transitions in ^{160}Dy are marked.

5.2.4 Experiment with 325 Mev ^{58}Ni on the Actinide Target ^{235}U

The easily-aligned $i_{13/2}$ proton and $j_{15/2}$ neutron orbital are both close to the Fermi surface in actinide nuclei. The rotation alignment in this region becomes an interesting subject for both experimental and theoretical study. Unlike the rare-earth region, the (HI, xn) reaction has limited use in the actinides because of the strong competition from fission. The majority of the information on actinide high-spin states has come from Coulomb excitation, which is limited by the number of stable targets. The rather "cold" mechanism for population of high-spin states for transfer reactions observed in the rare-earth region has stimulated us to extend such measuments to the actinides.

Fig. 5.27 shows the total γ-ray energy and multiplicity for the one-neutron transfer reaction ^{235}U(^{58}Ni,^{59}Ni)^{234}U. It was produced by summing gates on the $8^+ \rightarrow 6^+$, $10^+ \rightarrow 8^+$, and $12^+ \rightarrow 10^+$ transitions of ^{234}U. An approximate yrast line assuming no excitation of the Ni is shown as a dashed line. There are two maxima in this (E, M) map. The lower one lies approximately on the yrast line and peaks at (E, M) = (0.5 MeV, 1.5); inelastic events from the ^{234}U target contamination account for less than 10% of this peak. The higher one peaking around (E, M) = (3.0 MeV, 3.5) is the main entry state. It accounts for more than 90% of the total events and is $\sim$ 2 MeV above the yrast line, which is higher than the corresponding maximum position for the Ni + ^{161}Dy reaction in Fig. 5.6. There are several possible explanations for this: (1) the Q-window is about 2 MeV higher than for the rare-earth case; (2) the Z value of U is larger, leading to more Coulomb excitation; (3) the gap between the ground and two-quasiparticle bands in the relevant spin range is larger in actinides than in the rare earths.

Fig. 5.27 indicates clearly that this reaction is "cold", populating only states lying on and near the yrast line. The structure of the (E, M) map can be understood through the same machanisum as for the rare-earth region: the lower

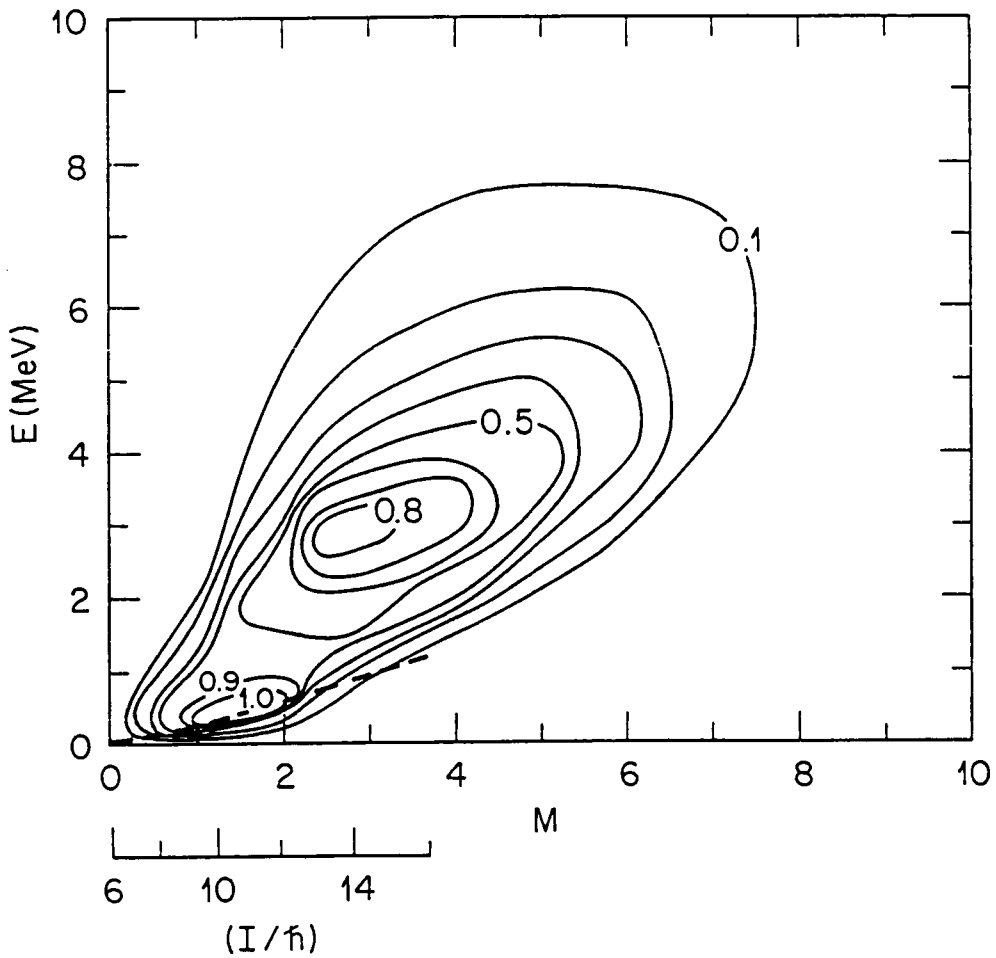


Figure 5.27: Total γ-ray energy and multiplicity plot for the one-neutron pickup reaction ^{235}U(^{58}Ni,^{59}Ni)^{234}U. The dashed line is the approximate yrast line for ^{234}U, assuming no ^{58}Ni excitation.

bump corresponds to pickup of the unpaired $j_{15/2}$ neutron, leading to direct population of the ground-state rotational band of ^{234}U; the upper bump represents the pickup of a deeper-lying paired neutron to form aligned two-quasiparticle states. In populating the upper bump the heavy-ion transfer reaction acts as an "alignment filter", preferentially transferring to the most aligned two-quasiparticle states, as has been explained in Guidry *et al.* (1985a) and Wu *et al.* (1987).

Fig. 5.28 shows γ-ray spectra summed over all the Ge detectors; (a) is the total spectrum; (b) is the two-fold spectrum gated on the transitions of ^{234}U; (c) is the spectrum gated on total energy larger than 2.9 MeV and multiplicity larger than 4. Most of the discrete lines in the spectra came from the inelastic and one-neutron pickup channels. No appreciable fission competition was observed. The differential cross section $\sim$ 20 mb/sr for the one-neutron pickup reaction is about 15% of that for the inelastic reaction at the grazing angle ($\sim$ 130 °). The transfer lines were identified from the energies for known transitions (Ower *et al.* 1982). The transition $24^+ \rightarrow 22^+$ of ^{234}U is clearly seen in Fig. 5.28(c), and there is a candidate for the $26^+ \rightarrow 24^+$ transition. This spin is $\sim$ 8 units higher than the highest spin excited in Coulomb excitation of ^{248}Cm by 260 MeV ^{58}Ni ions (Czosnyka *et al.* 1986).

5.3 Cross Sections for One and Two-Neutron Transfer Reactions

5.3.1 Introduction

By gating in the (H,K) plane to exclude the feeding from the quasicontinuum, a Ge γ-ray spectrum can be constructed for direct population of the Dy yrast states. As we have argued before, such excitation patterns may carry detailed information about the deformed single particle orbits and the effect of collective angular momentum. The ideal gate is a banana gate along the yrast line in the (H,K) plane, but due to the finite resolution in H and K ($\sim$ 30-40%) there is strong contamination

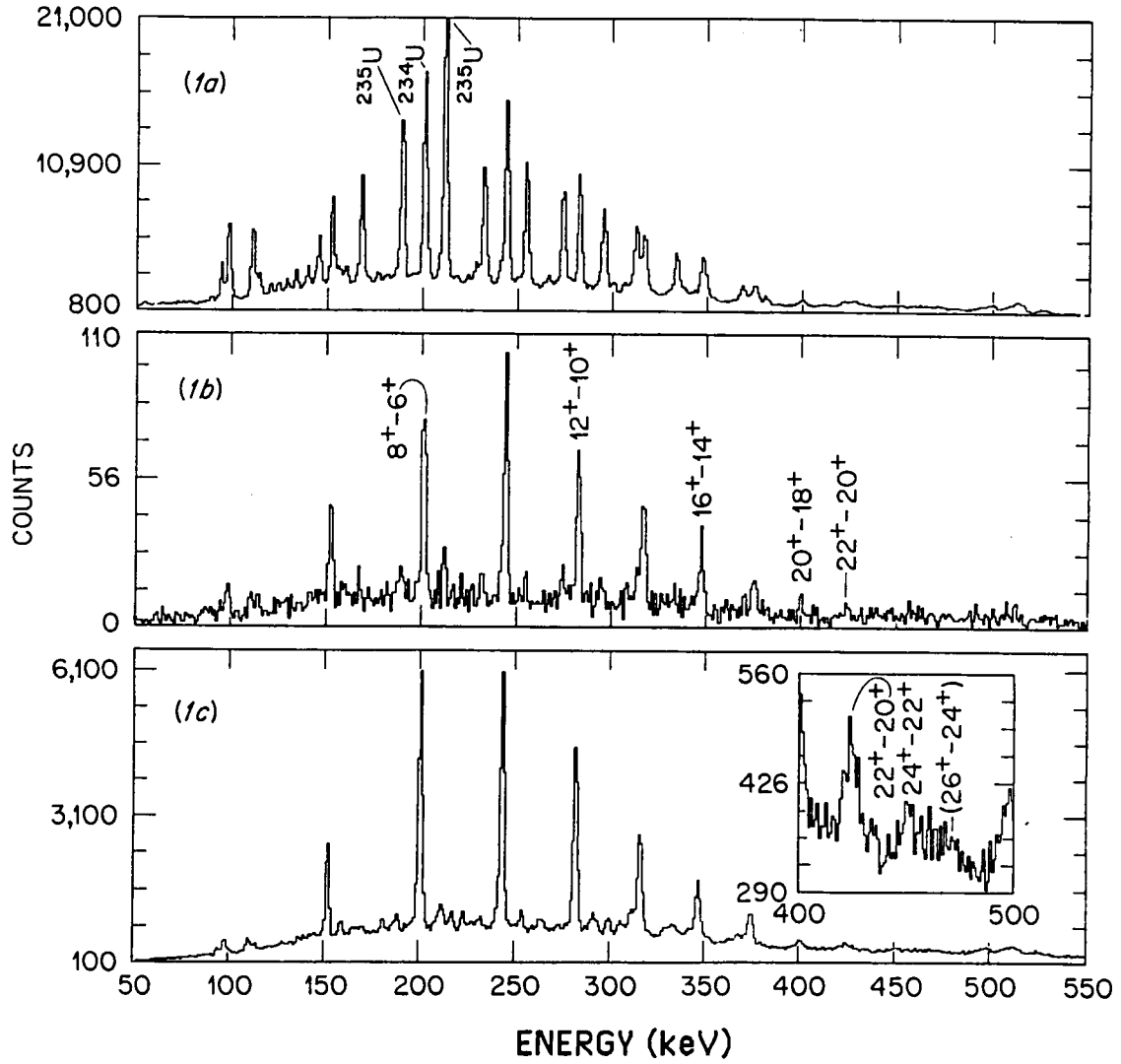


Figure 5.28: γ-ray spectra integrated over lab angle between 104° and 152° around the grazing angle $\sim$ 130° for the reaction ^{235}U + 325 MeV ^{58}Ni.

of quasicontinum population in higher-lying transitions of the ground band. Figs. 5.29 - 5.30 show projected H for one and two-neutron pickup reactions, and for the corresponding inelastic scattering reaction. Fig. 5.31 shows projected H for a two-neutron pickup reaction and the corresponding inelastic scattering reaction. In each case the relevant channel was selected by gating on the $4^+ \rightarrow 2^+$ transition of the outgoing ^{160}Dy ion. The lower lying inelastic ground band transitions are marked. These projections of the total γ-ray energy indicate a reasonable separation of the ground-band transfer from that populating 2-qp bands (two-quasiparticle bands) in the transfer reactions. For the approximate separation of ground-band and 2-qp population we set a gate in the total energy spectra from 0 to 1.2 MeV for the ^{116}Sn experiments and 0 to 1.4 Mev for the ^{58}Ni experiments

As mentioned in section 2.2, for sufficiently gentle collisions the differential cross section $d\sigma(\theta)/d\Omega$ for a transfer reaction can be written in the form

$$\frac{d\sigma(\theta)}{d\Omega} = \left(\frac{d\sigma(\theta)}{d\Omega}\right)_{elastic} P \tag{5.1}$$

where P is the probability for transfer along the scattering orbit, which is defined experimently as

$$P = \frac{Y(1+\alpha)}{\epsilon} \frac{1}{N_{single}} \tag{5.2}$$

Y is the γ-ray yield, α is the internal conversion coefficient, ϵ is the absolute detection efficiency of the Ge detectors, and N_{single} is the number of heavy-ion singles counts. With our assumptions, the elastic scattering cross section is given by the classical Rutherford formula

$$\left(\frac{d\sigma(\theta)}{d\Omega}\right)_{elastic} = \frac{\eta^2}{4k^2}\left(\csc\frac{\theta}{2}\right)^4 \tag{5.3}$$

5.3.2 Cross Section for Direct Population of the Dy Yrast States

The cross section for direct population of the Dy yrast states can be extracted from Ge spectra gated on H by using formula 5.1. Figs. 5.32 and 5.33 show

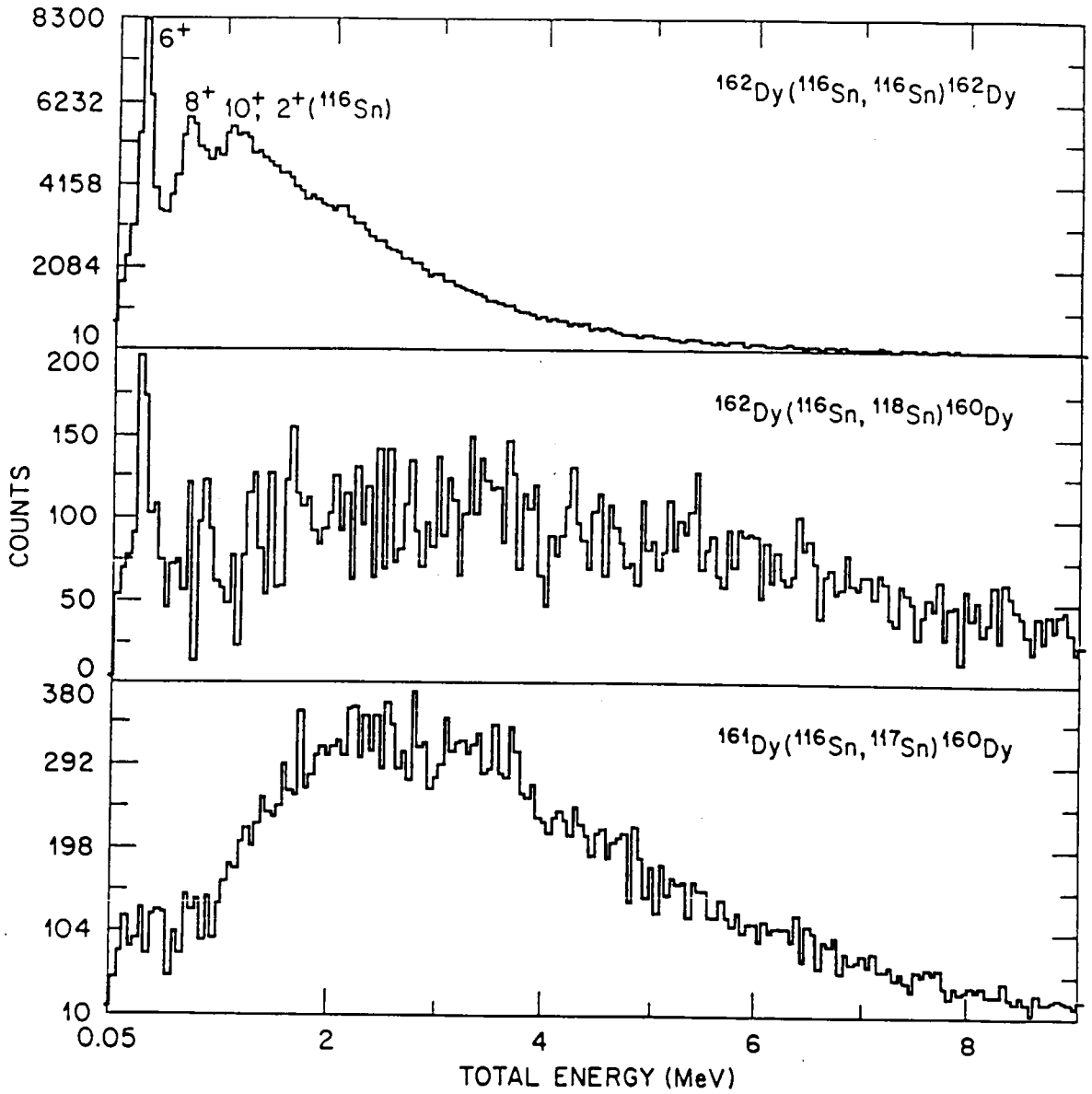


Figure 5.29: Summed NaI γ-ray energies in the inelastic and transfer channels for reactions with 637 MeV ^{116}Sn beam.

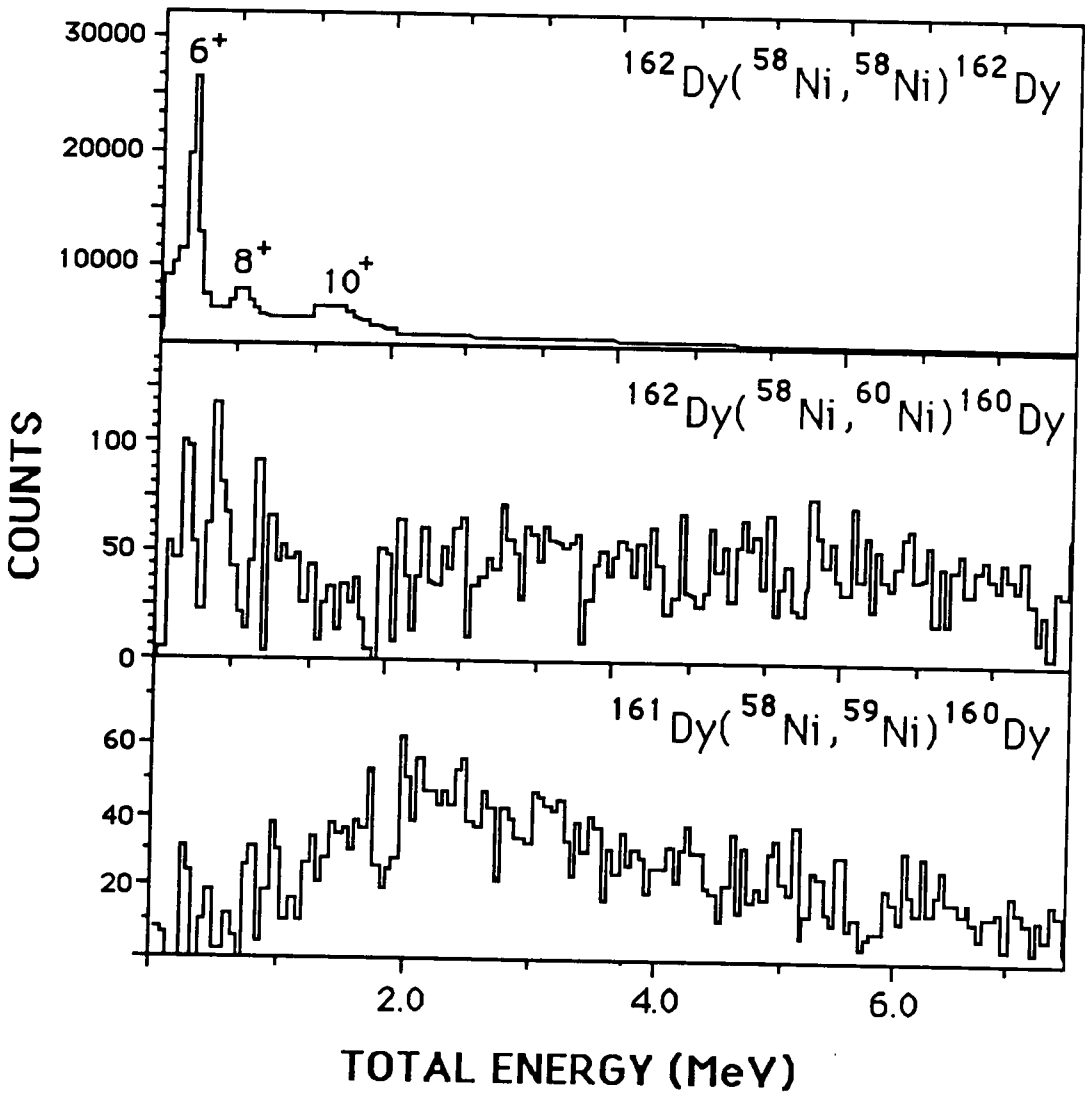


Figure 5.30: Summed NaI γ-ray energies in the inelastic and transfer channels for reactions with 345 MeV ^{58}Ni beam.

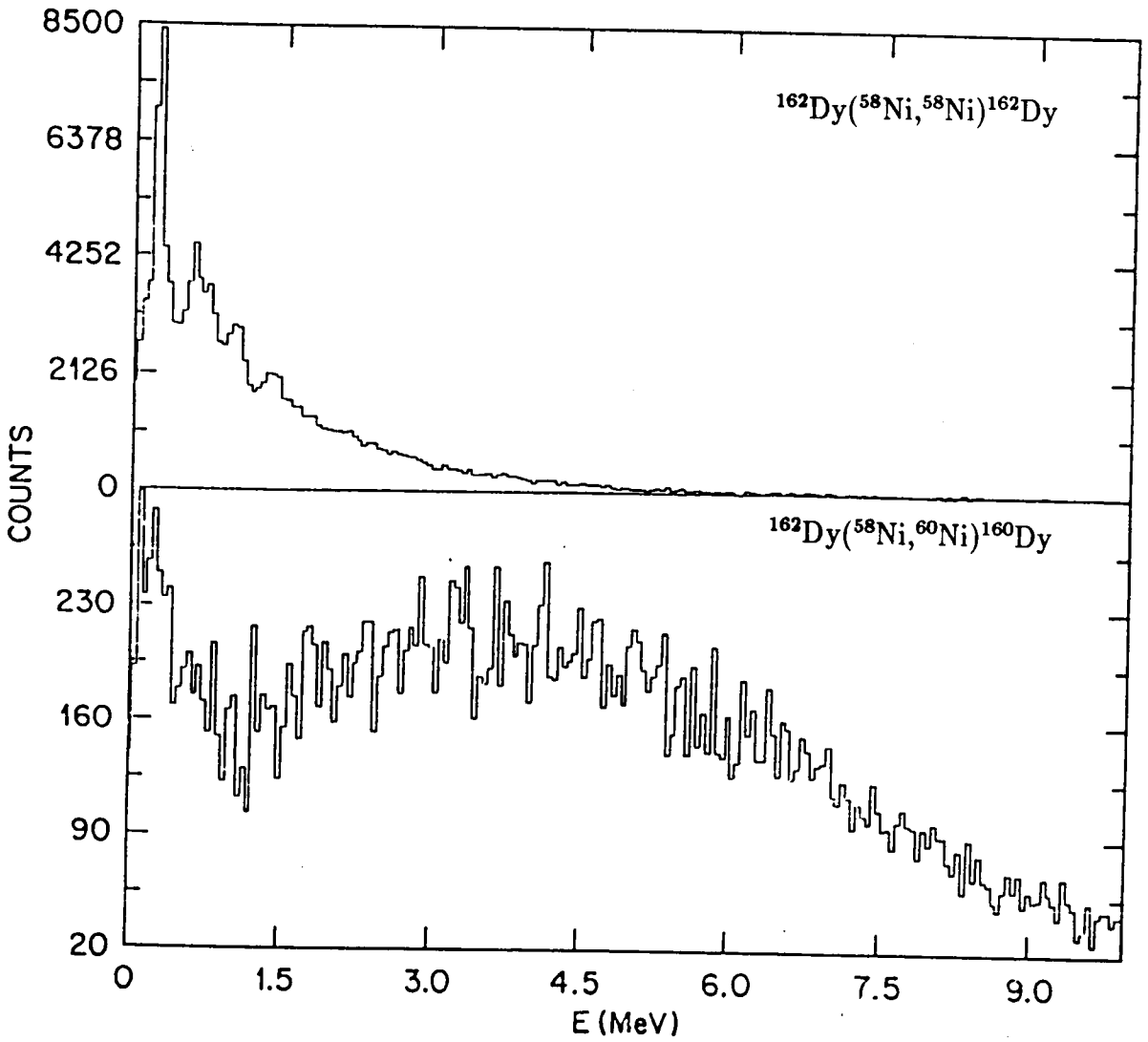


Figure 5.31: Summed NaI γ-ray energies in the inelastic and two-neutron transfer channels for reaction with 285 MeV ^{58}Ni beam.

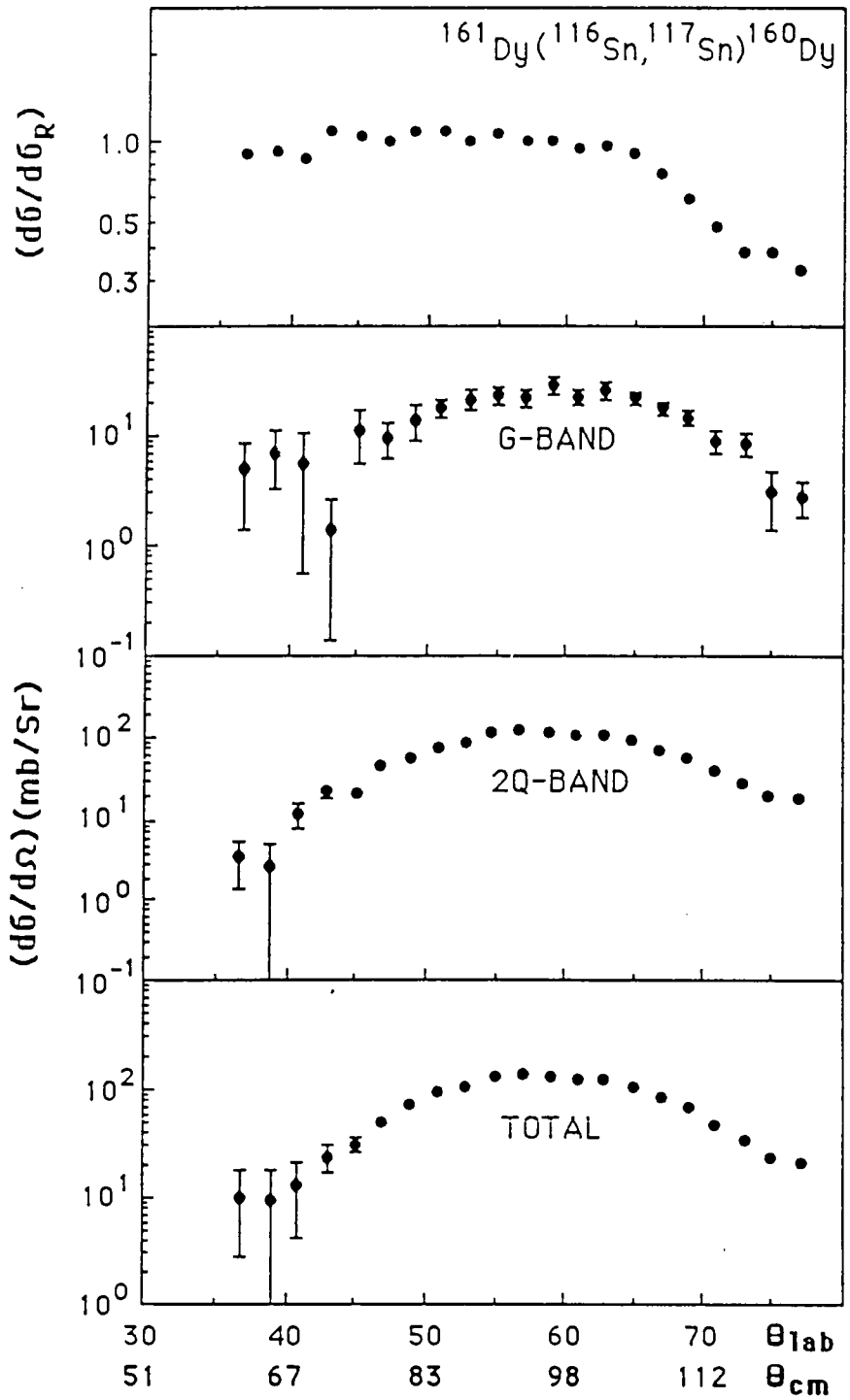


Figure 5.32: Cross sections for the reaction ^{161}Dy(^{116}Sn,^{117}Sn)^{160}Dy.

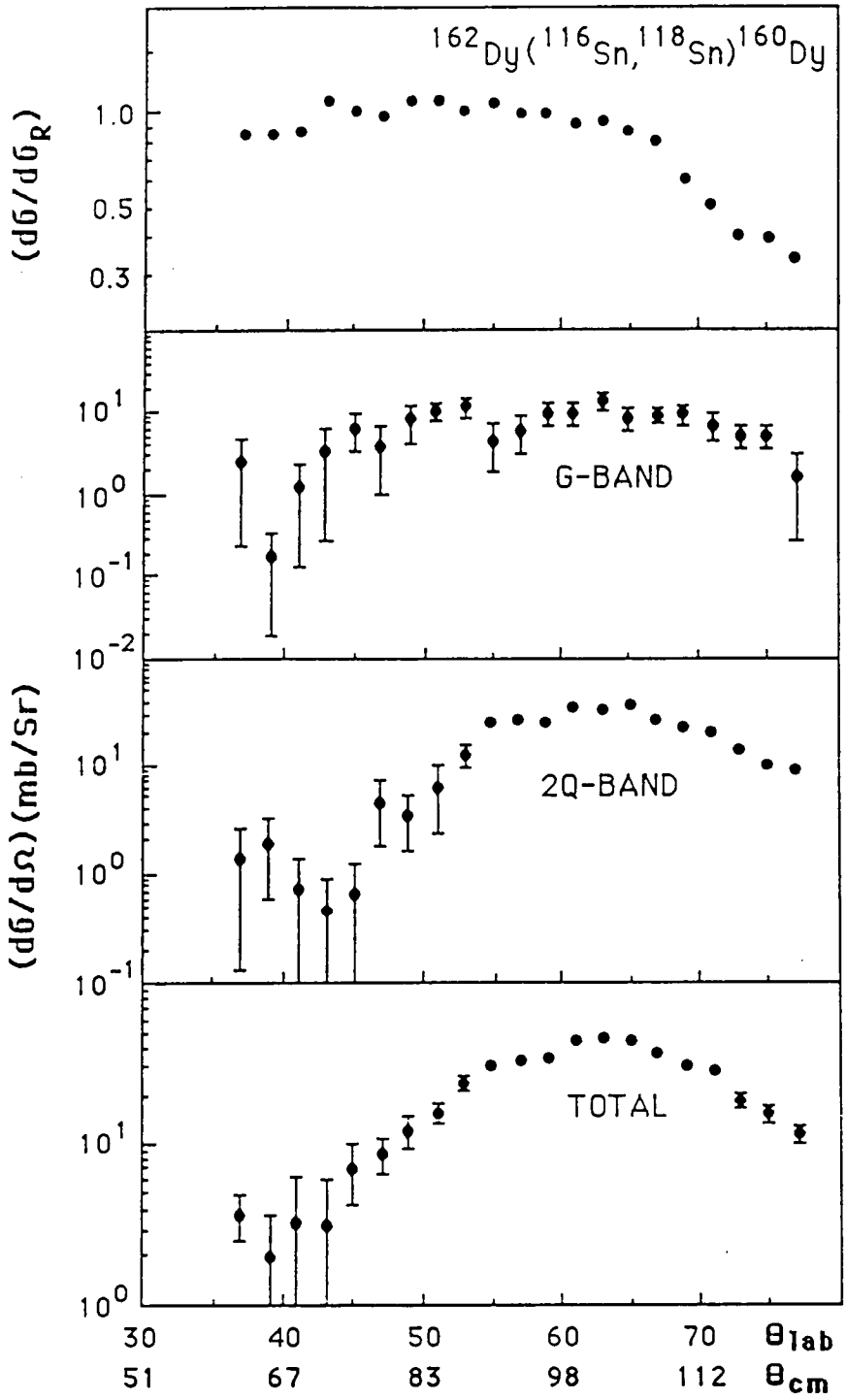


Figure 5.33: Cross sections for the reaction ^{162}Dy(^{116}Sn,^{118}Sn)^{160}Dy.

the cross section for one and two-neutron transfer reactions gated on the $4^+ \rightarrow 2^+$ ground-band transition of ^{160}Dy. Due to the strong Coulomb excitation present in these reactions the 4^+ yield is expected to incorporate $> 90\%$ of the total population, so this should be an excellent approximation to the total transfer cross section.

The total cross section for both one and two-neutron transfer has a smooth bell shape. The total cross section for the one neutron transfer reaction is approximately 3 times larger than that for the two-neutron transfer reaction, but for the direct population of the ground band they are of about the same size: approximately 25% of the total transfer cross section is due to direct population of the ground band for two-neutron transfer, and approximately 20% of the total transfer cross section is due to direct population of the ground band for one-neutron transfer in the grazing angle region.

The cross section for direct population of individual yrast states can be determined from the Ge spectrum by correcting for feeding beginning at the highest states seen. Fig. 5.34 and 5.35 show the cross section for direct population of the 4^+, 6^+, and 8^+ states of the ^{160}Dy ground band in the reactions ^{161}Dy(^{116}Sn,^{117}Sn)^{160}Dy and ^{162}Dy(^{116}Sn,^{118}Sn)^{160}Dy. These cross sections suffer from large error bars due to statistics, but may exhibit structure in the angular distribution, unlike the smooth bell shapes of the total cross section. Especially we note that in Fig. 5.35 the cross section for the 4^+ state has a valley at $\sim 90°$ (in the center of mass coordinates). The structure in the 4^+ distribution is well reproduced, and relative magnitudes of the cross section in the three spin states are accurately predicted, in calculations by Price *et al.* (1987), who interpreted the structure in terms of interfering amplitudes corresponding to different orientations of the deformed nucleus. Such effects had been predicted theoretically by Guidry *et al.* (1981).

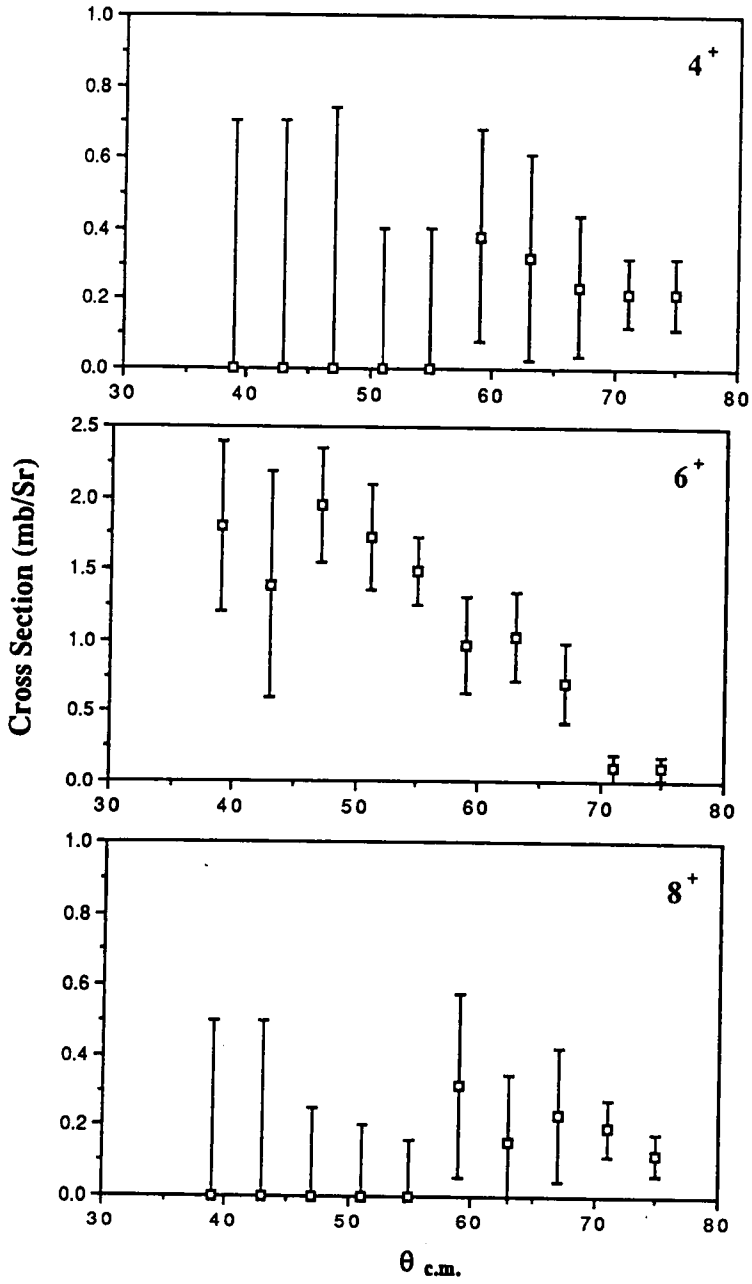


Figure 5.34: Cross sections for direct population of individual ground band states in the reaction ^{161}Dy(^{116}Sn,^{117}Sn)^{160}Dy.

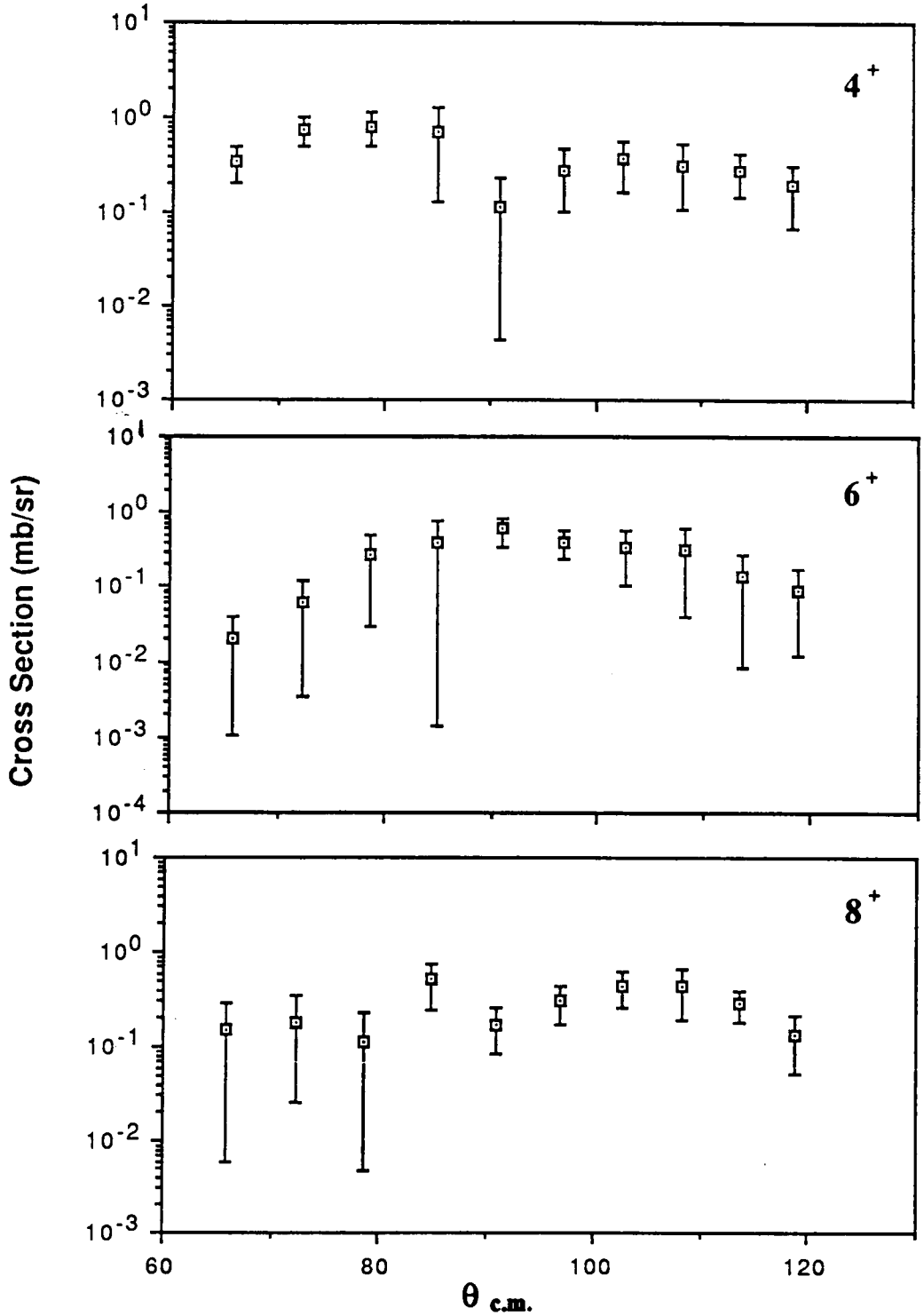


Figure 5.35: Cross sections for direct population of individual ground band states in the reaction ^{162}Dy(^{116}Sn,^{118}Sn)^{160}Dy.

5.3.3 Rotational Signatures for Transfer to High-Spin States

It has been argued that transfer reactions with very heavy ions provide nuclear structure information which is qualitatively different from that obtained in analogous reaction induced by light heavy ions (Guidry *et al.*1981). In particular the strong collective excitation inherent in such reactions implies that transfer could be induced between states carrying many quanta of collective excitation, and that localizations in coordinates conjugate to quantum numbers taking on large values can be expected. Thus, such reactions provide a unique perspective on single-particle and pairing effects under the influence of strong collective excitation. A major portion of the nuclear structure information in such reactions is expected to be contained in the probability pattern for excitation of particular states in the transfer (Guidry *et al.* 1981). For members of a rotational band this pattern is termed the *rotational signature.*

In the results described previously, it has been possible to measure the cross section for transfer to high-spin members of the yrast band of deformed nuclei. To obtain the rotational signatures for direct transfer to the ^{160}Dy yrast band the γ-ray spectrum integrated over the grazing angle is constructed subject to the ground band gate (the same as discussed in section 5.3.3), which suppresses side-feeding of the yrast line in the γ-ray cascade. Once the feeding is restricted to the E2 yrast cascade, the cross section can be determined by starting at the top of the cascade and correcting the measured peak areas for Ge efficiency and for feeding through the preceding transition in the cascade.

Fig. 5.36 shows the cross sections for the reactions ^{161}Dy(^{58}Ni,^{59}Ni)^{160}Dy (E_{lab}=270 MeV) and ^{162}Dy(^{58}Ni,^{60}Ni)^{160}Dy(E_{lab}=285 MeV), along with the corresponding inelastic scattering reaction ^{162}Dy(^{58}Ni,^{58}Ni)^{162}Dy. Since ^{160}Dy and ^{162}Dy have similar deformations and quadrupole moments, the inelastic scattering reaction should be quite similar to that expected for ^{160}Dy(^{58}Ni,^{58}Ni)^{160}Dy. The

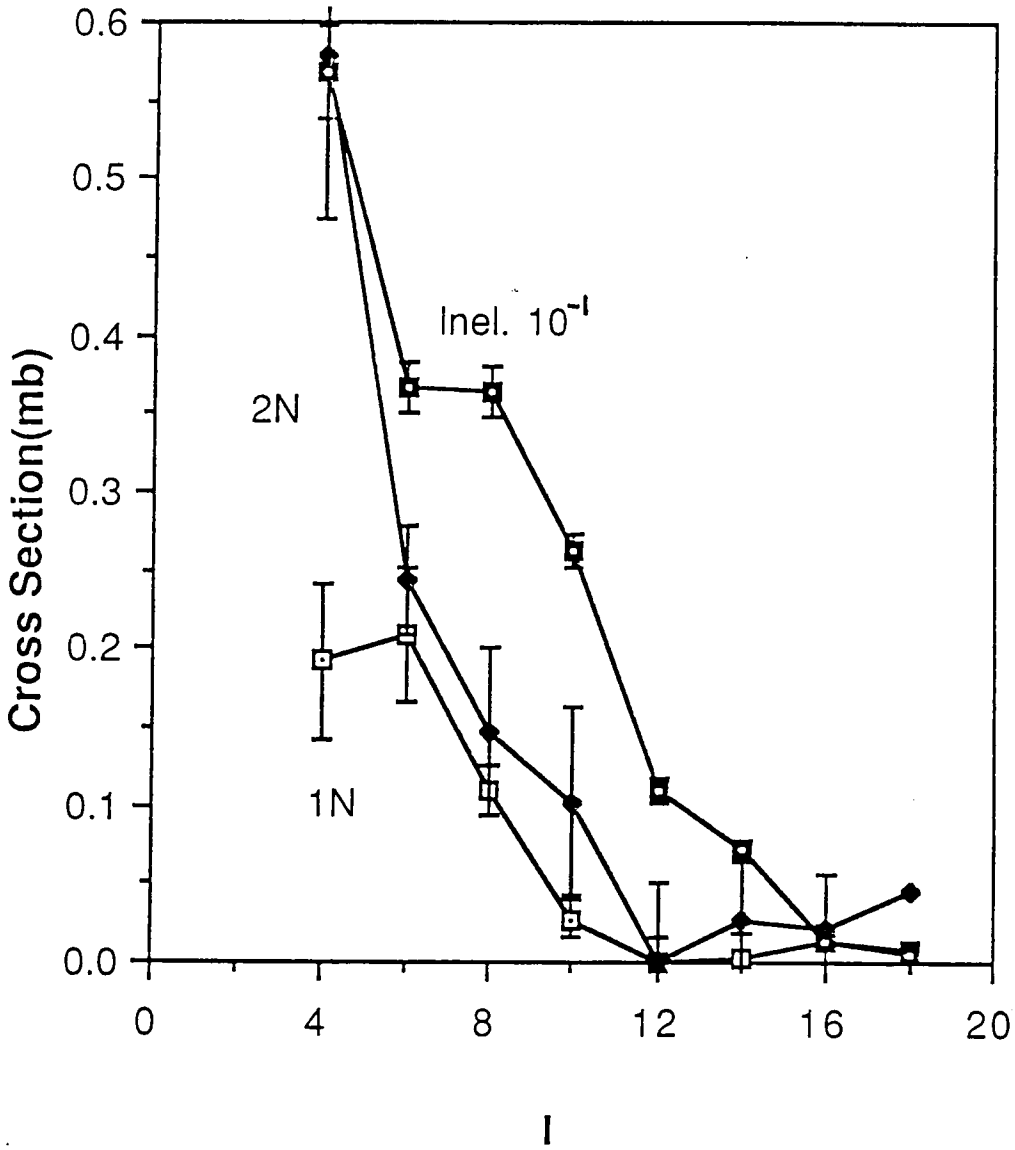


Figure 5.36: Rotational population signatures for one (1N) and two-neutron (2N) pickup reactions ^{161}Dy(^{58}Ni,^{59}Ni)^{160}Dy, ^{162}Dy(^{58}Ni,^{60}Ni)^{160}Dy, and the inelastic scattering reaction ^{162}Dy(^{58}Ni,^{58}Ni)^{162}Dy.

$2^+ \rightarrow 0^+$ transition is highly converted, so only states with $I^\pi \geq 4^+$ are shown. The resolution of the Spin Spectrometer is insufficient to separate the ground and first two excited states of ^{58}Ni; therefore, Fig. 5.36 represents the cross section for populating the ^{160}Dy ground band when the $p_{3/2}$, $f_{5/2}$, or $p_{1/2}$ Ni orbitals are populated. Fig. 5.37 shows the cross sections for the reactions ^{161}Dy(^{116}Sn,^{117}Sn)^{160}Dy and ^{162}Dy(^{116}Sn,^{118}Sn)^{160}Dy, along with that for the corresponding inelastic scattering reaction ^{162}Dy(^{116}Sn,^{116}Sn)^{162}Dy. Because the Spin Spectrometer has finite resolution, the total energy gating described in section 5.3.3 may not suppress all side feeding. For the 12^+, 14^+, and 18^+ states the sidefeeding uncertainty is as large as the measurement itself, so those cross sections should be viewed as upper limits.

Comparing the one-neutron transfer rotational signature in Figs. 5.36 - 5.37 with the inelastic scattering signature, the most striking difference is the strong suppression of the 4^+ state for one-neutron transfer. This suppression is much larger than expected from simple inelastic interference effects. A partial explanation may lie in the transfer energy window which would enhance higher spins over lower spins, but the difference between 4^+ and 6^+ states appears to be too dramatic to arise solely from this.

A more interesting prospect is that the pattern in Figs. 5.36 - 5.37 for one-neutron transfer reactions results from the effects of the orientation angle dependent formfactor on the deformed nuclear surface which was discussed extensively by Guidry *et al.* (1981, 1982) (see also Dasso *et al.* 1982, 1984, 1986). A transfer formfactor peaked near a polar angle of $\sim 45°$ on the deformed nuclear surface would favor high-spin and suppress low-spin collective excitation, and could account for the pattern seen in Figs. 5.36 - 5.37 (see Guidry *et al.* 1981). A test of this hypothesis will be afforded by systematic measurements of the kind described here for a variety of nuclei. If the signature pattern reflects the geometry of the orbits participating in the transfer, it should change as those orbits change for different nuclei.

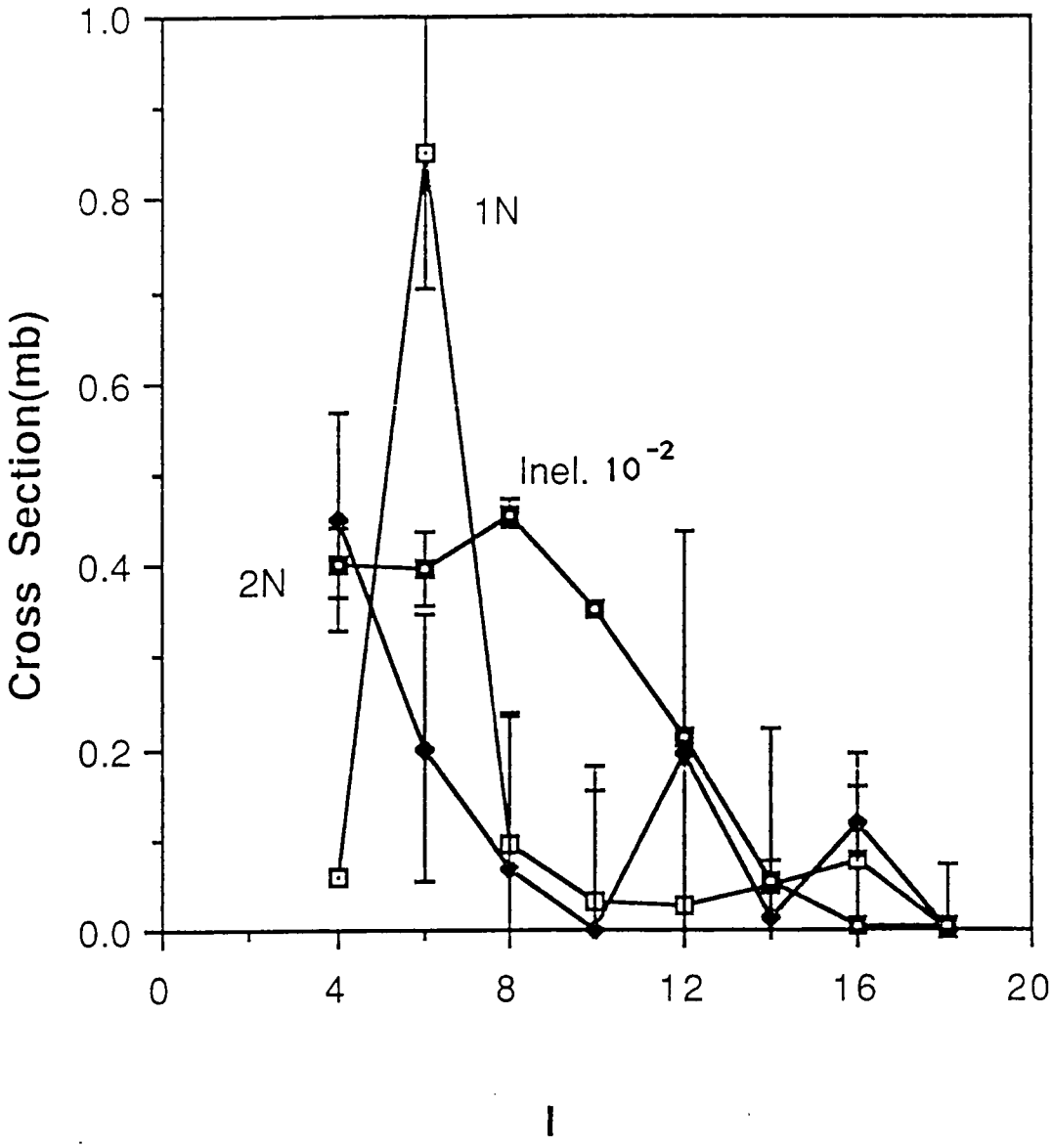


Figure 5.37: Rotational population signatures for one (1N) and two-neutron (2N) pickup reactions ^{161}Dy(^{116}Sn,^{117}Sn)^{160}Dy, ^{162}Dy(^{116}Sn,^{118}Sn)^{160}Dy, and the inelastic scattering reaction ^{162}Dy(^{116}Sn,^{116}Sn)^{162}Dy.

Comparing the two-neutron transfer rotational signature in Figs. 5.36 - 5.37 with the inelastic scattering signature, we observe a rapid decrease with angular momentum in the cross section for ground band population in two-neutron transfer. Recently Nikam and Ring (1986, 1987) have presented calculations of two-neutron transfer amplitudes between heavy deformed rotating nuclei. These amplitudes are defined as the matrix elements

$$A_{I,I}^{\lambda=0} =< A+2, I \mid (a^{+}a^{+})_{\lambda=0} \mid I, A > \tag{5.4}$$

where the operator denotes two-particle creation operators coupled to angular momentum zero, I is the nuclear spin, and the state vectors are cranked Hartree-Fock-Bogliubov wave functions projected onto states of good particle number A. Strong variations are observed in this amplitude for some deformed heavy nuclei as I increases from zero to moderately large values, as shown in Table 5.1. Therefore in Figs. 5.36 - 5.37 the two-neutron transfer rotational signature could be the first evidence for this new effect (nuclear SQUID effect). However, a more systematic investigation will be required to test this conjecture, particularly since the suppression of transfer to high spin states occurs earlier than predicted by the calculations. Such experiments are currently being prepared.

Table 5.1: Two-neutron transfer amplitudes for ^{160}Dy normalized to unity for I = 0. Reproduced from Canto *et al.* (1987)

I	$A^{0}_{I,I}$	I	$A^{0}_{I,I}$
0	1.00	14	-0.374
2	0.986	16	-0.440
4	0.951	18	-0.467
6	0.833	20	-0.463
8	0.769	22	-0.437
10	0.633	24	-0.416
12	-0.233	26	-0.386

5.4 Probability for One and Two-Neutron Transfer Reactions

5.4.1 Introduction

Fig. 5.38 shows the ratio of singles events to the calculated Rutherford cross section for several reactions. This ratio is nearly unity for a large angular range, over which we may assume that the Rutherford trajectory is valid. Therefore, the semiclassical model is the most intuitive way to understand transfer reactions in this region.

The nuclear structure information associated with the particle transfer is contained in the transfer formfactor. To first order in the transfer potential V, the form factor is obtained in DWBA as the overlap of the nuclear wave function of the initial $\psi_A\psi_a$ and final $\psi_B\psi_b$ states for the reaction a(A, B)b

$$f_t = < \psi_B\psi_b \mid V \mid \psi_A\psi_a > \tag{5.5}$$

The real part of the transfer potential is approximately the total real scattering potential minus the potential giving rise to elastic and inelastic scattering, either in the entrance channel or the exit channel. The elements of the T-matrix are matrix elements of the effective interaction defined by this formfactor evaluated between wave functions of relative motion for the system.

The probability for transfer is given by Eq. 2.15,

$$P(\theta) = \left[\frac{1}{\hbar}\int_{-\infty}^{+\infty} f_t(r(t))dt\right]^2 \tag{5.6}$$

In the semiclassical model that we will employ, the transfer will be treated as a barrier penetration by the transferred particles in the heavy-ion collision. The projectile acts only as a potential well which can donate or accept nucleons, and which causes collective inelastic excitation of the deformed nucleus. Fig. 5.39 shows the projectile and target potential wells. Since the target potential well is deformed, it will also vary with orientation angle. In addition, since the relative separation

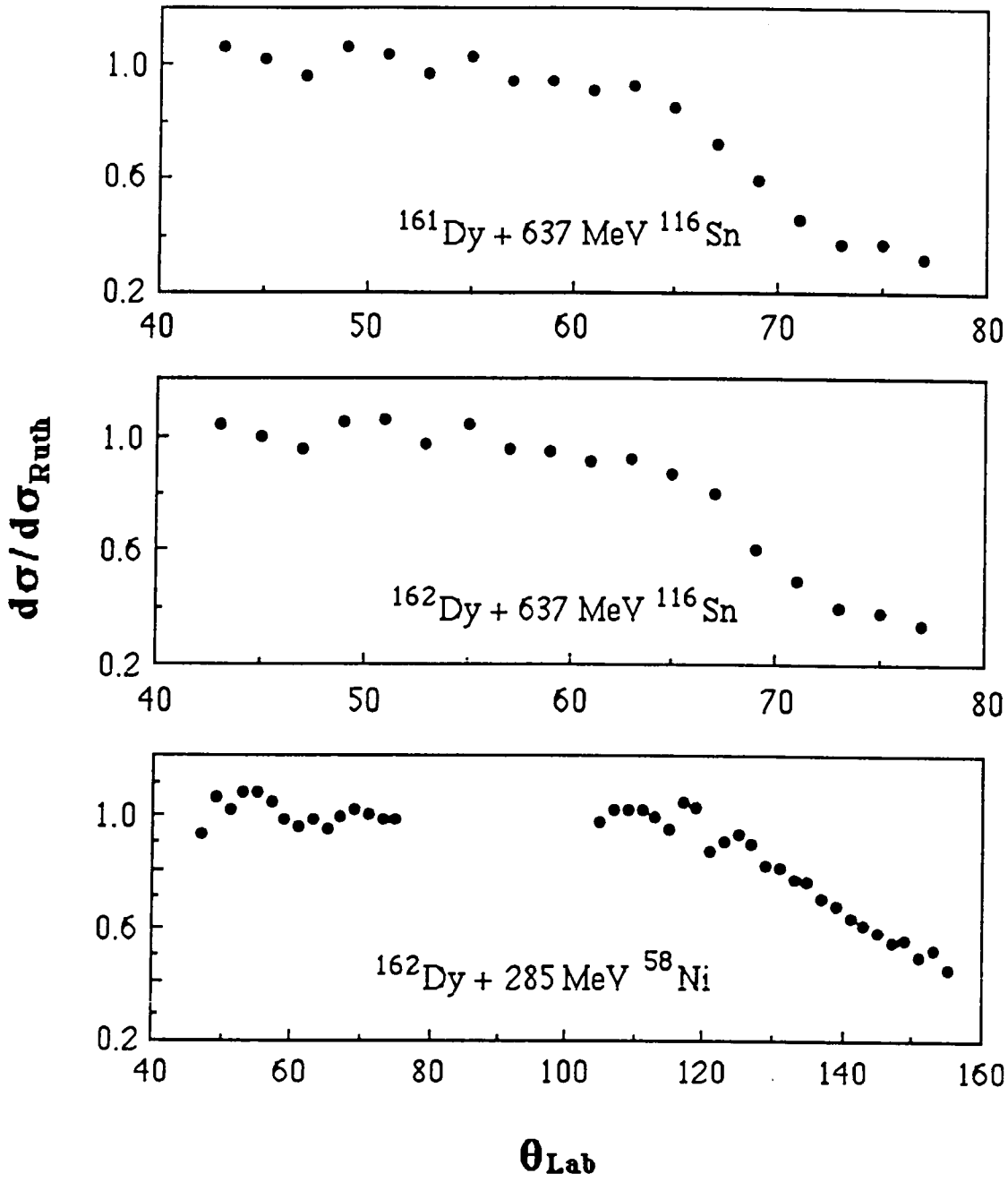


Figure 5.38: The quantity $d\sigma/d\sigma$ is the ratio of singles relative to the calculated Rutherford cross section.

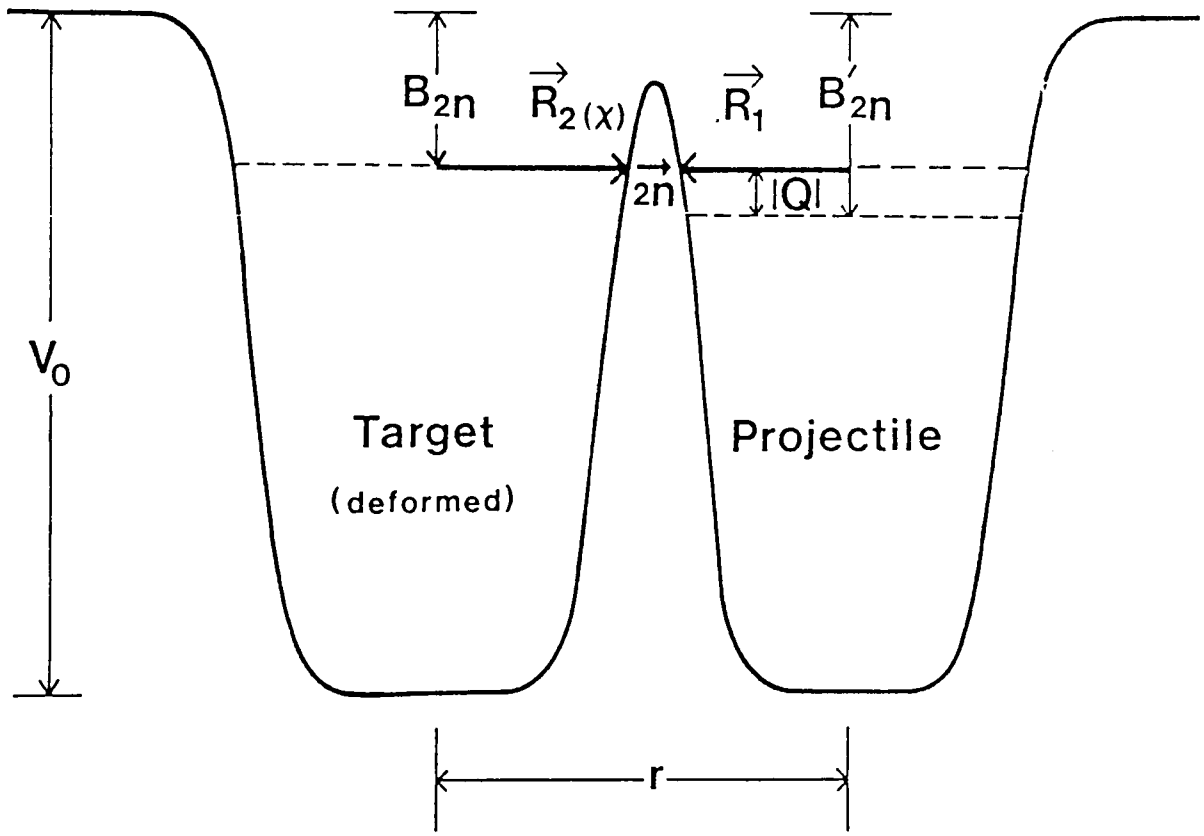


Figure 5.39: A schematic view of the projectile and target potential wells. In a pickup reaction the neutron bound by an energy E_B in the target tunnels from R_2 to R_1.

of the projectile and target varies with time, the effective barrier between the two potential wells will vary with time. Therefore Fig. 5.39 represents a schematic slice of the potential at a particular time on the trajectory, and the total tunneling amplitude involves an integration of such configurations over time. We assume that the nucleon tunnels between two levels with the same energy (binding energy E_B). In a WKB approximation the probability for the transmission through the barrier between two points x_1 and x_2 is given by

$$P = exp\left[\int_{x_1}^{x_2} \left(\frac{2\mu}{\hbar^2}(V(x) - E_B)\right)^{1/2} dx\right] \tag{5.7}$$

where μ is the reduced mass of the transferred particle. If we assume V(x) to be constant (=0), we obtain

$$P_1 \simeq exp(-2\alpha_1 D) \tag{5.8}$$

where $\alpha_1 = (2\mu\hbar^{-2} \mid E_B \mid)^{1/2}$, and D is the distance of closest approach. For sequential two-neutron transfer the probability is

$$P_2 \simeq P_1^2 \tag{5.9}$$

Therefore, in this simple picture we would expect that one and two-neutron transfer slope parameters are related by

$$\alpha_2 \simeq 2\alpha_1 \tag{5.10}$$

The same result is obtained if the 2 nutrons are transfer as a cluster: at this level of approximation the slope for two-neutron transfer does not depend on whether the neutrons are transferred simultaneously or sequentially.

In several recent publications the angular distributions of transfer reactions induced by very heavy ions have been used to examine the dependence of the formfactor on the separation between the colliding ions (Siekmann *et al.* 1982), (Von Oertzen *et al.* 1983, 1987), (Himmele *et al.* 1983), (Macchiavelli *et al.* 1985), (Sapotka *et al.* 1985). Assuming Rutherford trajectories to relate scattering angle to

distance of closest approach, it is found that for large separations the transfer cross sections fall exponentially in the ion-ion separation, while for smaller separations the cross sections begin to deviate from exponential behavior.

The picture outlined above is extremely simple, and it would not be surprising to find that it does not work. Nevertheless, it does work in many cases. For the data obtained with heavy ions on spherical targets the exponential falloff of the one and two-particle transfer probabilities at large distance in in accord with Eq. 5.10. (Siekmann *et al.* 1982), (Von Oertzen *et al.* 1983, 1987). However, for the data obtained with very heavy ions on heavy deformed target nuclei this is no longer true (Himmele *et al.* 1983), (Macchiavelli *et al.* 1985). For those cases the one-neutron transfer slopes indicate that E_B is comparable to ground-state separation energies, but the two-neutron transfer slopes are similar to those for the one-neutron transfer cases. In G. Himmele's (1983) and A. O. Macchiavelli's (1985) papers this was interpreted as meaning that two-neutron transfer in these reactions occurs predominantly though excited configurations (smaller binding energies than for the ground state). Assuming Eq. 5.8 to be applicable, it is estimated that the average excitation energy for the reactions studied in their papers is $\sim$ 10-15 MeV for two-neutron transfer, but no more than several MeV for one-neutron transfer.

In a series of experiments we have studied transfer reactions with very heavy ions in the Oak Ridge Spin Spectrometer. As mentioned in chapter 3, our measurements determine the total energy and multiplicity of γ-ray, and the neutron multiplicity. From these quantities the total exit-channel internal angular momentum and excitation energy can be estimated. In addition, the angular distributions of the scattered ions in the transfer reaction were measured. This information was used to address directly the question of the radial slope of the transfer formfactor and its relation to excitation energy and angular momentum of the heavy-ion system.

5.4.2 The Probability of One and Two-Neutron Transfer Reactions with Heavy-Ions on Spherical Target Nuclei

We studied the transfer reactions ^{117}Sn(^{112}Sn,^{113}Sn)^{116}Sn, and ^{118}Sn(^{112}Sn,^{114}Sn)^{116}Sn with a 570 MeV ^{112}Sn beam, which is $\sim$ 10% above the Coulomb barrier (519 MeV). The experimental probability for one and two-neutron transfer is shown in Fig. 5.40. This probability was calculated from the γ-ray yield for the $2^+ \rightarrow 0^+$ transition of ^{116}Sn according to equation 5.2. Our probability for one and two-neutron transfer reactions is about 30% of that in W. Von Oertzen's paper (1987). This discrepancy comes from the different measuring techniques. Our measurement represents transfer to states other than the ground state of the reaction product nucleus ^{116}Sn, while Von Oertzen's measurements include the ground state.

From Fig. 5.40 we find that for one-neutron transfer to ^{113}Sn there is a near perfect description of the data points by exponentials with a slope parameter α_1=0.616. These experimental values agree very well with the value $\alpha_{cal} = 0.635$ from calculations using equation 5.8. The two-neutron transfer reaction also gives the expected slope parameter (to within 10%). The information for the experimental and calculated slope parameters is summarized in Table 5.2.

Table 5.2: Decay constants and binding energies for the transferred particles in one and two-neutron transfer reactions.

reaction	E_B (MeV)	α_{cal}	α_{exp}
^{117}Sn(^{112}Sn,^{113}Sn)^{116}Sn	7.74	0.609	0.616
^{118}Sn(^{112}Sn,^{114}Sn)^{116}Sn	18.06	1.308	1.133

Generally, the probabilities for one and two-neutron transfer reactions with heavy-ions on spherical targets fall exponentially at large distance, and the slope for two-neutron transfer reactions is twice that of one-neutron transfer reactions, in acccordance with Eq. 5.10.

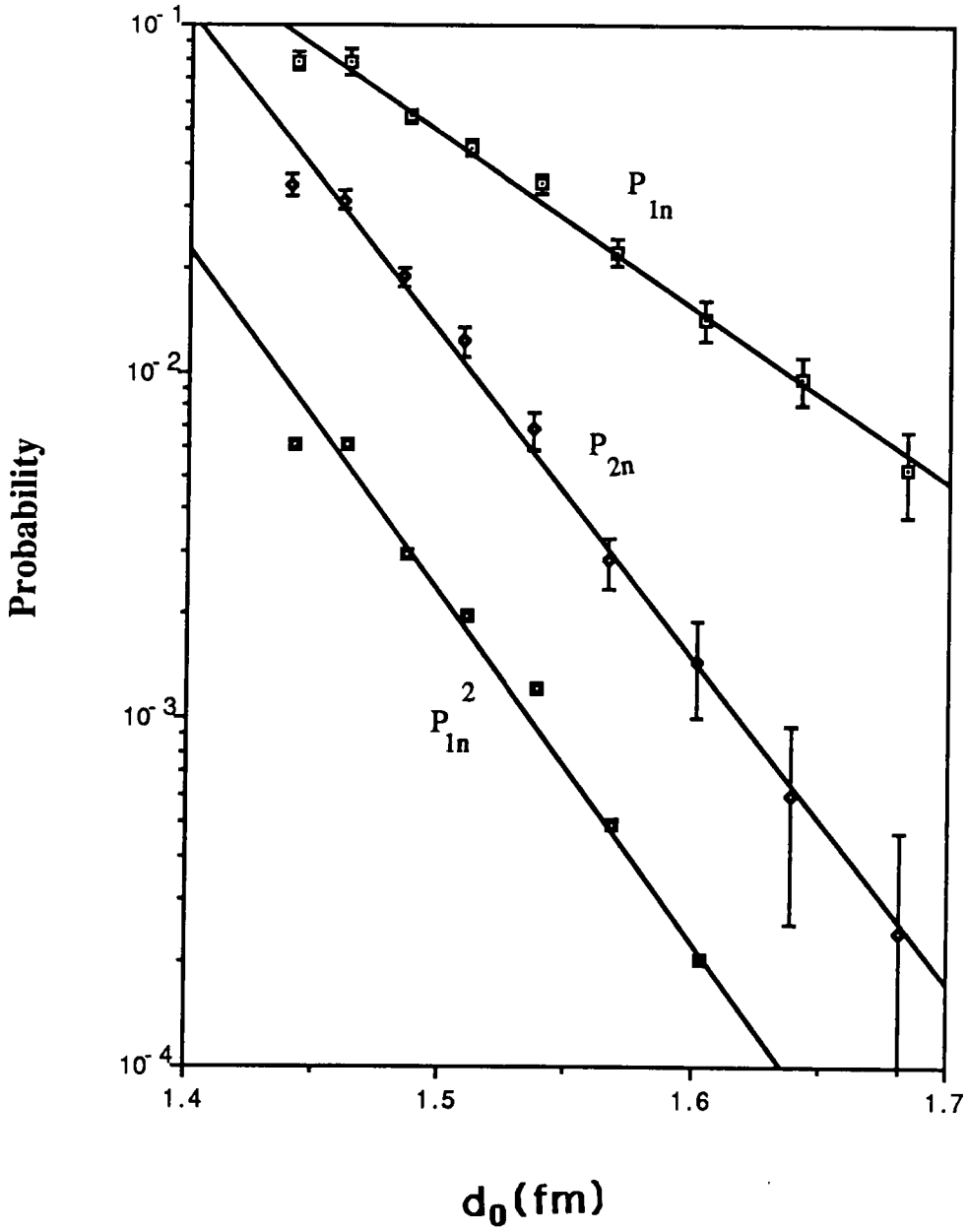


Figure 5.40: The measured transfer probabilities as a function of the separation parameter (equation 2.9) for one-neutron transfer in the reaction ^{117}Sn(^{112}Sn, ^{113}Sn)^{116}Sn, and for two-neutron transfer in the reaction ^{118}Sn(^{112}Sn, ^{114}Sn)^{116}Sn.

5.4.3 The Probabilities of One and Two-Neutron Transfer Reactions with Heavy-Ions on Deformed Nuclei Targets

In order to minimize systematic uncertainties we have studied pairs of reactions using Ni and Sn projectiles on deformed targets for which one and two-neutron pickup populated the same final deformed nucleus. The reactions studied used a 637 MeV ^{116}Sn beam on the targets ^{161}Dy and ^{162}Dy, and a 345 MeV ^{58}Ni beam on the same targets.

The angular distributions of the scattered particles taken in coincidence with the strong transfer γ-ray transitions in the Ge detectors were used to establish the transfer probability for one and two-neutron transfer according to Eq. 5.2. Assuming Rutherford trajectories, probabilities for the $4^+ \rightarrow 2^+$ ground-band transitions of the deformed product nucleus ^{160}Dy are plotted as a function of radial separation in Figs. 5.41 and 5.42. In each case the data have been corrected for inelastic excitation which comes from target contamination. The percentage contamination was determined from the Ge spectra at forward angles where only Coulomb excitation is important, and from isotopic analysis of the target material.

The data shown in Fig. 5.41 are gated on neutron multiplicity $K_N = 0$. The resolution in K_N has been determined from the forward-angle Coulomb excitation spectrum (which should correspond to $K_N = 0$), and we estimate upper limits of 10% on the events in the Fig. 5.41 which could involve the emission of a neutron. This largely excludes from the two-neutron transfer data set any events involving one-neutron transfer followed by evaporation of a neutron.

In Figs. 5.41 and 5.42 the data show an exponential decrease at large distance. The solid lines are exponential fits; dashed and dotted lines are calculated from Eq. 5.8 for one and two-neutron transfer respectively, using average experimental ground-state separation energies. The slope parameters 2α are listed in Table 5.3. In general, we see that slopes for one-neutron transfer are similar to

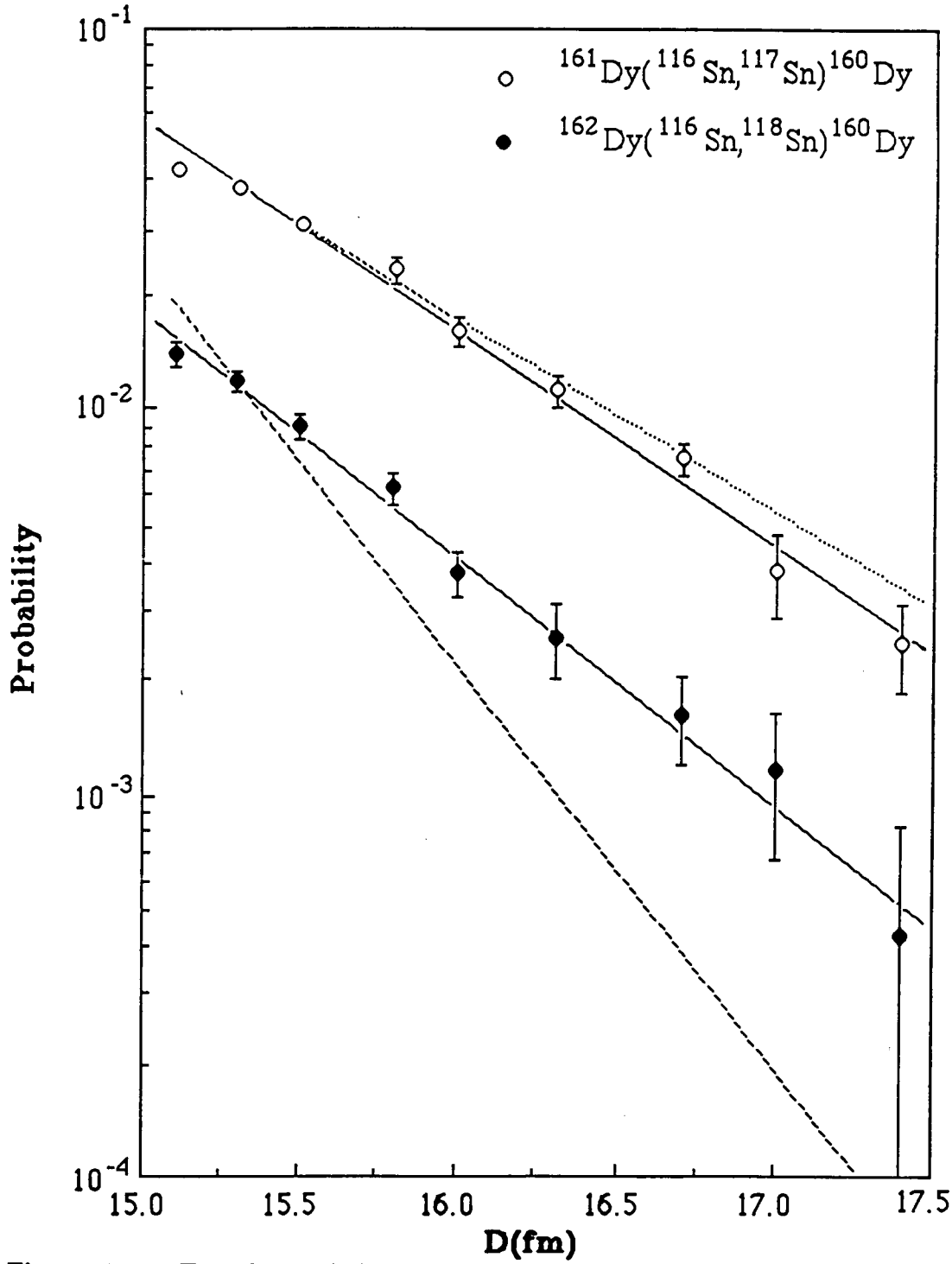


Figure 5.41: Transfer probability versus distance of closest approach assuming Rutherford trajectories. Probabilities are for the $4^+ \rightarrow 2^+$ ground-band transitions of the deformed product nucleus, and are gated on neutron multiplicity zero. Solid lines are exponential fits. dashed and dotted lines are calculated from Eq. 5.8 with experimental binding energies.

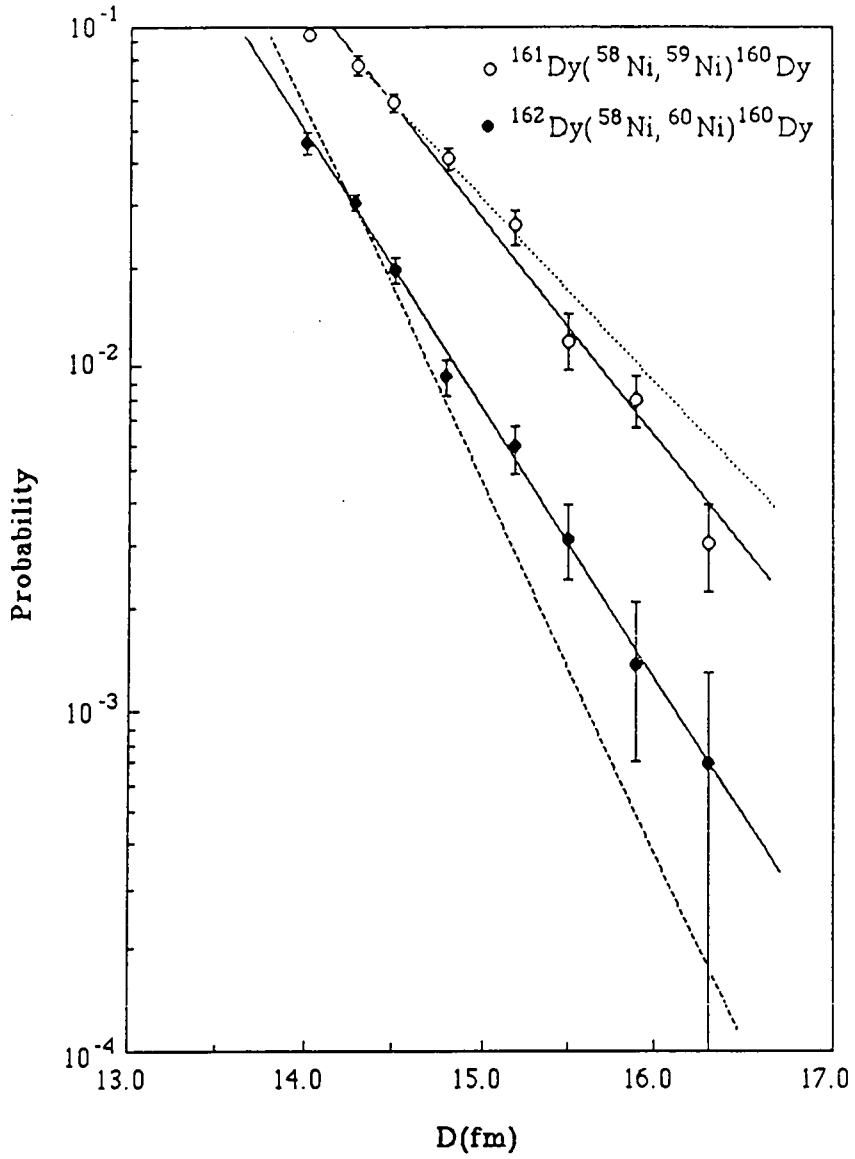


Figure 5.42: Transfer probability versus distance of closest approach assuming Rutherford trajectories. Probabilities are for the $4^+ \rightarrow 2^+$ ground-band transitions of the deformed product nucleus, and are gated on neutron multiplicity zero. Solid lines are exponential fits. dashed and dotted lines are calculated from Eq. 5.8 with experimental binding energies.

the calculated values, but the ones for two-neutron transfer are much smaller than expected, usually comparable to those for one-neutron transfer. These results are in general agreement with those found in Himmele (1983) and Macchiavelli (1985) using Xe and W projectiles.

Table 5.3: Values for the slope parameter 2α (the typical uncertainty in α is 10-20%). Gate 1 is E = 0 - 0.9 Mev, M = 0 - 3; Gate 2 is E = 0.7 - 4.7 Mev; M = 3 - 7. Gate 3 is E > 3.3 MeV, M = 7 - 15.

reaction	Gate 1	Gate 2	Gate 3	Total	Calculated
^{161}Dy(^{58}Ni,^{59}Ni)^{160}Dy	0.88	1.33	1.42	1.40	1.22
^{161}Dy(^{116}Sn,^{117}Sn)^{160}Dy	0.92	1.11	1.45	1.24	1.14
^{162}Dy(^{58}Ni,^{60}Ni)^{160}Dy	0.61	1.02	1.50	1.22	2.60
^{162}Dy(^{116}Sn,^{118}Sn)^{160}Dy	0.87	1.09	1.96	1.26	2.42

In Fig. 5.43 the total γ-ray energy (E) and multiplicity (M) for one and two-neutron transfer reactions are shown. As for Fig. 5.41, these data are gated on neutron multiplicity $K_N = 0$. The procedures for converting the γ-ray pulse height (H) and fold (K) to (E, M) are the same as those discussed in chapter 3, except that the conversion has been done in an approximate fashion for the ^{58}Ni experiment due to poor statistics (which makes the standard computer algorithm unstable). An approximate yrast line corresponding to no excitation of the spherical projectiles is shown. Since the data involve little neutron emission, Fig. 5.43 indicates that both one and two-neutron transfer in these reactions involve a remarkably cold mechanism. For the Ni data the two-neutron transfer population extends to somewhat higher energy and multiplicity than in the one-neutron case; this is probably a Q-window effect. For Sn data there is no evidence that the two-neutron transfer is populating more excited configurations relative to the yrast line than for one-neutron transfer.

Although the reactions studied in the Himmele (1983) and Macchiavelli

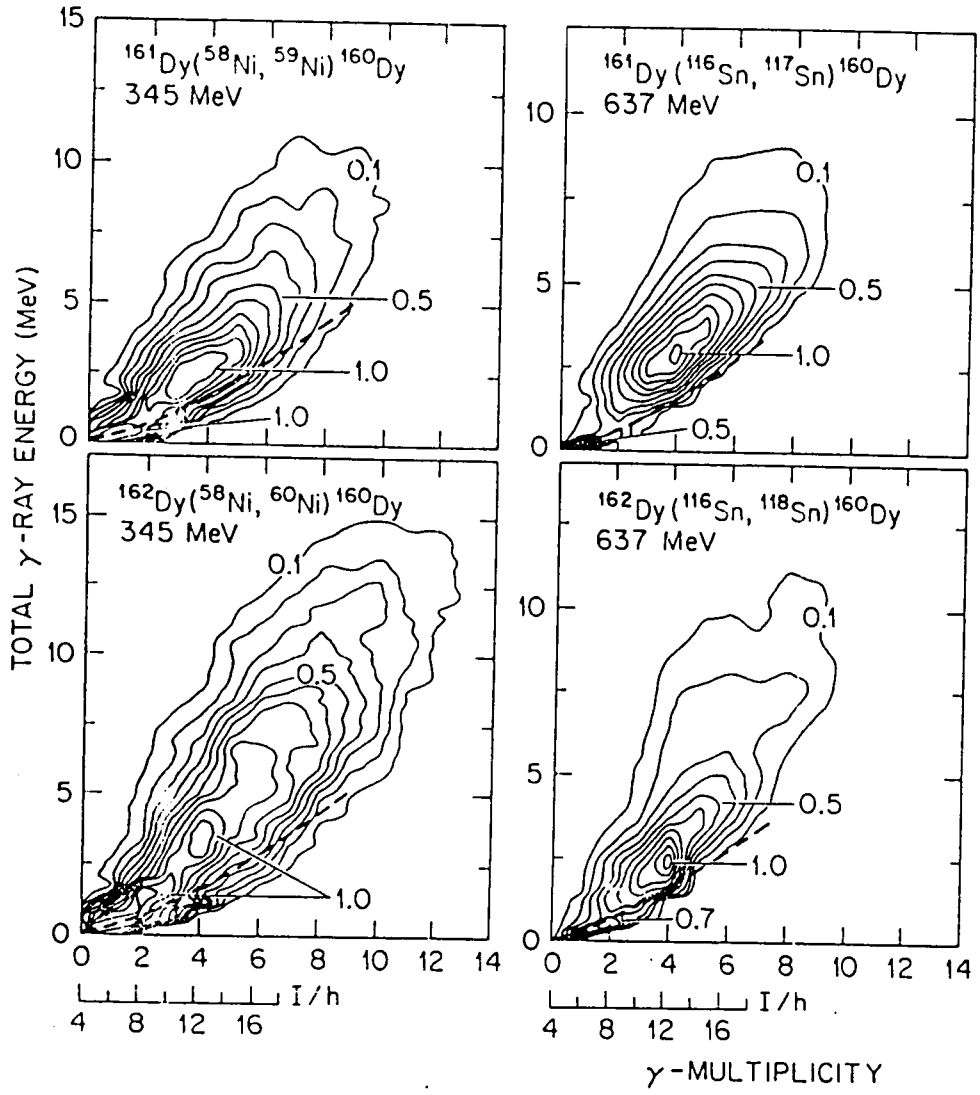


Figure 5.43: Total γ-ray energy versus γ-ray multiplicity for the reaction shown in Fig 5.41. The data are gated on neutron multiplicity zero. The dashed line is an approximate system yrast line assuming no projectile excitation.

(1985) papers involve different nuclei, their similarity to our Sn case casts doubt on any general interpretation of the decreased two-neutron slopes as due to excitation of high-lying final states in the transfer. If such states play a role in these data they must contribute as virtual intermediate states. The slope anomaly has been found for neutron pickup with deformed nuclei, but not with spherical nuclei (see previous section). However, the deformation is not likely to be responsible for the reduced two-neutron transfer slope in any simple fashion since it seems to have little effect on the one-neutron transfer slope.

By gating in the total energy-multiplicity (E, M) plane the slope can be studied as a function of average excitation energy and angular momentum of the transfer products. Fig. 5.44 displays such an analysis. The curves are arbitrarily displaced with respect to each other for plotting convenience, since only the slope is relevant for the present discussion; the values of the slope parameters are listed in Table 5.3. We see that increasing E and M generally increases the slope, for both one and two-neutron transfers. For two-neutron transfer this effect is quite dramatic, and the slope for the highest values of E and M approaches the expected results $\alpha_{2n} \simeq 2\alpha_{1n}$.

In Figs. 5.45 - 5.48 we show the probabilities for one and two-neutron transfer reactions populating the ground band and two-quasiparticle bands in the ^{116}Sn and ^{58}Ni experiments. The solid circles are the ratio of single events relative to the Rutherford cross section. In the region where these curves drop below unity our definition of probability is no longer valid, because the particle deviates from the Rutherford trajectory. Our analysis will be confined to the region where $d\sigma/d\sigma_R \sim 1$.

From Figs. 5.45 - 5.48 we see that the probability for transfer to two-quasiparticle bands falls exponentially with radial distance at large separation in all cases, and the experimental slope parameters approach the expected values. How-

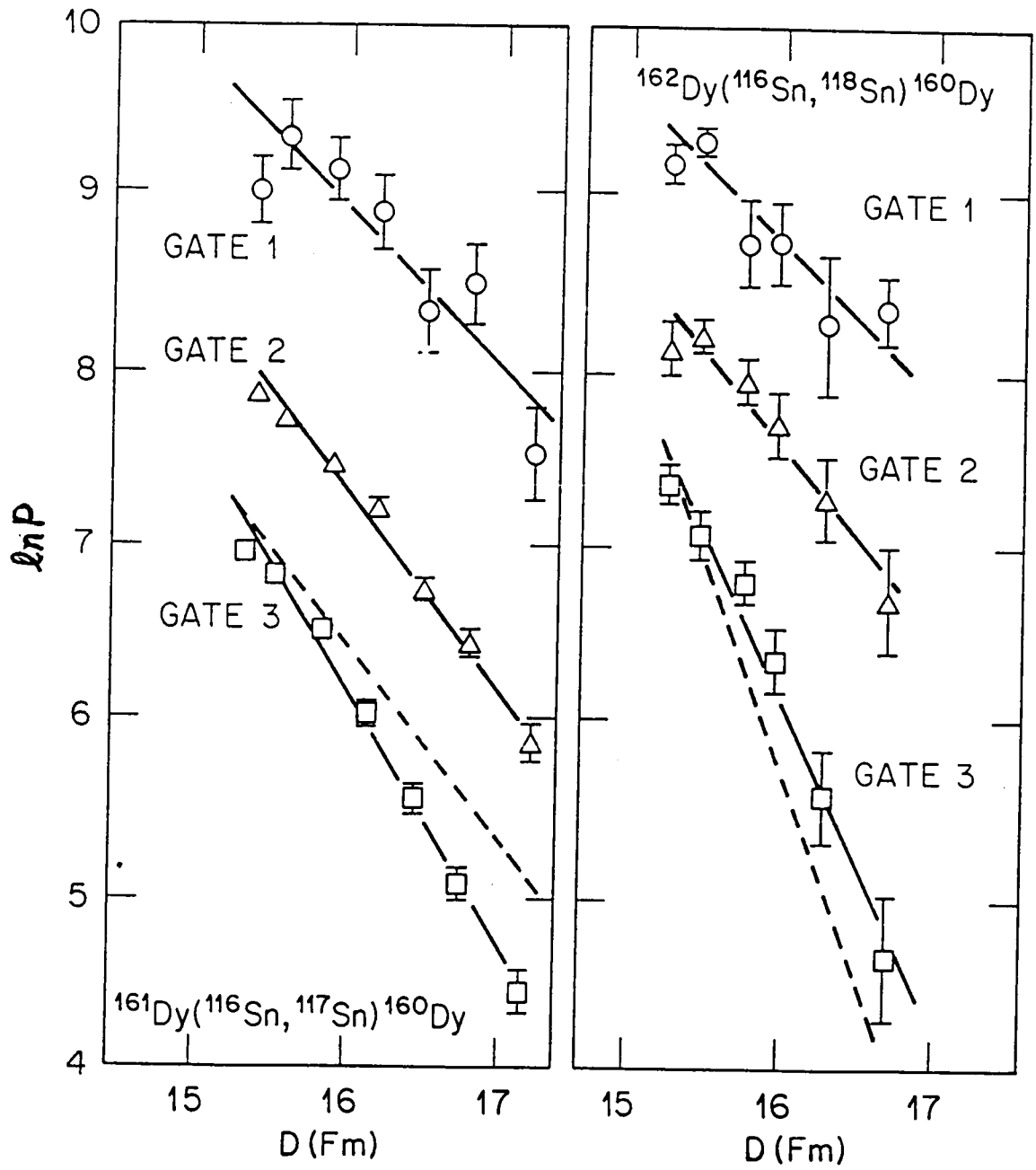


Figure 5.44: Transfer probability versus distance of closest approach assuming Rutherford trajectories with total energy and multiplicity (E,M) gates set. The three sets of data points correspond in descending order to gates 1, 2, 3 of Table 5.3. The dashed line defines the slope expected from Eq. 5.7-5.10.

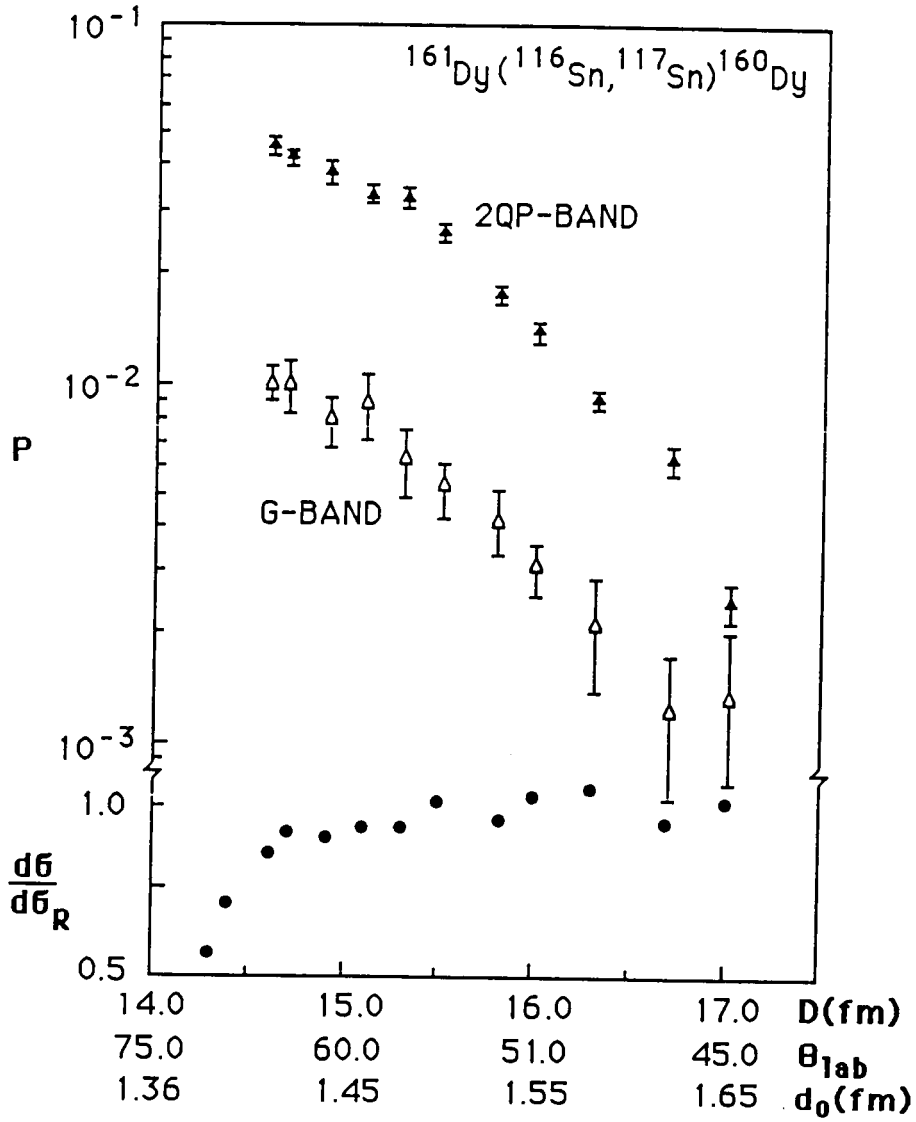


Figure 5.45: One-neutron transfer probability for ground-band and two-quasiparticle band population versus distance of closest approach in reaction, assuming Rutherford trajectories. Probabilities are for the $4^+ \rightarrow 2^+$ ground-band transitions of the deformed product nucleus ^{160}Dy and are gated on neutron multiplicity zero.

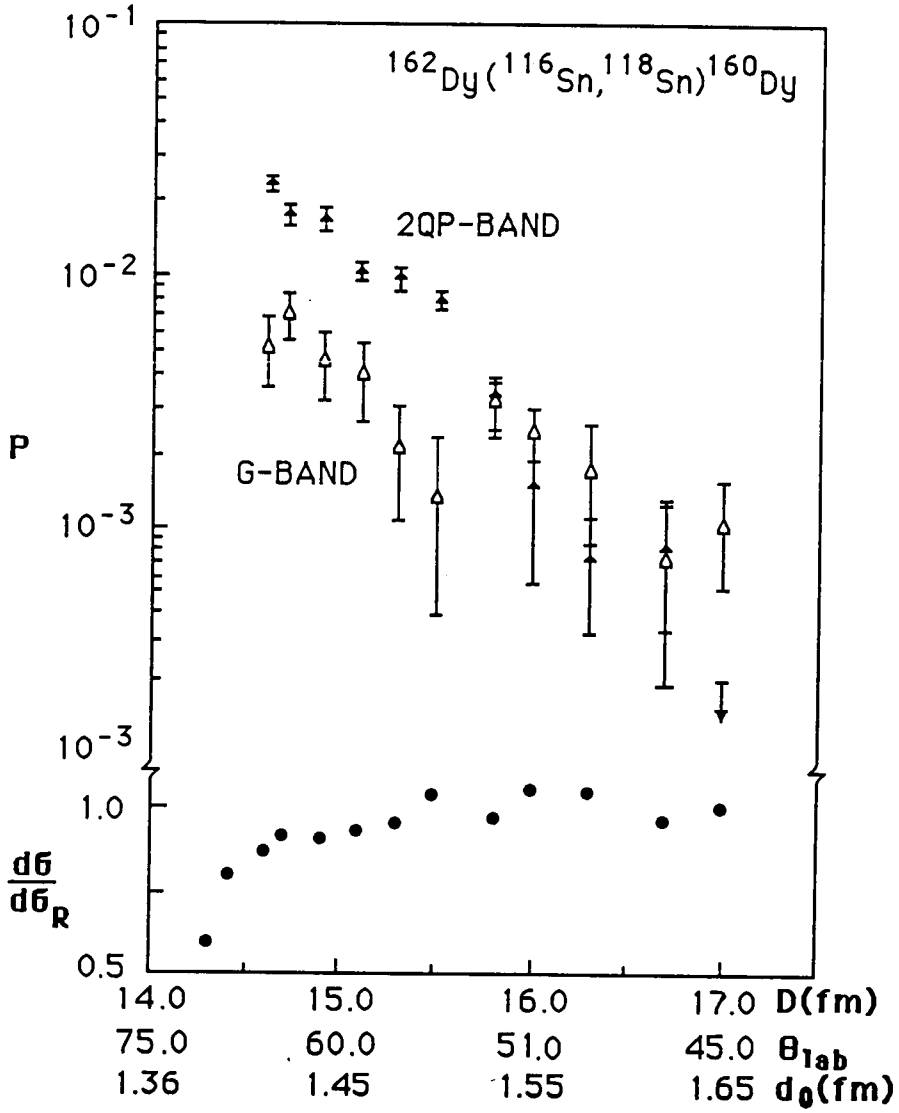


Figure 5.46: Two-neutron transfer probability for ground-band and two-quasiparticle band population versus distance of closest approach in the reaction, assuming Rutherford trajectories. Probabilities are for the $4^+ \rightarrow 2^+$ ground-band transitions of the deformed product nucleus ^{160}Dy, and are gated on neutron multiplicity zero.

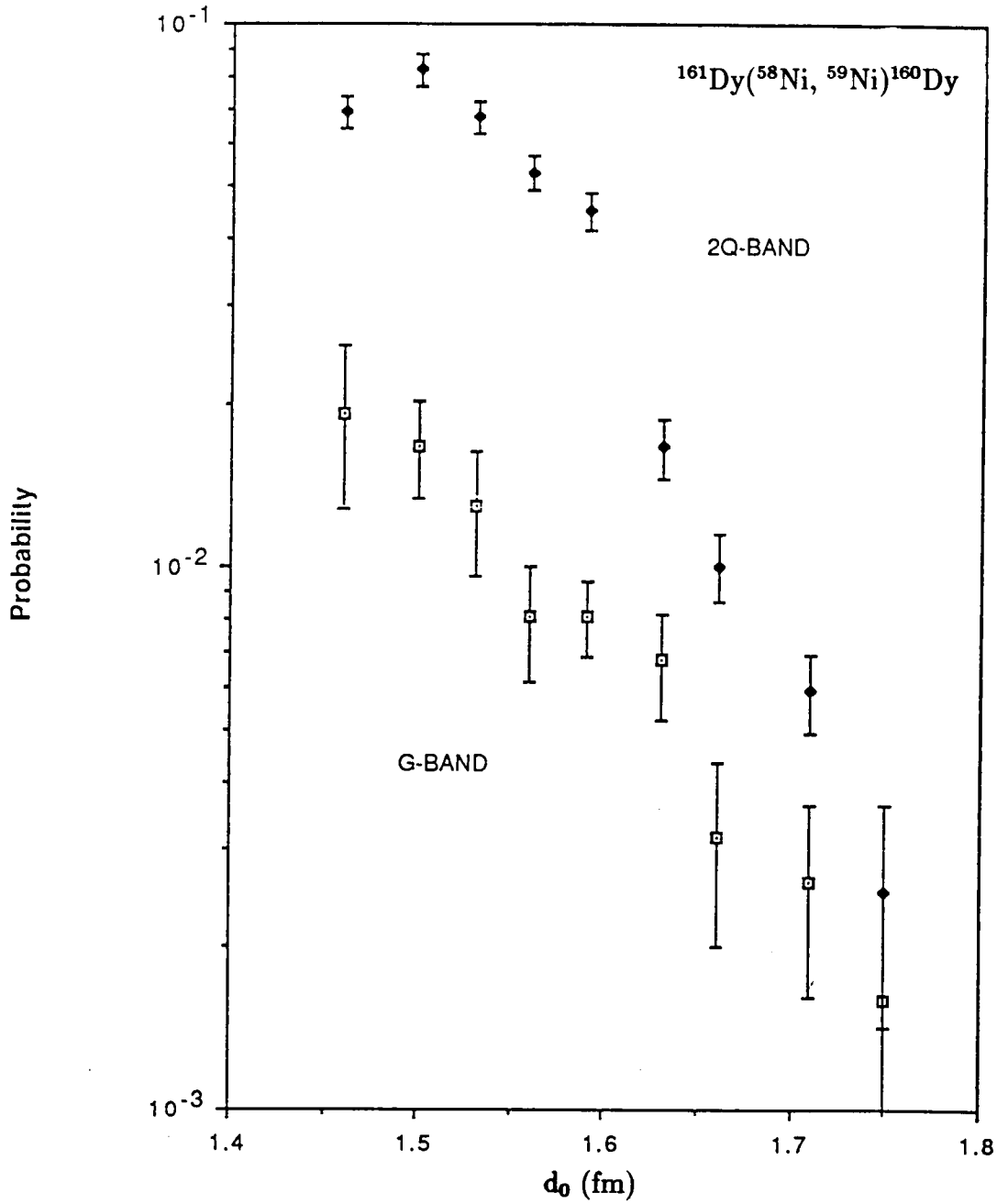


Figure 5.47: One-neutron transfer probability for ground-band and two-quasiparticle band population versus distance of closest approach in the reaction, assuming Rutherford trajectories. Probabilities are for the $4^+ \rightarrow 2^+$ ground-band transitions of the deformed product nucleus ^{160}Dy, and are gated on neutron multiplicity zero.

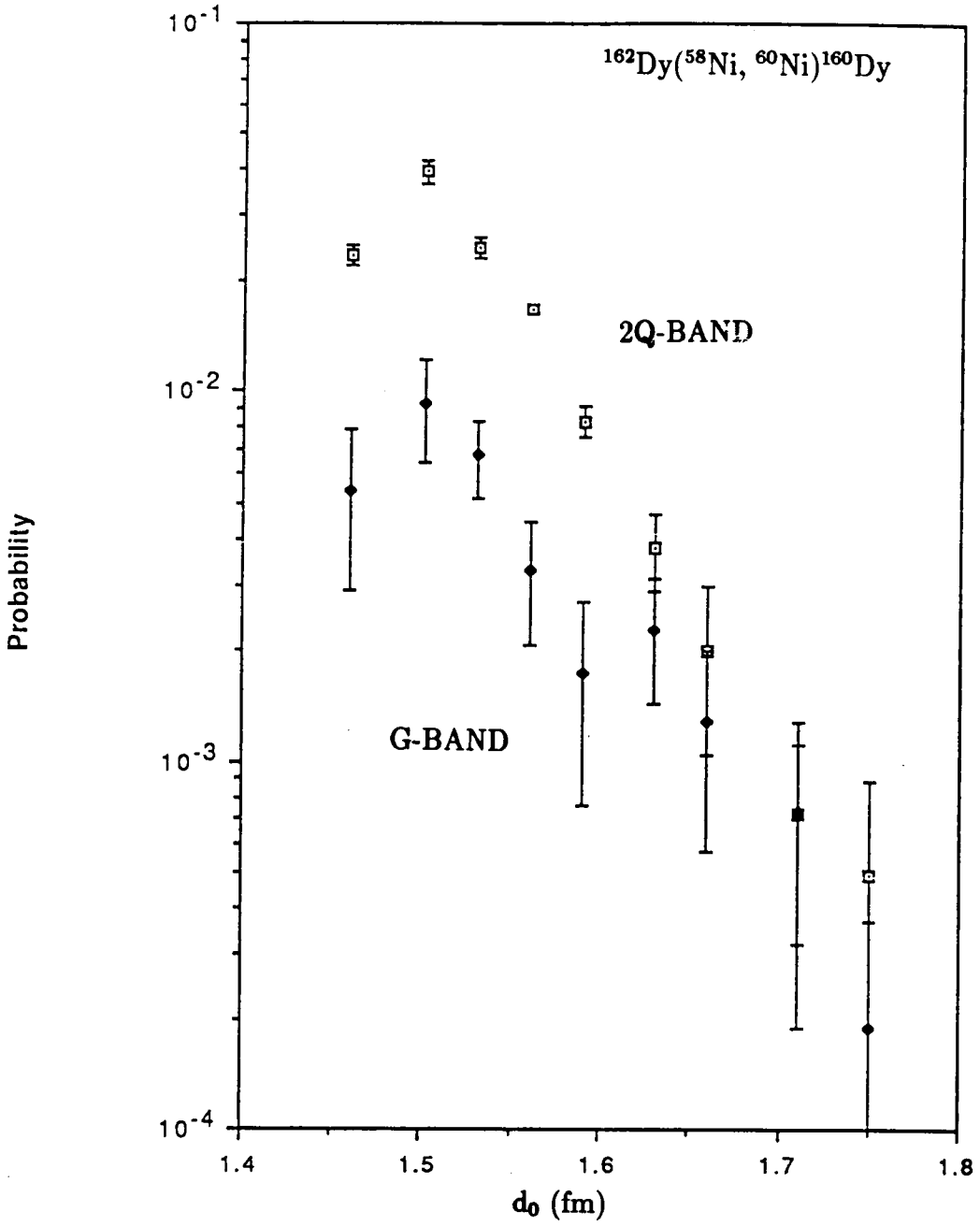


Figure 5.48: Two-neutron transfer probability for ground-band and two-quasiparticle band population versus distance of closest approach in the reaction, assuming Rutherford trajectories. Probabilities are for the $4^+ \rightarrow 2^+$ ground-band transitions of the deformed product nucleus ^{160}Dy, and are gated on neutron multiplicity zero.

ever, the probability for two-neutron transfer to the ground band is more complicated: it appears to oscillate, and the envelope of the oscillation decays slowly with distance. At distances < 15.5 fm, corresponding to grazing collisions the probability for ground band transfer is much smaller than the probability for two-quasiparticle band transfer, but at $D > 15.5$ fm the probability for the ground band is larger than that for the two-quasiparticle band.

Therefore, we have demonstrated that in neutron pickup reactions with very heavy ions scattering from deformed nuclei the probability for two-neutron transfer is anomalously large at large ion-ion separation relative to that at smaller separation, and that this can't be explained by intrinsic particle excitation in the transfer process. Rather, the slope anomaly comes from a superposition of two components of the transfer population. The first component dominates the transfer cross section near the grazing angle and it is associated with population of two-quasiparticle bands. The radial dependence of the probability for this component is in reasonably good agreement with Eqs. 5.8 and 5.10.

The second component is associated with transfer to the ground-state rotational band. It is a smaller component of the transfer cross section at the grazing angle, but it accounts for about half the total two-neutron transfer cross section at large distance. This component oscillates, and the envelope of the oscillation has a slope in severe disagrement with Eqs. 5.8 and 5.10. The cause of this oscillation has been discussed in section 5.3.2: it appears to be an interference between different orientations of the deformed nucleus in the transfer reactions.

5.5 Pairing Effects in Transfer Reactions with Very Heavy Ions

5.5.1 Introduction

The present understanding of many of the features of reaction mechanisms and nuclear structure is based on a picture of individual nucleons moving in the average nuclear potential. Two approaches are frequently employed to generate the single-particle spectra of deformed as well as spherical nuclei: the Nilsson and Woods-Saxon average field potentials. In addition to the average nuclear potential which determines the properties of the nucleon single-particle orbitals, a residual two-body interaction among the nucleons must be added in order to account for many specific properties of nuclei. One of the most important components in the two-body force is the short-range attractive pairing force (pairing correlation). Experimental evidence for the existence of the pairing correlation includes the following observations:

1. The ground state spins of all even-even nuclei are zero.

2. There are systematically smaller binding energies for odd-mass nuclei compared with the corresponding even-even nuclei, which cause odd-even mass differences.

3. There is a dramatic reduction of the number of levels in the low energy spectra of even nuclei (energy gap), as compared with the number possible from the available shell-model configurations.

4. The rotational moment of inertia of quadrupole deformed nuclei is small compared with the rigid rotor value.

In solid-state physics a pairing interaction was introduced to explain the effect of superconductivity (Bardeen *et al.* 1957). Bohr *et al.* (1958) suggested that there may exist an analogy between superfluid systems and finite nuclear systems. Since that suggestion, the pairing correlation has had remarkable success in nuclear effective interaction theory. In 1962 Josephson predicted a current of Cooper pairs between two weakly coupled superconductors due to the phase coherence of the superconducting ground state. This current is driven by the relative phase of the two superconductors rather than by a finite voltage. As many heavy nuclei exhibit properties similar to superconductivity, the pairing interaction is expected to introduce a very strong enhancement for transfer of pairs between ground states of the two nuclei.

In (t,p) or (p,t) reactions on superfluid nuclei the two-neutron transfer cross sections are enhanced by factors of $\sim$ 50 over that expected for independent particle motion, and the enhancement is ascribed to coherent pairing effects (Broglia *et al.* 1973). In the collision of two superfluid heavy ions it is expected that the enhancement could be considerably larger due to the strong pairing correlation in both interacting nuclei (Broglia *et al.* 1978). Various experiments have attempted to study two-particle transfer in the collision of two heavy nuclei (Von Oertzen *et al.* 1983,1987), (Macchiavelli *et al.* 1985), (Siekmann *et al.* 1982), (Himmele *et al.* 1983), (Dünnweber *et al.* 1981). They typically have concluded that the enhancement factors for these collisions are comparable to that for (t,p) or (p,t) reactions.

These experiments had low energy resolution and thus there was little information as to which states were being populated in the reactions. Here we report on the first measurement of enhancement factors for the heavy ions with sufficient resolution to distinguish transfer to the ground state band from transfer to other bands. As we will see, this resolution is crucial and our results will be seen

to cast serious doubt on all previous measurements which were unable to make this separation.

5.5.2 Two-Neutron Pairing Enhancement Factors

An enhancement factor for two-neutron transfer can be defined in the case of semiclassical conditions, because we have a direct measure of the one and two-neutron transfer probabilities defined in Eq. 5.2, as shown for several cases in Figs. 5.45 - 5.48. The enhancement factor F is defined as

$$F = \frac{P_{2n}}{P_{1n}^2} \tag{5.11}$$

where the one and two-neutron transfer probabilities are denoted by P_{1n} and P_{2n} respectively. This definition ignores possible differences in the ground state Q-value and the number of states involved, but it should be some measure of how strong two-neutron transfer is relative to that expected from sequential transfer of two uncorrelated neutrons.

Using the one and two-neutron transfer probabilities in Figs. 5.45 - 5.48 we calculated enhancement factors as a function of separation distance. These are shown in Figs. 5.49 and 5.50 for ^{116}Sn and ^{58}Ni experiments respectively. At distances between 14 and 16 fm the enhancement factors are approximately constant and F $\simeq$ 7-10. At distances larger than 16 fm the enhancement increases to around 70. Our measured total enhancement factors F $\simeq$ 7 - 70 are comparable to those found in previous experiments which had insufficient energy resolution to distinguish the ground-band transfer (Von Oertzen *et al.* 1883,1987), (Macchiavelli *et al.* 1985), (Siekmann *et al.* 1982), (Himmele *et al.* 1983), (Dünnweber *et al.* 1981). However, these enhancement factors are averages over reactions populating low-lying and higher-lying bands. We now use the Spin Spectrometer information to determine enhancement factors for these two separate components of the populations.

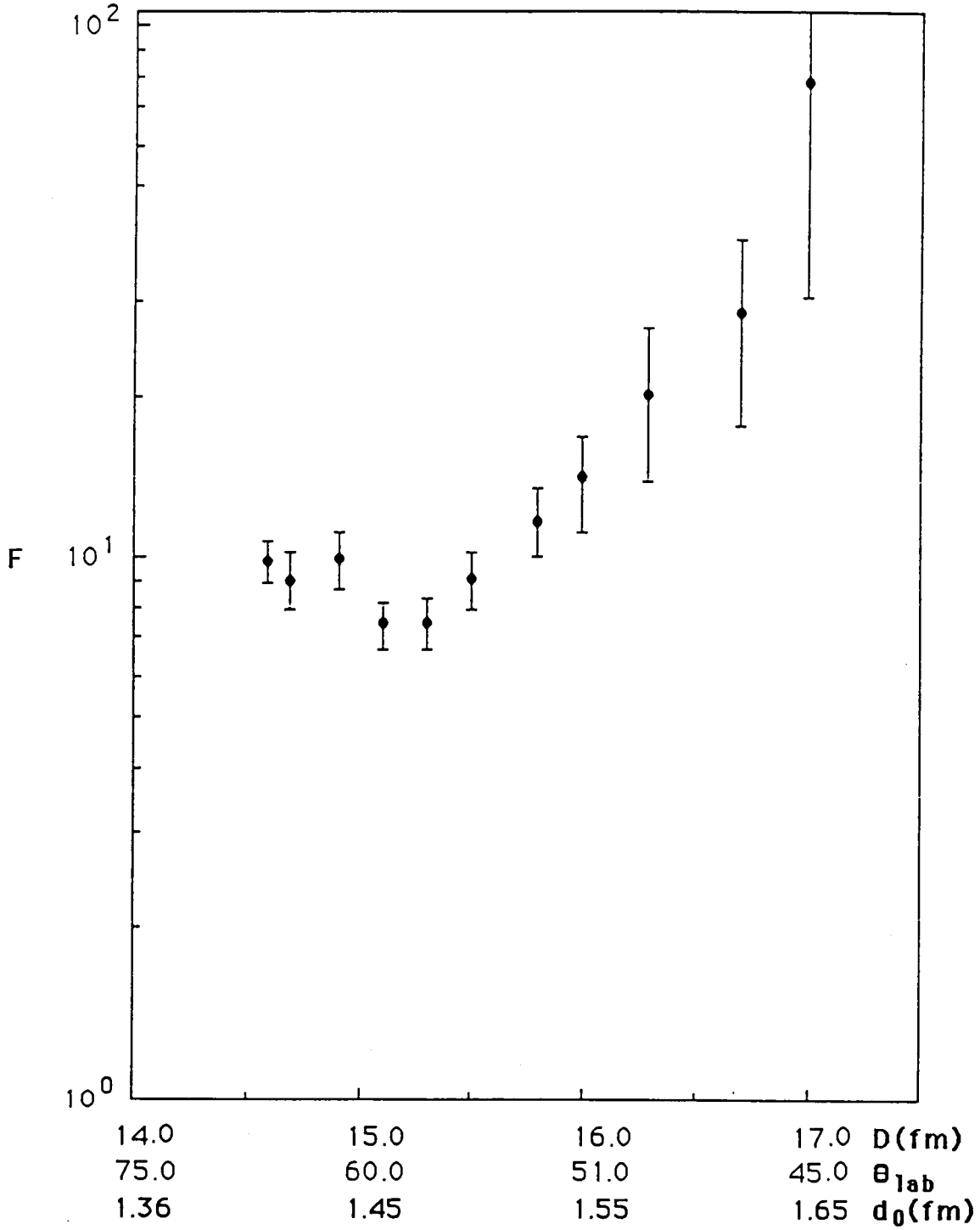


Figure 5.49: The total enhancement factors as a function of separation distance for the reactions ^{161}Dy(^{116}Sn,^{117}Sn)^{160}Dy, and ^{162}Dy(^{116}Sn,^{118}Sn)^{160}Dy.

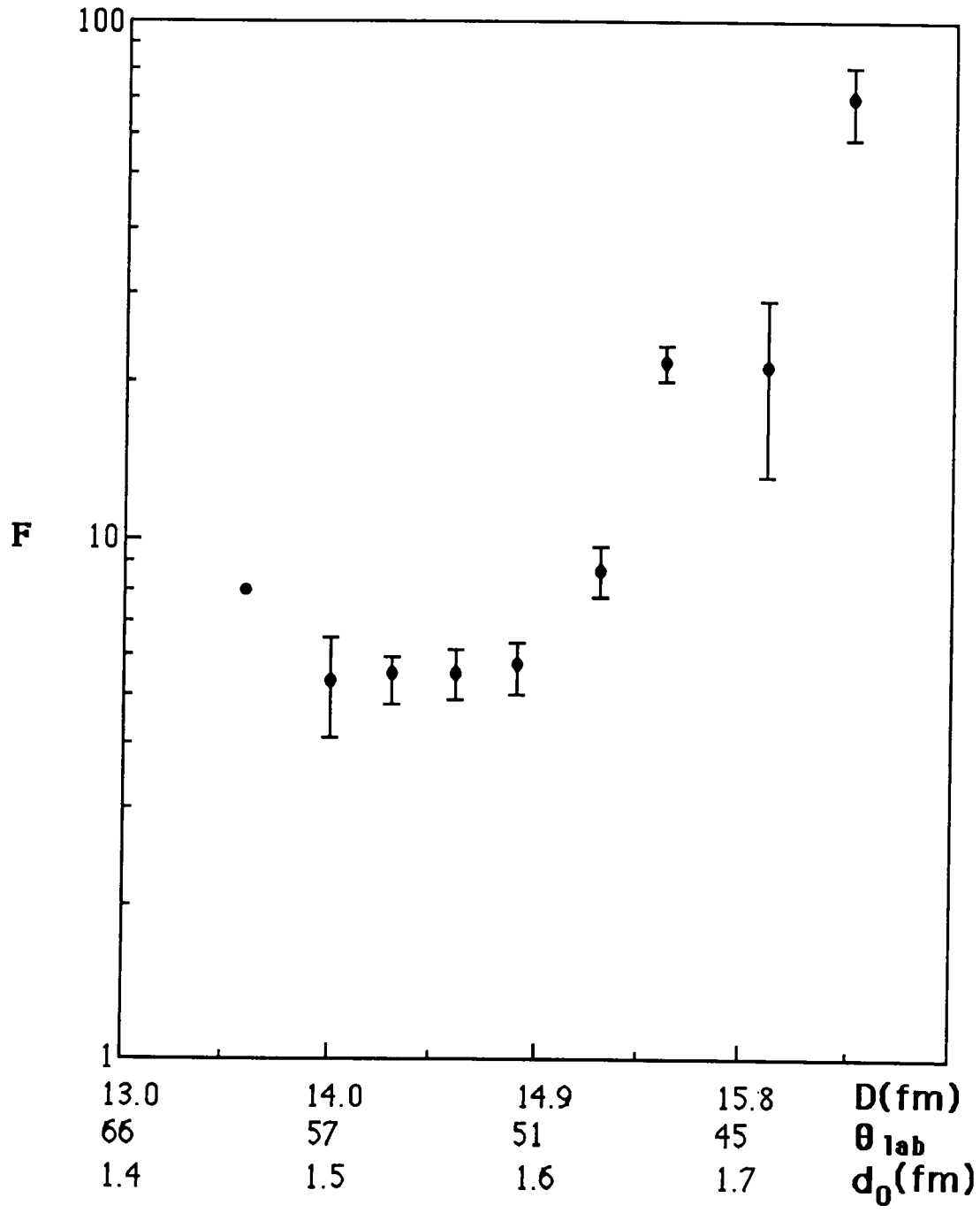


Figure 5.50: The total enhancement factors as function of separation distance for the reactions ^{161}Dy(^{58}Ni,^{59}Ni)^{160}Dy, and ^{162}Dy(^{58}Ni,^{60}Ni)^{160}Dy.

The enhancements of separated ground band and two-quasiparticle band populations are shown in Figs. 5.51 and 5.52 for ^{116}Sn and ^{58}Ni experiments respectively. We find two components in this population, with very different enhancement factors. The bulk of the reaction, > 80%, populates two-quasiparticle bands with F $\simeq$ 8 - 12 for the ^{116}Sn experiment and F $\simeq$ 6 - 11 for the ^{58}Ni experiment. However, the transfer to the ground band is found to have enhancement factors F $\simeq$ 70-500 for the ^{116}Snexperiment and F $\simeq$ 30-100 for the ^{58}Ni experiment, suggesting very large pairing effects in the transfer to the ground state band of ^{160}Dy.

At distances larger than 16 fm the enhancement for ground band transfer increases dramatically in Figs. 5.51 - 5.52. If pairing is predominantly a surface effect, it is reasonable that the enhancements would increase at large ion-ion separation.

The dramatic difference between the ground-band and two-quasiparticle band enhancements calls into question any discussion of pairing effects based on heavy-ion reactions which fail to resolve the ground band from other bands–a category which includes all previous attempts to measure the enhancement factors. These results are the first clear experimental evidence of strong pair-field enhancements in heavy ion reactions; they suggest that the collision of two heavy nuclei with structures far from closed shells may be reasonably approximated as the collision of two superfluid pieces of matter, if attention is focussed on transitions to low-lying states.

The Sn projectile is expected to have stronger pairing correlation than the Ni projectile, so the ground-band enhancement for the Sn experiment should be larger than that of the Ni experiment. For comparison we replot in Fig. 5.53 the enhancement factors as a function of surface distance, D_{ss}, between projectile and target nuclei with

$$D_{ss} = D - 1.25(A_1^{1/3} + A_2^{1/3}) \tag{5.12}$$

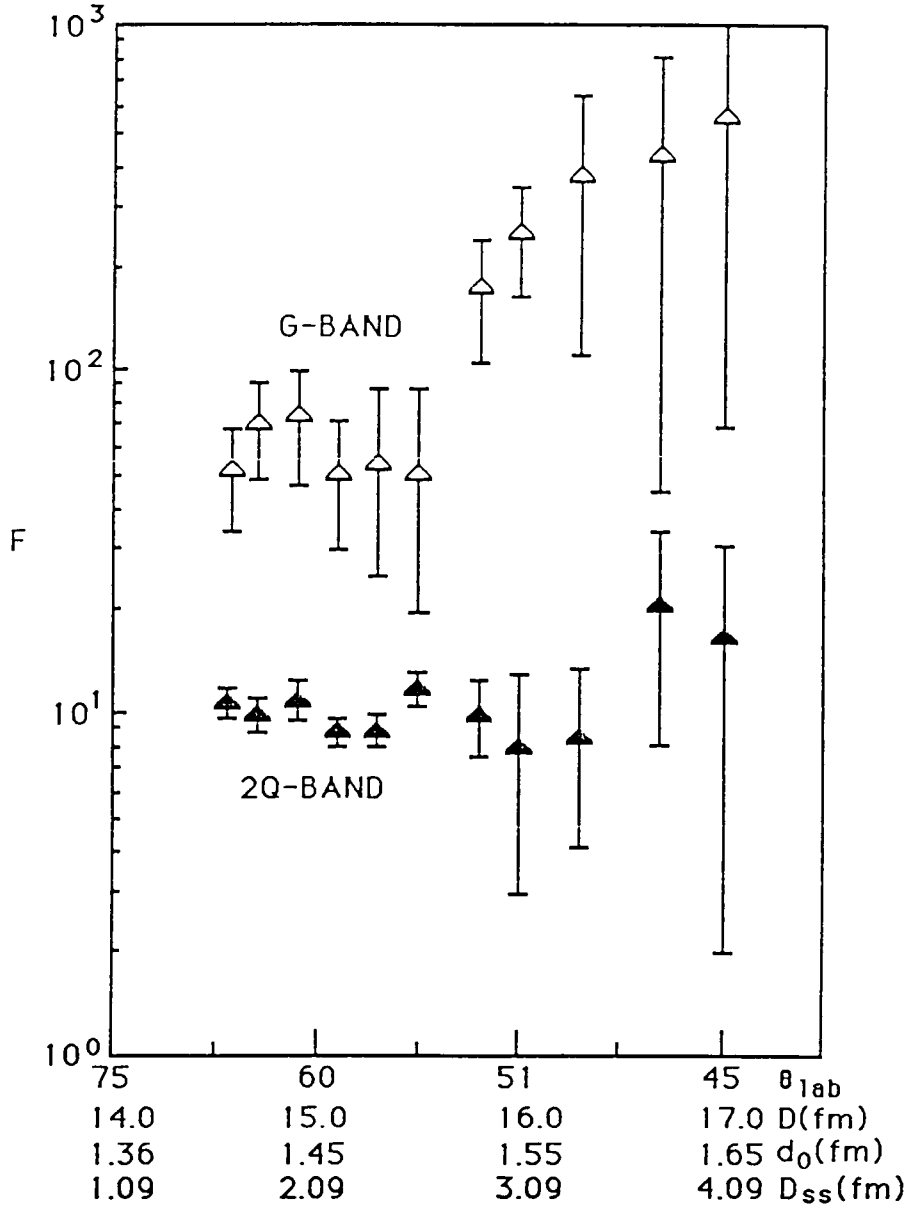


Figure 5.51: Enhancement factors for the ground band population and two-quasiparticle band population as a function of separation distance for the reactions ^{161}Dy(^{116}Sn,^{117}Sn)^{160}Dy and ^{162}Dy(^{116}Sn,^{118}Sn)^{160}Dy.

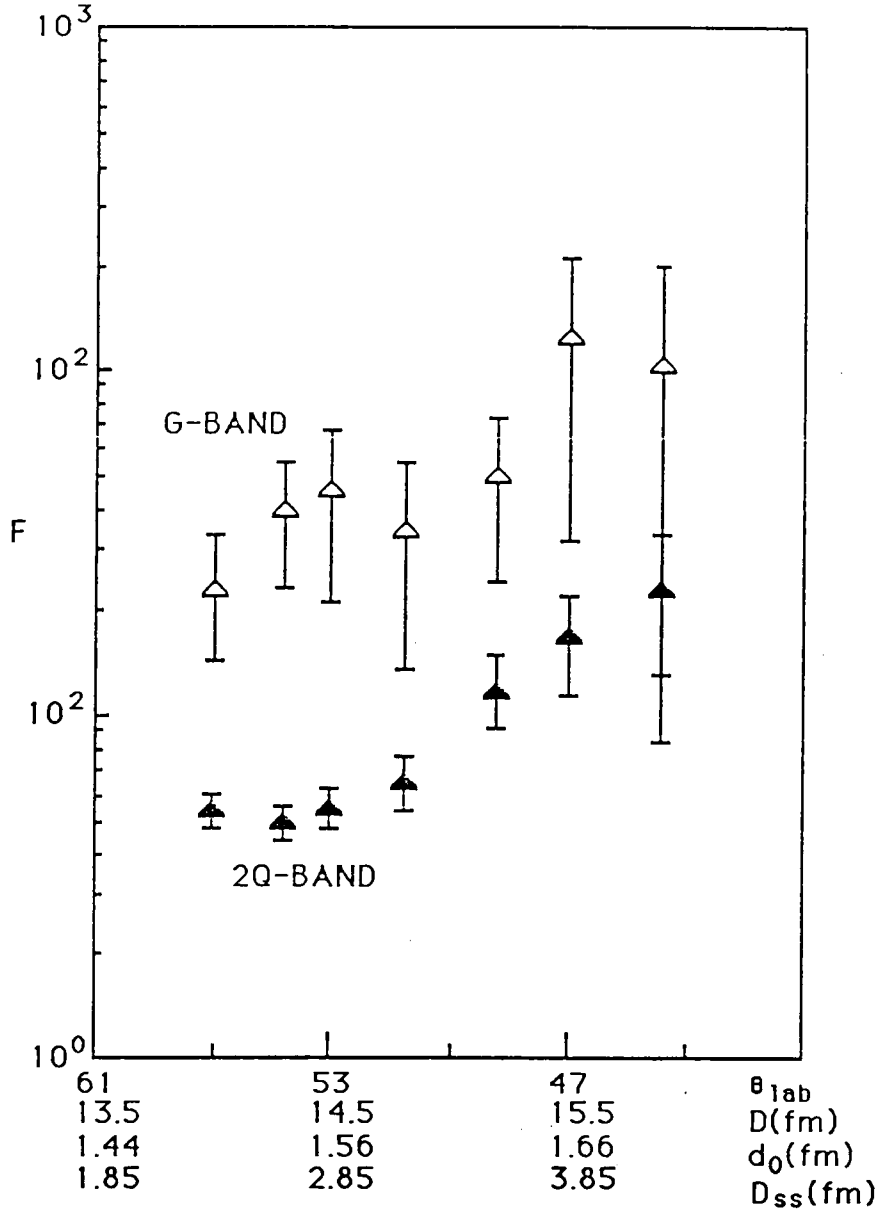


Figure 5.52: Enhancement factors for the ground band population and two-quasiparticle band population as a function of separation distance for the reactions ^{161}Dy(^{58}Ni,^{59}Ni)^{160}Dy and ^{162}Dy(^{58}Ni,^{60}Ni)^{160}Dy.

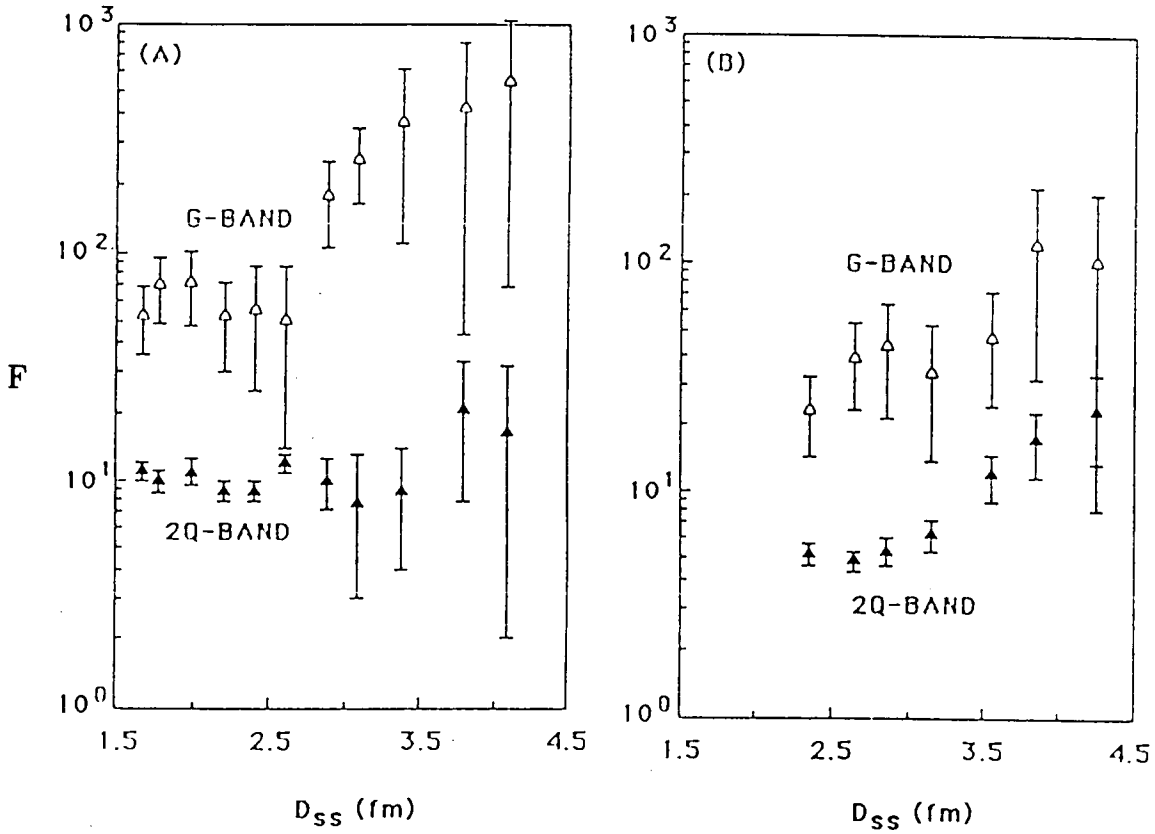


Figure 5.53: Enhancement factors as a function of surface-surface distance (Eq.5.12) between target and projectile nuclei for Sn (A) and Ni (B) experiments.

We find the enhancement factors for the two-quasiparticle band are approximately the same magnitude, but the enhancement factors for the ground band are quite different in the Ni and Sn reactions. At surface-surface distances < 3 fm the enhancement factors in the ground band for the Sn projectile are similar to those for the Ni projectile, but at surface-surface distances > 3 fm the enhancement factors of the ground band for the Sn projectile are 2 - 5 times larger than those for the Ni projectile. If the large distance behavior is dominated by pairing effects, as we would expect, this indicates that there are much larger pairing effects with Sn than with Ni projectiles

CHAPTER 6

SUMMARY AND CONCLUSION

Transfer reactions have long been used to probe nuclear structure. It is well known that one-neutron transfer reactions provide detailed information about nuclear single-particle structure, and two-neutron transfer reactions provide analogous information about pairing correlations. Most early transfer experiments were devoted to studies using light ions. This dissertation presents a series of experimental results for one and two-neutron transfer reactions with very heavy ion beams (^{58}Ni, ^{116}Sn, ^{206}Pb) on deformed and spherical nuclei targets (^{161}Dy, ^{162}Dy, ^{163}Dy, ^{164}Dy, ^{117}Sn, ^{118}Sn, ^{233}U, ^{235}U). The results presented in this work have concentrated on comparison of one and two-neutron transfer reactions to yield information about transfer mechanism and nuclear structure effects.

In summary, we have developed a new method which allows the yrast and near-yrast regions for I $\sim 20\hbar$ to be studied. The key technique is a particle-particle-γ coincidence used in conjunction with the Spin Spectrometer. The particle-particle-γ coincidence allows identification of the exit channel; the Spin Spectrometer provides the reaction total energy and γ-ray multiplicity, which allows identification of the reaction exit channel and an approximate separation of the ground band from other bands. The general features of the (E,M) distribution for one and two-neutron pickup reactions induced by ^{58}Ni and ^{116}Sn projectiles on Dy target nuclei indicates that there are two populations superposed: one centered around the yrast line corresponds to the direct transfer to the ground band; the other above the yrast line by $\sim$ 1 - 2 MeV corresponds to direct transfer to two-quasiparticle bands.

Ge spectra confirm that the bulk of the observed discrete-line γ-rays comes from inelastic excitation of target nuclei, and from one and two-neutron transfer reactions. This is consistent with a simple model for heavy ion induced transfer

reactions: Coulomb excitation in the entrance channel, transfer of nucleons, and Coulomb excitation again in the exit channel. The transfer reactions can populate high spin states: I $\sim 20\hbar$ in the rare earth region, and I $\sim 30\hbar$ in the actinide region are observed.

The cross sections for one and two-neutron transfer reactions are large. At the grazing angle the cross sections for one-neutron transfer reactions are about the same as those of inelastic reactions. The cross sections for two-neutron transfer reactions are about 10% of the inelastic cross sections for a ^{58}Ni beam on a ^{162}Dy target, and about 6% of the inelastic cross sections for a ^{116}Sn beam on a ^{162}Dy target around the grazing a ngle region. The total angular distributions of the transfer cross sections are approximately bell shaped, but the angular distributions for directly populated lower spin states exhibit oscillations which are interpreted as the interference between scattering from different orientations of the deformed nuclei. Such interference had been predicated on theoretical grounds eight years ago.

The one-neutron transfer probability falls exponentially at large distance. This can be explained in a semiclassical barrier penetration theory; the slope is consistent with the theoretically predicted value, but the slope for two-neutron transfer reactions is much smaller than the predicted value. The majority of the cross section populates two-quasiparticle states for which the probability decays exponentially in ion-ion separation with a slope similar to that expected theoretically, but the direct two-neutron transfer to the ground band oscillates at large distance, and the envelope of the oscillation decays very slowly with radial separation. The superposition of these two populations is responsible for the reported slope anomalies in these systems. Thus the long-standing slope anomaly problem has been solved in simple and elegant fashion.

Comparing the probability of one and two-neutron transfer reactions, we

obtained large pairing enhancements in heavy-ion reactions. We have found enhancements of magnitude 10 for transfer to two-quasiparticle states, and of magnitude 70 - 500 in transfer to the ground state rotational band with Sn projectiles on deformed rare-earth nuclei; of magnitude 5 for transfer to two-quasiparticle states, and of magnitude 30 - 100 in the transfer to the ground state rotational band with Ni projectiles on the same nuclei. These results are consistent with the theoretical expectation that superfluid Sn has stronger pairing correlations than Ni, and are the first conclusive demonstration of strong superfluid-superfluid correlations in heavy-ion collisions—effects which have been conjectured theoretically for more than a decade.

Rotational signatures for one and two-neutron transfer reactions have been established. The two-neutron transfer rotational signatures drop with increasing spin much faster than for inelastic scattering. This may be the first evidence of the nuclear "SQUID" effect, although more work is required to confirm this. The probability for one-neutron transfer is found to be anomalously low for transfer to low-spin states; this may be the first evidence for a theoretically-predicted orientation dependent formfactor in such reactions. Again, more work is required to firmly establish this.

In conclusion, transfer reactions with heavy ions are a powerful tool for the study of heavy-ion reaction mechanisms and nuclear structure. 4ϕ γ-ray detection used together with particle-particle-γ coincidence techniques appears to be the best method presently available for studying these reactions. This dissertation demonstrates that a method exists which is already sufficiently precise to answer long-standing and important structure questions with the Spin Spectrometer as the 4ϕ detector. The advent of the proposed "Superball" 4ϕ γ-ray detector would extend these techniques to much weaker reaction channels, and improve the precision in stronger channels by orders of magnitude. This, coupled with expected

advancements in particle detection, would allow information to be extracted from very heavy-ion transfer reactions with a precision and confidence previously thought impossible. The corresponding impact on understanding the interplay between collective and single-particle structure is potentially as great as that which light-ion transfer reactions had in the development of nuclear single-particle structure.

BIBLIOGRAPHY

BIBLIOGRAPHY

Almburger, J., I. Hamamoto, G. Leander, 1980, Nucl. Phys. **A333** 184.

Bantel, M., R. G. Stokstad, Y. D. Chan, S. Wald and P. J. Countryman, 1984, Nucl. Instr. and Meth. **226** 394.

Bardeen, J. L., L. Cooper, and R. Schrieffer, 1957, Phys. Rev. **108** 1175.

Bass, Reiner, 1980, *Nuclear Reactions With Heavy Ions*, (Springer-Verlag, Berlin Heidelberg New York), ed. W. Beiglböck, M. Goldhaber, E. H. Lieb and W. Thirring.

Beckerman, M., R. L. Auble, F. E. Bertrand, J. L. Blankenship, B. L. Burks, C. W. Glover, R. O. Sayer, G. R. Satchler, D. Shapira and R. L. Varner, 1987, Phys. Rev. Lett. **58** 455.

Bengtsson, R. and S. Frauendorf, 1979, Nucl. Phys. **A327** 139.

Bock, R., M. Grosse-Schulte, W. Von Oertzen, 1966, Phys. Lett. **22** 456.

Bohr, A., B. R. Mottelson, and D. Pine, 1958, Phys. Rev. **110** 936.

Boer, F. W. N. de, E. Grosse, W. Spreng, H. J. Wollersheim, E. G. Eckert and Ch. Lauterbach, 1984, GSI Annual Report.

Breit, G.,1959, *Handbuch der Physik*, Vol. XLI/1, (Springer-Verlag, Heidelberg), ed.

S. Flügge.

Broglia, R. A. and A. Winther, 1972, Phys. Rep. **4C** 155

Broglia, R., O. Hansen, and C. Riedel, 1973, Adv. Nucl. Phys. **6** 287.

Broglia, R. A., R. Liotta, B. S. Nilsson and A. Winther, 1977, Phys. Rep. **29C** 293.

Broglia, R. A., C. H. Dasso, S. Landowne, B. S. Nilsson and A. Winther, 1978, Phys. Lett. **73B** 401.

Broglia, R. A., C. H. Dasso, S. Landowne, B. S. Nilsson and A. Winther, 1978, Phys. Lett. **73B** 401.

Broglia, R. A., C. H. Dasso, S. Landowne, B. S. Nilsson, and A. Winther, 1978, Phys. Lett. **73B** 401.

Buttle, P. J. A., L. J. B. Goldfarb, 1966, Nucl. Phys. **78** 409.

Butler, P. A., C. Baktash, C. R. Bingham, M. Carpenter, D. Cline, B. Cox, M. W. Guidry, S. Juutinen, A. E. Kavka, W. J. Kernan, R. W. Kincaid, A. Larabee, I. Y. Lee, X. T. Liu, S. P. Sorensen, E. Vogt, C. Y. Wu, 1987, Phys. Lett. **B191** 333.

Canto, L. F., R. Donangelo, R. S. Nikam and P. Ring, 1987, Phys. lett. B **192** 4.

Chiao, R. Y. and Yong-shi Wu, 1986, Phys. Rev. Lett. bf 57 933.

Czosnyka, T., D. Cline, L. hasselgre, C. Y. Wu, R. M. Diamond, H. kluge, C. Roulet, E. K. Hulet, R. W. Lougheed, and C. Baktash, 1986, Nucl. Phys. **A458** 123.

Dasso, C. H., T. Dossing, S. Landowne, R. A. Broglia, and A.Winther, 1982, Nucl.

Phys. **A389** 191.

Dasso, C. H., S. Landowen, R. A. Broglia, and A. Winter, 1984, Z. Phys. A bf 317 187.

Dasso, C. H. and A. Vitturi, 1986, Phys. Lett. **179B** 337.

Dünnweber, W., H. Morinaga and D. E. Alburger, 1981, Phys. Lett. **106B** 47.

Elbek, B., and P. O. Tj Om, 1969, Adv. in Nucl. Phys. **3** 259.

Esbensen, H., S. Landowne and C. Price, 1987a, Phys. Rev. **C36** 1216.

Esbensen, H., S. Landowne and C. Price, 1987b, Phys. Rev. **C36** 2359.

Esbensen, H., and S. Landowne, 1987c, Nucl. Phys. **A467** 136.

Frahn, W. E., 1971, Phys. Rev. Lett. **26** 568.

Frauendorf, S. and V. V. Pashkevich, 1984, Phys. Lett. **141b** 23.

Garrett, J. D., 1984, Nucl. Phys. **A421** 313c.

Glendenning, N. K., 1983, *Direct Nuclear Reactions*, (Academic Press, New York-London).

Götz, U., M. Ichimura, R. A. Broglia and A. Winther, 1975, Phys. Rep. **16C** 117.

Guidry, M. W., T. L. Nichols, R. E. Neese, J. O. Rasmussen, L. F. Oliveira, and R. Donangelo, 1981, Nucl. Phys. **A361** 275.

Guidry, M. W. , R. E. Neese, C. R. Bingham, et al, 1984, Nucl. Phys. **A430** 485.

Guidry, M. W. , S. Juutinen, X. T. Liu, C. R. Bingham, A. J. Larabee, L. L. Riedinger, C. Baktash, I. Y. Lee, M. L. Halbert, D. Cline, B. Kotlinski, W. J. Kernan, T. M. Semkow, D. G. Sarantites, K. Honkanen, and M. Rajagopalan, 1985a, Phys. Lett. **163B** 79.

Guidry, M. W., R. W. Kincaid, and R. Donangelo, 1985b, Phys. Lett. **150B** 265.

Guidry, M. W., 1985, Conf. on Nucl. Structure with Heavy Ions, R.A. Ricci and C. Villi, eds., Italian Physical Society, p. 99.

Hillis, D. L., J. D. Garrett, O. Christensen, B. Fernandez, G. B. Hagemann, B. Herskind, B. B. Back, and F.Folkmann, 1979, Nucl. Phys. **A325** 216.

Himmele, G., H. Backe, P. A. Butler, D. Habs, V. Metag, H. J. Specht and J. B. Wilhelmy, 1983, Nucl. Phys. **A404** 401.

Hodgson, P. E., 1978, *Nuclear Heavy-Ion Reactions*, (Clarendon Press, Oxford).

Holm, G. B., J. R. Burwell, and W. D. Miller, 1961, Phys. Rev.**122** 1260.

Isoya, A., 1963, Phys. Rev. **130** 234.

Jääskeläinen, M. , D. G. Sarantites, R. Woodward, F. A. dilmanian, J. T. Hood, R. Jääskeläinen, D. C. Hensley, M. L. Halbert, and J. H. Barker, 1983, Nucl. Instr. Meth. **204** 385.

Josephson, B. D., 1962, Phys. Lett. **1** 251.

Johnson, N., I. Y. Lee, C. Baktash, F. K. McGowan, J. W. Johnson, R. P. Cumby, D. C. Hensley, M. L. Halbert, L. L. Riedinger, D. G. Sarantites, J. W. McConnell and M. E. Whitley, 1985, ORNL Physics Division Progress Report for the Period

Ending September 30, p. 158.

Juutinen, S., X. T. Liu, S. P. Sorensen, M. W. Guidry, D. Cline, W. J. Kernan, M. L. Halbert, I. Y. Lee, C. Baktash, 1985, ORNL Physics Division Progress Report, 104

Juutinen, S., X. T. Liu, S. P. Sorensen, B. Cox, R. W. Kincaid, C. R. Bingham, M. W. Guidry, W. J. Kernan, C. Y. Wu, E. Vogt, T. Czosnyka, D. Cline, M. L. Halbert, I. Y. Lee, C. Baktash, 1987, Phys. Lett. **B192** 307

Kahana, S. and A. J. Baltz, 1977, Adv. Nucl. Phys. **9** 345.

Koenig, J., H. Bohn, T. Faestermann, P. Kienle, H. J. Körner, W. A. Mayer, D. Pereira, K. E. Rehm, and H. J. Scheerer, 1981, Phys. Rev. **C24** 2076.

Kwato Njock, M., M. Maurel, E. Monnand, H. Nifenecker, J. Pinston, F. Schussler and D. Barneoud, 1986, Phys. Lett. B **175** 125.

Liu, X. T., S. Juutinen, C. R. Bingham, L. L. Riedinger, and M. W. Guidry, 1985a, Bull. Am. Phys. Soc. **30** 1027.

Liu, X. T., M. W. Guidry, S. Juutinen, S. C. R. Bingham, R. W. Kincaid, M. P. Carpenter, A. Larabee, C. Baktash, I. Y. Lee, M. L. Halbert D. Cline, C. Y. Wu, W. Kernan, E. Vogt, 1985b, ORNL Physica Division Progress Report, **ORNL-6233**, 106.

Liu, X. T., M. W. Guidry, S. Juutinen, S. P. Sorensen, R. W. Kincaid, C. Y. Wu, D. Cline, W. Kernan, E. Vogt, C. Baktash, I. Y. Lee, M. L. Halbert, 1986, Bull. Am. Phys. Soc. **31** 787.

Liu, X. T., C. Y. Wu, S. P. Rensen, R. W. Kincaid, X. L. Han, M. W. Guidry, D. Cline, W. J. Kernan, E. Vogt, T. Czosnyka, and A. E. Kavka, 1988, submitted to Phys. Lett. **B**.

Liu, X. T., M. W. Guidry, S. P. Sorensen, R. W. Kincaid D. Cline, C. Y. Wu, W. J. Kernan, T. Czosnyka, and A. E. Kavka, 1988b, to be published.

Macfarlane, M. H. and J. P. Schiffer, 1974, in *Nuclear Spectroscopy and Reactions* part B, (Academic Press, New York-London), Ed. J. Cerny.

Macchiavelli, A.O., M. A. Deleplanque, R. M. Diamond, F. S. Stephens, E. L. Dines, J. E. Draper, 1985, Nucl. Phys. **A432** 436.

Massmann, H. and J. O. Rusmussen, 1975, Nucl. Phys. **A243** 155.

Monaco, L. L. and D. M. Brink, 1985, Nucl. Phys. **11** 935.

Mottelson, B. R., and J. G. Valatin, 1960, Phys. Rev. Lett. **5** 5.

Nikam, R. S., P. Ring, and L. F. Canto, 1986, Z. Phys. **324** 241.

Nikam, R. S. and P. Ring, 1987. Phys. Rev. Lett. **58** 980.

Von Oertzen, W., B. Gebauer, A. Gamp, H.G. Bohlen, F. Busch, D. Schull, 1983, Z. Phys. **A313** 189.

Von Oertzen, W., H. G. Bohlen, B. Gebauer, R. Künkel, F. Pühlhofer and D. Schüll, 1987, Z. Phys. A Atomic Nuclei **326** 463.

Ower, H., T. H. Elze, J. Idzko, K. Stelzer, E. Grosse, H. Emling, P. Fuchs, D. Schwalm, H. J. Wollersheim, N. Kaffrel, and N. Trautmann, 1982, Nucl. Phys.

A **388** 421.

Phillips, W. R., 1977, Rep. Prog. Phys. **40** 345.

Preston, M. A. and R. K. Bhaduri, 1975, *Structure of the Nucleus*, (Addison-Wesley Publishing Company, Inc., Reading, Massachusetts) .

Price, C., H. Esbensen and S. Landowne, 1987, Phys. Lett. B **195** 524.

Rehm, K. E., D. G. Kovar, W. Kutschera, M. Paul, G. Stephans and J. L. Yntema, 1981, Phys. Rev. Lett. **51** 1426.

Rhoades-Brown, M. J. , R. J. Donangelo, M. W. Guidry,and R. E. Neese, 1984, Phys. Rev. **24** 485.

Sachs, M. W., V. Chasman, D. A. Bromley, 1965, Phys. Rev. **139** B92.

Sapotka, K., R. Bass, V. Hartmann, H. Noll, R. E. Renfordt, and K. Stelzer, 1985, Phys. Rev. **C31** 1297.

Sarantites, D. G., L. Westerberg, M. L. Halbert, R. A. Dayras, M. L. Halbert and J. H. Barker, 1978, Phys. Rev. **C18** 774.

Sarantites D. G., R. Lovett, R. Woodward, 1980, Nucl. Instrum. Methods **171** 503.

Satchler, G. R., 1958, Ann. Phys. **3** 275.

Satchler, G. R., 1964, Nucl. Phys. **55** 1.

Satchler, G. R., 1980, *Introduction to Nuclear Reactions*, (John Wiley and Sons, New York).

Satchler, G. R., 1983, *Direct Nuclear Reactions*, (Clarendon Press, Oxford and Oxford University Press, New York).

Schädel, M., W. Brügger, H. Gäggeler, K. J. Moody, D. Schardt, K. Sümmerer, E. K. Hulet, A. D. Dougan, R. J. Dougan, J. H. Landrum, R. W. Lougheed, J. F. Wild and G. D. O'Kelley, 1986, Phys. Rev. C **33** 1547.

Siekmann, H. , B. Gebauer, H.G. Bohlen, H. Kluge, W. Von Oertzen, P. Froebrich, B. Strack, K. D. Hildenbrand, H. Sann, and U. Lynen, 1982, Zeit. Phys. **A307** 113.

Tjϕm, P. O., I. Espe, G. B. Hagemann, B. Herskind, and D. L. Hillis, 1978, Phys. Lett. **72B** 438.

Van Den Berg, A. M., K. E. Rehm, D. G. Kovar, W. Kutschera and G. S. F. Stephans, 1987, Phys. Lett. **194** 334.

Vergnes, M. N. and R. K. Sheline, 1963, Phys. Rev. **132** 1736.

Weiss, H. , 1979, Phys. Rev. **19C** 834.

Wu, C. Y., X. T. Liu, S. P. Sorensen, R. W. Kincaid, M. W. Guidry, D. Cline, W. J. Kernan, E. Vogt, T. Czosnyka, A. E. Kavka, M. A. Stoyer, J. O. Rasmussen, and M. L. Halbert, 1987, Phys. Lett. **188B** 25.

Wu, C. Y., X. T. Liu, W. J. Kernan, D. Cline, T. C.zosnyka, M. W. Guidry, A. E. Kavka, R. W. Lincaid, B. Kotlinski, S. P. Sorensen, and E. Vogt, 1988, submitted to Phys. Rev. C

VITA

Xin-Tao Liu was born in Shen-Yang of Liao-Ning province of The People's Republic of China on September 18, 1944. In the fall of 1962, he entered Ji-Lin University, and in June 1968 he received his Bachelor of Science degree in Physics. On January 18, 1970, he married Rui-Fang Zhang. He began his graduate studies in nuclear physics at Ji-Lin University in the fall of 1979. In September of 1982, he accepted a teaching assistantship at the University of Tennessee, Knoxville in the Department of Physics and Astronomy in the United States. At the same time he began his studies towards a Doctoral degree in Physics. In the summer of 1983, he began working as a research assistant with the nuclear physics group at the university.

The author is presently employed by the University of Tennessee.